EPFL

High-throughput and adaptive super-resolution fluorescence microscopy of organelles

Dora MAHECIC

■ École
polytechnique
fédérale
de Lausanne

2020

Acknowledgements

First, I would like to thank my thesis supervisor and mentor Prof. Suliana Manley for giving me the opportunity to be a part of her lab, meet amazing scientists and work on fascinating projects. I have learned so much over the past 4 years, and the skills and experience I have gathered here will follow me throughout my future career, wherever that might be.

I would also like to thank the members of my thesis defense jury Prof. Bo Huang, Dr. Uri Manor, Prof. Aleksandra Radenovic and Dr. Martin Weigert, for their time and valuable feedback. While I am saddened to not have met all of you in person, I am hopeful that our paths will cross in the near future!

Next, thank you to all the past and present lab members for enriching my every workday with stimulating discussions. More specifically, a big thank you to Anna Archetti, Isabelle Coke, Gaby Correa, Kyle Douglass, Davide Gambarotto, Juliette Griffié, Khalid Ibrahim, Tatjana Kleele, Ambroise Lambert, Sofia Magkiriadou, Hélène Perreten Lambert, Timo Rey, Christian Sieben, Jenny Sülzle, Aster Vanhecke, Quentin Wannebroucq, Julius Winter, Sofia Zaganelli, Chen Zhang. Finally, special thanks to Lina Carlini for her contagious enthusiasm for science and teaching me so much when I first joined.

During my time here, I got to work with many amazing scientists and I would like to acknowledge their contributions and thank them for joining me on my scientific projects: Niccoló Banterle, Charlotte Bost, Adai Colom, Denis Fortun, Prof. Pierre Gönczy, Antoine Goujon, Maeva Le Guennec, Prof. Paul Guichard, Virginie Hamel, Prof. Stefan Matile, Prof. Aurélien Roux. Along the way I also got to meet and talk to a lot of wonderful scientists and I thank them for inspiring discussions and great feedback: Alistair Curd, Raoul Kirchner, Daniel Sage, Lin Shao, Hari Shroff, Phan Than, Andrew York.

Finally, an infinite thank you to my friends and family – especially my mum Darja, my dad Andrej and my brother Janko for their unconditional love and support! Whether to share good news or during more difficult times, I always knew I could count on you!

Abstract

Fluorescence super-resolution microscopy has allowed unprecedented insight into the workings of biological systems below the diffraction limit of light. Over the past decade, it has overcome several challenges to deliver 3D, multi-color and faster imaging techniques, which have found many applications in deciphering the workings and structure of organelles – specialized cellular compartments whose shape and dynamics serve their specific functions. However, most super-resolution techniques are laborious and slow, and there are existing challenges in achieving sufficient throughput for collection of large datasets and capturing dynamic processes in living cells. The aim of this thesis is to address issues of limited throughput, temporal resolution and live-cell compatibility, with application to centriole architecture and mitochondrial dynamics.

The design of a novel flat-fielding module for multi-focal excitation which – once integrated into an instant structured illumination microscope – allows the capture of larger fields of view with uniform illumination and hence results in increased throughput. This flat-fielded microscope allows multi-color, 3-dimensional imaging at double the diffraction-limited resolution of up to 100 mammalian cells within 1-2 minutes. Furthermore, combined with advanced sample preparation using expansion microscopy, the setup achieves an effective resolution of ~35 nm, comparable to some of the more powerful super-resolution techniques, but at 100-1000 times increased throughput. To showcase this improvement, we study the distribution of post-translational modifications within the centriole, revealing previously unobserved molecular organization.

Second, with fast, live-cell imaging, we investigate the role of membrane bending energy and tension in mitochondrial division. While many molecular factors involved in this process have been identified, little is known about its physical requirements. By analyzing mitochondrial constrictions enriched in Drp1 that divide successfully or reverse, we establish that mitochondrial constrictions with higher bending energy are more likely to divide. Furthermore, by analyzing changes in mitochondrial shape and employing a novel membrane tension sensor, we observe that conditions under which mitochondrial membrane tension is increased, result in more successful divisions. These observations are supported by a model in which membrane bending energy increases the elastic energy at the constriction site, bringing it closer to the energy barrier to fission, while membrane tension acts as a fluctuation to overcome the remaining residual energy.

Finally, to overcome existing trade-offs between temporal resolution and imaging duration, we develop a acquisition framework for smart and adaptive temporal sampling. By adapting the temporal resolution is in response to events of interest, they are captured at high imaging speed, while preserving the sample during a lack thereof. Using the accumulation of Drp1 to detect mitochondrial constriction sites allowed us to adapt the imaging speed to capture mitochondrial constrictions at high temporal resolution while preserving the sample when such events are lacking. Overall, this framework provides both high temporal resolution and long imaging times when needed, decreasing resulting phototoxicity, photobleaching and amount of redundant data.

Keywords

Résumé

La microscopie à super-résolution a fourni une perspicacité au fonctionnement des systèmes biologiques en dessous de la limite de diffraction. Au cours des derniers ans, il a surmonté plusieurs défis pour fournir des techniques d'imagerie 3D, multicolores et plus rapides, qui ont trouvé de nombreuses applications dans les études des organites - des compartiments cellulaires spécialisés dont la forme et la dynamique servent leurs fonctions spécifiques. Mais, la plupart des techniques de super-résolution sont complexes et lentes, et il existe des défis pour atteindre un débit élevé pour de grands ensembles de données et capturer des processus dynamiques dans des cellules vivantes. Le but de cette thèse est d'aborder les problèmes de débit limité, de résolution temporelle et de compatibilité avec des cellules vivantes, avec une application à l'architecture centriole et à la dynamique mitochondriale.

La conception d'un nouveau module de champ plat pour une excitation multifocale qui - une fois intégré dans un microscope instantané à éclairage structuré - permet la capture de grands champs de vision avec un éclairage uniforme et donc une augmentation du débit. Ce microscope à champ plat permet une imagerie 3D multicolore à une résolution doublée de jusqu'à 100 cellules en 1-2 minutes. En outre, combinée avec la microscopie à expansion, on atteint une résolution effective de ~35 nm, comparable à des techniques de super-résolution les plus puissantes, mais à un débit 100-1000 fois plus élevé. Pour mettre en évidence cette amélioration, nous étudions la distribution des modifications post-traductionnelles de centriole, révélant une organisation jusque-là cachée.

Ensuite, nous étudions le rôle de l'énergie et de la tension membranaire dans la division mitochondriale. Bien que de nombreux facteurs moléculaires impliqués aient été identifiés, on en sait peu sur les exigences physiques. En analysant les constrictions mitochondriales enrichies en Drp1 qui se divisent ou s'inversent, nous établissons que les constrictions mitochondriales avec une énergie plus élevée sont plus susceptibles de se diviser. En outre, en analysant les changements de forme mitochondriale et en utilisant un nouveau capteur de tension membranaire, nous observons que les conditions dans lesquelles la tension membranaire mitochondriale est augmentée, entraînent des divisions plus réussies. Ces observations sont soutenues par un modèle dans lequel l'énergie de la membrane augmente l'énergie élastique au site, la rapprochant de la barrière énergétique à la fission, tandis que la tension membranaire agit comme une fluctuation pour surmonter l'énergie résiduelle restante.

Enfin, pour surmonter les compromis existants entre la résolution temporelle et la durée d'imagerie, nous développons un cadre d'acquisition pour un recueil temporel intelligent et adaptatif. En adaptant la résolution temporelle en réponse à des événements d'intérêt, ils sont capturés à une vitesse d'imagerie élevée, tout en préservant le spécimen en cas d'absence. L'utilisation de l'accumulation de Drp1 pour détecter les sites de constriction mitochondriale nous a permis d'adapter la vitesse d'imagerie pour les capturer à haute résolution temporelle tout en préservant l'échantillon lorsqu'en cas contraire. Dans l'ensemble, ce cadre fournit à la fois une résolution temporelle élevée et de longs temps d'imagerie, ce qui diminue la phototoxicité, le photoblanchiment et la quantité de données redondantes.

Mots-clés

microscopie à super résolution de fluorescence, microscopie instantané à illumination structuré, convertissement de faisceau à intensité uniforme, architecture de la centriole, division mitochondriale, microscopie intelligente

Table of Contents

List of Figures

List of Tables

List of Equations

List of Equations

Chapter 1
Introduction

The ability to visualize structures of interest with high specificity has made fluorescence microscopy one of the most popular tools in the life sciences. However, the diffraction limit of light poses a barrier in resolving features below ~250 nm, obscuring many cellular structures such as organelles. The development of super-resolution microscopies[1,2] has since overcome this limit, and enabled the study of biological structures in molecular detail. Since then, super-resolution microscopy has undergone constant improvement and overcome initial challenges[3], to address numerous previously unresolvable biological questions[4].

While super-resolution microscopy has become an established tool in biological research, limited throughput remains a major bottleneck in extending its application to quantitative biology and advanced analysis tools that often require access to large datasets. Furthermore, important challenges remain in achieving simultaneously improved resolution, fast imaging speed and live-cell compatibility required for studying highly dynamic biological processes.

The aim of this thesis is to develop methods for high-throughput and adaptive super-resolution fluorescence microscopy for studying subcellular organelles, including mitochondria and the centriole. Capturing larger datasets requires technical improvements such as optimized illumination strategies for simultaneous imaging of larger parts of the sample. Furthermore, adaptive imaging strategies improve the imaging conditions and resource allocation on the fly to produce better quality and more useful data. Finally, the tools developed here are applied to study the architecture of the centriole, and the mechanical requirements of mitochondrial division. The work is presented along the following outline:

Chapter 2 presents the necessary background and concepts relating to the work presented in the thesis, and a brief overview of the state of the field.

Chapter 3 presents a novel flat-fielding solution for multifocal excitation based on the Koehler integrator, termed the multi-focal flat illumination for field-independent imaging (mfFIFI). Integrating mfFIFI into a custom-built iSIM enables fast, multi-color, 3D imaging of mammalian cells and expanded samples over FOVs spanning >100x100 μm^2. Furthermore, a combination of this high-throughput iSIM setup with expansion microscopy allows the study of post-translational modification distribution within the centriole at an effective resolution of ~35 nm to reveal previously unobserved molecular organization.

Chapter 4 uses live-cell super-resolution SIM imaging to study the physical parameters required for mitochondrial division. By examining many mitochondrial constriction events, we find that not all constrictions result in division, but a subset reverses back to an unconstricted state. Using these events to compare the bending energy and membrane tension requirements for mitochondrial division allows us to establish a physical model, based on in situ estimates of membrane bending energy and tension, which accounts for the observed probability distribution of mitochondrial division.

Chapter 5 presents a novel imaging framework, termed smart and adaptive temporal sampling (SATS) which balances the trade-off between imaging speed and duration by adapting the temporal resolution during events of interest, while not exposing the sample to unnecessary irradiance. As proof of principle, we consider the specific case of mitochondrial division – a relatively fast but infrequent event. The SATS framework allows us to capture mitochondrial division events at high temporal resolution, while reducing unnecessary photobleaching and photodamage, and producing less but more useful data.

Chapter 6 summarizes the outcomes of the thesis and discusses the outlook for future experiments and outstanding questions that come out of this work.

The results presented in this thesis are the work of the author, Dora Mahecic, unless noted otherwise. All other contributions from collaborators are noted in the Acknowledgement section and disclosed at the beginning of each chapter.

Chapter 2
Background

Super-resolution principles and methods

Different functions within the cell are compartmentalized into organelles. For example, mitochondria are responsible for energy production and their network is constantly remodeled in response to cellular demand[5], while the centrioles harbor microtubule organizing centers and their number is tightly controlled throughout the cell cycle[6]. The structure of these organelles has evolved to serve their specific function. Therefore, the ability to visualize these organelles is critical for our understanding of the underlying biological processes. Fluorescence light microscopy is a popular tool in biological research due to its ability to fluorescently label specific targets and has enabled biologist to capture the dynamic and sub-cellular localization of these organelles. However, fluorescence microscopy is affected by the diffraction limit of light, and hence to a minimum resolvable length scale d:

$$\text{Lateral direction: } d_{x,y} = \frac{\lambda}{2n \sin \theta} = \frac{\lambda}{2NA} \qquad \text{Axial direction: } d_z = \frac{2\lambda}{n^2 \sin^2 \theta} = \frac{2\lambda}{NA^2}$$

Equation 1 - Abbe's diffraction limit of light

Where λ is the wavelength of light, n the refractive index, θ the half-angle of the collected light and NA the numerical aperture of the system[7]. In the context of conventional fluorescence microscopy, this sets the limit on features that can be correctly resolved at ~250 nm laterally and ~700 nm axially. In other words, imaging an object smaller than diffraction limit through a microscope will produce a diffraction limited spot – which will approximate the impulse response of the microscope, termed the point-spread function (PSF). Extending this to more complex structures results in an image $I(x,y)$ that will be the result of a convolution of the underlying object $O(x,y)$ with the PSF:

$$I(x,y) = O(x,y) \otimes PSF(x,y)$$

Equation 2 - Image formation equation

This effect is illustrated in Figure 1.
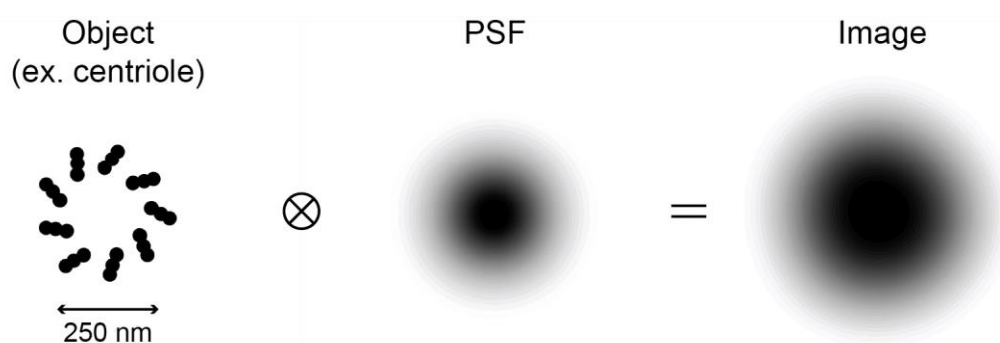
Figure 1 - Visual representation of the image formation equation.
An organelle such as the centriole (left) is convolved by the microscope PSF (middle) to form the image as observed through the microscope (right).

Overall, biological processes take place across a range of length-scales, where proteins and molecules on the nanoscale dictate the fate of organelles, cells and beyond. While diffraction-limited resolution is sufficient to capture larger features of these organelles such as their general shape, it becomes problematic for studying their sub-organellar organization, especially for smaller organelles such as

centrioles which span 250 nm in diameter. Even for larger organelles such as mitochondria that can span several micrometers in length, most sub-organellar features, such as mitochondrial constrictions which can reach <200 nm diameters and are not resolvable by conventional light microscopy. Therefore the ability to surpass the diffraction limit of light to capture the nanoscale dynamics and structure of these processes is essential. The development of super-resolution microscopy has led to a group of techniques capable of resolving features below the diffraction limit of light. They employ different optical tricks or priors, but the two main strategies rely on localizing individual point emitters in single molecule localization microscopy (SMLM) and/or by patterning the excitation light to reshape the size of the effective microscope PSF.

Single molecule localization microscopy

Single molecule localization microscopy (SMLM) techniques rely on the ability to determine the position of a single point emitter with a better precision than the size of its PSF, depending on the number of collected photons. This is achieved by fitting the imaged diffraction limited emission spots to the microscope PSF. The PSF is commonly estimated by a Gaussian profile, such that fitting the PSF to find the center of the profile allows a localization with precision σ [8]:

$$\sigma \sim \frac{\sigma_{PSF}}{\sqrt{N}}$$

Equation 3 - Thompson localization precision formula

Where N is the number of collected photons and σ_{PSF} the standard deviation of the PSF.
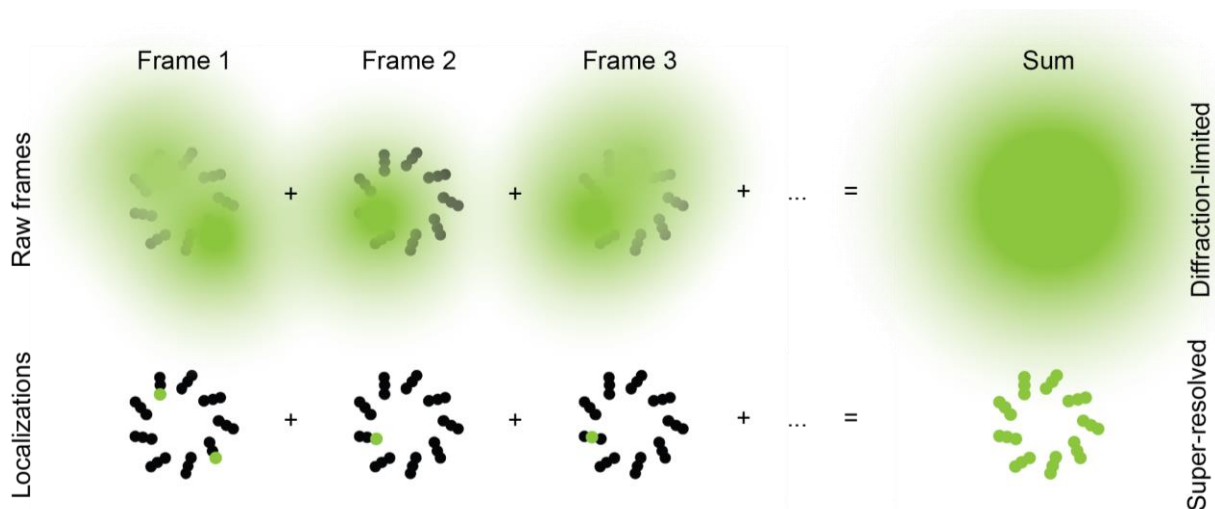
Figure 2 - Principle of single molecule localization microscopy.
All emitters are turned off, before being stochastically turned into a light emitting on state, localized and turned off again. By iterating this procedure through hundreds-thousands of frames, a super-resolved image can be reconstructed by summing together all the individual localizations.

To localize individual emitters within a structure, they must be separated in time by switching from an emissive on state to a dark off state – termed photoswitching or blinking. The photoswitching behavior needs to be tuned to achieve a sufficiently low emitter density, so the emitters can be well separated and localized with good precision. Different subsets of emitters are then iteratively turned on and off, until a sufficient number of localizations is collected to sample the underlying structure. Finally, the localizations from the individual frames are combined into a single super-resolved image (Figure 2).

This principle can be implemented with fluorescent proteins in photo-activated localization microscopy (PALM)[2] , synthetic dyes in stochastic optical reconstruction microscopy (STORM)[9] or other methods that use the binding and unbinding of diffusing probes to achieve similar blinking behaviour[10,11].

In SMLM, there is a clear trade-off between the density of emitters, spatial and temporal resolution. Having a low emitter density, avoids overlap between emitters and allows their precise localization, providing better resolution but requires longer acquisition times to sample the whole structure of interest. On the other hand, by relaxing the requirement for isolated emitters, they are more likely to overlap degrading the resolution, but more localizations can be collected faster. Inducing efficient photoswitching usually requires high laser irradiances and toxic chemical buffers, limiting the applicability of STORM to live cells. An attractive alternative are chemically reduced dyes which can be spontaneously re-oxidized within the living cell without the need for toxic imaging buffers, providing higher brightness and density of emitters[12], which can also be used for live-cell time-lapse STORM imaging[13].

Patterned illumination techniques

The second group of techniques encodes additional information into the excitation pattern, the knowledge of which allows the size of the effective PSF to be reduced and therefore improves the resolution. Recently, techniques such as MINFLUX[14], and variants thereof[15–17] have emerged that combine the SMLM principle with patterned illumination to improve the localization precision.

Stimulated emission depletion

Stimulated emission depletion (STED)[1] uses a focused excitation beam and a hollow, donut-shaped depletion beam to reduce the size of the region in the sample in which the fluorophores are allowed to emit light. This effectively shrinks the size of the excitation PSF, improving the resolution. However, STED requires high laser irradiances and is hence incompatible with long-term live-cell imaging.

Interference-based structured illumination microscopy

Structured illumination microscopy (SIM)[18,19] uses a sinusoidal excitation pattern to create an interference with the underlying structure of the sample. To understand the principle behind the improvement in resolution, it is easier to consider the imaging process in frequency or Fourier space. The frequency content of the imaging process can be described in Fourier space through the optical transfer function (OTF) – the Fourier transform of the PSF. The diffraction limit presents itself in the OTF as a ring or spheroid (depending on 2D or 3D acquisition) encircling the observable region and marking the cut-off frequency, i.e. the smallest resolvable feature (Figure 3).
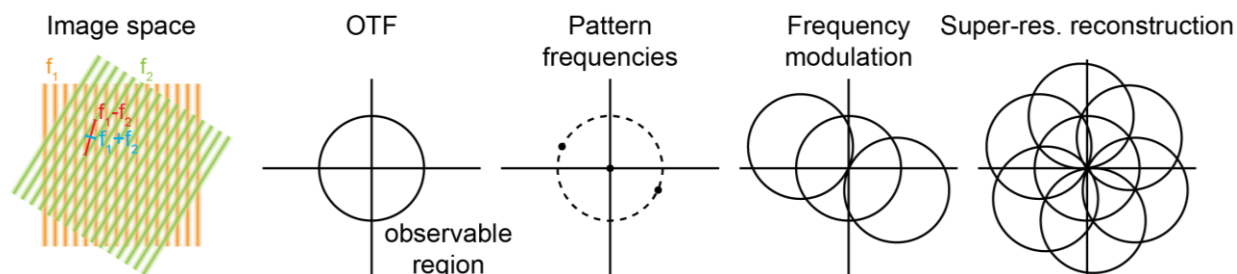
Figure 3 - Principle of structured illumination microscopy.
Superposing two patterns of frequencies f_1 and f_2 produces beat frequencies corresponding to the sum (f_1+f_2) and difference (f_1-f_2). In Fourier space, this this convolves the existing OTF with the beat frequencies, and hence projects some of the high frequency content from outside the observable region, to a lower observable frequency. Using knowledge of the pattern then allows the reconstruction of the super-resolved image by placing back the

different frequency components to their correct position. Shifting and rotating the pattern is then necessary to completely cover the frequency domain to achieve homogeneous resolution. Figure inspired by ref[18].

Superposing the sample with the structured illumination with a known frequency results in frequency mixing. Frequency mixing creates two new frequencies - the sum and difference of the superimposed frequencies. While the summed frequencies are usually lost since they fall outside of the observable region of the microscope, the lower, difference frequency will cause some of the unobservable frequencies beyond the cut-off frequency in the OTF to get shifted into the observable region (Figure 3). Therefore, knowledge of the frequency of the superimposed pattern allows one to digitally reassign the different frequency components to their correct positions during post-processing. While linear SIM is limited to a two-fold improvement in resolution (due to the finest projected pattern being diffraction limited), non-linear SIM[20,21] has promised theoretically unlimited resolution. Linear SIM is compatible with live-cell imaging, as it uses orders of magnitude lower laser intensities.

Confocal and point-scanning structured illumination microscopy

While traditional SIM uses sinusoidal excitation for interference-based improvement in resolution, another set of techniques relies on point scanning structured illumination. Fundamentally, these are based on one of the most commonly used microscopes – the confocal microscope. The confocal principle effectively narrows the size of the PSF by a factor of $\sqrt{2}$, by focusing the excitation light on the sample and detecting the emission through a pinhole. While confocal microscopy is not commonly used as a super-resolution technique, it has potential for a 2-fold improvement in resolution[22].

In the confocal microscope, the effective PSF is defined as the product of the excitation PSF (PSF_{ex}) and the emission PSF (PSF_{em}) convolved by the size of the detection pinhole (PH):

$$PSF = PSF_{ex} \cdot (PSF_{em} \otimes PH)$$

Equation 4 - Point-spread function of a confocal microscope

Using an infinitely small pinhole ($PH \approx \delta(x)$) therefore allows a confocal microscope to achieve a PSF that is 1.4-fold narrower. In frequency space, multiplying the PSFs corresponds to convolution the OTFs and therefore provides a doubling in the frequency content[22], i.e. deconvolving the raw image will lead to the full 2-fold improvement in resolution. However, there is a trade-off in the size of the pinhole used for detection – having a closed pinhole improves the resolution but rejects a lot of light resulting in a low signal-to-noise ratio (SNR). On the other hand, opening the pinhole will improve the signal but at a cost to the resolution.

A proposed solution was to instead use an array of nearly closed pinholes (such as pixels on a camera detector) to achieve the doubling in resolution, and combine their readouts to maintain the high signal[22]. However, since this requires the use of a spatial detector, some pixels will detect the signal off-axis compared to the center of the excitation beam. This misalignment will cause a shift in the images recorded by off-axis pixels, i.e. the collected image is displaced by half the distance of the detector to the optical axis (Figure 4). Therefore simply summing the off-axis signals from the off-axis pixels will not improve the resolution. Instead the signal from each off-axis pixel should be shifted back by half the distance of the detector to the optical axis[22,23] (Figure 4) in order to correct the effect of misalignment, before summing. In other words, for a pixel displaced by a distance d, the position of the effective PSF will be offset by $d/2$ and should be shifted by $d/2$ towards the optical axis.
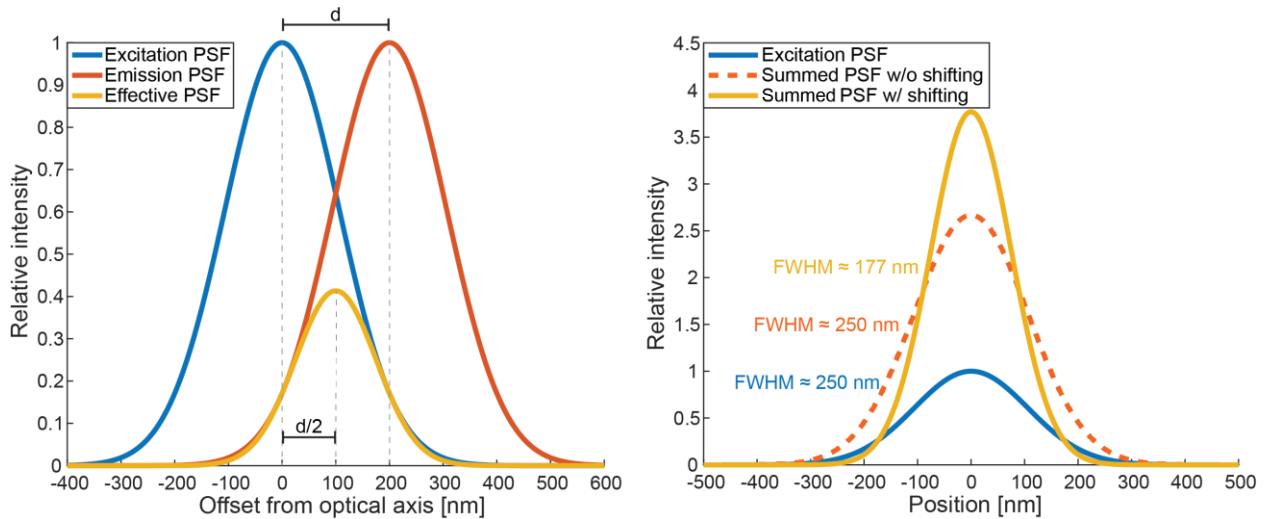
Figure 4 - Principle of image scanning microscopy or point-scanning structured illumination microscopy.
In confocal microscopy, the effective PSF (left, yellow curve) is the product of the excitation and emission PSFs (left, blue and red curves respectively). Detecting with a pinhole offset by a distance d from the optical axis, will cause the effective PSF to be shifted by a distance $d/2$ from the true position of the signal (left, yellow curve). Summing the signals from the individual shifted pinholes will therefore not improve the resolution (right, dashed orange curve), although the FWHM of the effective PSF is sharper (left, yellow curve) with respect to the excitation and emission PSFs (left, blue and red curves respectively). Instead, the position of the effective PSFs must be corrected before summation (right, yellow curve), to result in a $\sqrt{2}$ improvement in resolution, while simultaneously improving the SNR of the resulting image.

Digitally reassigning pixels to their correct position to improve the resolution of confocal imaging has been implemented in several techniques, such as image scanning microscopy (ISM)[23], the commercial Airyscan system[24] and in parallelized versions such as multifocal SIM (MSIM)[25]. However, due to digital image post-processing, these techniques are relatively slow since they require acquiring an image at each scan position to correct and combine multiple exposures into a single super-resolved image.

This issue was addressed by the realization that the same image processing operations done in post-processing could be implemented in an analog manner using optical components. In fact, a $d/2$ shift correction applied to a pixel at a distance d, corresponds to locally rescaling the field incident on the detector by a factor of ½, which can be implemented using a single lens and simple ray optics:

$$\frac{1}{o} + \frac{1}{i} = \frac{1}{f}$$

Equation 5 - Thin lens equation

To rescale the image by a factor of 2, a magnification of $M = -\frac{i}{o} = \frac{1}{2}$ is imposed and hence:

$$\frac{1}{-2i} + \frac{1}{i} = \frac{1}{f} \quad \Rightarrow i = f, o = -2f$$

Equation 6 - Achieving 2-fold contraction with a single lens.

Therefore, using a lens and positioning it correctly to resize the image by a factor of 2 would provide the correct shift of the signal optically.

Hence the first all-optical, parallelized implementation of this principle was implemented in the instant SIM (iSIM)[26]. The iSIM uses parallelization in the form of multi-focal excitation and analog image processing using optical components to achieve the same 2-fold improvement in resolution. A first microlens array (MLA) is used to create the multifocal excitation, which is relayed through a scanning mirror and imaged onto the sample. The emitted light is collected through the objective, de-scanned

and passed through a physical pinhole array, which acts to reject out of focus light and provides optical sectioning. An additional MLA is then used to locally rescale each emission spot, providing the shift correction for each of the parallelized beamlets. The emission light is then finally rescanned onto the camera during a single camera exposure, reconstructing the super-resolved image.

	SIM	iSIM	HT-STORM	STED
Irradiance	1-10 W/cm^2	5-50 W/cm^2	10^3-10^4 W/cm^2	10^3-10^5 W/cm^2
Excitation	Sinusoidal pattern	Multi-focal pattern	Widefield	Excitation focus and depletion donut
Lateral resolution	~110 nm	~140 nm	20-40 nm	~50nm
Axial resolution	~360 nm	~350 nm		
Temporal resolution	10^{-1} - 10^0 s	10^{-2} - 10^{-1} s	5-10 min	60-80 min
Imaging depth	0 - 20 μm	0 - 50 μm	0 - 10 μm	0 - 50 μm
Multi-color	3+	3+	1-2	1-2
Effective FOV size	<60x60 μm^2	<80x80 μm^2	100x100 μm^2	100x100 μm^2
Effective throughput	3'600 μm^2/s	640'000 μm^2/s	~32 μm^2/s	~3 μm^2/s
References	ref[18,19,27]	refs[26,28]	refs[9,29]	refs[1,30]

Table 1 - Summary of the main properties of different microscopy techniques.
Inspired by ref[3]

The need for complex reconstruction algorithms such as used in SIM[18,19] is avoided and a simple deconvolution retrieves the full doubling in resolution. Since the image is processed optically (literally at the speed of light) before even reaching the detector, the iSIM achieves single-shot super-resolution, enabling imaging speeds of up to 100 Hz[26], limited mainly by the framerate of the camera.

Other methods, such as re-scan optical microscopy[31] or optical photon reassignment microscopy (OPRA)[32] apply this correction optically through a rescanning system or beam expander respectively, but only on a single scanning spot and can be integrated into a simple confocal microscope.

Expansion microscopy

Unlike the super-resolution methods presented above, instead of relying on optical tricks, expansion microscopy (ExM)[33] physically magnifies the sample so previously unresolvable features are brought outside of the diffraction limit of light and can be resolved with standard microscopy. Traditionally, an expansion factor of ~4 results in an effective resolution of ~70 nm laterally, on a conventional microscope. Furthermore, expanded samples can be combined with super-resolution techniques to achieve even higher effective resolution.

However, the improvement in resolution comes at a cost. Therefore, while the effective resolution is improved by the expansion factor, the effective FOV is shrunk proportionally along each dimension,

which could signify decreased information throughput. Nevertheless, since the imaging speed of faster, diffraction-limited microscopes is preserved, ExM has potential for orders of magnitude faster super-resolution imaging than comparable techniques. For example techniques such as widefield epifluorescence microscopy, spinning disk confocal microscopy (SDCM)[33] and light sheet microscopy (LSM)[34] have all been combined with ExM to deliver effective sub-diffraction resolution with fast imaging speeds. Recently, the combination of ExM with lattice light sheet microscopy has enabled capturing the entire super-resolved Drosophila brain, at orders of magnitude faster acquisition rates[35].
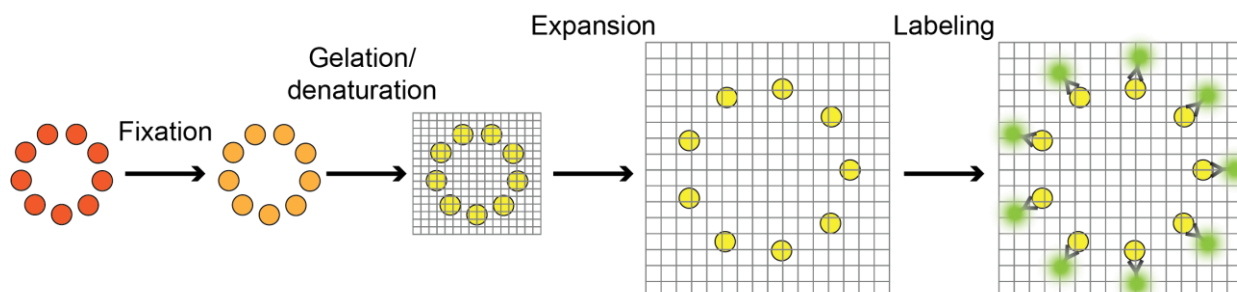
Figure 5 - Example of expansion protocol with post-expansion labelling.
The sample is fixed before all content is denatured. The sample is then incubated with a monomer solution, which polymerizes to form the gel. Upon water addition, the gel swells, expanding the sample uniformly. The sample is then labelled expansion for better labelling precision and efficiency.

The main steps in preparing an expanded sample include fixation, anchoring, digestion, labelling and expansion (Figure 5). Other variants of ExM differ either in the kind of gel and anchoring molecules used, but an important aspect is also whether the gel is labelled before or after expansion. Labelling before expansion, as used in the standard ExM protocol[33] and some variants[36–40], suffers from the same limitations as conventional labelling protocols, such as steric hindrance between label molecules and exacerbate issues linked to the size of the labels, since the labelling error will also be increased during expansion. Furthermore, the harsh digestion and denaturation steps of the protocol can diminish the brightness of the fluorophores. In contrast, protocols relying on post-expansion labelling[34,36,41,42] may result in improved labelling efficiency, since the structures within the sample are physically separated, opening up new epitopes and reducing steric hindrance after expansion (Figure 5). Furthermore, labelling precision is improved since the probe size is effectively divided by the expansion factor. Overall, ExM provides the best of both worlds – the super-resolution information at the speed of faster, traditional microscopes.

Limitations in throughput of super-resolution microscopies

While super-resolution microscopy has become an established tool in biological research, several challenges remain[43]. The pursuit for increased resolution comes at a cost to the size of the imaging field-of-view (FOV), making whole cell, multi-cell or tissue sized imaging increasingly challenging. Furthermore, most super-resolution techniques are laborious and time consuming – for example reconstructing a single SMLM super-resolved image traditionally requires localizations from thousands of raw frames to be combined, increasing the amount of time required to reconstruct a single super-resolved image. Overall both factors limit the imaging throughput – roughly defined as the area of FOV imaged per unit time – and remain a major bottleneck in the application of super-resolution imaging to quantitative biology, which requires access to large datasets to capture the variability of biological processes, but also overcome the noise of the imaging process itself.

The issue of information throughput has been challenged using different approaches combining chemical, computational, engineering and optical methods. Regardless of implementation, these strategies can be generalized and grouped as either improving the size of the imaging FOV and/or the time required to acquire an image.

Increasing the field-of-view

Even the fastest super-resolution techniques are limited in space by the size of the accessible FOV. To this end, simultaneous imaging over a larger area of the sample can be achieved within the same timeframe by combining enlarged detection[44] and parallelizing the acquisition – as long as the required imaging conditions can be maintained across the larger FOV.

For instance, widefield illumination is traditionally achieved by focusing the excitation beam at the back focal plane of the objective[45]. Using a traditional Gaussian beam, however, will result in the center of the image to appear brighter than the edges. This inhomogeneity in the delivered illumination will in turn be reproduced in the emission intensity and vary across the FOV. The final image will therefore produce a spatially dependent SNR and image quality and compromise the performance and reliability of fundamental image analysis such as segmentation, intensity measurements and image stitching. Generally, quantitative bioimaging relies on the collected emission intensities encoded in the pixel values of the captured image to extract information about the sample. Therefore, it is imperative to minimize and account for intrinsic bias influencing pixel values, such as uneven imaging conditions.

Achieving uniform illumination is crucial to ensuring optimal imaging conditions and uniform image quality across larger FOVs. Popular solutions such as post-processing flat-field correction[46,47] of spatially varying illumination improves the image uniformity, but the processed images can still have a spatially varying SNR, and non-linear effects such as molecule blinking for SMLM cannot be compensated after the acquisition[29,48–52]. Similarly, in patterned illumination techniques, maintaining the quality of the illumination pattern across a larger FOV is crucial in increasing the throughput, without compromising image quality or speed.

Flat-fielding for widefield illumination and background on the Köhler integrator

While post-processing flat-fielding correction algorithms[46,47] mitigate the consequences of inhomogeneous illumination, beam shaping solutions tackle the problem at the source by reshaping the incident inhomogeneous beam into a flat-top. There are different flat-fielding solutions available, such as the outputs of multi-mode fibers[48,53,54], refractive beam shapers[49–51,55], diffractive optical elements[56,57] or Köhler integrator technology[29,58–60].

This work mostly focuses on the Köhler integrator[29,58–60] – which uses beam integration to average out any inhomogeneity in the spatial and angular illumination distributions of the light source. Traditionally, most microscopes use the Köhler illumination[45] configuration to illuminate the sample, mapping each position of the illumination source to each position on the sample and therefore averaging out any spatial variations. However, different angular components are always mapped to distinct positions on the sample. While light sources with a uniform angular distribution (such as a lamp)[45] achieve homogeneous illumination this way, Köhler illumination does not provide homogeneous illumination in the case of light sources where the intensity has an angular dependence, such as a laser.
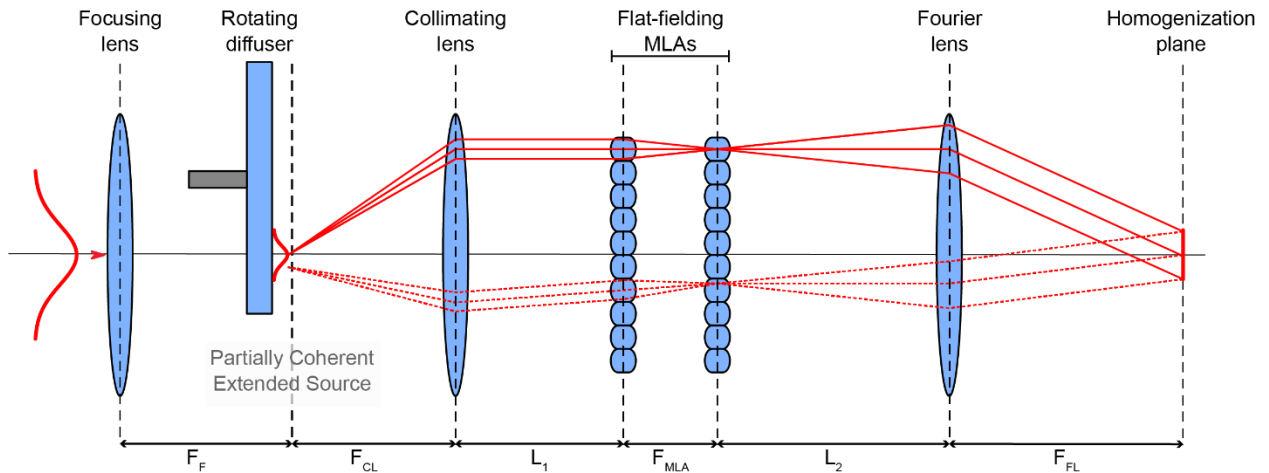
Figure 6 - Traditional Köhler integrator.
The focusing lens focuses the light near the rotating diffuser, which serves to scramble the incoming coherent light producing a partially coherent, extended source. The light from the extended source is then collimated by the collimating lens. The beam propagating further represents the angular spectrum of the extended source. The image of the extended source is formed at each lenslet of the second microlens array. The first microlens array effectively splits the angular spectrum of the extended source into multiple beamlets corresponding the individual microlens channels. The second microlens array and the Fourier lens combine the channels of the first microlens array to generate a flat-top intensity profile at the homogenization plane, located in the focal plane of the Fourier lens. Effectively, this results in each single point and each emission angle of the extended source being mapped across the entire homogenization plane.

The Köhler integrator overcomes this by effectively using a set of multiple parallel Köhler illumination systems. It is made up of a collimating lens with focal length F_{CL}, two MLAs displaced by their focal length f and a Fourier lens with focal length F_{FL} (Figure 6). The MLAs form separate MLA channels, which serve to sample different parts of the angular spectrum of the light source. The Fourier lens then images the light from each of the MLA channels and superimposes them in the homogenization plane, located at the front focal plane of the Fourier lens. This results in each position of the light source being imaged onto each point on the sample, but each angular projection as well – overcoming the problem of traditional Köhler illumination. The Köhler integrator has been adapted to different illumination sources, such as LEDs[61] or lasers[59,60]. In case of coherent illumination, a focusing lens and a rotating diffuser should be used to create a partially coherent extended source[59,60] and prevent interference from degrading the flat-field uniformity (Figure 6).

The quality of the homogenization depends strongly on the number of microlens channels used in the Köhler integrator since using more microlens array channels will result in a better averaging out in the homogenization plane. Therefore, illuminating the whole flat-fielding microlens array is usually preferred. Similarly, to avoid crosstalk between the adjacent microlens channels, the size of the extended source imaged onto the second microlens array should be smaller than the size of an individual lenslet in the second microlens array[59,60]. This no-crosstalk condition can be formulated as:

$$\frac{f}{F_{CL}} \cdot R_{source} \leq \frac{p}{2}$$

Equation 7 - No crosstalk condition for the Köhler integrator

Where R_{source} is the radius of the extended source and p the pitch of the flat-fielding MLAs. Crosstalk will cause multiple, partially overlapping flat fields to appear in the homogenization plane and will decrease the quality of the flat field.

Other important aspects include assuring the microlenses act like refractive elements, and not pinholes. This requires MLAs with a relatively high Fresnel numbers FN[59,60] :

$$FN = \frac{p^2}{4\lambda f}$$

Equation 8 - Fresnel number for the Köhler integrator

Where λ is the wavelength of light. Usually $FN \gtrsim 5$ provides good homogeneity from the Köhler integrator.

Assuming the above conditions are met, the size of the flat field S in the homogenization plane is set by the properties of the flat-fielding microlenses and the Fourier lens[59,60]:

$$S = \frac{F_{FL}p}{f}$$

Equation 9 - Flat field size for the Köhler integrator

The modular design of the Köhler integrator allows tuning the properties of the flat-field, through the above presented design equations.

Commercially available refractive beam shapers such as TopShape and PiShaper provide an alternative flat-fielding solution. These use a pair of aspheric lenses arranged in a telescope configuration[49,50,55] and work on the principle of field-mapping by reassigning light from a Gaussian beam into a flat-top. Other flat-fielding solutions and their respective strengths and weakness have been characterized in ref[62] and are summarized in Table 2.

Flat-fielding strategy	Advantages	Disadvantages	References
Refractive beam shapers (PiShaper, TopShape,…)	High transmission efficiency, simple, cheap, TIRF compatibility	Sensitive to aberrations, rigid design	49–51
Diffractive beam shapers	Cheap	Low transmission efficiency, rigid design, wavelength dependent	56
Multi-mode fiber	High homogeneity, flexible design, cheap	Low transmission efficiency due to coupling losses	48,53,54
ASTER	Flexible illumination, high transmission efficiency	Complex scanning-based implementation	63
Waveguide TIRF	TIRF, high homogeneity, cheap	Complex implementation, TIRF only	52
Köhler integrator	High homogeneity, flexible design	Complex implementation	29,60,64,65

Table 2 - Summary of popular widefield flat-fielding techniques

Parallelization for patterned excitation

Similarly to how extending the FOV of SMLM techniques requires flat-fielded illumination, maintaining a uniform image quality in patterned excitation techniques relies on the ability to reproduce the pattern

across larger regions on the sample with the same quality. This work focuses on multi-focal excitation, i.e. an array of diffraction-limited excitation spots characterized by a constant pitch and spot size. Common ways to create homogeneous multi-focal excitation include the use of diffractive optical elements[56], SLMs[30,66], multi-mode fibers[53], beam splitters[67] or prisms[68]. In the case of STED[69–71] and RESOLFT (MoNALISA)[72], optical lattices have also been used to parallelize the depletion beam. A summary of previously implemented techniques for homogeneous patterned illumination is shown in Table 3.

However, most of these solutions suffer from one or several of these factors: poor transmission efficiency, low homogeneity, limited number and rigid geometry of the multi-focal excitation. Diffractive optical elements have relatively low efficiency, limited number of excitation spots and the generation of additional unwanted orders[56]. While SLMs are popular since they enable adaptive correction of aberrations, they present a trade-off between the generated number of excitation spots and their uniformity, in addition to low efficiency[66]. Beam splitters and prisms have the advantage of high efficiency, but are difficult to align and limited in the number of excitation spots[67,68]. A popular commercially available solution for spinning disk microscopes is sold as the Borealis system from Andor, which implements a multi-mode fiber[53] to illuminate the MLA generating multi-focal excitation, but at limited transmission efficiency.

Flat-fielding strategy	Advantages	Disadvantages	References
Diffractive optical elements	Cheap	Rigid design, low transmission efficiency, limited parallelization, not compatible with spinning disk implementation	56
Spatial light modulators	High flexibility, adaptive	Expensive, limited transmission efficiency, not compatible with spinning disk implementation, limited uniformity/parallelization	66
Multi-mode fibers	Good homogeneity, flexible design	Limited transmission efficiency due to coupling losses	53
Beam splitters	Simple and cheap, high transmission efficiency	Limited number of excitation spots, not compatible with spinning disk implementation	67,68
Prisms	Simple and cheap	Limited number of excitation spots, not compatible with spinning disk implementation	68

Table 3 - Summary of popular flat-fielding techniques for patterned illumination

Interestingly, the Köhler integrator has spot or line generating properties. Using a coherent beam, by removing the beam scrambling element (rotating diffuser), will cause the plane waves interfere in the homogenization plane, resulting in an array of spots or lines with a periodicity[59,60,73]:

$$\Lambda_{FP} = \frac{\lambda F_{FL}}{p}$$

Equation 10 - Spot generating property of the Köhler integrator

However, due to the dependence of the pitch on the wavelength of light λ, this feature cannot be used for multi-chromatic applications such as multi-color fluorescence microscopy. Nevertheless, the Köhler integrator has good potential for generating homogeneous multi-focal excitation.

Decreasing acquisition time

While this work focuses mostly on the engineering and optical tools, the field has also tackled the issue of slow acquisition speed using other chemical and computational approaches. Super-resolution techniques usually require a combination of complex sample preparation, optimization of acquisition and reconstruction parameters and need for user intervention on a per sample basis. Automation has helped overcome some of these issues and minimized the need for user intervention in some applications[74–78], improving reproducibility and speed at which experiments can be performed. Other computational tools used during post-processing include the development of new algorithms for improving the fitting procedures for high-density SMLM imaging[79–82], as well as sparse reconstructions[83] or imposing priors[84].

A simple way of improving information throughput in the case of scanning techniques is by parallelization, which can serve to both increase the FOV size and acquisition speed. Scanning with a single beam results in an acquisition time that scales proportionally as the area of the FOV is increased, limiting the FOVs that can be captured within a desired timeframe. On the other hand, parallelization provides a straightforward way of improving both the speed and FOV size of the acquisition, i.e. simultaneously parallelizing over n beams directly improves the imaging speed and hence information throughput n-fold. Furthermore, in scanning methods such as RESOLFT[85] and confocal microscopy, intelligent scanning procedures have been used to speed up the imaging time by avoiding scanning areas not containing useful information during the acquisition.

Finally, there are also intrinsically faster super-resolution techniques than others. For example, the need for 9-15 raw frames for reconstructing a SIM image[18,19] and the need for thousands of raw frames in the case of SMLM[2,9,86], represent the most important rate limiting factor for these techniques. On the other hand, parallelization and analog image processing employed in techniques such as iSIM[26], enable single-shot super-resolution and contribute towards the technique's fast acquisition speed. Therefore, requirements on the raw data and the complexity of the reconstruction also influence the overall acquisition speed.

Trade-off between imaging speed and duration

In live-cell fluorescence imaging, the temporal resolution of even the fastest techniques is limited due to the trade-off in imaging parameters[87] (Figure 7). Fluorescence microscopy techniques rely on the ability to fluorescently label the structure of interest with good specificity, with the most common labelling strategies using fluorescent proteins or synthetic dyes. However, imaging fluorescently labelled specimens causes them to gradually lose fluorescence over time due to irreversible photobleaching of the fluorescent label[88]. Therefore, it is not possible to image the sample indefinitely, and the available photons that can be collected from the sample are referred to as the sample photon budget. While the size of the photon budget is mostly determined by the choice of labelling strategy and its photophysical properties, how the limited photon budget is spent depends on the acquisition itself and different imaging parameters such as the excitation irradiance, exposure time, acquisition speed and imaging duration.
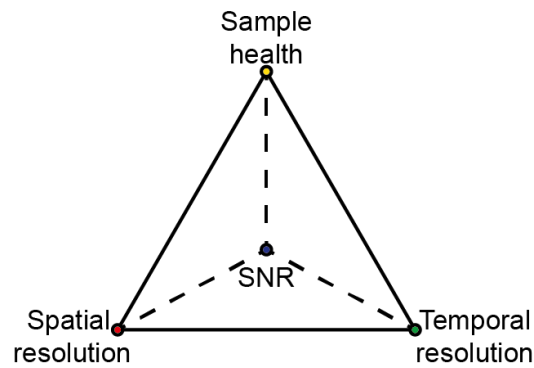
Figure 7 - Imaging parameter space.
Inspired by ref.[87,89]. Improving one imaging parameter comes at a cost to the others.

Most importantly for time-lapse imaging, the limited photon budget usually presents a trade-off between the acquisition speed and imaging duration, where prioritizing one comes at a cost to the other[87,89] (Figure 7). Therefore, the temporal resolution of a time-lapse acquisition must be carefully weighed to capture the dynamics of the event of interest, while not spending the available photon budget too quickly to allow imaging over sufficiently long periods of time.

Different approaches have been used to increase the available photon budget such as the design of more stable probes[88], or to allow the most efficient use of the limited photon budget through gentler imaging strategies, sparse reconstructions[84] and denoising algorithms[90,91]. However, there is currently no approach that adapts the consumption of the sample's limited photon budget over time, in order to distribute the limited resources most efficiently in response to cues from the sample.

Chapter 3
Homogeneous multifocal excitation for high-throughput super-resolution imaging

Abstract

Super-resolution microscopies, which allow features below the diffraction limit to be resolved, have become an established tool in biological research. However, imaging throughput remains a major bottleneck in using them for quantitative biology, which requires large datasets to overcome the noise of the imaging itself and to capture the variability inherent to biological processes. Here, we develop a multi-focal flat illumination for field independent imaging (mfFIFI) module, and integrate it into an instant structured illumination microscope (iSIM). Our instrument extends the field of view (FOV) to >100 µm x100 µm without compromising image quality, and maintains high-speed (100 Hz), multi-color, volumetric imaging at double the diffraction-limited resolution. We further extend the effective FOV by stitching multiple adjacent images together to perform fast live-cell super-resolution imaging of dozens of cells. Finally, we combine our flat-fielded iSIM setup with ultrastructure expansion microscopy (U-ExM) to collect 3D images of hundreds of centrioles in human cells, as well as of thousands of purified Chlamydomonas reinhardtii centrioles per hour at an effective resolution of ~35 nm. We apply classification and particle averaging to these large datasets, allowing us to map the 3D organization of post-translational modifications of centriolar microtubules, revealing differences in their coverage and positioning.

Generating homogeneous multi-focal excitation

Generating a uniform irradiance over a large FOV while retaining the highest achievable resolution requires the following properties of the excitation focal spots in a multi-focal microscope: 1) homogeneous intensity, 2) constant pitch and 3) diffraction-limited size across the field of view. Existing methods for generating uniform excitation are often limited to producing a low number of excitation spots, with residual heterogeneity and low transmission efficiency. Thus, we set out to extend the Köhler integrator[59,60], which averages over the spatial and angular distributions of the light source to homogenize the beam, for use with multifocal excitation. The Köhler integrator is primarily composed

of a rotating diffuser to scramble coherent light, a pair of microlens arrays (MLAs) that serve as parallelized imaging channels and a Fourier lens to average those channels into a flat-top[59,60].

Design of novel Köhler integrator

Previously, multifocal excitation for the iSIM was generated by illuminating a microlens array (MLA) with a collimated Gaussian beam[26,28]. As expected, the non-homogeneous beam profile results in excitation points whose intensity depends on their location (Figure 8a). Alternatively, illuminating the excitation MLA with a flat-top beam – such as that produced by a Köhler integrator – results in an array of multifocal excitation spots of homogeneous intensity (Figure 8b). Therefore, to combine the flat-field generated by the Köhler integrator, with the MLA for spot generation, we place the excitation MLA (characterized by a focal length f_x and pitch p_x) at the front focal plane of the Fourier lens of the Köhler integrator, where the flat-top is focused.

However, if the incident wavefront is not flat, the non-telecentric illumination of the excitation MLA produced by this configuration alters the pitch of the excitation spots in the focal plane of the excitation MLA (Figure 8c). This periodicity – usually determined by the pitch of the excitation MLA p_x – must match the periodicity of additional components that are typically placed in conjugate image planes of confocal microscopes, such as a pinhole array. In the case of a mismatch of array elements, the light will be gradually occluded and decrease in intensity away from the center of the optical path.

Maintaining the structure (pitch and uniform spacing) of the grid of excitation spots requires telecentric illumination of the excitation microlens array. To solve this problem and achieve telecentric illumination of the excitation MLA, we place the Fourier lens of the Köhler integrator so that its back focal plane lies at the second flat-fielding MLA[61], resulting in a flat wavefront and thereby ensuring that the pitch of the excitation is conserved and matches p_x (Figure 8d). Additionally, adjustment of the distance between the second flat-fielding MLA and the Fourier lens can be used to capture the incoming wavefront at different curvatures. Sampling the wavefront at different curvatures can be used to finely adjust the resulting periodicity of the excitation spots to match that of the other optical elements (Figure 8e). This feature, not shared by refractive beam-shapers, allows us to optimize transmission efficiency.

Finally, in confocal microscopy and its variants such as iSIM, maximizing the achievable resolution requires focusing the excitation light to a diffraction-limited spot on the sample. This imposes a limitation on the spot size that should be generated in the excitation path. However, implementing a traditional Köhler integrator in the excitation path would produce large excitation spots due to the nature of the partially coherent extended source created by the rotating diffuser (Figure 8f). In that case, the accessible improvement in resolution would not be based on diffraction-limited performance. A possible solution would be to introduce a pinhole array to mask the excitation spots that are focused onto the sample, but at a significant cost to the transmission efficiency (Appendix B).
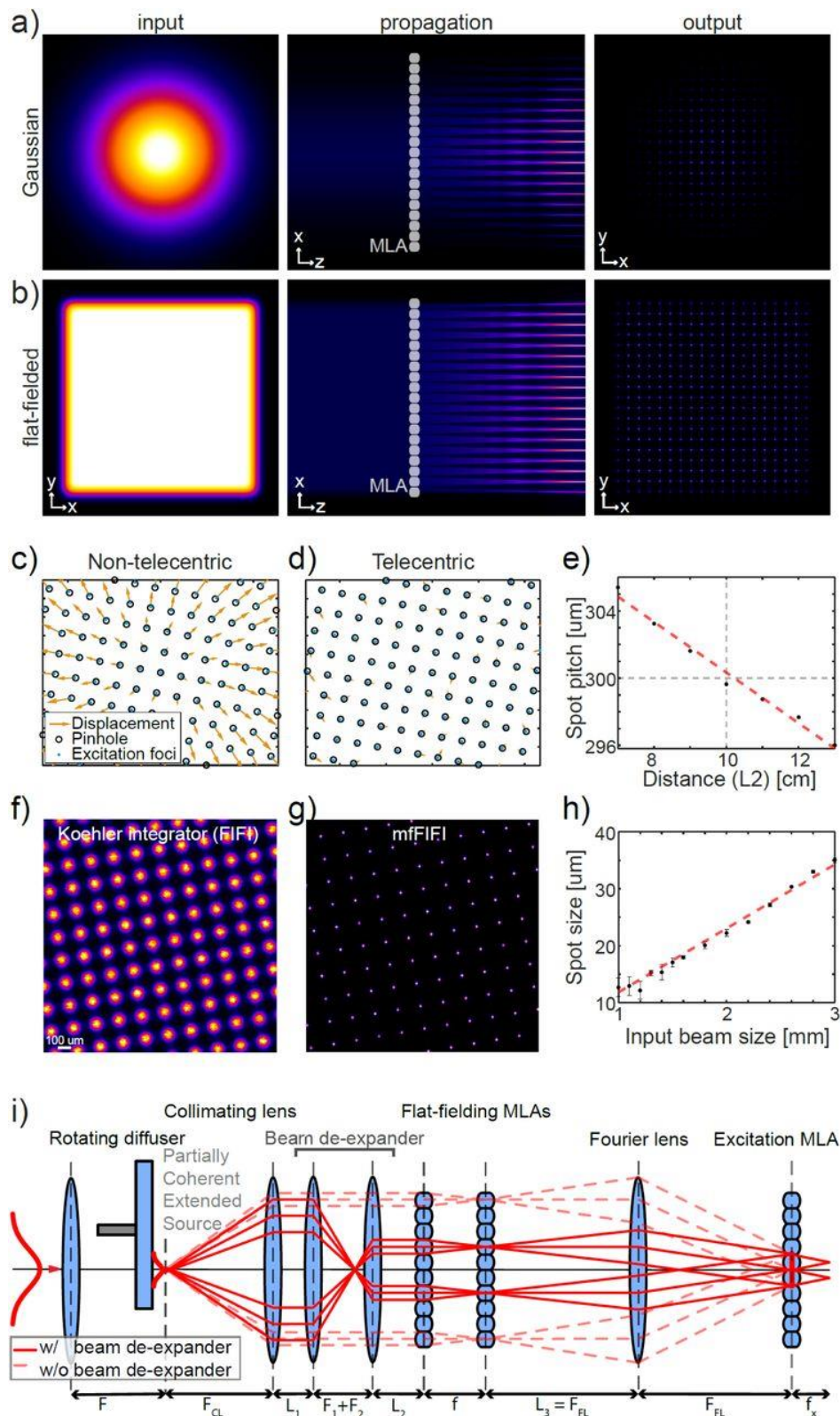
Figure 8 - Design and features of the mfFIFI module.

a,b) Wave optics simulation with (a) a Gaussian beam or (b) a flat-top beam used as input onto the excitation MLA, showing their propagation and their effect on the output intensity of the generated excitation spots. c,d) Experimental positions of the excitation spots (blue dots) overlaid on a conjugate pinhole array (black circles) and the displacement between the two (yellow arrows) for (c) non-telecentric and (d) telecentric illumination of the excitation MLA reveals a change in the pitch of excitation spots caused by non-telecentric illumination. Data are from separately acquired images of pinholes and excitation spots. e) Plot showing the dependence of the pitch of

the excitation spots on the offset of the Fourier lens back focal plane to the second flat-fielding MLA. Dashed line represents zero offset on the x-axis and the ground truth set by the pitch of the MLA on the y-axis. f) Image of excitation spots generated with a Gaussian beam as input into the excitation MLA. Directly implementing the Köhler integrator as the input results in large excitation spots. g) Limiting the number of flat-fielding MLA channels used for beam homogenization partially recovers the size of the excitation spots as achieved using Gaussian excitation (a), while maintaining uniform intensity of the Köhler integrator (f). h) The spot size increases with the diameter of the beam incident on the flat-fielding MLAs over the given range. Error bars represent standard error of the mean, dashed line shows a linear dependence. Figure reproduced with the permission of Springer Nature, material from: Mahecic, D. et al. Homogeneous multifocal excitation for high-throughput super-resolution imaging. Nat. Methods **17**, *726–733 (2020).* [92]

Therefore, in an alternative design, we find that – contrary to the typical Köhler integrator where illuminating a maximal number of flat-fielding microlenses is preferred[59,60] – illuminating fewer microlenses offers a solution to control the excitation spot size and ensure diffraction-limited excitation at the sample (Figure 8g-I, Appendix A). Incorporating a beam expander to contract the light incident on the flat-fielding MLAs allows us to tune the apparent size and angular distribution of the extended source. This shrinks the size of the excitation spots, while maintaining efficient light transmission and homogeneity across the excitation illumination. This configuration, which we call multifocal flat illumination for field-independent imaging (mfFIFI), meets all the above requirements for homogeneous multifocal excitation.

The above requirements can be described by geometrical optics and are a direct outcome of ray transfer matrix calculations (Appendix A, Appendix C), but the large parameter space makes the design and optimization of the mfFIFI module non-trivial. For example, it should be noted that the quality of homogenization of the Köhler integrator depends on the number of flat-fielding microlens channels over which the flat-field is averaged. Therefore, maximizing the number of microlens channels is usually preferred. Decreasing the radius of the beam incident on the first microlens array may seem counter-intuitive, as averaging over fewer microlens channels will reduce the homogeneity of the flat-field. Therefore beam contraction presents a trade-off between homogeneity of the multifocal excitation and the ability to achieve diffraction-limited excitation and requires careful optimization. To facilitate the optimization and choice of components for efficient mfFIFI, we provide the main design equations and an extended version of our existing wave optics simulation platform[29] (Appendix D).

iSIM integration and performance characterization

To overcome the limitations to FOV size caused by Gaussian beams, we combined mfFIFI excitation and sCMOS detection in the custom built iSIM (Figure 9a). The mfFIFI module was placed before the excitation MLA, so that the front focal plane of the Fourier lens overlaps with the position of the excitation MLA (Figure 9b,c). We then tested the performance of the mfFIFI module when integrated into the excitation path of the HT-iSIM.
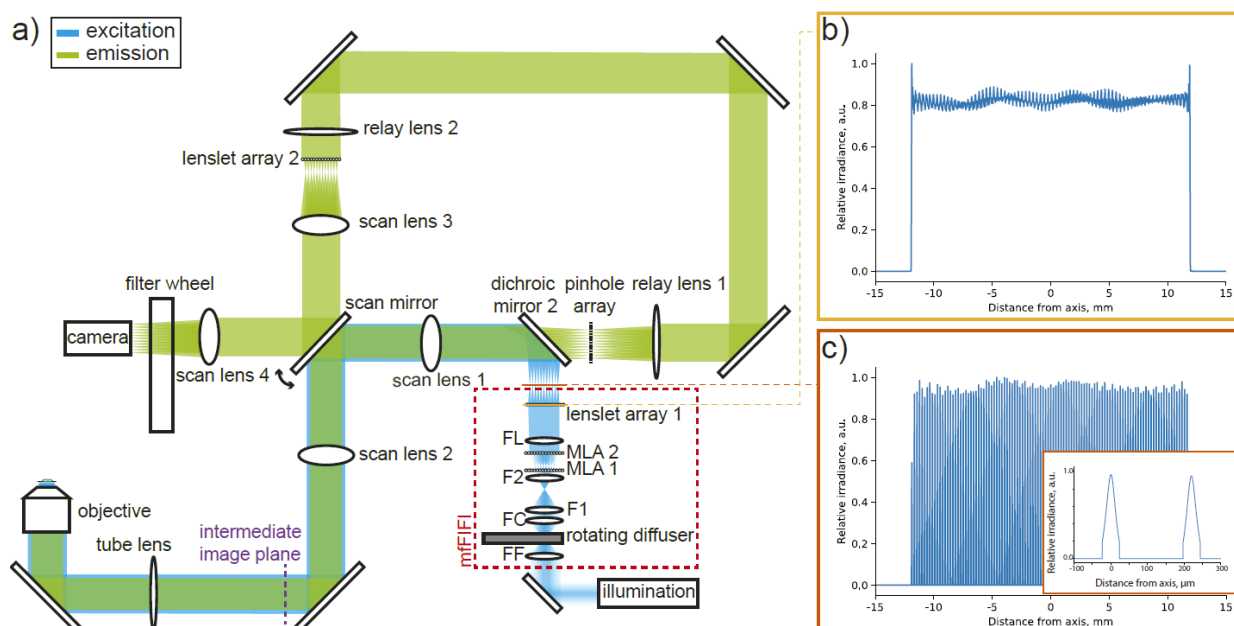
Figure 9 - Integrating mfFIFI into the iSIM.
*a) Schematic representation of the iSIM setup, showing where the mfFIFI module is integrated into the excitation path prior to the excitation MLA. b) Simulated flat-field incident on the excitation MLA. c) Simulated intensity profile in the front-focal plane of the excitation MLA, showing an array of excitation points (inset). Figure reproduced with the permission of Springer Nature, material from: Mahecic, D. et al. Homogeneous multifocal excitation for high-throughput super-resolution imaging. Nat. Methods **17**, 726–733 (2020).* [92]

To visualize the excitation illumination of the iSIM, we used a concentrated dye solution[93], and imaged the emitted light onto the camera without scanning. Using an approximately Gaussian beam (M2<1.1, FWHM diameter ~12 mm) to create the excitation pattern, as used in the initial iSIM design[26,28], results in excitation points of spatially varying intensity closely following a Gaussian distribution (Figure 10a), as expected from the simulation. Scanning the Gaussian excitation points partially homogenizes the excitation along the scan direction; however, the resulting illumination features a bright central region and strong roll-off away from the central optical axis (Appendix E). In comparison, generating the excitation using the mfFIFI module results in a more uniform multifocal excitation covering an area of approximately 100x100 μm^2 (Figure 10b), and a more homogeneous excitation during scanning (Appendix E).
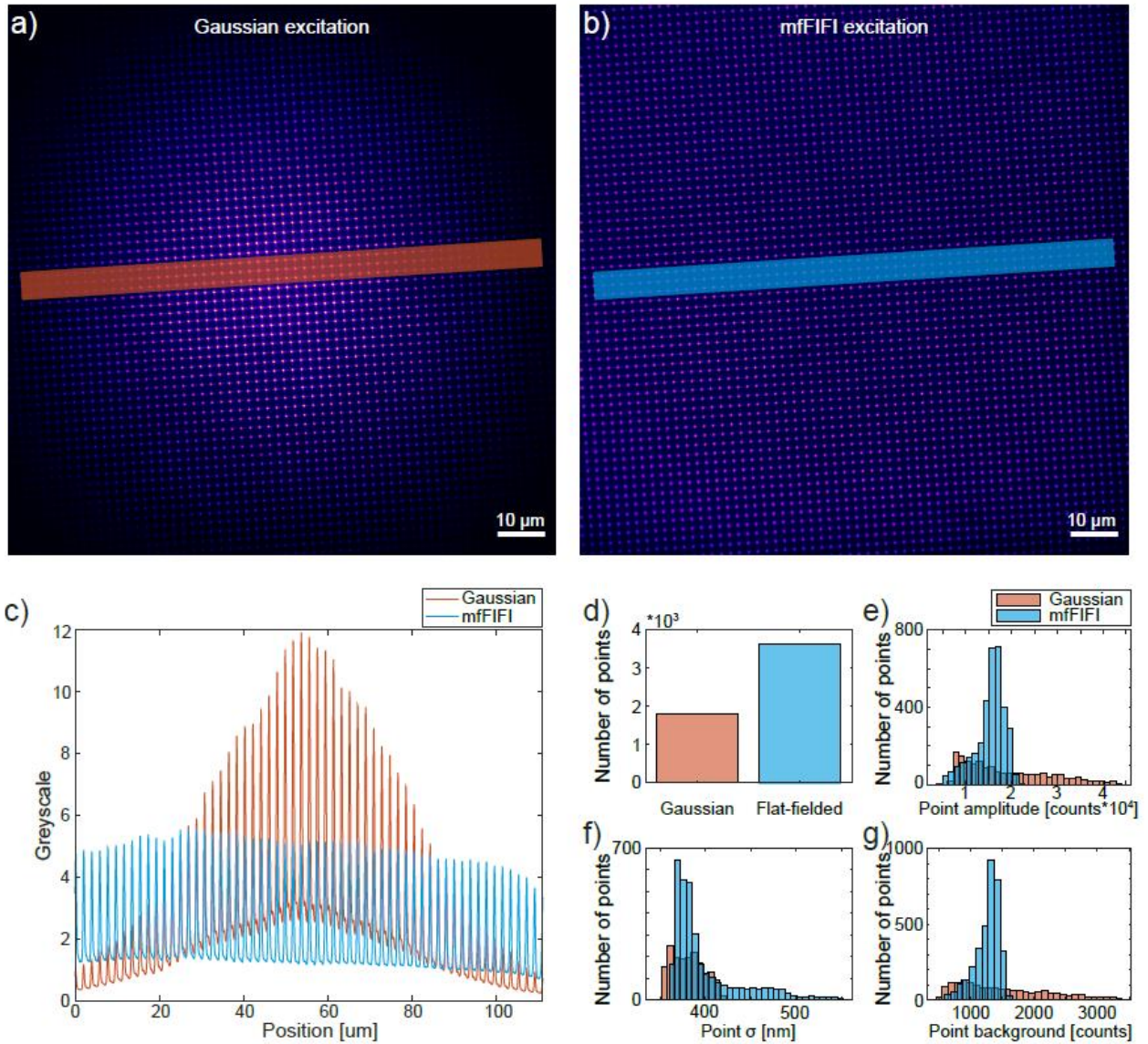
Figure 10 - Performance comparison between Gaussian and mfFIFI excitation.
*a,b) Excitation points imaged onto a NaFITC fluorescent dye sample with (a) Gaussian and (b) mfFIFI excitation. c) Intensity profiles measured along lines in (a, b). d) Number of excitation points with a signal-to-noise ratio (SNR) above 3 in Gaussian and mfFIFI excitation. mfFIFI increases the number of excitation points by a factor of two. e-g) Histograms of excitation point (e) amplitudes, (f) variance and (g) background levels for Gaussian and mfFIFI excitation. Figure reproduced with the permission of Springer Nature, material from: Mahecic, D. et al. Homogeneous multifocal excitation for high-throughput super-resolution imaging. Nat. Methods **17**, 726–733 (2020).* [92]

Comparing intensity profiles along the rows of excitation spots shows that mfFIFI efficiently redistributes the spatially varying input Gaussian excitation over a larger area (Figure 10c). Quantifying these differences, we find that mfFIFI doubles the number of excitation spots above background levels compared to the Gaussian excitation, while resulting in a much narrower distribution of spot amplitudes and background (Figure 10d-g). Furthermore, this improvement comes at no measurable cost to the quality of the structured illumination. We find that both the size of the excitation spots required for resolution improvement in confocal microscopy and their periodicity (222.3±0.3 µm (Gaussian) and 222.2±0.3 µm (mfFIFI) (mean ± S.D.), measured using a concentrated dye sample[93]) are maintained, and compare well with the ground truth (222 µm excitation MLA pitch). This was further verified by imaging 100 nm fluorescent beads, showing comparable lateral resolution between mfFIFI (214 ± 5 nm, mean ± S.D.) and Gaussian illumination (219 ± 12 nm), based on FWHM measured on raw iSIM data

before Lucy-Richardson deconvolution[94,95], or ~140 nm lateral and ~350 nm axial resolution after deconvolution (Appendix E)[26].

Characterizing mfFIFI performance as function of scrambling speed

Since iSIM is a scanning technique, it is imperative to ensure illumination homogeneity during the scan of an individual excitation point across the sample. Thus, to characterize the relationship between the scrambling speed of the rotating diffuser and the averaging out of diffraction patterns, thereby defining the parameter range necessary to achieve illumination homogeneity.

The role of the rotating diffuser is to ensure that the scrambling and averaging out required to homogenize the excitation is occurring fast enough compared to the scanning and imaging speeds. As the excitation points are scanning the sample during a single camera exposure, the intensity of the excitation points during the scanning should not vary significantly between different positions along the scan. Therefore, the rotating diffuser needs to be scrambling and averaging out the excitation light faster than the scanning motion of the excitation point.

With no diffuser, the homogenization plane will not produce a flat-field but instead a highly inhomogeneous interference pattern making up a periodic array of spots[59,60]. The rotating diffuser serves to scramble the incoming wavefront and produce an extended partially coherent source. However, when the rotating diffuser is static, it produces a speckle pattern in the homogenization plane that is not homogeneous, but spatially random with respect to the interference pattern without the rotating diffuser.

Rotating the diffuser causes different, spatially random, scrambled wavefronts to be projected in the homogenization plane where the excitation microlens array (MLA) is located. In the front focal plane of the excitation MLA, each incoming scrambled wavefront will in turn produce spots with varying intensities, and might cause variations in the size and position of the spots. However, if many different, spatially random, scrambled wavefronts are averaged over time (by a rapidly rotating diffuser), they will produce a homogeneous flat-field in the homogenizing plane and therefore a homogeneous array of excitation points in the front focal plane of the excitation MLA.

How fast does the diffuser need to rotate to achieve homogeneity in the scanned spots? To characterize the scrambling speed of the rotating diffuser, we perform a back of the envelope calculation given the characteristics of the rotating diffuser and the imaging process. We then use the simulation platform and real data to quantify the relationship between the scrambling speed of the rotating diffuser and the variations in position, width and amplitude of the excitation points at different timescales.

Back-of-the-envelope calculation of scrambling speed

In order to give an estimate of how fast the rotating diffuser is averaging out the incoming wavefronts during imaging, we characterize the rotating diffuser by its rotation speed ω, distance of the rotation axis from the optical axis r and a grain size d:

Rotation speed: $\omega \approx 6000 \text{ rpm} = 100 \text{ rps}$

Distance from optical axis $r \approx 10 \text{ mm}$

Diffuser grain size $d \approx 10 \text{ μm}$

Therefore we can approximate that as the diffuser is rotating, it will average out over n grains per unit time, and therefore produce at least n random wavefronts per unit time:

$$n = \frac{2\pi r}{d} \omega \cong 6.28 \cdot 10^5 \text{ s}^{-1}$$

Equation 11 - Scrambling speed as number of random wavefronts generated per unit time

This is a conservative estimate of the scrambling rate, since changing sub-grain position on the diffuser is likely to produce a differently spatially distributed wavefront.

In the iSIM design, the points are array of points is slightly tilted so that a scan along a single axis will reconstruct the entire two-dimensional image when integrated over time during a single camera exposure. Now, given an imaging frame rate f and assuming that on the sample, each point needs to scan a distance s, we can approximate how many scan positions p this requires given a diffraction limited spot size on the sample s_{PSF}:

Imaging frame rate $f = 10 - 100$ Hz

Scan distance $s \approx 10$ μm

Diffraction limited spot size $s_{PSF} \approx 0.25$ μm

Number of scan positions on sample $p \approx \frac{s}{s_{PSF}} \cong 40$, rounded up to 100

Finally, we can estimate the number of wavefront iterations over which each point is averaged at each scan position on the sample as N:

$$N = \frac{n}{pf}$$

Equation 12 - Number of random wavefronts iterated at each scan position

At the fastest frame rate of iSIM imaging $f_{max} = 100$ Hz, this results in $N_{max} \cong 62.8$ iterations. At the imaging rate used in the majority of this work $f_{real} = 10$ Hz, this results in $N_{real} \cong 628$ iterations.

Importantly, these numbers represent a purely technical limitation, and that higher scrambling rates can be easily achieved by increasing the distance of the axis of rotation of the rotating diffuser from the optical axis, finding a rotating diffuser with a faster rotation speed or smaller grain size, placing two rotating diffusers in series but rotating in opposite directions[60] or switching to speckle reducers with higher operating frequencies such as the Optotune Speckle Reducers sold by Edmund Optics.

Characterizing spot variation from simulated results

To test whether the numbers of iterations from the calculation are sufficient to provide homogeneous spots during scanning, we use our extended simulation platform to address how the position, size and intensity of the spots change when averaged over different numbers of iterations. To do this, we generated 8000 random wavefronts as previously described[29,96] using our extended simulation platform (Figure 11a), before bootstrapping over different numbers of iterations and examining how the intensity of the same point varies between the different averages and their realizations (Figure 11b). Specifically, we measured the position of the maximum of each peak, its FWHM and maximal value representing the amplitude, and compared the same parameters across 10 different realizations of bootstrapping together a varying number of iterations N (Figure 11c-e), representing the cumulative illumination profile produced by N random wavefronts. Each realization contained ~90-110 excitation spots, depending on the number of microlenses and size of the generated flat-field, both determined by the experimental setup design.
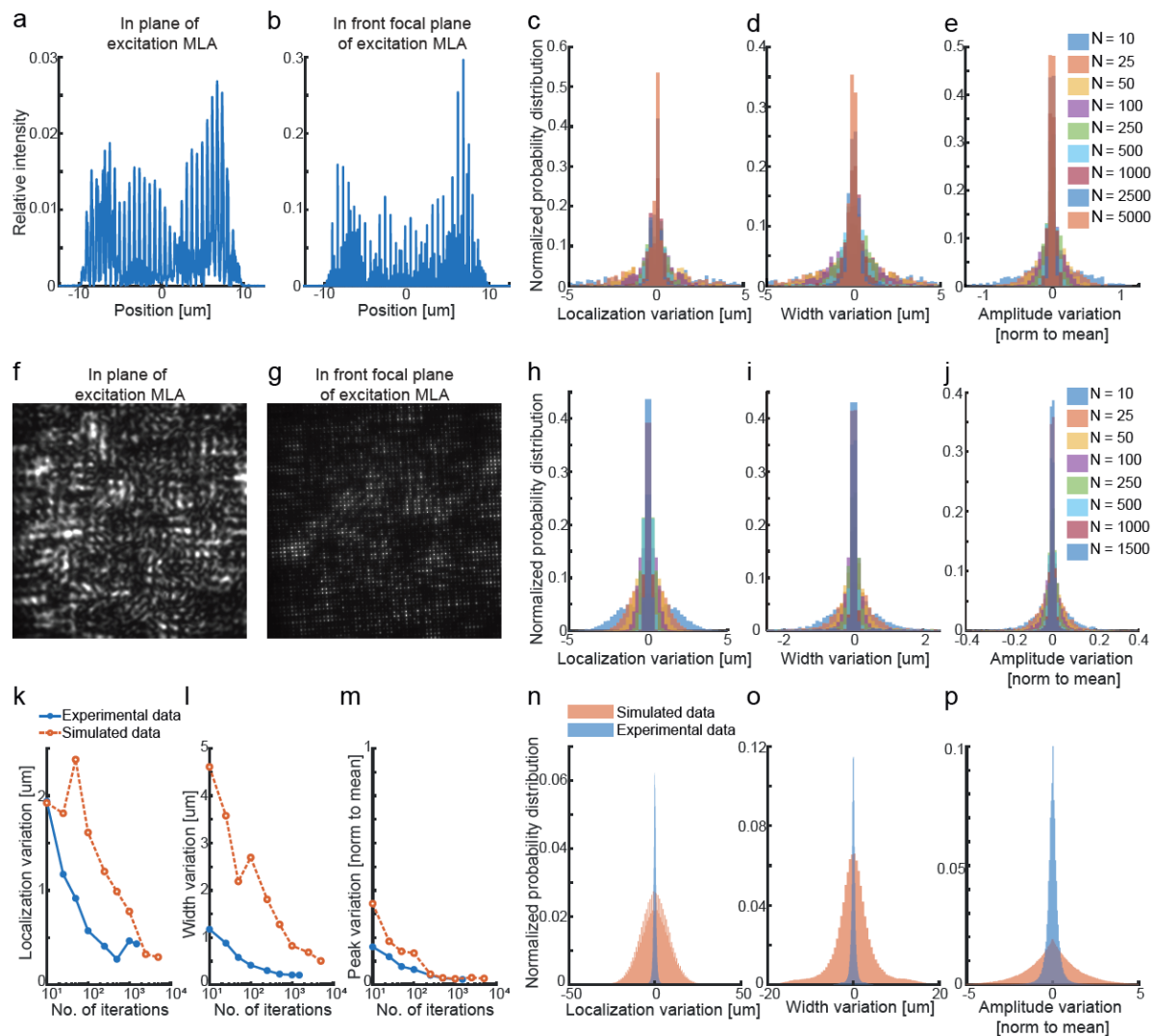
Figure 11 - Quantifying excitation homogeneity as function of rotating diffuser scrambling speed.
a) Simulated data showing the relative field intensity in the plane of the excitation MLA and b) at the front focal plane of the excitation MLA. c-d) Variation in excitation spot localization, width and amplitude for illumination averaged over different numbers of simulated random wavefronts. f) Real data showing the field intensity in the plane of the excitation MLA and g) at the front focal plane of the excitation MLA. In this case the two fields were not acquired at the same random wavefront, but are intended to give a general idea of what the fields look like. h-j) Variation in excitation spot localization, width and amplitude for illumination averaged over different numbers of random wavefronts acquired experimentally. k-m) Dependence of the spot localization, width and amplitude as function of the number of iterations over which the illumination is averaged over (representing different scrambling speeds, or acquisition speeds). n-p) Variation in the localization, width and amplitude between individual random wavefronts for simulated and experimentally acquired data. Figure reproduced with the permission of Springer Nature, material from: Mahecic, D. et al. Homogeneous multifocal excitation for high-throughput super-resolution imaging. Nat. Methods **17**, *726–733 (2020).* [92]

We then quantified how these parameters varied between 10 different realizations, by computing their difference for each excitation point between the 10 different realizations and for varying values of N, representing integrating over N random wavefronts. Plotting the variation distributions allowed us to measure their FWHM and reported those values as function of the N, the number of iterations over which the illumination is averaged out (Figure 11k-m). Similarly, we can study how the intensity of a single point varies between different scrambled wavefronts (Figure 11n-p, without temporal averaging, corresponding to N=1).

Characterizing spot variation from real images

Since the rotating diffuser rotates too fast to capture the individual wavefronts corresponding to different positions of the diffuser, we manually rotated the diffuser by random amounts to acquire 2064 images of the resulting scrambled wavefronts (Figure 11f,g), analogous to the simulated data. We then repeated a similar analysis as for the simulated data, by comparing the variation in spot position, size and intensity by bootstrapping over different numbers of iterations (Figure 11h-j).

By measuring the FWHM of the variation profiles, we could study how the spot localization, width and amplitude varied as function of the number of iterations (Figure 11k-m). Specifically, we measured the subpixel localization of each spot by fitting it to a 2D Gaussian profile, from which we also extracted the FWHM of each spot. There were generally ~472 spots in different frames and bootstrapped realizations. The amplitude was measured by taking the raw pixel value at the peak location. Similarly, by not bootstrapping over multiple iterations, we could compare how a single point varies between individual scrambled wavefronts.

The results show that the simulation is conservative compared to the real data (Figure 11n-p). This could be because the simulation is performed in one dimension (for improved computation time), while the real data is two-dimensional, and that averaging over an additional dimension could produce better results. Nevertheless, the simulated and real results show that averaging over an order of magnitude of 10 iterations produces excitation spots with <20% variation in intensity, while averaging on the order of 100 provides <10% variation in intensity (Figure 11m). Interestingly, the values appear to plateau at ~2-3% which could be due to the limited size of the simulated and experimental datasets, or suggesting that averaging out further does not bring additional improvement to the homogeneity.

The variation in spot localization and width also decreases as the excitation is averaged over more iterations. The plotted variations in localization and width are represented before magnification (x116). Therefore, on the sample these represent ~10 nm variation in localization and width, which does not compromise the ability to focus the excitation to a diffraction-limited spot (Figure 11k,l). In fact, the slight variation in localization of the excitation spot might be beneficial in reducing the striping artefact often present in scanning methods.

Application: High-throughput imaging at doubled resolution

We used our custom-built iSIM setup as a platform to combine the capability of mfFIFI excitation with a scientific complementary metal-oxide semiconductor (sCMOS) camera for detection to perform large FOV volumetric imaging at doubled resolution. While existing commercial SIM setups are mostly limited to FOVs with a linear dimension of 30-60 μm, our setup reaches >100x100 μm^2, thus providing a ~4- to 10-fold increase in FOV area (Figure 12a). We used mfFIFI iSIM to simultaneously image multiple mammalian cells within a single FOV at doubled resolution. Accessible imaging speeds are limited merely by the frame rate of the detector; thus, frame rates of up to 100 Hz as reported for iSIM[26,28] are preserved across >100x100 μm^2, since the increase in FOV is achieved by improved parallelization from the increased number of illumination spots. Thus, the increase in FOV translates directly into an increase in throughput.
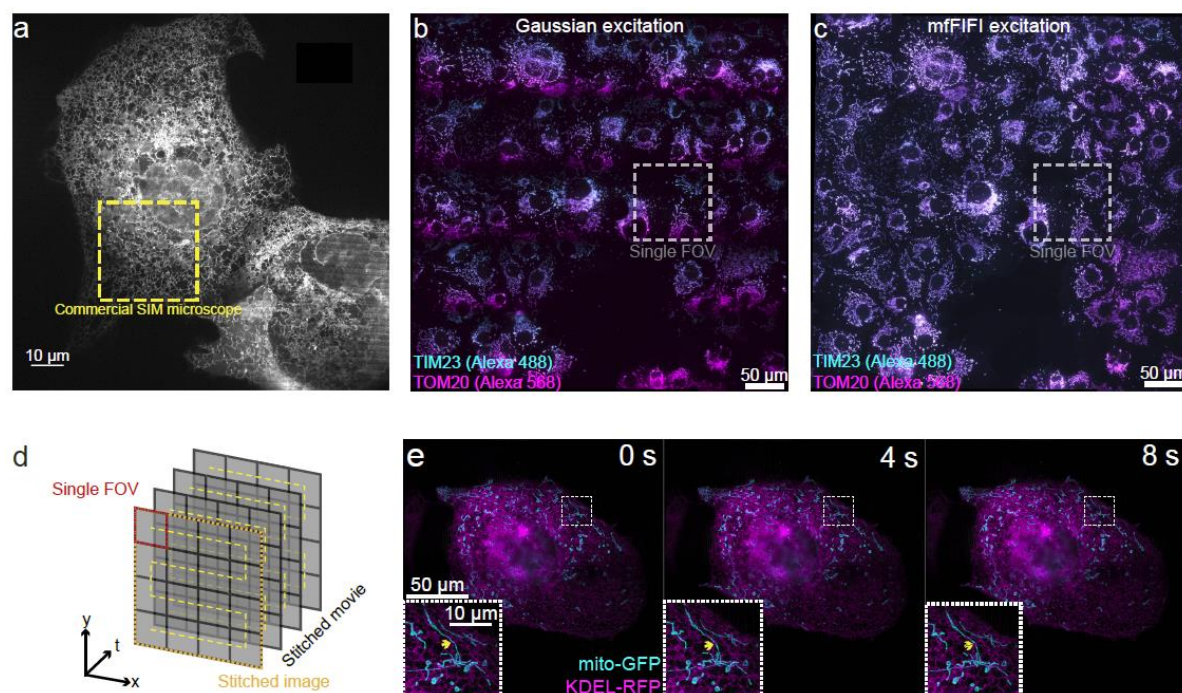
Figure 12 - Large FOV imaging and multi-FOV stitching.
a) Cos7 cell expressing KDEL-RFP imaged with an iSIM using mfFIFI excitation and an sCMOS camera enabling imaging of FOVs up to ~115x115 µm2 at doubled resolution compared to diffraction limited performance. Yellow square shows the size of a 30x30 µm2 FOV available on a standard commercial SIM setup. b,c) Raw iSIM images of Cos7 cells immunolabelled for TIM23 and TOM20, stitched from a 5x5 grid of FOVs using (b) Gaussian and (c) mfFIFI excitation. d) Introducing an additional layer of parallelization into iSIM imaging by iterating over multiple FOVs allows trading off the speed of iSIM imaging to construct larger FOVs at high speed and doubled resolution compared to diffraction limited performance. e) Montage showing frames from a high-speed movie built up over a 2x2 grid of FOVs (original movie 2s temporal resolution) of cells expressing mito-GFP and KDEL-RFP. Figure reproduced with the permission of Springer Nature, material from: Mahecic, D. et al. Homogeneous multifocal excitation for high-throughput super-resolution imaging. Nat. Methods 17, 726–733 (2020). [92]

The effective image size can be further extended by stitching together adjacent FOVs[97,98]. Such an approach requires homogeneous illumination to allow seamless stitching. The speed of iSIM imaging combined with the large FOV enabled by mfFIFI allowed us to stitch together dual-color 3D stacks covering a 500x500x5 µm³ volume with a 5x5 grid of FOVs, each acquired within 5 seconds (25 planes per FOV, 100 ms exposure time). With this approach, within 2 minutes, we could capture 3D images of more than 80 cells stained for the mitochondrial inner (TIM23) and outer (TOM20) membrane translocases, revealing coupled geometries of the two membranes (Figure 12b,c). The current limiting factor for multi-FOV imaging is the speed of stage translation and synchronization between stage translation and the rest of the iSIM acquisition control. In contrast, the same acquisition without mfFIFI resulted in varying intensity across each FOV, with pronounced dark boundaries at the borders of individual FOVs (Figure 12b).

For time-lapse imaging, we introduced an additional layer of parallelization by iterating the acquisition procedure over a grid of FOVs (Figure 12d). By trading temporal resolution for a gain in imaging area, we can use the speed of iSIM imaging to cover multiple FOVs. For example, by iterating over a 2x2 grid of FOVs we could reliably track over 270 mitochondria and their contact with the ER, known to serve as hotspots for mitochondrial division[99] at a temporal resolution of 2 seconds (Figure 12e), limited by the translation speed of the stage. Mitochondria are motile organelles which require fast, high-throughput imaging to capture their dynamics and heterogeneity. This illustrates how processes with less demanding temporal dynamics can benefit from mfFIFI to extend the throughput of iSIM without compromising spatial resolution.

Application: Mapping post-translational modifications of centriolar tubulin

Centrioles are organelles found in most eukaryotic cells that seed the formation of the axoneme in cilia and the centrosome in animal cells. Centrioles have a characteristic nine-fold radial symmetric arrangement of microtubule triplets towards the proximal end of the organelle, composed of complete A-microtubules and incomplete B- and C-tubules[100], with a transition to A- and B- microtubule doublets towards the centriole distal end[101] (Figure 13a). It is known that centriolar tubulin is enriched in post-translational modifications (PTMs), including acetylation and polyglutamylation[102,103]. Acetylation is known to stabilize microtubules, increase their flexibility and protect them against mechanical aging[104–106]. Glutamylation has been postulated to likewise stabilize microtubules in the centriole and protect the organelle from pulling and pushing forces acting during mitosis[103,107,108]. Although these observations indicate that centrioles might be stabilized via tubulin acetylation and polyglutamylation, the spatial organization of these PTMs on the organelle remains largely unexplored.

The recently developed variant of ExM termed ultrastructure expansion microscopy (U-ExM)[42] enables preservation of the structure and molecular identity of multi-protein assemblies. When combined with iSIM imaging, an expansion factor of ~4 results in an effective resolution of ~140 / 4 = 35 nm laterally and ~350 / 4 ≈ 90 nm axially after deconvolution. Compared with current state-of-the-art super-resolution microscopes with similar resolution performance, such as the HT-STORM[29] capable of imaging a 100x100 µm^2 FOV in ~5-10 minutes or a similar FOV with easySLM-STED[30] in 60-80 minutes, the iSIM is capable of stitching together images of expanded samples to form an equivalent FOV within 2-5 seconds (since the effective FOV is shrunk after expansion). This represents a 100-1000-fold improvement in imaging throughput. Therefore, acquiring datasets of thousands of particles that would take weeks or months to acquire on a conventional STORM or STED microscope require only 1-2 hours on the high-throughput iSIM.
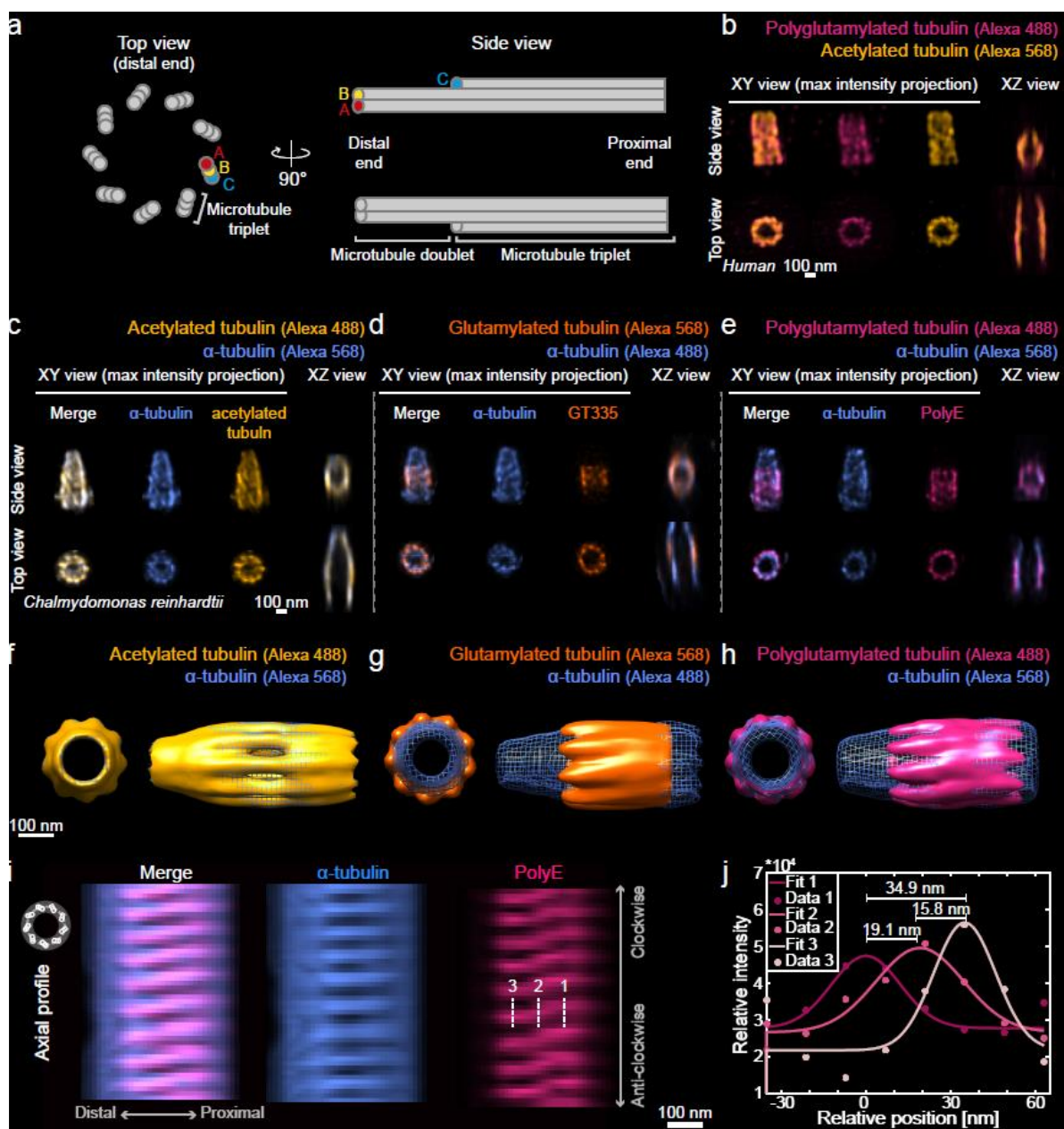
Figure 13 - High-throughput super-resolution imaging of expanded centrioles for mapping post-translational modifications of centriolar tubulin.

a) Schematic representation of the centriolar microtubule wall viewed from the side (left) and top from the distal end. The A-, B- and C-microtubules are indicated. b) Examples of individual mature human centriole particles orthogonal (side view) or parallel (top view) to the optical axis collected in expanded RPE-1 cells labelled for acetylated tubulin and polyglutamylation (PolyE). The lateral (XY) maximum intensity projection and axial (XZ) cross sections are shown. c-e) Examples of individual purified *Chlamydomonas reinhardtii* centriole particles viewed orthogonal (side view) or parallel (top view) to the optical axis labelled for α-tubulin as reference and (c) acetylated tubulin, (d) glutamylated tubulin (GT335) and (e) polyglutamylated tubulin (PolyE). f-h) High resolution particle averaging reconstructions of (f) acetylated tubulin, (g) GT335 and (h) PolyE with α-tubulin as reference. Scale bars: 100 nm (pre-expansion). Top views shown from the distal end. i) Circular axial projection (XZ profile) of the centriole reconstruction from (h) showing α-tubulin and PolyE signal around the centriole (viewed from the outside). j) Intensity profiles measured along the dashed lines from (i) showing the radial displacement of the PolyE signal. Figure reproduced with the permission of Springer Nature, material from: Mahecic, D. et al. *Homogeneous multifocal excitation for high-throughput super-resolution imaging.* Nat. Methods **17**, 726–733 (2020). [92]

Imaging expanded human centrioles in situ

To analyze human centrioles in a similar stage of the cell cycle and of the centriole duplication cycle, we synchronized RPE-1 cells with thymidine to arrest them at the G1/S transition and with the Plk4 inhibitor Centrinone to prevent the formation of new centrioles[109]. After expansion and staining with antibodies against acetylated and polyglutamylated tubulin, we imaged >100 centrioles in 3D in their cellular context per hour, revealing the distribution of these PTMs along the organelle (Figure 13b, Appendix F). Analyzing over 400 individual particles extracted from these images revealed that centriolar tubulin appears uniformly acetylated, while polyglutamylation terminates ~30 nm before the distal end (Appendix F). Moreover, the polyglutamylation signal exhibits a larger diameter, in line with the fact that acetylation occurs within the microtubule wall and polyglutamylation on the outer surface of the polymer[42] (Appendix F).

Imaging expanded isolated *Chlamydomonas reinhardtii* centrioles

By expanding purified centrioles we sought to capture dozens of pairs within a single FOV rather than just one per cell. We used centrioles purified from Chlamydomonas reinhardtii to this end since the U-ExM protocol had been optimized for this species[42]. Similarly to what we observed with human centrioles in the cellular context, we observe that in centrioles purified from Chlamydomonas reinhardtii, acetylated tubulin colocalizes with the microtubule wall along the entire length of the organelle (Figure 13c), in agreement with previous reports[110]. In contrast, we found that tubulin glutamylation (GT335) is concentrated in the central core region of Chlamydomonas reinhardtii centrioles (Figure 13d), as previously reported[110]. Since GT335 recognizes the first glutamylation branching required for polyglutamylation (PolyE), we would expect the distribution of PolyE to partially or completely overlap with that of GT335. Surprisingly, we found that although PolyE also localizes on the outer surface of the microtubule triplets where it has been suggested to localize to the C-microtubule[42], it covers a wider band along the length axis than GT335 (Figure 13e, Appendix F). This difference could reflect lower GT335 antibody labelling efficiency, since saturating the signal shows similar GT335/PolyE localization (Appendix G).

The high throughput offered by mfFIFI-iSIM allowed us to collect 3D images of thousands of purified expanded Chlamydomonas reinhardtii centrioles per hour. Having obtained 3D rather than 2D particles allowed us to use fewer particles to perform averaging and high-resolution multicolor reconstruction[111] compared to previous approaches using STORM[112] or electron microscopy[113,114]. Thus, we classified particles before reconstruction to identify and average only those particles sharing a high degree of similarity (ranging from 10-50% of the whole dataset, Table 4) (Appendix G), and thereby achieve even higher resolution reconstructions (Figure 13f-h). Here, we have focused on the most frequently appearing class, but other classes could also be independently reconstructed.

The resulting reconstructions revealed an unexpected shift in the tangential position of the PolyE signal from the proximal to the distal end (Figure 13i,j), which is also sometimes visible in individual raw particles. To account for this shift, we considered two possibilities: 1) the whole microtubule triplet twists around its axis while the PolyE signal remains localized to the C-microtubule[115] giving it an apparent twist (Figure 14a,b, Appendix H), and 2) the PolyE signal changes microtubule localization within the microtubule triplet (Figure 14a,b, Appendix H). Arguing against the first possibility, the microtubule triplet twists only within ~100 nm of the proximal end[116], while in our reconstruction the PTM twist occurs within a wider region covering ~250 nm from the proximal end (Figure 14c,d). Moreover, we determined that the first possibility would be expected to cause a moderate ~6 nm shift of the PolyE signal, and the second a more pronounced ~35-40 nm shift (Appendix H).

Dataset	No. segmented particles	No. of particles in reconstruction
Dataset #1 – *Chlamydomonas reinhardtii* acetylated tubulin (A488) + α-tubulin (A568)	2129	387
Dataset #2 – *Chlamydomonas reinhardtii* Glutamylation (GT335) (A568) + α-tubulin (A488)	6527	830
Dataset #3 – *Chlamydomonas reinhardtii* PolyE (A488) + α-tubulin (A568)	1865	910
Dataset #4 – human centrioles PolyE(A488) + acetylated tubulin (A568)	392	-

Table 4 - Dataset size and number of particles used for reconstruction.
Numbers of segmented particles obtained from the raw data of purified centrioles and used for particle averaging and reconstruction. The segmentation had a ~50% efficiency and improving the segmentation pipeline could possibly extract more particles from the same raw datasets.

Overall, we observe a ~10 nm change in the relative radial position of PolyE, compared to the reference α-tubulin signal (Figure 14d,e). Therefore judging by the relative displacement of PolyE, and not the relative position of PolyE with respect to a-tubulin, this is consistent with the "Twist + Shift" model. Similarly, from our reconstruction, we measure a twist of ~34.9 nm (Figure 13i,j, Figure 14f,g), which cannot be explained purely by twisting of the microtubule triplet. Therefore, we propose that polyglutamylation changes localization within the microtubule triplet along the centriole, moving from A- on the proximal end to the C-microtubule more distally.
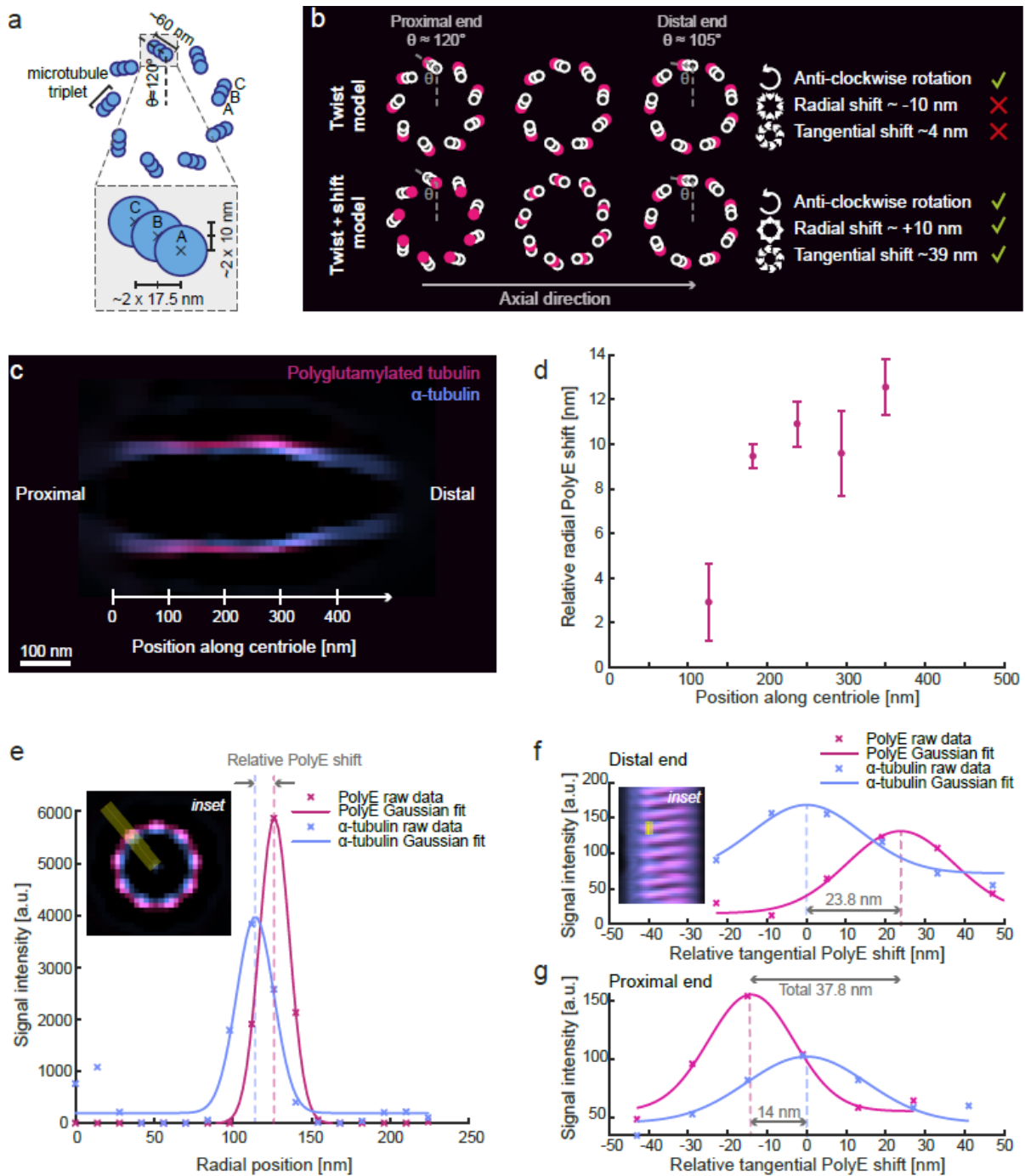
Figure 14 - Twist of polyglutamylated tubulin along Chlamydomonas reinhardtii centrioles.

a) Schematic illustration of centriolar microtubule triplets and expected radial and tangential displacements between microtubules in neighboring triplets (inset) viewed from the proximal end. b) Schematic representation of XY planes between the shift and twist models of PolyE shift along the proximal-distal centriole axis and their predictions (cross sections viewed from the proximal end). c) Cross section of the reconstruction YZ profile showing the barrel diameter with α-tubulin and PolyE signal. d) Radial position of PolyE signal relative to α-tubulin, measured at different positions along the reconstructed centriole for all 9 microtubule triplets, from the proximal to the distal end. Points mark the mean of the 9 measurements and error bars their standard deviation. e) The relative radial PolyE shift was calculated with respect to the α-tubulin signal by taking the difference between their radial positions, determined by Gaussian fitting. The profiles were measured from top views of the reconstructed centriole (inset). f,g) The relative tangential shift of PolyE is measured from the tangential projection (inset) with respect to α-tubulin at the f) distal and g) proximal end. The relative shift in PolyE compared to the α-tubulin signal was measured from reconstruction cross sections at different positions along the centrioles. Figure reproduced with the permission of

Multi-color 3D reconstruction

For mapping multiple PTMs within the centriole, we employ dual-color labeling, using α-tubulin staining of the microtubule triplet wall as a reference to subsequently align all PTMs (Figure 15). Overlapping all models shows that glutamylation presents a similar twist as polyglutamylation, which is expected since glutamylation would be required for polyglutamylation to take place. Although the GT335 signal appears to terminate earlier than the PolyE signal, saturating the GT335 signal shows similar localization at the proximal end.

Discussion

To summarize, we designed a flat-fielding method for efficient multifocal excitation, accompanied by a wave optics simulator which ensures optimal resolution performance. While the Koehler integrator has spot generating properties when used with coherent illumination, it introduces a strong wavelength dependence of the periodicity, making it unsuitable as such for multi-color applications[60]. mfFIFI provides a largely wavelength-independent solution for generating homogeneous multi-focal excitation, while benefiting from the homogenizing properties of the Koehler integrator. We implemented the mfFIFI module into an iSIM microscope, since its fast acquisition speeds and resolution doubling give it good potential for high-throughput super-resolution imaging. However, the mfFIFI module could be extended to any multi-focal excitation microscope such as a spinning disk confocal microscope[117] using a Nipkow disk configuration, but not with other flat-fielding solutions using diffractive optical elements[56], spatial light modulators (SLM)[66] or beam splitters[67]. Furthermore, combining mfFIFI with phase masks required for donut beam shaping could extend its application to parallelized STED[68,70,71] and RESOLFT microscopes.
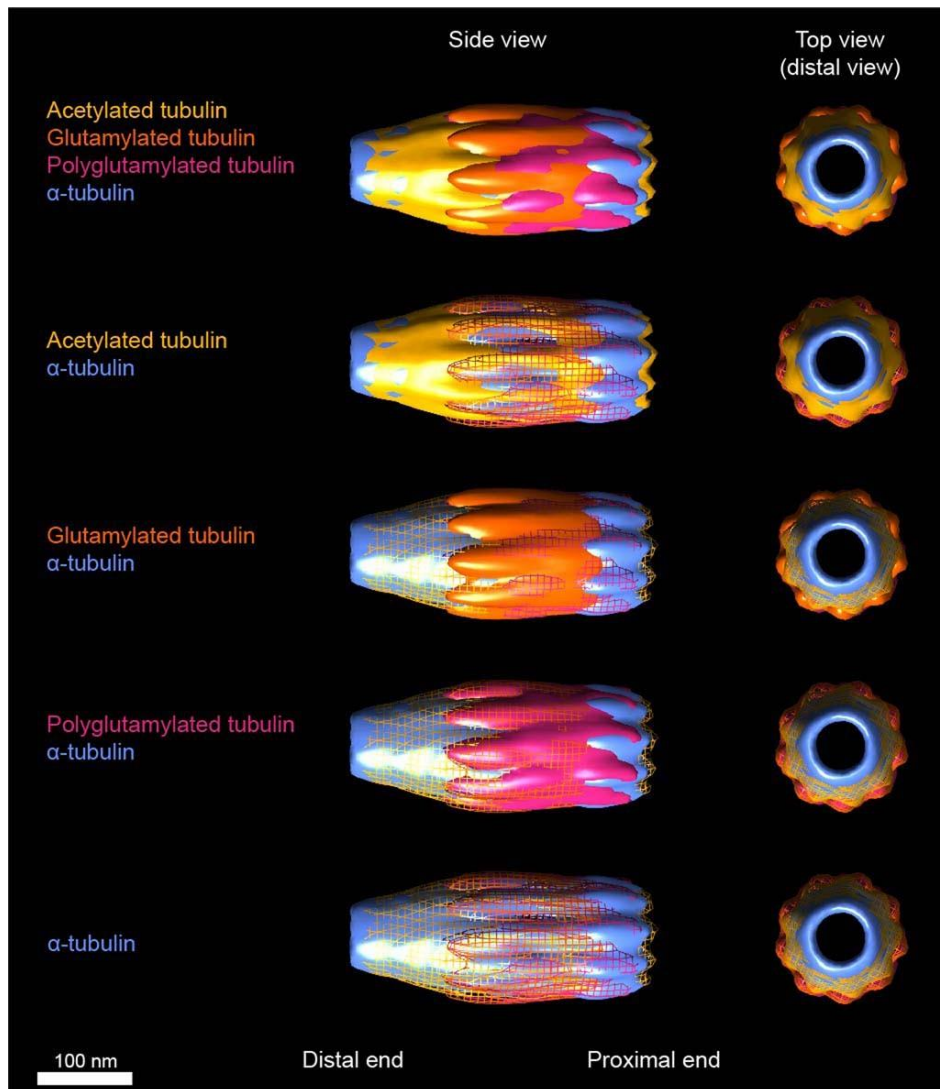
Figure 15 - Multi-color particle averaging and reconstruction of tubulin PTMs in Chlamydomonas reinhardtii centrioles.
a) Side and top views of α-tubulin reference with different PTMs. Top views are taken from the distal side toward the proximal side. Scale bar: 100 nm. Figure reproduced with the permission of Springer Nature, material from: Mahecic, D. et al. Homogeneous multifocal excitation for high-throughput super-resolution imaging. Nat. Methods **17, 726–733 (2020).** [92]

Flat-fielding enables multi-field of view imaging, which is a powerful way to maintain resolution while increasing the effective image size to span more length scales. This is important for sample spanning multiple fields of view, as in the case of tissues, or expanded samples. ExM sacrifices the effective FOV to increase resolution, and stitching provides a way to maintain throughput, allowing cellular features or structures to be imaged in situ, as we demonstrate by imaging hundreds of human centrioles in cells.

Particle averaging and reconstruction is traditionally used in ultrastructural biology, and leverages large datasets to capture the intrinsic variability within particles through classification before reconstruction, while averaging out the noise. In the case of ExM, different gels can have slightly different expansion factors, but this issue is circumvented by our iSIM setup since thousands of particles can be acquired from a single gel section ($\sim$5×5 mm^2). In our case, the collected datasets were sufficiently large to allow particle classification prior to averaging, an approach which improves the resolution of the reconstruction and which, to our knowledge, has not been previously used for fluorescence super-resolution. In addition to a 100-1000-fold improvement in throughput of iSIM/U-ExM over HT-STORM[29,112] or easySLM-STED[30], expanded samples offer enhanced accessibility of antibodies to bind

proteins in crowded assemblies. Beyond particle averaging, high-content or machine learning approaches rely on large datasets for training or screening, and can benefit from the combination of throughput and resolution described here.

Our previous attempts to image centriolar microtubules with STORM proved largely unsuccessful, restricting previous studies to the more accessible epitopes[112]. Here, we reveal previously unobserved molecular organization, showing high coverage of polyglutamylation in human centrioles, as well as precise localization to microtubule triplets along the *Chlamydomonas reinhardtii* centriole. We find that polyglutamylation appears to shift from the A-microtubule proximally to the C-microtubule more distally. It is possible that such a glutamylation shift reflects a centriolar tubule code that defines the spatial boundaries of the various elements that compose it, which could determine the positioning of different structural elements along the length of the organelle.

Chapter 4
Membrane bending energy and tension govern mitochondrial division

Parts of this chapter have been uploaded as a preprint at ref[118]:

> Mahecic, D., Carlini, L., Kleele, T., Colom, A., Goujon, A., Matile, S., Roux, A., Manley, S., 2019. Membrane bending energy and tension govern mitochondrial division. *bioRxiv*. https://doi.org/10.1101/255356

Contributions: Lina Carlini contributed to conceptualization, data acquisition, analysis, software and writing of the original manuscript. Tatjana Kleele contributed to conceptualization and data acquisition. Adai Colom contributed to the FLIM imaging. Antoine Goujon synthesized the mitochondrially targeted FliptR probe.

Abstract

Many molecular factors required for mitochondrial division have been identified; however, how they combine to physically trigger division remains unknown. Here, we report that constriction by the division machinery does not ensure mitochondria will divide. Instead, potential division sites accumulate molecular components and can constrict before either dividing, or relaxing back to an unconstricted state. Using time-lapse structured illumination microscopy (SIM), we find that constriction sites with higher local curvatures – reflecting an increased membrane bending energy – are more likely to divide. Furthermore, analyses of mitochondrial motion and shape changes demonstrate that dividing mitochondria are typically under an externally induced membrane tension. This is corroborated by measurements using a newly synthesized fluorescent mitochondrial membrane tension sensor, which reveal that depolymerizing the microtubule network diminishes mitochondrial membrane tension. We find that under reduced tension, the number of constrictions is maintained, but the probability that constrictions will divide is concomitantly reduced. These measurements allow us to establish a physical model, based on in situ estimates of membrane bending energy and tension, which accounts for the observed fates of mitochondrial constriction events.

Mitochondrial division – a division of labor

Mitochondria are highly dynamic organelles, transported through the cytoplasm along cytoskeletal networks as they change in size and shape. Mitochondrial morphologies can range from a filamentous, connected network to a fragmented collection of individuals. Underlying such morphological changes are altered equilibria between fusion and division[119,120]. These transformations have been linked to an adaptive response to cellular energy requirements, for example in response to stress[121–123] and influence a range of cellular functions including cell cycle progression[124]. As a vestige of their bacterial origins, mitochondria cannot be generated de novo, but must multiply by division, or fission, of existing mitochondria[120]. Division has also been suggested to act as part of a quality control mechanism and an intracellular signal for mitophagy[125,126].

In cellular division systems, internal assembly of the division machinery is tightly regulated and a series of cell cycle checkpoints ensure daughter cell viability. In contrast, the mitochondrial division machinery has been largely outsourced to the eukaryotic host cell and assembles on the outer surface of the organelle. Initially, the division site is marked by a pre-constriction defined by contact with ER tubules[99]

and deformed by targeted actin polymerization[127–129]. Subsequently, surface receptors including MiD49/51[130], Mff[131,132] and Fis1[133] recruit dynamin related protein (Drp1)[134,135] at the constriction site. Drp1 then oligomerizes into helices that wrap around mitochondria and hydrolyze GTP to provide a mechano-chemical force for constriction[136–139]. The dynamin family protein Dyn2 is also reported to play a role in the final membrane scission downstream of Drp1[140], although its role remains controversial[141,142].

All of these factors combine to deform mitochondria and ultimately define the constriction site. Intriguingly, pre-constrictions induced by a variety of mechanical forces can recruit the mitochondrial fission machinery[143]. However, it remains unknown how mitochondria integrate forces imposed by the cytoplasmic machinery to regulate division, and how physical constraints are combined to trigger mitochondrial fission. This is in part because it is challenging to quantify the relevant physical parameters in living cells.

Here, we use time-lapse Structured Illumination Microscopy (SIM) to measure dynamic changes in membrane shape down to ~100 nm, during mitochondrial division in living cells. A custom-written image analysis package (Appendix I) allowed us to trace the contour and measure the curvature of constriction sites, quantify local Drp1 intensities, and track the motion of daughter mitochondria. Our analysis revealed that more highly curved constriction sites were predictive of a higher likelihood of division. After dividing, daughter mitochondria often recoiled away from the scission site, suggesting that they were under tension. Fluorescence lifetime measurements of a newly developed membrane tension probe provided additional evidence that overall mitochondrial membrane tension was reduced under nocodazole treatment. Intriguingly, under this perturbation we also observed decreased fission rates and a delay in fission time, underscoring the importance of membrane tension in mitochondrial division. Finally, using quantitative shape and motion analysis and classical elasticity theory we could estimate the energy barrier to fission, as well as membrane tension. Taken together, our results are consistent with a model in which mitochondrial fission is a probabilistic process, with elastic energy and membrane tension governing the kinetics and probability of fission.

Live-cell SIM imaging

We performed live-cell SIM imaging of COS-7 cells transiently transfected with mitochondrial matrix-localized GFP (mito-GFP) and Drp1-mCherry. We observed that highly constricted sites were typically marked by Drp1-mCherry, but while some proceeded to fission (Figure 16A), others lost enrichment of Drp1 and relaxed to an unconstricted state ('reversal') (Figure 16B). For quantification purposes, we defined 'reversals' as instances when a mitochondrion accumulated Drp1 at its constriction site and reached a diameter below 200 nm before relaxing (Figure 16C,D). Overall, 66% of constriction sites with Drp1 proceeded to fission (N=112), while the remaining 34% relaxed to an unconstricted state (N=57).

Similar "reversible" or "non-productive" Drp1 constrictions were previously observed in yeast[144] and higher eukaryotes[129]. However, the features that distinguish reversals from fissions remain unclear.

To investigate the role of the division machinery in distinguishing fissions and reversals, we first examined colocalization between the ER and mitochondrial constrictions, as such contacts mark pre-constrictions which can become fission sites[99]. We found that both fissions and reversals occurred at ER contact sites (Figure 16E-H). Next, we examined the recruitment of Drp1; by quantifying the integrated intensity of Drp1, we found that its accumulation at constriction sites was similar for fissions and reversals. An increase of Drp1 typically coincided with an increased rate of constriction, measured at ~ 17 for fissions and 18 nm/s for reversals during the 5 seconds leading up to maximal constriction. Some sites underwent multiple rounds of constriction and relaxation, coupled with Drp1 accumulation and disassembly. However, both fissions and reversals sometimes displayed cyclic dynamics, 3±2 constriction cycles/min and 2±1 cycles/min respectively (N=61 and 38), implying that cyclic activity does not distinguish fissions from reversals.
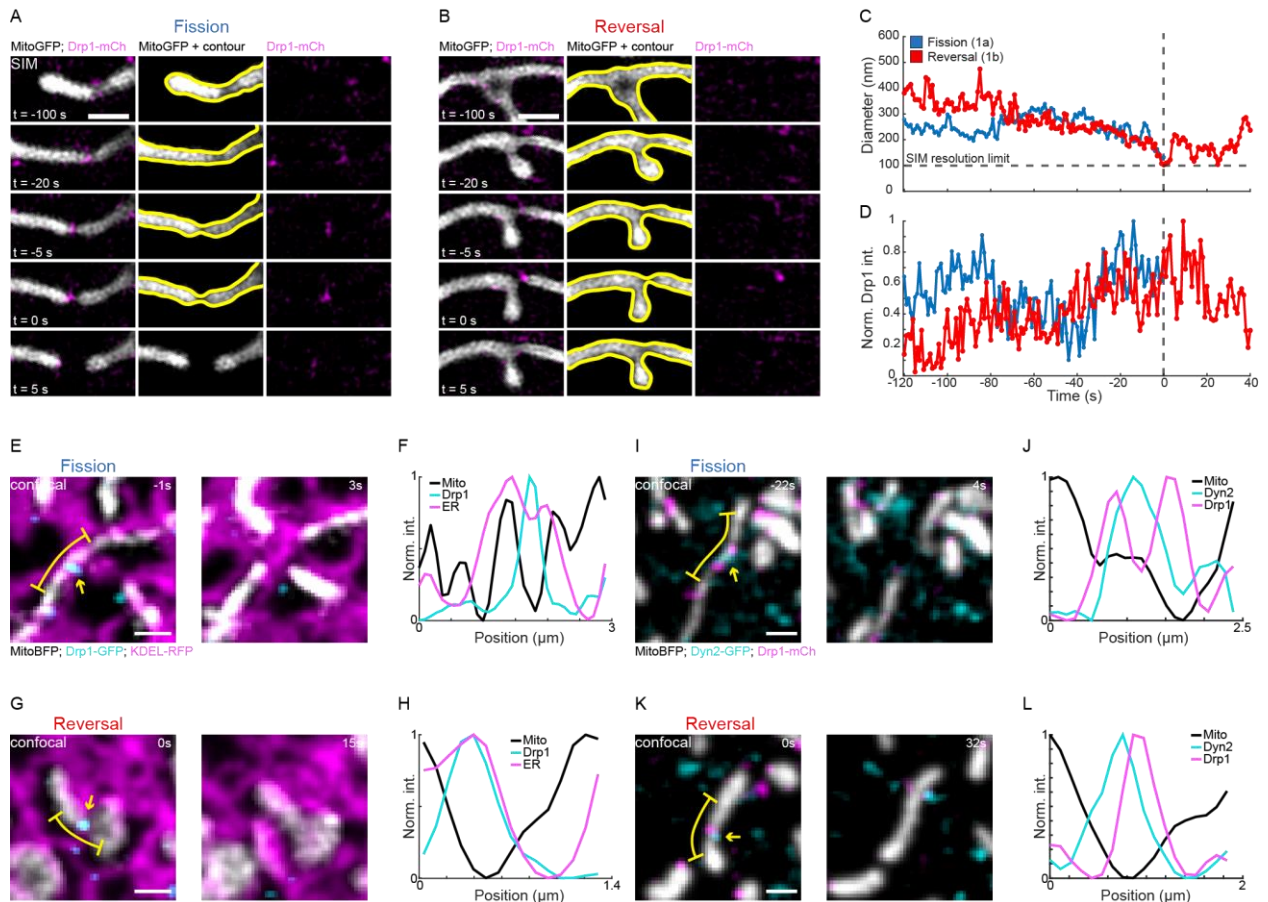
Figure 16 - Drp1 intensity and constriction diameters at constriction sites.
(A, B) Time-lapse SIM imaging of COS-7 cells transiently transfected with mito-GFP (greyscale) and mCherry-Drp1 (magenta) showing an example (A) fission and (B) reversal (see Movies S1,2, SFig 1). (C) Time evolution of diameter at the mitochondrial constriction site measured for fission (blue) and reversal (red) events shown in A, B. (D) Integrated intensity of Drp1 at the constriction site over time measured for fission (blue) and reversal (red) events shown in A, B, normalized to the maximum value. (E, G) Time-lapse live-cell confocal imaging of Mito-BFP, Drp1-GFP and KDEL-RFP showing examples of fission and reversal. (F, H) Intensity profiles of ER, Mito and Drp1 intensities adjacent to the yellow dashed lines in E,G. (I, K) Time-lapse SIM imaging of mitochondria and Dyn2 showing a reversal at a Dyn2-enriched constriction site. (J, L) Intensity profiles of ER, Mito and Drp1 intensities adjacent to the yellow dashed lines in I, K. Scale bar represents 500 nm in A and B. Scale bar represents 1 µm in E, G, I, K, yellow arrows mark the constriction site.

Since Dyn2 is implicated in mitochondrial fission[140], we also investigated whether its presence distinguishes fissions from reversals. Since our SIM imaging was limited to two colors, we performed fast (1 Hz) three-color live-cell confocal imaging of mitochondria, Drp1 and Dyn2. We observed both fissions and reversals, but found that Drp1 and Dyn2 could be present in both classes of constrictions. To determine whether these events satisfied our definition of reversals, we used the higher resolution of SIM to image mitochondria and Dyn2.

Constriction sites which reversed in the presence of Dyn2 also reached diameters down to ~130 nm. We noted that among mitochondrial division sites, only 30% were enriched in Dyn2 (N=30) as well as only 36% of reversals (N=18) (Figure 16I-L). These observations are consistent with recent reports that Drp1, but not Dyn2 is necessary for mitochondrial division[141,142]. Overall, no significant differences in the assembly of mitochondrial division machinery were observed between fissions and reversals, including ER, Drp1 and Dyn2. This led us to hypothesize that both fissions and reversals are distinct outcomes of a shared, but nondeterministic process.

Fission events are characterized by higher bending energy

The forces exerted by the division machinery deform the mitochondrial membrane. The resultant build-up of elastic energy is an important physical precursor to the hemi-fission state that membranes transit before undergoing scission[145]. We wondered whether fission and reversal sites could differ in membrane bending energy, which is a function of the two principal membrane curvatures (Figure 17a). To test this idea, we measured the local envelope curvature ($1/R_{env}$) and tube curvature ($1/R_{tube}$) in the vicinity of mitochondrial constriction sites (Figure 17b), assuming mitochondria are radially symmetric using our custom written analysis software (Appendix I). The local curvatures exhibited extrema: maximal tube curvature ($1/R^*_{tube}$) (related to the diameter) and minimal envelope curvature ($1/R^*_{env}$) near the same location along the mitochondria.

We monitored the time evolution of the curvature extrema. On average, constrictions leading to fission achieved measured diameters ($2R^*_{tube}$) of 120±4 nm (mean ± SEM, N=61) in the frame before fission (defined as time t=0), while reversals reached minimum diameters of 119±5 nm (N=38) (Figure 17c). These sizes are consistent with the diameter at which Dnm1/Drp1 is proposed to form a complete molecular assembly[137,146]. We also imaged mitochondria using live stochastic optical reconstruction microscopy (STORM), which offered higher spatial resolution but a reduced, ~6-second temporal resolution (Appendix J). Fission and reversal events measured by STORM had negligible differences in their minimum measured diameters, 90±18 (N=13) and 82±10 nm (N=10) respectively, marginally smaller than those measured by SIM (Appendix J). Our measurements are consistent with previously reported sizes of mitochondrial constrictions found with photoactivated localization microscopy (PALM)[147] and STORM[148]. Thus, within the resolution of SIM and STORM, we found no significant differences in tube curvature between fissions and reversals.

In contrast, distributions of envelope curvatures ($1/R_{env}$) were initially similar for fissions and reversals, but beginning at $t \sim -30$ seconds, deformations leading to fission achieved and maintained a lower minimum envelope curvature ($1/R^*_{env}$) on average: at $t = 0$, $(-8.1 \pm 0.5) \cdot 10^{-3}$ nm^{-1} compared to $(-6.4 \pm 0.6) \cdot 10^{-3}$ nm^{-1} in the case of reversals (N=61 and 38 respectively) (Figure 17d). To investigate the energetic consequences of this difference in shape, we calculated the bending energy at mitochondrial constriction sites (Appendix K). A single membrane may be modeled as an elastic sheet, whose bending energy, E_B, is given by the Helfrich equation[149]:

$$E_B(z) = \frac{\kappa_B}{2} \iint J^2 dA = \frac{\kappa_B}{2} \iint J(r,z)^2 dA(r,z)$$

Equation 13 - Helfrich equation for bending energy.
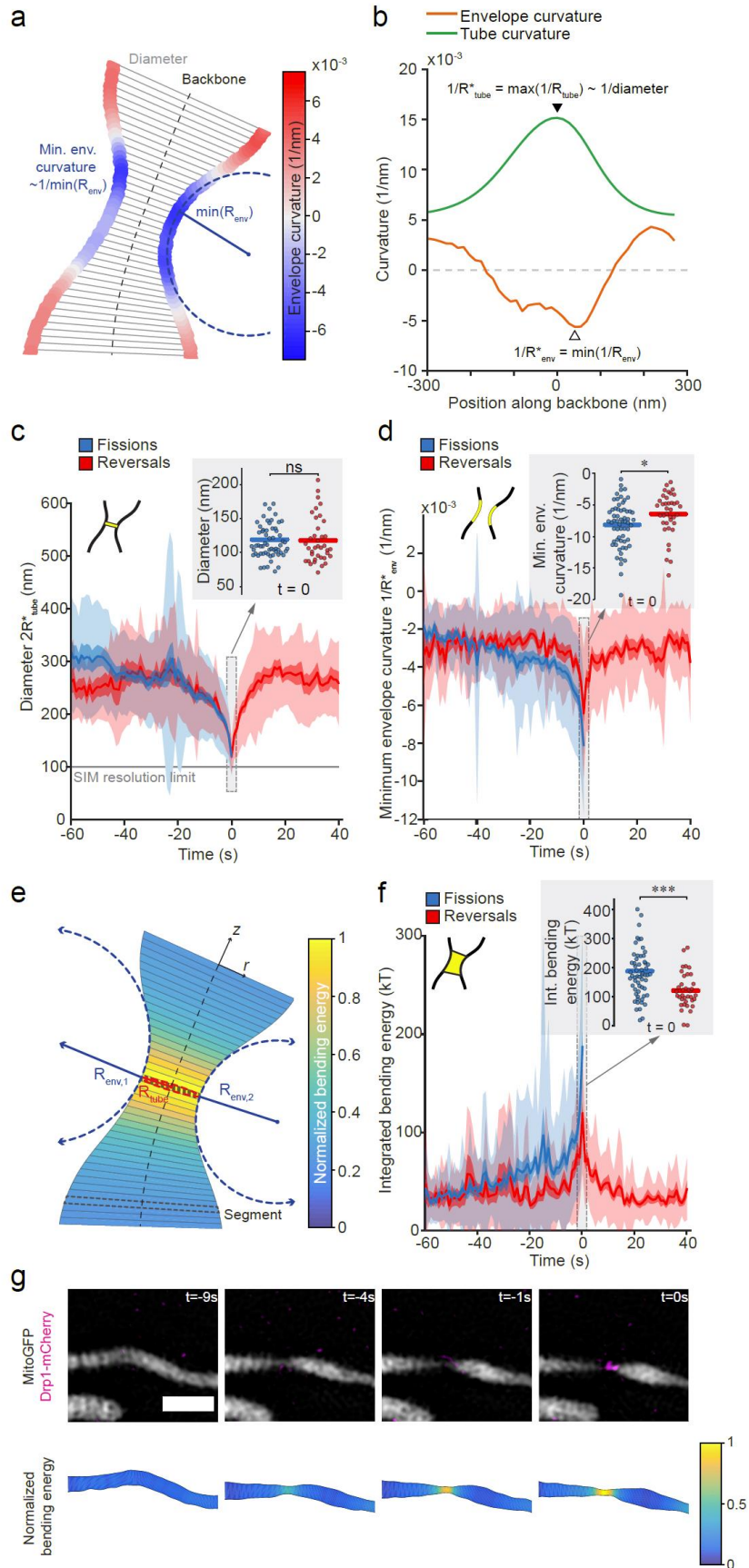
Figure 17 - Curvature and bending energy at the constriction site for fissions and reversals

(a) Schematic showing the envelope curvature at a constriction site (colormap). The minimum envelope curvature corresponds to the inverse of the radius of the smallest circle fit to the contour at the constriction site. (b) Tube curvature and envelope curvature measured along the backbone at the constriction site in (a). (c) Binned curves showing the evolution of the constriction diameter for fissions (blue, n=61) and reversals (red, n=38). Inset shows the distribution of minimal diameters of fission and reversals at t=0 (horizontal line shows mean) (d) Binned curves showing the evolution of envelope curvature at the constriction site for fissions (blue, n=61) and reversals (red, n=38). Shaded regions represent SD (light shade) and SEM (dark shade). Inset shows the distribution of minimal envelope curvatures of fission and reversals at t=0 (horizontal line shows mean). (e) Schematic showing the bending energy calculation. The local envelope curvature R_env was computed as the local mean of opposing sides R_(env,1) and R_(env,2). Analysis of the local tube (R_tube) and envelope (R_env) radii for individual segments (striped region) allowed estimation of the local bending energy (colormap). (f) Binned curves for the calculated local bending energies over time for fissions (blue, n=61) and reversals (red, n=38). Shaded regions represent SD (light shade) and SEM (dark shade). Inset shows the distribution of integrated bending energies at the constriction site of fission and reversals at t=0 (horizontal line shows mean). (g) Time-lapse showing the raw data (first row), computed local envelope curvatures (second row, colormap), and estimated local bending energies (third row, colormap) of a Drp1 mediated constriction site. Scale bar: 1um. Statistical significance calculated by 2-tailed Mann Whitney U test: n.s. P>0.05, *P<0.05, ***P<0.001.

Here, κ_B is the membrane bending rigidity, dA is the membrane area of a segment, J is the sum of local principal curvatures $J = (1/R_{tube} + 1/R_{env})$ measured for each segment along the mitochondrion, z the coordinate following the axis of the mitochondrion and r the radial coordinate (Figure 17e, Appendix K). The mitochondrial envelope is composed of two membranes, which are constrained to be in close proximity at the constriction site[150]. Thus, as a first approximation, we considered both membranes as a composite system with a rigidity of 40 $k_B T$, double the value of single lipid bilayers from in vitro measurements[151].

We followed the temporal evolution of the bending energy at the constriction site and estimated the energy of the constriction site as a whole by summing the local contributions over its area (Appendix J,H). As seen for the envelope curvatures, the time evolution of the bending energy was similar for fissions and reversals until $t \sim -30$ seconds, when the distribution shifted to higher values for constrictions resulting in fission ($188 \pm 15 \, k_B T$ versus $120 \pm 10 \, k_B T$ mean±SEM, N=60 and 37 respectively) (Figure 17f,g). This result might at first appear obvious, since constrictions resulting in fission must eventually overcome the energy barrier, while reversals do not. However, there is significant overlap between the distributions, and a range of values of constricted state bending energies can result in either outcome. We wondered whether other contributions to the membrane elastic energy besides bending might help distinguish fissions and reversals.

Fission events are characterized by increased membrane tension

Mitochondrial membrane pulling experiments

Another contribution to the membrane elastic energy arises from membrane tension[149], previously proposed to play a role in mitochondrial division[152]. In vitro experiments can be used to estimate membrane tension by exerting a pulling force on a membrane and measuring the size of the resulting membrane tubule[153,154]. Analogously, in living cells, mitochondria can exhibit membrane tubules (Figure 18a), which are dynamic, reversible structures spontaneously pulled out by microtubule-based motors[155,156]. These structures were observed at similar frequencies just before fissions or reversals (19% and 24% for N=101 and 59 respectively). We can infer the membrane tension by assuming it minimizes the elastic energy of cylindrical membrane (Figure 18b, Appendix L), in which case the diameter of the tube d is related to the membrane tension τ and the membrane bending rigidity κ_B[153,154]:

$$\tau = \frac{2\kappa_B}{d^2}$$

Equation 14 - Membrane tube pulling equation.

The average diameters of tubules pulled from mitochondria that subsequently either divided or reversed were 176 ± 4 nm and 229 ± 7 nm respectively (Figure 18c). Using Equation 14, we could infer that the population of mitochondria undergoing fission was under significantly higher average membrane tension at $5.81 \pm 0.54 * 10^{-6}$ N/m, compared to the population undergoing reversals at $3.85 \pm 0.75 * 10^{-6}$ N/m (Fig. 4d, N=19 and N=14 respectively, mean±SEM) (Figure 18d).
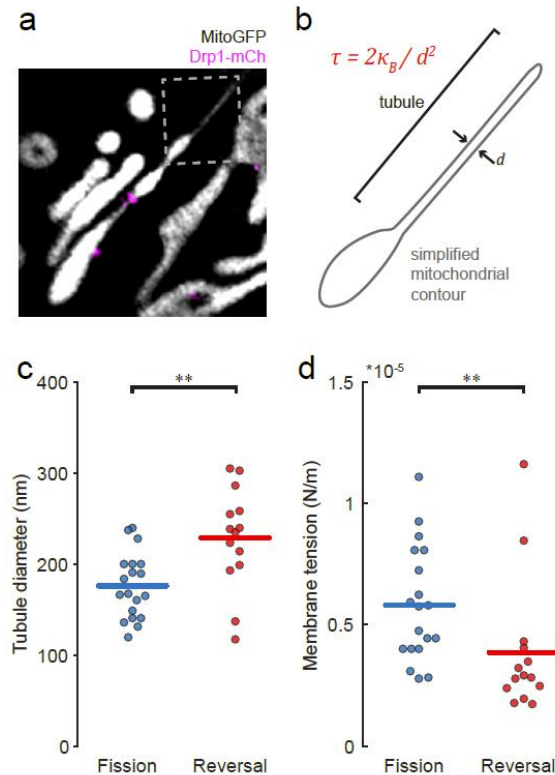
Figure 18 - Estimated membrane tension for fissions and reversals.
(a) Fluorescence image showing a constricted mitochondrion with a pulled membrane tube (outlined region). Scale bar: 1 μm. (b) Schematic diagram of the outlined region in (a) showing the radius of the tube r, used as a readout for tension τ. (c) Distribution of tubule radii measured between fission and reversal events. (d) Distribution of calculated membrane tension values between fission and reversal events. Statistical significance calculated by 1- and 2-tailed Mann-Whitney U test where appropriate: **P<0.01.

Mitochondria-targeted FliptR membrane tension sensor

Next, we set out to explore underlying mechanisms for differences in membrane tension between mitochondria. We noticed that after division, daughter mitochondria would recoil from each other, in a directed manner away from the division site. The presence of recoil after division suggests external forces are present and pulling the mitochondria in opposite directions, which could give rise to an increased membrane tension (Figure 19a). This coordinated motion was distinct from typical, sporadic mitochondrial mobility and was consistent with what one would expect when cutting an elastic body under tension. The recoil motion also allowed us to independently estimate membrane tension in individual mitochondria, with results consistent with those estimated from membrane tubules (Appendix L).

Mitochondrial transport is mainly mediated through microtubule based motor proteins[157], and we hypothesized that the same motors could exert an external pulling force and generate membrane tension. To test this hypothesis, we depolymerized microtubules using nocodazole[158,159]. Indeed, we observed a decrease in recoil velocities reflected in a reduction of estimated membrane tensions by 40% (N=33 fission events from control and 26 from nocodazole treated cells, Figure 19b).
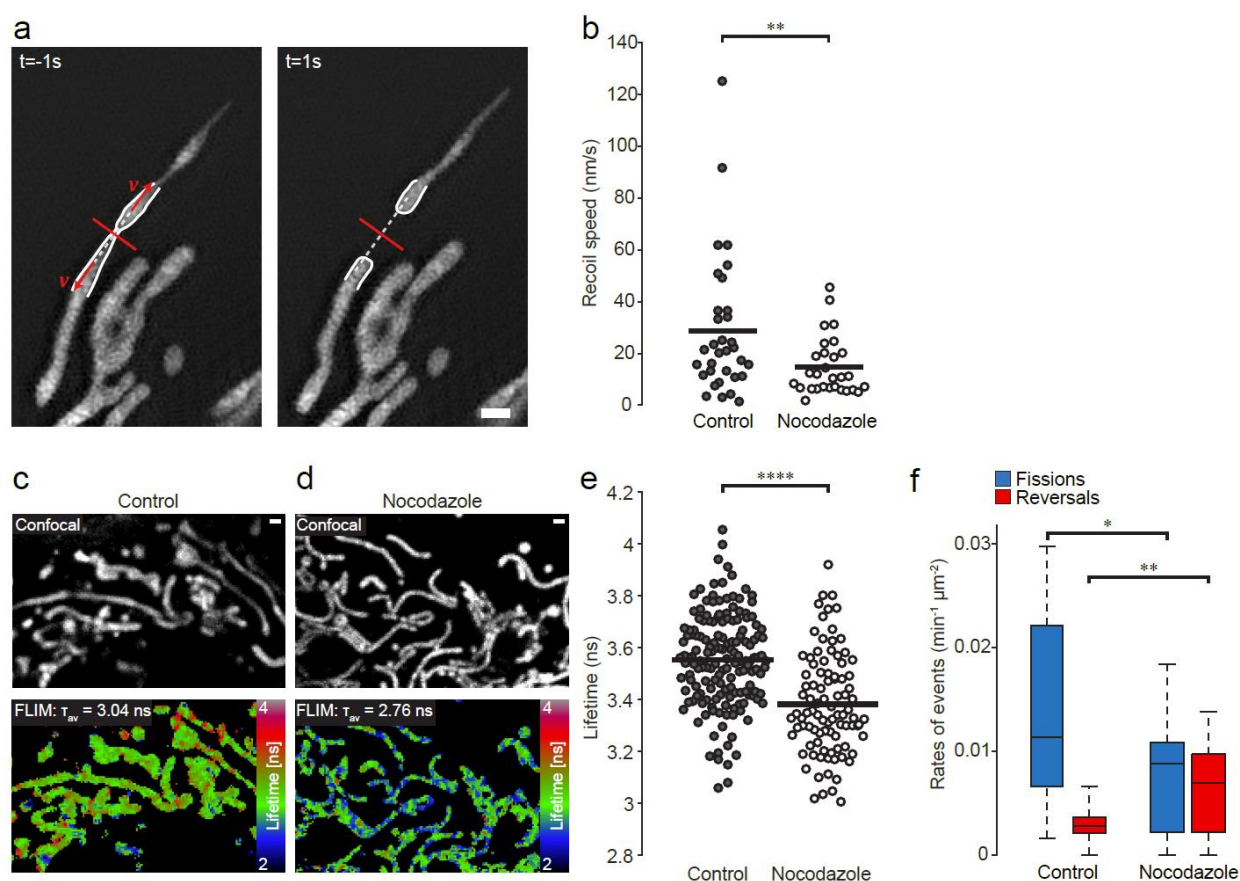
Figure 19 - Membrane tension under nocodazole perturbation.
(a) Time-lapse SIM images of a mitochondrion (mito-GFP) 1 sec before (left) and after (right) fission showing the recoil of daughter mitochondria post fission. Red line marks the constriction site with radius r. Measured retraction velocities v (red arrows) were projected perpendicular to the constriction site (white dashed line). (b) Distribution of recoil speeds of mitochondria post-division, between control and nocodazole treated cells. (c) Confocal and FLIM images of mitochondria in control cells marked with the FliptR fluorescent tension probe. (d) Confocal and FLIM images of mitochondria in nocodazole treated cells marked with the FliptR fluorescent tension probe. (e) Distributions of bulk fluorescence lifetimes of the FliptR fluorescent tension probe between control and nocodazole treated cells. (f) Box chart showing rates of fission and reversal in Nocodazole treated (N=16) and control (N=16) cells. Scale bars: 1µm. Statistical significance calculated by 1- and 2-tailed Mann-Whitney U test where appropriate: *P<0.05, **P<0.01, ****P<0.0001.

We further assessed changes in membrane tension with a mitochondria targeting variant of the mechanosensitive FliptR probe targeted to mitochondria[160–162]. The fluorescence lifetime of FliptR depends on the orientation between its chromophoric groups, which is sensitive to membrane tension (Appendix M). Comparing cells under control versus nocodazole-treated conditions, FliptR showed significantly shorter average fluorescence lifetimes, indicative of an overall loss of membrane tension (Figure 19c-e).

After establishing that nocodazole treatment reduced mitochondrial membrane tension, we examined the consequences of the loss of membrane tension on mitochondrial division. Importantly, the rate of Drp1-induced constrictions per mitochondrial area was unperturbed by nocodazole treatment (~ 0.014 $min^{-1}\mu m^{-2}$). Furthermore, the degree of overlap between mitochondria and ER remained unchanged, as

did mitochondrial membrane potential and diameter (Appendix M). However, we found a 2.4-fold increase in the rate of reversal events, and a concomitant decrease in the rate of fission (Figure 19f).

Probabilistic model of mitochondrial fission

Our measurements show that fission occurs over a wide range of bending energies, membrane tensions, and timescales. While many sites undergo fission within 20 seconds of the onset of rapid constriction, others take 4-5 times as long. Models developed for other fission processes, such as dynamin-mediated endocytosis, explain the distribution of fission times as an outcome of a stochastic process[163] in which thermal fluctuations allow the membrane to overcome the energy barrier to fission. Constricted membranes with higher elastic energy, and thus a lower residual energy barrier, will undergo fission more rapidly. Conversely, sites with lower bending energies should take longer, making it more likely for the fission machinery to disassemble within this timeframe, and lead to reversal. In such a stochastic fluctuation-activated model, the average time $\langle t_f \rangle$ to undergo fission is set by the fluctuation energy λ, and the residual energy barrier ΔE, given by the difference between the constricted membrane energy E and the total energy E_f required for membrane fission:

$$\langle t_f \rangle \propto \exp\left(\frac{\Delta E}{\lambda}\right) \propto \exp\left(-\frac{E}{\lambda}\right)$$

Equation 15 – Timing of fission in a probabilistic, fluctuation-activated model.

In the case of mitochondria, the relationship we observe between fission times and bending energy also follows an exponential form (Figure 20a). Equation 15 can be reformulated into an expression for the probability of fission $p(E)$ given a certain membrane energy $E \in [0, E_f]$:

$$p(E) \propto \exp\left(-\frac{\Delta E}{\lambda}\right) = \exp\left(\frac{E - E_f}{\lambda}\right)$$

Equation 16 - Fission probability in a probabilistic, fluctuation-activated model.

Since bending increases the energy of the constricted state, it brings constrictions closer to the energy required for fission, implying that constrictions with higher bending energy will be more likely to divide. This idea is supported by the experimentally measured probability of fission, defined as the ratio of the number of fissions to total constrictions with a given energy at maximum constriction, which increases with local bending energy and closely matches the relationship given by Equation 16 (Figure 20b).

Importantly, fitting the timing and experimental probability of fission to equations Equation 15 and Equation 16 allowed us to estimate the fluctuation energy and the energy barrier (Figure 20b). From Equation 16 we found an energy barrier $E_f \sim 250\ k_B T$, corresponding to the deformation energy above which we expect fission to dominate. Considering that mitochondria are double-membraned organelles, this value is consistent with previous simulations for dynamin mediated scission[163], as well as theoretical estimates of the energy barrier to a hemifission state, which spontaneously leads to fission[145]. We found from Equation 15 the fluctuation energy, $\lambda \sim 90\ k_B T$; consistent with this, we estimated the residual energy barrier, $\Delta E \sim 90\ k_B T$ as the difference between the estimated energy barrier and constriction site energies on average. This is far too large a barrier to be frequently overcome by thermal fluctuations alone, so what could account for this fluctuation energy?
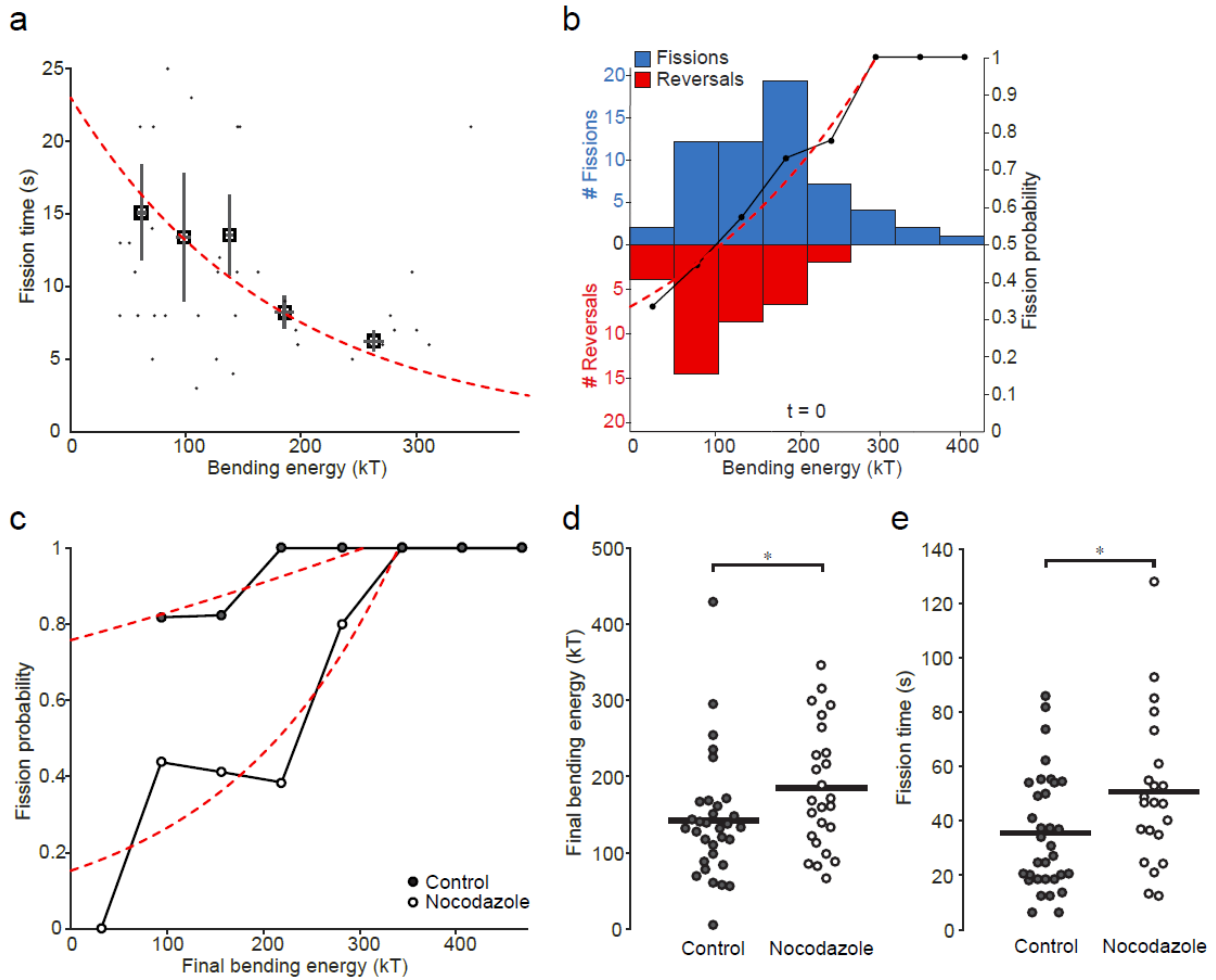
Figure 20 - Fission timing and probability related to bending energy and tension.
*(a) Fission time as a function of bending energy (averaged over last 3 frames before fission). Squares represent average values within different local bending energy intervals (30 k_BT bin size). Grey dots represent a subset of original data points. Error bars represent SEM. Fit curve (red dashed line) $y = a\,exp(-x/b)$ with $a = 23\ s$ and $b = 90\ k_BT$. (b) Left: Histogram showing numbers of fissions and reversals at different local bending energy intervals. Right: Experimental probability of fission calculated as ratio of fissions to total constrictions at different local bending energy intervals. Fit curve (red dashed line) $y = a\,exp(bx)$, with $a = 0.335$ and $b = 0.004\ k_BT^{-1}$ (c) Experimental probability of fission of control and nocodazole treated cells. Fits (red dashed line) $y = a\,exp(bx)$, with $a = 0.758$ and $b = 0.00091\ k_BT^{-1}$ for control and $a = 0.1528$ and $b = 0.00553\ k_BT^{-1}$ for nocodazole respectively. (d) Distribution of final bending energies between control and nocodazole treated fission events. (e) Distribution of fission times between control and nocodazole treated fission events. Statistical significance calculated by 1- and 2-tailed Mann-Whitney U test where appropriate: *P<0.05.*

A membrane under tension can stretch, producing small changes in its surface area[149,164], which contribute to its elastic energy. Consequently, stretching energy could contribute to overcome the residual energy barrier, ΔE, between the constricted and hemi-fission states. Using the values we found for membrane tension, we estimated the stretching energy at $\sim 50\ k_BT$, consistent across two independent estimates (Appendix N). This nearly matches the fluctuation energy, λ estimated above; we thus propose that membrane tension could act as a fluctuating source of energy, enabling constriction sites to overcome the energy barrier to fission. If this is the case, reducing the membrane tension by nocodazole treatment should reduce the values we extract for λ (Figure 20c). Fitting Equation 16 to both datasets indeed shows that while the barrier to fission remains mostly unchanged, the size of the energy fluctuations working to overcome the barrier was decreased as predicted, by 6-fold (Figure 20c). Examining the measured probability of fission between control and nocodazole treated cells, we

found it was shifted towards higher bending energies when membrane tension is decreased (Figure 20d). This is consistent with our model, since achieving a similar probability of fission would now require more deformation from Drp1 or other cellular machinery to increase the energy of the constricted state (N=33 control and 22 nocodazole). We also noticed that Drp1 appeared to reside for longer time periods at mitochondrial constriction sites in nocodazole-treated cells. Fission events in nocodazole-treated cells required on average ~12±7 s longer (N=33 control and N=22 nocodazole), also consistent with a major role for membrane tension in driving the final step of fission (Figure 20e).

Discussion

The mitochondrial division machinery is composed of multiple force-generating elements, including the cytoskeleton, other organelles, and Drp1/Dyn2 assemblies. These elements interact in a complex manner and their activity may depend on context, giving rise to cell-specific differences. However, mitochondria might also possess internal mechanisms that generate curvature such as accumulation of negatively curved lipids, like cardiolipin[165], at the constriction site to promote fission. Indeed, a dominant negative Drp1-mutation, which does not interact with cardiolipin, leads to lower fission rates[166]. Our physical framework is intended to account for how mitochondria integrate these forces to decide whether and when to divide, in a manner that is independent of the precise origin of the forces. Such a model can be readily adapted to include contributions from other, yet unknown molecular or context-specific factors.

We propose a probabilistic model of mitochondrial fission, where membrane bending energy and tension determine fission probability. Bending energy at the constriction site, induced by the constriction machinery, sets the distance to the energy barrier (Figure 21). Separately, membrane tension determines the range of stochastic fluctuation energies available to overcome the energy barrier (Figure 21). We show that microtubules, and more likely microtubule-based motor proteins, account for a significant portion of mitochondrial membrane tension. As predicted, with a nocodazole-induced decrease in membrane tension, there are fewer fluctuations large enough to overcome the fission barrier, which increases fission times and lowers the probability of fission. Interestingly, the decrease in fission rates under nocodazole treatment matches the increase in reversal events, suggesting that these two events are different outcomes of the same non-deterministic process. Within this model, any constriction can be assigned a probability of undergoing fission, which will depend on its distance from the energy barrier and the available fluctuation energies. Of course, constrictions cannot be maintained indefinitely, so if during their lifetime they do not experience a large enough fluctuation, they will become reversals.

As further evidence for excess membrane tension, we observed pearling modes on 11% of dividing mitochondria (N=88)[167], also previously reported in neuronal mitochondria[168] (Appendix M). We found that mitochondria exhibiting pearling modes eventually underwent fission of at least one of the constriction sites (100%, N=10). Conversely, reversals of pearling modes were rarely observed (4%, N=57) and occurred exclusively following fission at a neighboring constriction site, suggesting that the loss of tension released during fission could be responsible (Movie S4, S5).

Mitochondrial fission contrasts with many other fission processes since it requires the scission of two membranes (Appendix O). Our initial model considers the two membranes together, as a composite elastic sheet with a mean geometry, and is sufficient to capture the timing and probabilities of fission. However, it is readily extended to encompass more complex interactions, as we demonstrate by considering coupling that allows transmission of force from the outer to the inner membranes (Appendix O). Despite experiencing a lower membrane tension, we expect fission of the inner membrane will occur first, since its bending energy is geometrically constrained to be higher. Fission of the outer membrane could then follow due to a sudden increase in the local stress, since it must now bear the load which was previously shared with the inner membrane. Sequential timing is required for a non-leaky fission process, which is predicted for mitochondria[166,169] to avoid inadvertently triggering apoptosis or

disruption of membrane potential[143,170]. Further models could take into account the contributions of intrinsic curvature and Gaussian curvature.
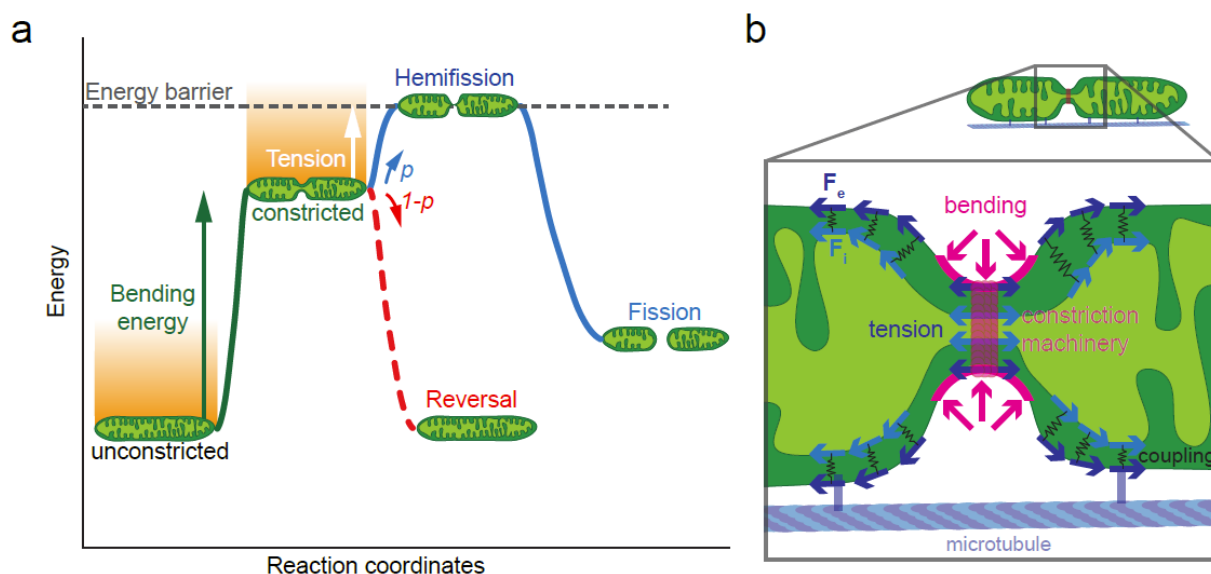
Figure 21 - *Physical model of mitochondrial fission controlled by bending energy and membrane tension.*
(a) Cartoon of the probabilistic model of mitochondrial fission showing the contribution of bending energy (green line) and membrane tension (orange shaded area) in reaching the energy barrier for fission (grey dashed line). Both bending energy and tension set the probability p of fission (blue line). Reversals occur either due to a lack of bending energy or low probability of necessary fluctuation energies. (b) Schematic representation of the different contributions to fission probability: bending energy (magenta) and tension (blue). Coupling transduces a fraction of the force acting on the outer membrane (Fo) to the inner membrane (Fi).

The probabilistic nature of mitochondrial fission could be of functional significance. At first glance, it appears inefficient that the cell assembles the molecular machinery, and provides the energy to constrict mitochondria, yet they sometimes fail to divide. But perhaps this could allow cells to adjust mitochondrial fission rates rapidly, by altering the probability for fission without changing expression levels. Regulating fission by modulating the bending energy or the longevity of constriction sites by post-translational modifications to Drp1[171–173] or altering pulling forces and membrane tension induced by Ca2+-dependent mitochondrial transport[174–176] could achieve this. Future experiments are needed to investigate whether and how extracellular stimuli, transduced through signaling cascades, are transformed into forces that can alter mitochondrial network morphology.

Chapter 5
Smart and adaptive temporal sampling for live-cell imaging

Contributions: Juliette Griffié wrote the SASS simulation platform and assisted with feature-based machine learning algorithms for event detection. Khalid Ibrahim assisted with image-based machine learning algorithms for event detection.

Abstract

Super-resolution fluorescence microscopy has enabled an unprecedented insight into the workings of biological samples below the diffraction limit. However, photobleaching and phototoxicity still present big challenges when imaging living samples, making fast and long-term live-cell super-resolution imaging mutually incompatible. Here, we propose a smart and adaptive acquisition strategy which modifies the imaging speed in real time in response to feedback from the sample, to achieve both fast and long-term live-cell imaging. Integrating this framework into an instant structured illumination microscope (iSIM)[26] allows it to better capture events of interest, while reducing photobleaching, phototoxicity and enriching the data. As a proof of principle, we image mitochondrial division – a fast (<10 s) but infrequent (~1 event/cell/min) event whose location and occurrence are difficult to predict. Combining information on mitochondrial shape and the biological molecular marker Drp1 with on-the-fly image processing, we identify mitochondrial division sites and capture them with increased temporal resolution (0.1 s), while reducing overall light exposure by up to 4-fold.

Smart microscopy

In fluorescence microscopy, the image captured at the camera is related to the fluorescently labelled sample by a function considering the microscope itself i.e. the optical components, and the imaging parameters used to acquire the image. The quality of the final image, especially in more advanced super-resolution microscopies, depends on choosing the appropriate imaging parameters, such as the exposure time and laser irradiance. Recently, methods that adapt the imaging parameters have evolved to optimize the imaging performance or tailor the imaging procedure to changes in the sample[89]. Examples of acquisition-oriented approaches include on-the-fly correction and minimization of imaging aberrations[177–180] and optimization of imaging parameters[181–184]. Sample-oriented approaches instead detect specific cues from the sample for recognition of specific phenotypes[78], sample-triggered complex protocol execution[78] or adaptive illumination applications[85,185–188]. For example, adaptive, spatially varying illumination has applied to light sheet[188], confocal microscopy[185,186], SIM[187] and RESOLFT[85], minimizing unnecessary exposure of the sample to excitation light, therefore reducing photobleaching and phototoxicity.

Photobleaching and phototoxicity impose limitations on time-lapse fluorescence microscopy of living samples. These constraints are represented by a confined imaging parameter space – a trade-off between sample health, SNR, spatial and temporal resolution – such that improving one parameter comes at a cost to the others[87,89]. The boundary of the imaging parameter space is set in part by the limited photon budget present within the sample. While the size of the photon budget is mostly determined by the choice of labelling strategy and its photophysical properties, how the limited photon budget is spent depends on the acquisition itself and the resulting photobleaching and phototoxicity induced during imaging. Due to these limitations, achieving high temporal resolution and long-term imaging are mutually incompatible and necessitate a compromise.

Biological processes can effectively occur across a range of spatio-temporal scales and can display varying dynamics. For example, during the bacterial cell cycle the constriction diameter changes at

different rates[189,190], or microtubules have different growth and shrinkage dynamics[191,192]. Furthermore, rare events such as mitochondrial divisions are difficult to predict and usually occur within a short timeframe (~10 s) once the main molecular player Drp1 starts to accumulate[118,129,135]. The infrequent nature of mitochondrial divisions necessitates long-term imaging, as sampling over a longer time period will increase the likelihood of an event occurring. On the other hand, due to the fast nature of the process, capturing the intermediate structures during mitochondrial division requires fast imaging speed. Therefore, rare but dynamics events such as mitochondrial divisions require at times different imaging speeds – fast to capture the event at good temporal resolution, and slow during a lack thereof to preserve the sample. However, there is currently no imaging technique that adapts the temporal resolution of the acquisition in response to dynamic changes and presence of events of interest in the sample. In other words, traditional acquisition procedures do not represent an efficient allocation of the sample's limited photon budget at all times.

Here, we propose a dynamic imaging framework for smart and adaptive temporal sampling (SATS) to use the sample's limited photon budget more efficiently by allocating resources when they are needed. SATS works by adapting the temporal resolution in response to events of interest and better sample the dynamic behaviour during rapid changes or capture events of interest at high temporal resolution. As proof of principle, we integrate these approaches into an iSIM setup and apply this framework to study mitochondrial division – a relatively fast but infrequent event that is difficult to predict. Using the SATS driven iSIM, we capture more events simultaneously and better sample their dynamics, while reducing unnecessary photobleaching and phototoxicity.

Basic principle of SATS

The principle behind SATS relies on adapting the temporal resolution in response to specific events in the sample. This allows the microscope to continuously adapt the trade-off between imaging speed and duration, choosing which one to prioritize and distributing the limited resources in the most efficient way, in response to the information collected from the sample.

The smart or adaptive imaging framework relies on three main steps similar to previous autonomous control systems[181,193]: sensing, computation and actuation (Figure 22) – which are iterated throughout the imaging procedure. Sensing serves to collect information from the sample, which is then interpreted by the computation step, resulting in adaptation in imaging conditions during the actuation step. Dividing the framework into separate steps allows for a more modular implementation where different sensing, computation and actuation strategies can be substituted without the need to re-design the entire framework[181].
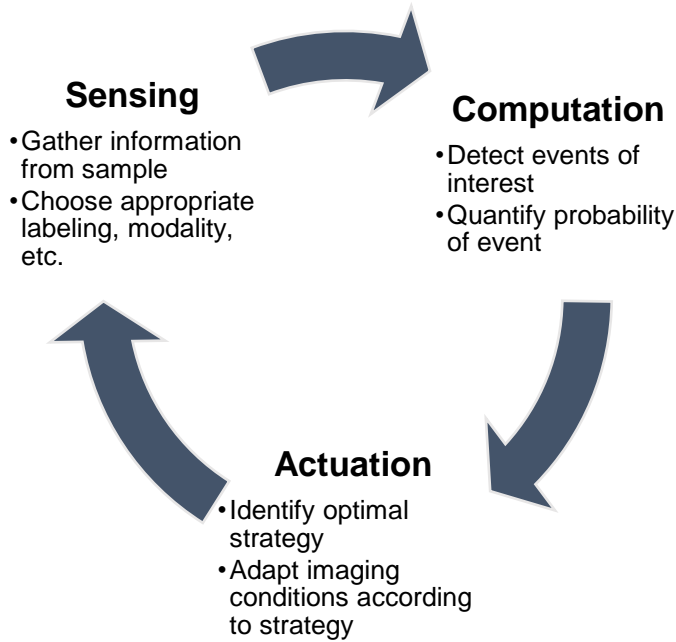
Figure 22 - Stages for adaptive microscopy.
Sensing refers to collecting information from the sample, such as acquiring a fluorescence image. Computation refers to interpreting the result of the sensing step to detect/quantify features or events of interest. For example, determining whether mitochondrial constrictions are present within an image. The actuation step determines and implements the appropriate response in response to the output from the computation step. For instance, if there is a strong likelihood of a mitochondrion dividing determined during computation, the actuation determines the appropriate imaging speed to capture the event of interest controls the hardware to respond appropriately.

Sensing

For the purpose of sensing, it is important to choose the imaging modality and labeling strategy that facilitate the detection of events of interest during the computation step further on. To detect mitochondrial constrictions, we considered using fluorescently labelled mitochondria to identify constrictions and hence potential division sites. However such an approach would rely on advanced image analysis of mitochondrial geometries and could entail long processing times. Furthermore, detection based purely on mitochondrial shape could also lead to a significant number of false positives, since fusion intermediates[194] and transient mitochondrial contact could be misinterpreted as constriction sites. Unlike these other geometrically similar mitochondrial morphologies, active mitochondrial constrictions are usually associated with a significant accumulation of the Drp1 protein, as it constricts mitochondria[118,129,135]. Therefore, combining a fluorescent mitochondrial marker with Drp1 as a molecular marker during the sensing step is designed to improve the accuracy of event detection during computation.

Computation

From the acquired image, computation serves to detect and quantify the probability of an event of interest. Examples of previous implementations have either relied on the presence of fluorescence as a binary switch to mark regions of interest[85,185,187], or required more advanced analysis of the acquired image to detect events of interest, for instance using cell circularity to detect mitotic rounding[78]. To detect mitochondrial constrictions, since the presence of a mitochondrial signal or Drp1 alone is not specific to the event of interest, the second approach is needed, using more advanced analysis of the

acquired image. Therefore, to specifically detect active mitochondrial constrictions in the presence of Drp1, we propose the following metrics (Appendix P):

1. **Relative Drp1 spot intensity** (Appendix P): Comparing the intensity of the brightest Drp1 spot to other non-productive Drp1 spots[129], should show a relative increase as Drp1 increases in intensity during constriction. Therefore, a simple strategy would rely on:
    ➢ Localizing Drp1 spots: N number of Drp1 spots within the FOV
    ➢ Measuring spot intensities: $I_n, n \in [1, N]$
    ➢ Comparing the intensity ratio of the brightest spot to the mean intensity I:

$$I = \frac{\max_{n \in [1,N]} I_n}{\sum_{n=1}^{N} \frac{I_n}{N}}$$

   The output is a scalar value which could then be used as a direct readout of the interest factor to scale the temporal resolution appropriately. Alternatively, the output could be rescaled between 0 and 1 to represent the probability of an event of interest within the FOV.

2. **Hessian eigenvalue filter** (Appendix P): Searching for mitochondrial constriction sites as low intensity, local saddle points in the mitochondrial channel with a corresponding high intensity maximum in the Drp1 channel. The output of this method is a map (2D array) of scalar values representing the output of the filter at different spatial positions. Similarly, the output map can be rescaled into a probability map indicating the spatial distribution of the likelihood of a mitochondrial division event.

Both metrics can be directly used to follow dynamic changes in the sample and adapt the imaging conditions such as the temporal resolution appropriately. Furthermore, machine learning and deep learning approaches might prove particularly useful for detecting features or events of interest, assuming sufficiently large labelled datasets are available[195].

Actuation

The response of the microscope to the metrics from the computation step and how it is implemented defines an actuation strategy. Examples from previous works include binary actuation steps – where readout from the sample triggers a binary response such as whether to illuminate that region of the sample or not[85,187], or gradual responses such as tuning the pixel dwell time[185] or laser irradiance[181]. The goal of the SATS strategy is to adapt the temporal resolution (by modulating the time interval between frames) to scale with the probability of the most likely event of interest, representing a mitochondrial constriction. To characterize the performance of different SATS strategies and compare to non-adaptive strategies, we developed a SATS simulation platform (Appendix R, Figure 24).

SATS strategies characterization and comparison

To remain general, we assume the output from the computation step is a variable x, such as the probability of a mitochondrial division event. To interpret changes in x, we introduce responses similar to the terms used in PID controllers and variants thereof[196], however with the important difference that while in PID control systems the actuation affects the output readout (such as changing the power of a heater will affect the room temperature), in a SATS strategy adapting the temporal resolution will (in principle) have no effect on the probability of a mitochondrial division event. Therefore, we eliminate the need for an integral component since the history of events should not contribute much to the likelihood of a mitochondrial constriction appearing, and there is no setpoint for the system to tend to. Instead, the strategy uses either proportional terms for direct feedback, and derivative terms to anticipate changes in the sample[196]:

- **Proportional**: the actuation scales proportionally with x
- **Derivative**: the actuation scales with the nth derivative of x, written as $d^n x / dt^n$

Overall, a strategy can use multiple of these components, such as combining the proportional approach with derivatives up to a certain order. More specifically, while the proportional term serves as a direct positive feedback for mitochondrial constrictions, the derivative terms serve to anticipate changes in the variable x, and can be used to maintain a uniform sampling of the event of interest, at a resolution Δx (Figure 23, Appendix S).
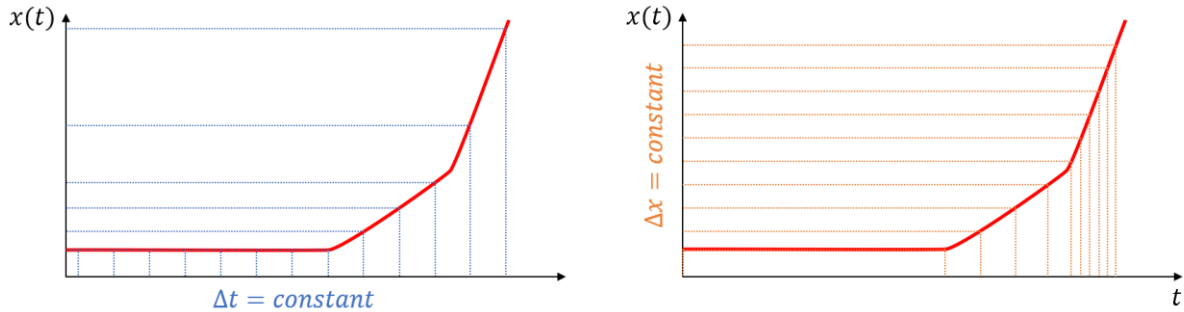
Figure 23 - Proposed SATS strategy using derivative terms.
Left: traditional time-lapse imaging strategies acquire images at fixed time intervals regardless of changes in the sample or feature of interest x. Right: Proposed derivative SATS strategy adapts the time interval between frames to maintain a constant sampling and resolution Δx of the feature of interest x.

To test the performance of adaptive strategies and compare them to the best possible performance achievable by traditional non-adaptive strategies, we also compute the optimal fixed temporal resolution that corresponds to the fixed temporal resolution required to capture the fastest rates of change in x while maintaining the desired sampling resolution Δx. This is computed as:

$$T_{opt} = \left(\max \left| \frac{dx_{GT}}{dt} \right| \right)^{-1} \Delta x$$

Equation 17: Optimal non-adaptive temporal resolution.

While this represents the optimal non-adaptive temporal resolution, it is generally impossible to know this value in advance and therefore near-impossible to achieve using traditional non-adaptive imaging procedures.

To quantitatively compare the different strategies, all strategies are evaluated based on three performance metrics:

- **Sampling-based reward**: rewards a strategy for updating the temporal resolution so that the sampling resolution Δx of the feature of interest x is maintained within ±20% of the fixed value (Figure 24C)
- **Intensity-based reward**: rewards a strategy for scaling the temporal resolution proportionally to the readout variable x within ±20% of the real ground truth intensity value
- **Light dose penalty**: represents the effective delivered light dose computed as the total number of timepoints acquired by the strategy
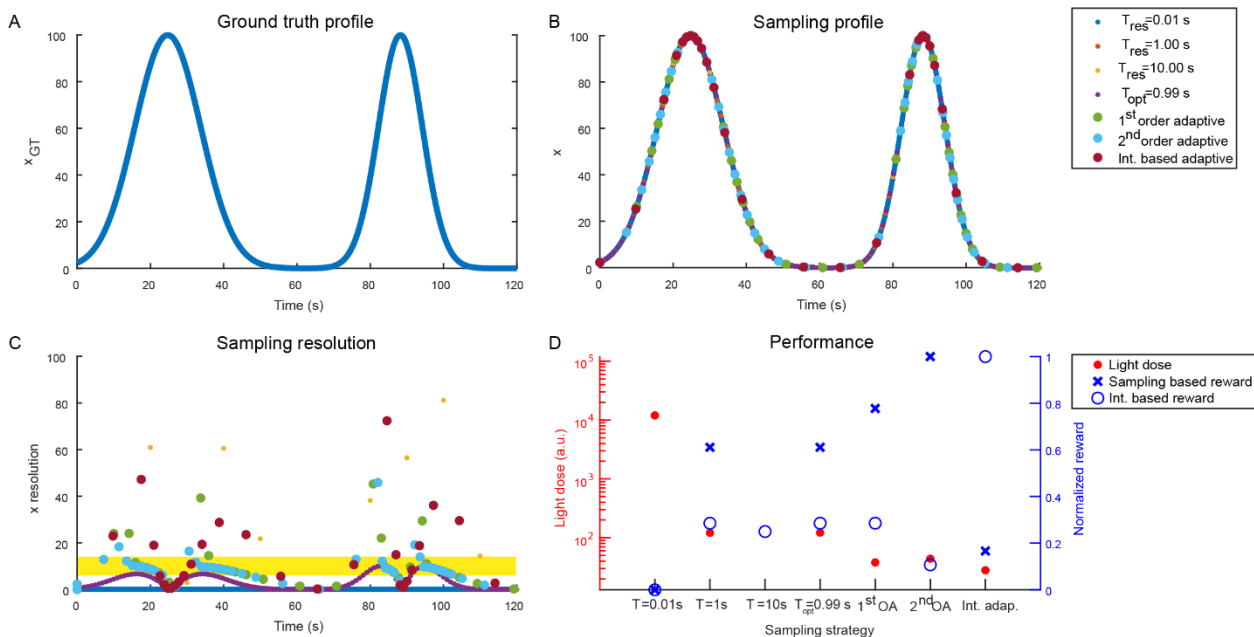
Figure 24 - SATS platform for strategy comparison.
A) Ground truth profiles generated by the simulation platform. In this case, x represents the output of the computation step, for instance the probability of a mitochondrial division event. B) The ground truth profile, as sampled by different sampling strategies. C) The resolution with which the variable x is detected. The yellow region highlights the region within which the sampling corresponds to that specific by the user. D) Performance evaluation of the different strategies. OA = order adaptive refers to the derivative based strategies. Int. adap. = intensity-based adaptive refers to the proportional based strategies.

The results of the SATS simulation platform show that all adaptive strategies generally outperform all non-adaptive strategies, while using comparable or lower light doses. For instance, traces that contain 1-2 events during the simulated time duration tend to sample the events as well as the optimal temporal resolution strategy T_{opt}, but do so using 3-4 times lower light doses (Figure 24D). This is because while the optimal strategy keeps illuminating the sample at the same rate regardless of the presence of events of interest, the adaptive strategies scale down the temporal resolution during a lack thereof, delivering significantly less light to the sample.

Furthermore, to test the effect of noise on the strategies, we introduce a random noise model to simulate computation readouts with different SNRs (Figure 25).
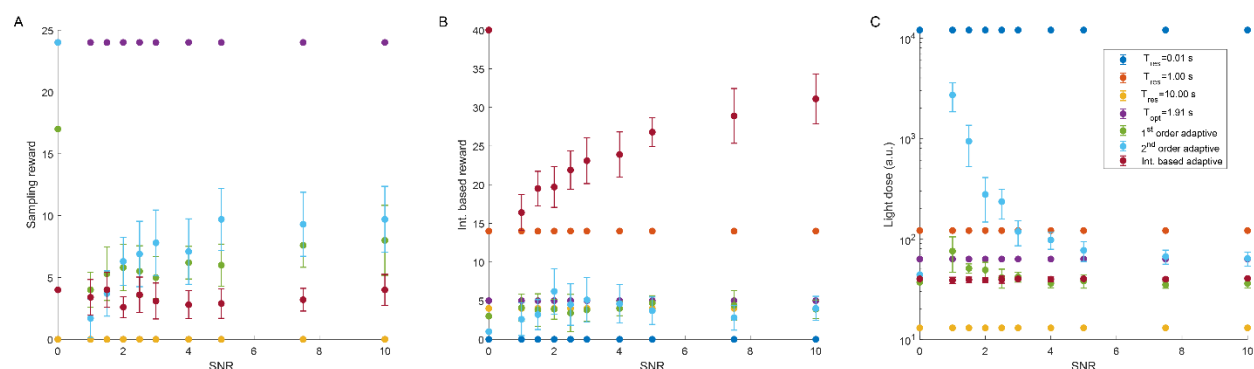
Figure 25: Effect of noise on the performance of SATS strategies.
A) Sampling-based reward for different strategies at different SNR levels of the ground truth signal. SNR=0 represents the case without noise. B) Intensity-based reward for different strategies at different SNR levels of the ground truth signal. C) Total delivered light dose for different strategies at different SNR levels of the ground truth signal. All simulations performed on a 2 peak sinusoidal curve, imitating two consecutive events of interest.

As expected, the traditional, non-adaptive techniques maintain constant performance across different SNRs (Figure 25). Importantly, the calculated derivative terms are susceptible to noise, especially the higher the derivative order. While higher order derivative terms improve the ability to predict changes further ahead, due to their sensitivity it is unlikely that orders higher than the 2nd order would significantly improve the performance (Figure 25A). Overall, under conditions more representative of experimental data, strategies relying more on the proportional term perform better and more consistently in the presence of noise. In fact, even at high SNR values, the derivative strategies tend to achieve <50% of their performance without noise (Figure 25A), while proportional strategies recover >80% of their maximal performance (Figure 25B). Similarly, proportional strategies perform more consistently across varying SNRs, delivering similar total light doses, while strategies using increasing proportional terms appear sensitive increasingly sensitive to noise at high order terms (Figure 25C). More work is required to mitigate the effects of noise on the actuation step.

Application of SATS to mitochondrial division

To showcase the applicability and advantages of the SATS network, we implement it into an iSIM to capture mitochondrial division events. Mitochondrial division is a dynamic event which usually takes from 5 to 30 s to complete after the onset of constriction. However, such events are difficult to predict in advance and tend to be infrequent, with rates of 0-5 mitochondrial events taking place within a 5 minute period, depending on the size of the FOV. The dynamic range in the timing of mitochondrial division makes it a good application for SATS.

We integrated the SATS framework into the custom-built iSIM[26,92]. The ability of iSIM to achieve single-shot super-resolution and the lack of a complex reconstruction algorithm make it a good candidate for on-the-fly image processing. Since iSIM offers a 2-fold improvement in resolution, this additional information can prove useful for detecting certain events of interest reaching sizes below the diffraction limit of light, such as mitochondrial constrictions. Finally, the temporal dynamic range of the iSIM spans over 5 orders of magnitude, from minutes to tens of milliseconds[26]. This flexibility in the temporal resolution gives the iSIM a unique advantage for SATS, compared to more advanced super-resolution techniques. Nevertheless, the framework remains generalizable to other applications and imaging strategies.

Once implemented into the acquisition software and hardware control, the microscope could successfully vary the temporal resolution, by adapting the time interval between sequential frames, while keeping a constant exposure time. This way we ensure that the changing temporal resolution does not result in images with varying quality.

To summarize, the sensing, computation and actuation steps were implemented as follows:

- **Sensing**: To gather most useful information for detection of mitochondrial constrictions, the sample consists of plated COS-7 mammalian cells transfected with a mitochondrially targeted GFP (mitoGFP) and Drp1-mCherry. The sample is imaged using dual-color iSIM imaging and both channels are forwarded to the computation step.
- **Computation**: For an initial test, we implemented the relative Drp1 spot intensity algorithm for event detection. Therefore, the computation step is done only on the Drp1 channel.
- **Actuation**: Based on the computed event probability, the temporal resolution is adapted using only the proportional components of the SATS strategy. Therefore, the temporal resolution is adapted proportionally to the output of the computation step and bounded by minimal and maximal temporal resolution fixed by the user. The temporal resolution was updated every second.
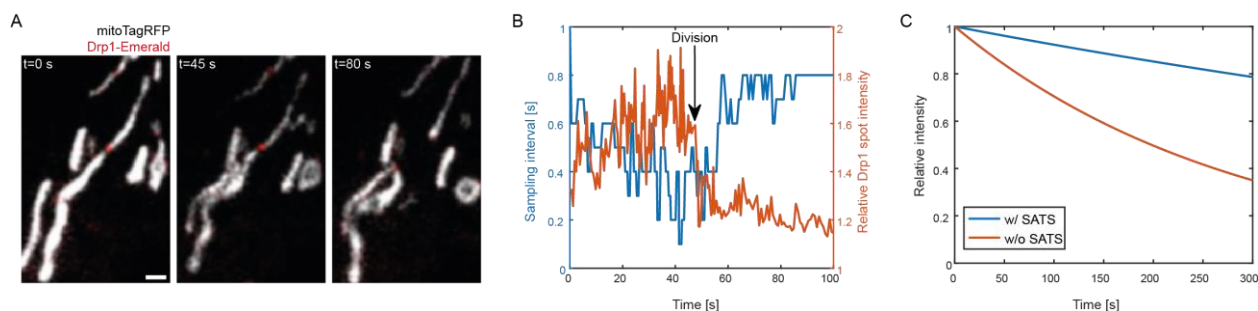
Figure 26 - SATS application to mitochondrial division.
A) Frames at different timepoints of a mitochondrial constriction and division captured using SATS. Scale bar: 1 μm. B) Right: Changes in the readout from the sample during the computation step (here using relative Drp1 spot intensity as readout). Left: Changes in the temporal resolution of the acquisition during the SATS acquisition. C) Normalized bleach curves obtained from a mitochondrial division event captured with and without SATS. The acquisition without SATS was done with the fastest temporal resolution of 0.1 s.

Analyzing the movies and changes in temporal resolution during the acquisition confirms that as constriction events become more prominent with a corresponding increase in relative Drp1 intensity, the temporal resolution increases (Figure 26A,B). Analyzing the bleaching curves between movies acquired with and without SATS show that SATS results in significantly less bleaching during the acquisition time, compared to acquisitions with a fixed temporal resolution (Figure 26C). Therefore, SATS allows the capture of mitochondrial constriction and division events at increased temporal resolution, while preserving the photon budget of the sample in the absence of these events. Further work is required to integrate and test the performance of alternative computation and actuation strategies, and test their performance on mitochondrial division.

Discussion

Traditional imaging is presented with a trade-off between the temporal resolution and imaging duration, where prioritizing one comes directly at a cost to the other. The SATS framework overcomes this limitation by providing both high temporal resolution of events of interest, while preserving the sample and extending the imaging duration when possible. Finally, an increasing difficulty of high-throughput imaging is handling large datasets and isolating useful data from increasingly large datasets. SATS tackles this problem by reducing the amount of acquired unnecessary data, while producing more informative data on a specific event of interest.

To overcome some of the effects of noise during the sensing and computation steps, it is possible to introduce a stepwise change and limit the rate at which the actuation can take place. For instance, instead of directly adjusting the temporal resolution based on the computation step, it would be possible to constrain the adaptation to either a gradual increase, gradual decrease or no change. This way the effect of noise would effectively be averaged out over a longer time period. However, a gradual change might limit the ability of the strategy to capture rapid changes in the sample.

While the aim of SATS is to adapt the acquisition procedure to the sample, there are potential pitfalls of such as approach that should be carefully considered when interpreting the underlying biology from such data. Firstly, as good scientific practice, decoupling real effects from experimental and biological variability requires that different samples are compared under identical experimental conditions. This would no longer be the case within the SATS framework, as the acquisition would be tuned to each sample separately. Therefore, while it could be possible to account for differences in imaging procedures as part of post-processing, the SATS framework might not be appropriate for specific studies aiming to evaluate condition specific differences. Furthermore, it is currently not fully understood how cells respond to changes in imaging conditions, but it is thought that sample health and the delivered light dose are not related linearly but depend on other factors[197–199], such as maximal intensity,

exposure time, recovery time, etc. Due to the varying exposure of the sample to the excitation light in SATS, it might become more difficult to account for nonlinear effect on cell health during such constantly changing imaging conditions.

While in this work we focus on a specific process of mitochondrial division, the general SATS framework can be extended to a range of other biological contexts and microscopes. The overall modular approach to adaptive imaging as consisting of separate sensing, computation and actuation approaches provides more flexibility in adapting it to a variety of problems. For instance, highly dynamic events such as cell division, or rare events such as cell extrusion or specific phenotypes could be captured better with the SATS framework. Similarly, the SATS framework is not specific to the iSIM alone, but could be extended to other microscopy techniques. While the iSIM has the advantage of generating single-shot super-resolution, the main constraint on other applications would be that the computation step based on the acquired images should be possible to do on the fly. While this is not a problem for simple microscopy techniques such as widefield imaging or confocal, more advanced techniques such as SIM or SMLM where multiple frames are needed to reconstruct a single super-resolved image might have to identify alternative means of detecting events or features of interest within the raw images, or provide a preliminary reconstruction for on-the-fly data processing.

Finally, in this work we focus on temporal sampling of events of interest, or in other words adapting the temporal resolution in response to specific cues from the sample signaling an event of interest. This adaptation refers to only a limited number of imaging parameters, and one could imagine different frameworks adapting the spatial resolution or imaging modality to further explore the imaging parameter space. For instance, sensing is not limited to detecting events of interest, but could instead prioritize other features of the sample such as sample health. For instance, imaging using different sensors such as TMRE[200], could be used as a readout for cell health since mitochondrial depolarization is one of the early effects of phototoxicity[201]. Therefore, detecting changes in sample health could adapt the imaging conditions to prevent further photodamage and this way ensure viable imaging over prolonged time periods.

Chapter 6
Conclusions and outlook

Conclusions

Since its ground-breaking development over a decade ago, super-resolution microscopy has become an established tool in biological research and has led to a range of new insights and the influence of which was acknowledged by the 2014 Nobel Prize in chemistry. Over the past decade, the field has overcome numerous challenges such as achieving multi-color, 3D and live-cell imaging. Nevertheless, with the emergence of big data and machine learning, the application of super-resolution microscopy to quantitative biology remains limited due to the bottleneck in information throughput. For instance, the increased use of machine learning in microscopy requires access to large datasets for training – datasets that have been challenging to collect for super-resolution microscopy.

This work provides several developments to increase the throughput of super-resolution imaging: Firstly, ensuring uniform illumination and image quality allows imaging over larger FOVs, and therefore capturing larger regions of the sample simultaneously. The development of a novel strategy for multi-focal flat illumination for field-independent imaging (mfFIFI) provides a flexible flat-fielding solution for multi-focal systems such as the iSIM. Integrating mfFIFI into the iSIM has allowed the capture of FOVs spanning >100x100 µm^2, preserving the speed of iSIM imaging while ensuring homogeneous illumination across the sample. Secondly, combining such a setup with expansion microscopy enables high-speed multi-color imaging at an effective resolution of ~35 nm, however at a 100-1000-fold larger throughput than other super-resolution techniques reaching similar spatial resolution. Third, using adaptive imaging strategies such as SATS for sampling across temporal scales, the information throughput is increased since more events can be captured by following the cell for longer periods of time, at better temporal resolution.

To showcase these different developments, we have studied the nanoscale architecture of centrioles, and mitochondrial dynamics. Super-resolution has emerged as a complementary tool for structural biology due to its high spatial precision and molecular contrast[112,202–204], but still suffered from limited throughput. Hence combining the HT-iSIM with expansion microscopy allowed us to overcome these issues and visualize the distribution of different PTMs within the centriole with sufficient resolution. On the other hand, mitochondria are highly dynamic organelles that change shape and size through cycles of fission and fusion. Capturing mitochondrial constrictions and divisions is technically challenging since it is difficult to predict where mitochondria will constrict and divide. Furthermore, once constricted, division can follow within a few seconds, meaning the mitochondrion will undergo significant morphological change within this short timescale, and as it constricts, approach intermediate shapes far below the diffraction limit. Therefore, capturing such events with sufficient temporal and spatial resolution is difficult. Employing both existing super-resolution techniques and tools developed in this thesis, allowed us to capture the shape of fission intermediates in large numbers and at sufficient resolution to describe the mechanical properties of the membranes during fission.

Outlook and future work

The aim of this section is to provide a perspective of outstanding questions resulting from this work and possible future experiments and discussion of what they could bring.

HT-iSIM

The HT-iSIM enables imaging over FOVs spanning >100x100 µm², enabling live-cell super-resolution imaging of multiple cells simultaneously. As such, it will be a useful tool in studying intra- and inter-cellular processes at high throughput and double the resolution, compared to conventional diffraction-limited microscopy techniques. Furthermore, combining HT-iSIM with U-ExM[42] preserves the speed of iSIM imaging while achieving resolution comparable to STED[1,30] and STORM[9,29] microscopy.

Nevertheless, what are the remaining limitations in extending the FOV even further for an even higher increase in throughput? One factor is the size of the detector – the required sampling and hence image pixel size in iSIM is ~56 nm[26,28], twice smaller than that required for SMLM techniques. This is because – while SMLM detection is still diffraction limited – in iSIM the raw image recorded at the camera is already super-resolved. This limits the FOV on a standard sCMOS camera (composed of 2048x2048 pixels) to ~115 µm in the linear dimension. Therefore surpassing this limitation would require using a detector with a larger pixel array size such as the Kinetix high speed, back-illuminated sCMOS in development by Photometrics. Secondly, once enlarged detection can be achieved, extending the FOV further would require overcoming field-curvature[205], which would become more apparent over larger FOVs. Therefore, different strategies for mitigating field curvature such as SLMs or deformable mirrors, would become necessary. Alternatively, one could imagine exciting and detecting molecules from the curved image plane caused by uncorrected field curvature and mitigating the effects at the camera or during post-processing.

On the other hand, a simple way of obtaining larger FOVs is comprised of stitching together multiple adjacent FOVs[97,98]. In this work, this is done by pseudo-synchronizing the translation stage to the microscope control by leaving a large enough time interval between the microscope controls to allow the stage to move to the adjacent FOV. However, significant time is lost since the stepper-motor translation stage is controlled through software and not using analog voltage signals like the rest of the microscope. While a piezo translation stage would allow better synchronization between to the rest of the microscope controls, piezo stages tend to have much smaller travel ranges (several 100 µm) compared to stepper-motor stages (spanning several 10 mm). A combination of both might provide both the large travel range and speed to enable faster multi-FOV imaging for image stitching. Alternatively, by carefully tuning the speed of the translation stage and the different scanning / de-scanning / rescanning speeds of the scanning mirror, one would be able to continuously move the stage and directly correct for motion blur with the scanning mirror, resulting in no motion blur in the captured images. Such an approach would significantly improve the speed at which multiple FOVs could be captured since the stage would never have to stop moving.

Finally, approaches combining high-throughput super-resolution imaging with particle averaging and reconstruction are emerging as a complementary tool for structural biology studies[112,202–204]. While in this work we chose to study the centriole, the combination of HT-iSIM and U-ExM provides a robust and flexible framework that can be used to study other cellular structures or other multi-molecular machines, such as for example viruses.

Physical model of mitochondrial division

In this work, we provide a physical framework, explaining the role of physical parameters such as bending energy and tension in setting the probability that mitochondrial constrictions result in division. While the framework accounts for the roles of these parameters, agnostic of their origins, questions arise about how different physical parameters are influenced by the division machinery. In this work, we explore the potential role of the microtubule network in establishing mitochondrial membrane tension. Nevertheless additional factors such as transient interactions with other organelles[99], or targeted actin polymerisation[127–129] could serve a similar purpose. Therefore, establishing how mitochondrial tension is regulated could bring further insight into how mitochondria are targeted for

division and how the cell controls their numbers. Multi-color super-resolution imaging of mitochondria with other components of the division machinery such as ER, combined with the novel FliptR sensor for super-resolution applications[206], could provide valuable insight into how mitochondrial membrane tension is organized. Furthermore, the FliptR sensor could be used with different drug perturbations, such ionomycin[129,207,208] or Lat-B[168] targeting actin polymerization, to decouple different contributions to mitochondrial membrane tension.

Furthermore, several observations made during this work could bring further insight into the mechanical properties of mitochondria. For instance, under control conditions, mitochondrial membrane tension increased locally at the constriction site, as would be expected for a constricted body under tension (Figure 27a,c). However, a surprising result was that under nocodazole treatment, the opposite trend was observed where mitochondrial constriction sites overlapped with regions of decreased local membrane tension (Figure 27b,c). While it is important to account for possible effects of different lipid domains on the fluorescence lifetime readout of the FliptR membrane tension sensor[161,162], these observations could also suggest that mitochondria can respond differently to mechanical stimuli depending on their mechanical properties (Figure 27c,d).
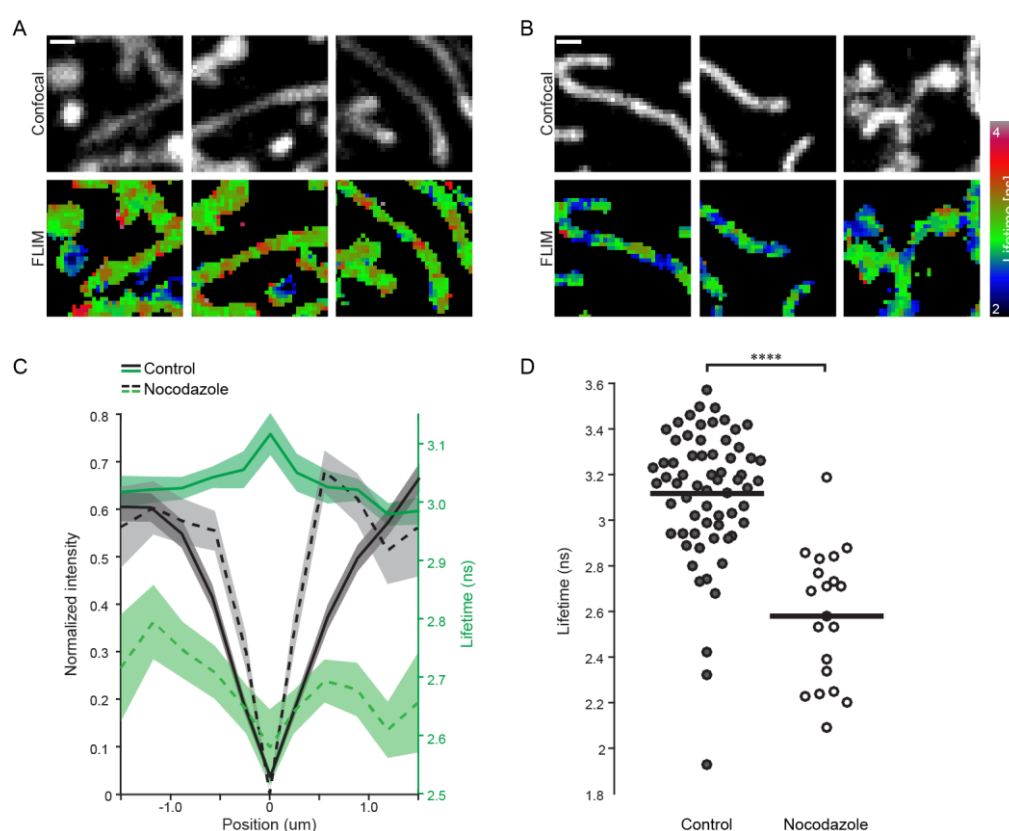
Figure 27 - Local membrane tension at mitochondrial constrictions.
*A,B) Example confocal and FLIM images of mitochondrial constriction sites in (A) control and (B) nocodazole-treated cells. C) Intensity and FLIM lifetime profiles drawn through mitochondrial constriction sites between control and nocodazole-treated cells. Curve shows mean and shaded area represents SEM. D) Distribution of FLIM lifetimes measured at mitochondrial constriction sites between control and nocodazole-treated cells. Scale bar: 1 µm. Statistical significance calculated by 2-tailed Mann-Whitney U test where appropriate: ****P<0.0001.*

In this work, we were limited to snapshots of mitochondrial constrictions with the mitochondrial FliptR probe due to challenges including high laser intensities and phototoxicity that prevented time-lapse FLIM imaging. While work on improving the live-cell compatibility of the probe is ongoing, an alternative solution could rely on detecting membrane tension from mitochondrial morphologies and extrapolating the trends observed in static images to time-lapse movies. While how mitochondria keep their shape is not completely understood, two factors that likely play a role are their internal architecture such as

cristae, and external forces exerted on mitochondria[209,210]. Such external forces are coupled to the mitochondrial membrane tension, so we wondered whether by inverting the problem, it would be possible to predict mitochondrial tension based on their shape. With this aim, we trained a neural network attempt to "learn" the tension FLIM lifetime readout based on the intensity signal and hence morphology of mitochondria (Figure 28, Appendix T).
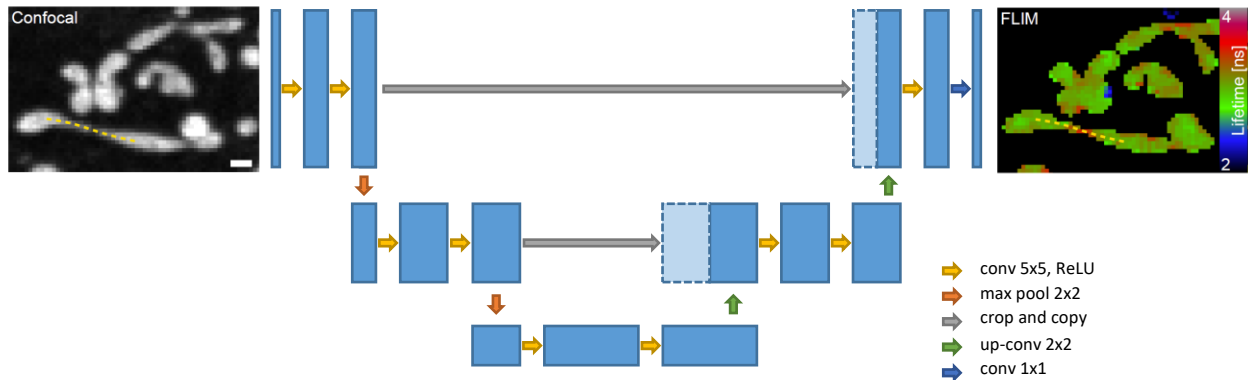
Figure 28 - Concept for deep learning FliptR readout.
A U-net designed to predict the fluorescence lifetime of the membrane tension sensor, from the intensity based image.

In an initial implementation, we used a U-net[211] and trained it to predict the fluorescence lifetime channel from the intensity channel acquired using the mitochondrial FliptR probe[162]. By visually inspecting the outputs of the network and the evolution of the loss and accuracy metrics, it appeared that there were situations in which the network could successfully predict regions of higher or lower tension, although only to a certain degree as it struggled more with predicting the exact values (Appendix T). Nevertheless, examining a few constriction sites suggested that, if correctly trained and validated, the network had potential to provide a complementary tool to get tension readout from fluorescence images.

Although trained on static images, the idea was that the network might be able to reconstruct the temporal evolution of membrane tension by inputting into a trained network the individual frames from the dynamic movie (Figure 29). Indeed, by recombining the output of the network into a movie of the predicted outputs, the network produced data such that the neighboring frames appeared coherent. Furthermore, on the few events tested, the network appeared to show an increase in membrane tension at the constriction site, which built up until the constriction site divided. While there is no ground truth for the movie data and therefore no way to know if these predictions are true, the network still provides valuable insight since it extrapolates based on the data shown, what the most likely results are. Therefore, further work and validation of such a network is required.
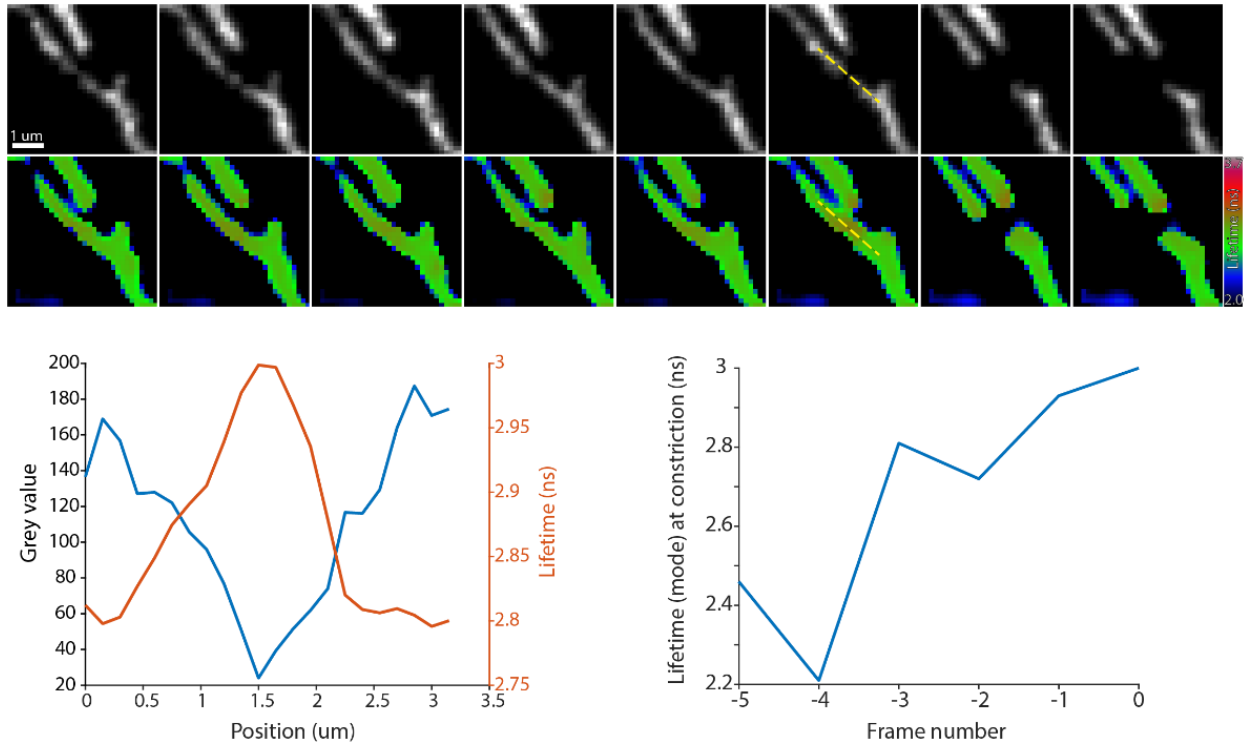
Figure 29 - Example movie dataset input through the neural network.
Top panel shows the raw intensity frames used as input, and the bottom row the predicted lifetime images outputs from the network. Bottom left plot shows the intensity and lifetime profiles measured along the yellow dashed line. The right bottom plot shows the dynamic evolution of the lifetime at the constriction site.

Finally, while in this work we extracted the forces experienced by mitochondria from changes in their shape, further insight into the role of mechanical forces in organelle dynamics could be gained by combining this approach with novel tools in mechanobiology to sense or exert such forces. For instance, optogenetic tools[212] have been developed to control microtubule-based organelle transport, and would allow one to exert forces on mitochondria in a controlled way and further study the role of microtubules in establishing mitochondrial tension and their potential role in division.

Smart and adaptive spatio-temporal sampling

Chapter 5 presented a simple implementation of the SATS framework to detect mitochondrial constrictions using the relative Drp1 intensity for event detection and a simple proportional strategy. Further steps should integrate more advanced event detection such as the Hessian eigenvalue filter and evaluate the performance in a real experiment.

In this work, the improvement gained by SATS can only be compared to traditional imaging by either using the simulation platform, or from separate data acquired with and without the SATS framework. While the simulation platform provides a useful tool for developing, testing and comparing different adaptation strategies, it is far from the real data acquired at the microscope. Based on real acquisitions however, it is not possible to capture the same behavior in the sample using multiple strategies simultaneously. Therefore, as a control, it would be beneficial to test the computation and actuation steps within a more controlled environment like the simulation platform, however while using real data. By capturing a time-lapse acquisition at a high temporal resolution, it would be possible to generate a "ground truth" dataset which the different strategies would choose how to sample from. This way it would be possible to observe the same datasets are subsampled by the adaptive imaging strategy, compared to the original non-adaptive acquisition procedure and better characterize the resulting improvements.
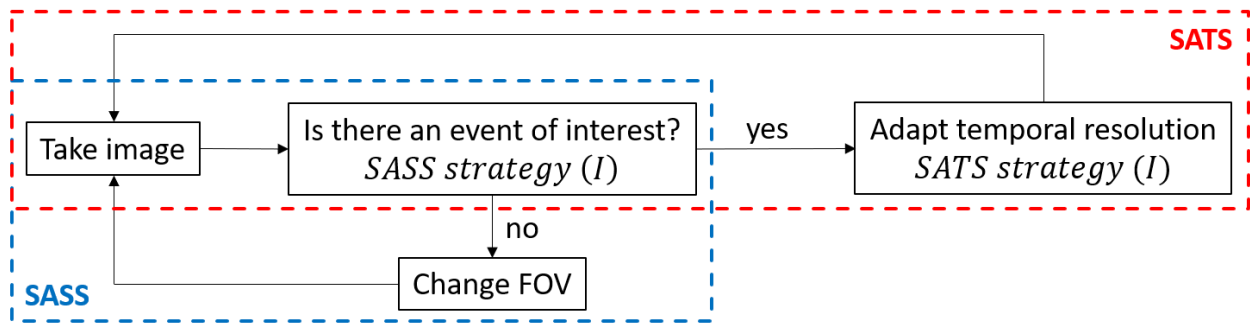
Figure 30 - Smart and adaptive spatio-temporal sampling framework.
The spatial (SASS) and temporal (SATS) components of the framework are independent and can be used jointly or independently. The SASS framework determines based on a SASS strategy which FOV to prioritize, while the SATS strategy determines the appropriate temporal resolution for the chosen FOV.

The SATS framework presented in Chapter 5 is part of a larger framework, termed smart and adaptive spatio-temporal sampling (SASTS) (Figure 30) – work which is ongoing. The framework itself is composed of two independent modules: smart adaptive spatial sampling (SASS) and smart adaptive temporal sampling (SATS) presented in Chapter 5. The aim of SASS, currently in development, is to increase the imaging throughput by sampling over multiple FOVs for events of interest. These strategies address the problem of the limited photon budget by optimally allocating more resources when and where they are needed. Combined, they increase the information throughput by sampling for events over multiple FOVs, as well as increase the imaging duration by not exposing the sample when not needed, hence reducing phototoxicity, photobleaching. While the SATS and SASS components are largely independent, they can be used simultaneously and share some of the implementation steps, such as sensing and computation (Figure 30).

Basic principle of SASS

The basic principle behind SASS takes advantage of actively searching for events of interest across multiple FOVs to, instead of imaging a single FOV and waiting for an event of interest to take place. By sampling from a larger distribution, the microscope identifies regions where events of interest are more likely to take place and prioritizes imaging those regions. This way, the microscope would spend most of the acquisition time in information-rich regions and increase the information throughput by prioritizing locations likely to contain events of interest. Simultaneously, this also ensures that regions lacking events of interest are not unnecessarily exposed to excitation light, decreasing photobleaching and phototoxicity. Combined with SATS, the overall SASTS framework aims to control the spatial and temporal sampling of events of interest. Due to the modular design of the sensing, computation and actuation steps, it is possible to consider SASS and SATS as separate strategies, with separate actuation procedures.

Preliminary results using the SASS simulation platform suggest that already the simple iterative method outperforms the standard single FOV imaging approach by at least a factor of 2 (Figure 31). Furthermore, this simple strategy generally performs better than if the most informative FOV had been picked from the start (not possible in a real experiment). Therefore, since even a simple adaptive strategy leads to a 2-fold improvement in the information throughput, more advanced strategies taking into account the history of each FOV and the travel time in between should lead to even better performance.
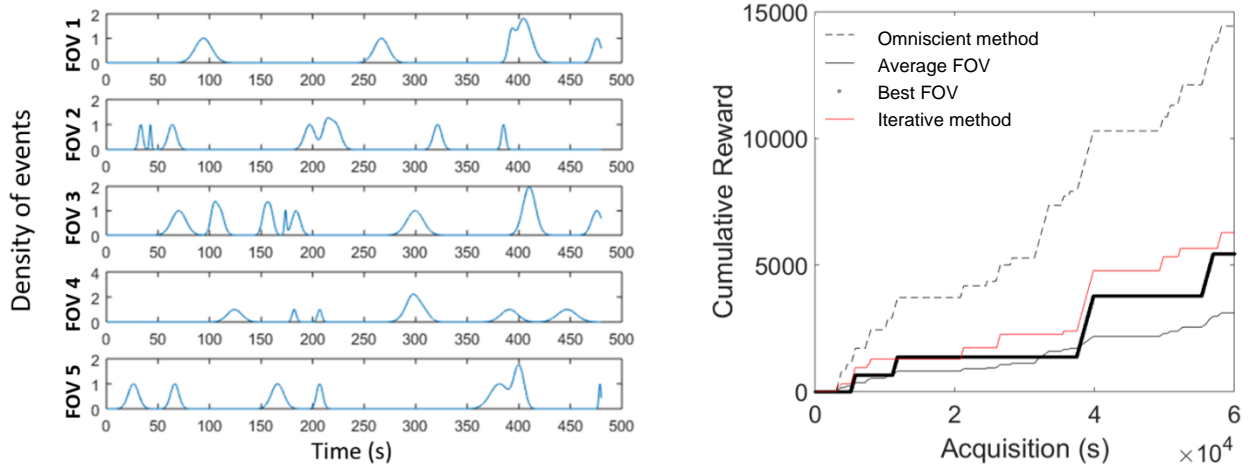
Figure 31 - Example of temporal traces generated by the SASS simulation platform
Left: Different rows represent the readout analogous to density of events of interest, for different FOVs. Right: Cumulative reward achieved by different SASS strategies. The Omniscient method represents the maximal theoretical throughput assuming all FOVs are captured. The iterative method represents a simple SASS strategy that is triggered to stay or move between FOVs by a threshold value applied to the output of the computation step. The Best FOV represents the maximal throughput if only one FOV is imaged at a time. The Average FOV represents the average reward gained for staying at a single FOV during the whole acquisition.

Overall SASTS aims to provide an adaptive framework that aims to use the sample's limited photon budget more efficiently compared to traditional imaging procedures. By spatiotemporally targeting events of interest, the sample is not exposed to unnecessary illumination in the absence of such. Therefore, SASTS directly prevents unnecessary photobleaching and phototoxicity. Similarly, preliminary results using the SASS framework results in increased throughput since it can capture events of interest taking place in close proximity across multiple FOVs. While standard imaging procedures would only capture the events within a single FOV, SASS ensures the acquisition captures the most informative FOV available and therefore results in an increase in throughput as more events will occur across multiple FOVs compared to a single one. Further work is required to test the integration of SASS into the microscope controls, and evaluation using real samples.

Materials and methods

Chapter 3

This section is adapted from ref. [92]

Sample preparation

Cos-7 and RPE-1 cells were grown in Dulbecco's modified Eagle medium (DMEM) supplemented with 10% fetal bovine serum (FBS). Cells were plated on 25 mm, #1.5 glass coverslips (Menzel) 16-24 h prior to transfection or fixation at a confluency of ~105 cells per well.

Transfections using KDEL-RFP and mito-GFP, were performed with Lipofectamine 2000 (Life Technologies) using 150 ng of KDEL-RFP and 150 ng of mito-GFP and 1.5 µL of the Lipofectamine 2000 reagent in 100 µL Opti-MEM medium per 6 well.

For synchronization of RPE-1 cells at the G1/S transition and the onset of centriole assembly, ~125'000 cells were seeded for 24 h in six well-plates (Merck, TPP, 92006) on 12 mm coverslips in DMEM. Thymidine (Merck, T1895, 1 mM) and Centrinone (Lucerna-Chem, MCE-HY-18682, 300 nM) were added for 18 h, before fixation of cells with -20°C methanol for 5'.

For immunofluorescence experiments with COS-7 cells, cells were washed in pre-warmed PBS before being fixed in pre-warmed fixation buffer (4% paraformaldehyde in PBS). Cells were then permeabilized in 0.25 % Triton-X in PBS for 10 min. After washing in PBS for 5 min, cells were incubated in blocking buffer (1% BSA in PBS) for 60 min. The primary antibodies (Tom20-rabbit (1:50, FL-145 sc-11415 Santa Cruz Biotechnologies), Tim23-mouse (1:100, 611222 BD Biosciences)) diluted in blocking buffer were incubated for 60 min before washing 3 times in 0.2% BSA with 0.25% Triton-X in PBS for 10 min. Secondary antibodies (AlexaFluor 488 goat anti-mouse IgG (H+L) (1:150, A28175 ThermoFisher), AlexaFluor 568 goat anti-rabbit IgG (H+L) (1:150, A11011 ThermoFisher)) were diluted in blocking buffer before incubation for another 30 min. The sample was incubated in the dark, then washed 3 times with PBS before imaging.

Centriole expansion protocol

Chlamydomonas reinhardtii centrioles were isolated from the cell-wall-less strain CW15-[213] and expanded using the U-ExM protocol[42]. Briefly, isolated centrioles were spun on 12mm Poly-D-Lysine-coated (ThermoFisher, A3890401) coverslips prior to U-ExM. For human cell expansion, cells were initially seeded on 12 mm coverslips before being fixed with 4% PFA. Coverslips were then incubated in a solution of 0.7% formaldehyde and 1% acrylamide in PBS for 4-5 hours at 37˚C. Next, coverslips were incubated in the monomer solution for 1 minute on ice and then shifted to 37˚C, for 1 hour in a dark and humidified chamber. For one gel, the monomer solution is made of 25 µL sodium acrylate (Sigma-Aldrich, 408220, 38% (wt/wt, diluted with nuclease-free water)), 12.5 µL acrylamide (Sigma-Aldrich, A4058, 40% stock solution), 2.5 µL N,N'-methylenbisacrylamide (Sigma-Aldrich, M1533, 2% stock solution), and 5 µL 10X PBS, supplemented with 2.5 µL TEMED and 2.5 µL APS (from 10% stock solutions). Once polymerized, gels were moved into denaturation buffer (200 mM SDS, 200 mM NaCl and 50 mM Tris in nuclease-free water, pH 9) for 15 minutes at room temperature with gentle shaking and then shifted for 30 minutes to 95˚C in an 1.5 mL Eppendorf tube with 1 mL of fresh denaturation buffer. Then, gels were placed at room temperature in beakers with 200 mL of distilled water. Water was exchanged twice (every 30 min) and the sample was incubated overnight at room temperature.

The following day, water was changed with PBS for 15 min at room temperature. Gels were then incubated for 3h at 37°C with gentle shaking in 1 mL of primary antibody solution (in 3% BSA and 0.05% Tween20). Samples were then washed three times for 10 min with PBS supplemented by 0.1% Tween20 while shaking, followed by incubation with secondary antibodies for 3h at 37°C in 3% BSA and 0.05% Tween20. Finally gels were washed 3x in T-PBS. For RPE-1 cells, the sample was supplemented in the second wash with Hoechst 33258 (1:2'000) dye and place in beakers with 200 mL of distilled water for final expansion, with again water being exchanged twice for 30'. Before imaging, gels were again expanded overnight in ddH20. Primary antibodies used to image centrioles in expanded RPE-1 cells were rabbit anti-polyglutamate chain (PolyE), pAb (IN105, 1:250) and mouse monoclonal anti-acetylated tubulin (Merck, T7451, 1:500). Secondary antibodies were goat anti-Rabbit Alexa488 (Thermo-Fisher Scientific, A11034, 1:500) and goat anti-mouse IgG Alexa 568 F(ab')2 (Thermo-Fisher Scientific, A11019, 1:500).The following primary antibodies were used for imaging expanded purified *Chlamydomonas reinhardtii* centrioles: rabbit polyclonal anti-polyglutamate chain (PolyE, IN105,1:500, AG-25B-0030-C050, Adipogen), mouse monoclonal anti-α-tubulin (DM1α,1:500, T6199, Sigma-Aldrich), mouse monoclonal anti-polyglutamylation modification (GT335,1:200, AG-20B-0020, Adipogen), mouse monoclonal anti-acetyl-α-tubulin (Lys40,1:50, 32-2700, Invitrogen, ThermoFisher). Secondary antibodies were goat anti-rabbit Alexa Fluor 488 IgG H+L (1:400, A11008), goat anti-mouse Alexa Fluor 488 IgG H+L (1:400, A11029), goat anti-rabbit Alexa Fluor 568 IgG H+L (1:400, A11036), goat anti-mouse Alexa Fluor 568 IgG H+L (1:400, A11004 all from Invitrogen, ThermoFisher).

Comment on the effective resolution with potentially larger expansion factors

The effective resolution improvement X is determined by the resolution improvement of the method (X_{res}) and the expansion factor (X_{exp}) such that $X = X_{res} * X_{exp}$. Therefore, in the case of iSIM (X_{res} = 2) and U-ExM (X_{exp} = 4-5), the effective improvement in resolution is in the range of 8-10-fold (X = 8-10).

Achieving the same improvement is therefore possible on a standard diffraction-limited microscope (X_{res} = 1), by achieving an 8-10-fold expansion factor (X_{exp} = 8-10), but raises several issues. Firstly the main issue is that, while methods for achieving larger expansion factors are available[40,214–216], they are generally more complicated than the U-ExM protocol and could involve multiple expansion steps. Secondly, these expansion methods with larger expansion factors have not been optimized for expanding multi-molecular complexes such as the centriole. Thirdly, assuming a larger expansion factor X_{exp} is achievable, the field-of-view (FOV) would be reduced along each dimension by X_{exp} and would therefore require stitching together X_{exp}^2 individual images. This would in turn reduce the throughput of the method by X_{exp}^2, and result in a 4-fold lower throughput than combining iSIM and U-ExM (assuming similar sampling requirements or that both methods start with similar FOV sizes). The same applies to a spinning disk microscope, which could achieve a $\sqrt{2}$ improvement in resolution and hence require an expansion factor of 5.5-7, and a decreased throughput by a factor of 2.

Overall there are specific advantages to prioritizing X_{res}, since X_{exp} increases the physical sample size effectively reducing the size of the FOV. Furthermore, achieving X_{exp} beyond the traditional factor of 4-5 involves more complicated expansion protocols. On the other hand, additional advantages of increasing X_{exp} come from the fact that sample expansion does not just improve the resolution by the expansion factor, but also other optical (sectioning, aberrations) and mechanical (drift) features of the method. Therefore combining fast super-resolution techniques with moderate expansion is likely to provide the best of both worlds.

iSIM imaging

The iSIM setup was partly based on previously described implementations[26,28]. Two lasers with wavelengths of 488 nm (Sapphire 488-300 CW CDRH, Coherent) and 561 nm (gem 561, Laser Quantum GmbH) were combined using a dichroic mirror (F48-486, Analysentechnik) and controlled

through an acousto-optic tunable filter (AOTFnC-400.650-TN, AA Optoelectronic). In the case of Gaussian excitation, the beam was expanded with a 10x beam expander (f_{1a} = 40 mm, f_{2a} = 400 mm, Thorlabs). In the mfFIFI path, a focusing lens (f_{FC} = 50 mm) was used to focus the light near a rotating diffuser (2.5° ± 0.25° FWHM at 650 nm, 24-00066, Süss MicroOptics SA) before collimation by a collimating lens (f_{CL} = 60 mm, Thorlabs). The collimated beam was contracted by a factor of 4 by two lenses (f_{1b} = 120 mm, f_{2b} = 30 mm, Thorlabs) before illuminating two flat-fielding MLAs (300 μm pitch, 10mm x 10 mm, f = 4.78 mm, square lenses, 18-00157, Süss MicroOptics SA). The flat field was then focused by a Fourier lens (f_{FL} = 300 mm, Thorlabs). Both paths then illuminated the excitation MLA (222 μm pitch, 1" diameter, f = 6 mm, square lenses APO-Q-P222-R2.74, Advanced Microoptic Systems GmbH). The excitation was relayed by scan lenses (f_{SL} = 190 mm, 55-S190-60-VIS, Special Optics) to and from the scanning mirror (SPO9086 Rev B Coated X Mirror, Sierra Precision Optics) mounted on a galvanometer scanner (QS-12, N-2071, Nutfield Technology). The excitation was then imaged onto the sample using a tube lens (f_{TL} = 350 mm, 49-289-INK, Edmund Optics) and an objective lens (APON60XOTIRF, Olympus), resulting in a final magnification of 350/3 ≈ 116x. The sample was placed on a precision aligned microscopy platform including a micropositioning control (RM21-AZ-AXY-RMS-M, Mad City Labs) and a Z piezo stage (Nano-Z200, Mad City Labs). The emission was relayed back through the excitation side of the scanning mirror and split using a dichroic mirror (F58-488S, Semrock). The emission was then pinholed with a pinhole array (chrome on 0.090-inch-thick quartz, 222 μm pitch, 40 μm diameter, Photosciences) and relayed by two relay lenses (f_R = 300 mm, Thorlabs) before contracting each emission spot by a factor of 2 using another MLA (222 μm pitch, 1" diameter, f = 0.93 mm, square lenses APO-Q-P222-R0.425, Advanced Microoptic Systems GmbH). The emission was then relayed using scan lenses on the emission side of the scan mirror, towards a filter wheel (Lambda 10-B, Sutter Instruments, Science Products) with 2 notch filters (NF-03-488E-25 and NF-03-561E-25, Semrock) mounted to block the excitation wavelengths. The transmitted emission was then collected by a sCMOS camera (PrimeBSI, 01-PRIME-BSI-R-M-16-C, Photometrics). The size of a square camera pixel corresponds to 56 nm on the sample.

The microscope was controlled using a custom written MATLAB script which controlled an analog output card (PCI-6733, National Instruments) and breakout box (BNC-2110, National Instruments) for precise control and synchronization of the scan mirror, AOTF, camera and Z-stage. The XY stage and camera were controlled through MicroManager[217].

For live cell imaging, imaging was performed at 37 °C in pre-warmed Leibovitz medium in a top stage incubator (H301-PRIOR-NZ100-H117, Okolab). Imaging of immunostained samples was performed in PBS. Expanded samples were mounted as previously described[42]. Briefly, the expansion factor was determined before imaging by measuring the gel size with a caliper (precision ±0.01 mm). The gel was then cut using a razor, before removing excess water and placing the gel on a poly-D-lysine treated coverslip (25 mm round coverslips, Mendel #1.5) already placed inside the imaging chamber. After gently pressing on the gel to ensure attachment to the coverslip, a few drops of ddH2O were added on top of the sample to avoid shrinkage during imaging.

Image acquisition was performed using a custom written MATLAB script, in combination with MicroManager[217].

iSIM deconvolution

Raw iSIM images were deconvolved using the Lucy-Richardson deconvolution algorithm[94,95], implemented in MATLAB and provided by Dr. Hari Shroff[26]. Each raw z-stack was deconvolved for 40 iterations.

Discussion on methods to mitigate the striping artefact

iSIM imaging can produce substantial striping artefacts due to its scanning mechanism, especially in thick samples with significant out of focus light. While careful alignment can diminish the intensity of the

stripes, there are also mechanical solutions that mitigate the striping on the sample, or computational tools for filtering out the effect during post-processing. For example, the commercial Visitech Ingwaz system introduces extra scanning mirrors to fluctuate the position of the beam and hence reduce the striping artefact. Furthermore, a similar effect might be introduced by mfFIFI due to the slight fluctuation in the localization of the excitation spots, although this might not be sufficient to fully overcome this effect.

mfFIFI characterization platform

An optical characterization setup was built to measure the variation in pitch and spot size of the multifocal points. A laser beam with a wavelength of 640 nm (CUBE 640-100C, Coherent) was expanded with a 6x beam expander (f = 50 mm, f = 300 mm, Thorlabs) with a pinhole (P50D, Thorlabs) at the joint focal plane of the two lenses to spatially filter the beam. The beam is passed through a Köhler integrator, made of the following components: focusing lens (f = 80 mm, Thorlabs), rotating diffuser (2.5° ± 0.25° FWHM at 650 nm, 24-00066, Süss MicroOptics SA), collimating lens (f = 40 mm, Thorlabs), two flat-fielding MLAs (300 µm pitch, 10mm x 10 mm, f = 4.78 mm, square lenses, 18-00157, Süss MicroOptics SA), Fourier lens (f_{FL} = 300 mm, Thorlabs). An iris (ID25, Thorlabs) is used before the two MLAs to control the portion of the beam which is allowed to propagate forward to reach and illuminate MLAs, by adjusting the opening diameter of the iris. An excitation MLA (300 µm pitch, 10mm x 10 mm, f = 8.72 mm, square lenses, 18-00221, Süss MicroOptics SA) is used to produce the multifocal points. The size of the multifocal illumination is reduced by a factor of 0.6x by a beam de-expander (f = 50 mm, f = 30 mm, Thorlabs) to be of appropriate size for the sensor of the camera (DCC1545M, Thorlabs).

To obtain the data shown, we used the characterization platform to test the parameters affecting the spot size and pitch. A Vernier caliper was used to measure the iris opening diameter, which was varied methodically to control the size of the beam which illuminates the MLAs. Images of the beam at different iris opening diameters were analyzed using a MATLAB script, which allowed us to fit each excitation point to a 2D Gaussian and measure the multifocal points' mean spot FWHM as function of iris diameter. In order to study the variation in the pitch of the multifocal points, the distance between the Fourier lens and the second flat-fielding MLA was varied by displacing the flat-fielding MLAs. A MATLAB script is used to measure the mean pitch at each distance, so that the relationship between this distance and the pitch can be determined.

Image analysis

Plateau uniformity quantification

The homogeneity was quantified using the plateau uniformity definition based on the FWHM of the histogram of the intensity values, according to ISO, ISO 13694:2018: Optics and optical instruments - lasers and laser-related equipment - test methods for laser beam power (energy) density distribution.

Illumination profile measurement

The illumination profiles used to optimize the pitch (telecentricity) and spot size of the multifocal excitation were visualized using a small color CMOS camera (DCC1645C, Thorlabs), placed in an intermediate image plane of the iSIM, between the second scan lens and tube lens, to avoid introducing other aberrations along the whole optical path of the iSIM.

The excitation profile at the sample was measured using a highly concentrated fluorescent dye sample[93], as previously described[29]. Briefly, sodium fluorescein (NaFITC) powder was diluted in deionized water, followed by vortexing and sonication until the powder was completely dissolved. A 10 µL drop was placed on a 25 mm coverslip, before covering with a 12 mm coverslip. The sample was

then sealed using nail polish. The same dye sample was used to measure both the 488 nm and 561 nm illumination profiles. The illumination spots were characterized by fitting a 2D Gaussian to the intensity image. The threshold was set so that no points in the background were detected. The scanning profiles were measured with a 150 pixel thick line in Fiji[218].

In the case of excitation spots visualized and quantified directly, the illumination profile was imaged directly onto a camera placed in a conjugate image plane.

Bead FWHM analysis

To characterize the performance of the iSIM microscope, we used 100 nm Tetraspeck beads (ThermoFisher Scientific, T7279) deposited on poly-L-lysine treated coverslips. Bead size was determined by fitting a Gaussian profile to the intensity profile of the bead and extracting the FWHM.

Centriole shape and coverage analysis

To analyze the diameters of different PTM localizations within the centrioles, we measured the intensity profile through the centers of top view centrioles (central plane, centriole barrel parallel to the imaging axis). The profile was measured using a 7 pixel thick line in Fiji[218]. Each peak was fitted to a Gaussian profile to localize its center, before calculating the diameter as the distance between the two peaks on opposing sides of the centriole ring.

To analyze the PTM distribution along the length of the centriole and their coverage, we measured the intensity profile along the length of the centriole using a 10-pixel thick line and from summed intensity projections of side view centrioles (centriole barrel orthogonal to the imaging axis). We then took the width of the profile at ¼ of the maximal signal as the length, to be less susceptible to noise. The coverage was then calculated by dividing the length of the PTM in question, by the length of the reference label (acetylated tubulin for human centrioles and α-tubulin in the case of *Chlamydomonas reinhardtii* centrioles).

Multi-FOV stitching

For stitching of multiple images, raw images or z-stacks were acquired with a 10% overlap for both Gaussian and mfFIFI excitation. The acquired images were then combined using the Grid/Collection stitching tool[97] in Fiji using the linear blending method with the default values of 0.30 for regression threshold, 2.50 for max/avg displacement threshold and 3.50 for absolute displacement threshold.

Wave optics simulations

The mfFIFI simulation platform has been adapted based on previous work[29]. All simulations are based on standard numerical Fourier optics algorithms and rely on angular spectrum propagation methods to simulate the propagation of an optical wave. An initial simulation showing the effect of illuminating the excitation MLA with Gaussian and flat-fielded profiles was performed using phase masks to represent optical components.

The parameters used for the simulation are summarized in.

Parameters	Simulation 1: effect of L_2 (Supplemental Figure 3a-d)	Simulation 2: effect of beam de-expander (Supplemental Figure 3e-h)	Multi-focal excitation test (Supplemental Figure 3)

Δr, Diffuser offset [mm]	-5	-5	-5
f_{OBJ}, Objective focal length [mm]	300	300	550
D_{BFP}, objective BFP diameter [mm]	50	50	25
f_c, collimating lens focal length [mm]	60	60	50
L_2, Distance between second MLA and objective BFP [mm]	See figure	0	1
p, Lenslet periodicity [µm]	300	300	1015
N, number of lenslets	33	33	11
f_{MLA}, lenslet focal length [µm]	2200	2200	11000
L_1, distance between collimating lens and MLA's [mm]	5	5	5
λ, wavelength [µm]	0.561	0.561	0.561
σ_f, diffuser correlation length [µm]	10	10	10
σ_r, diffuser variance	1.75	1.75	1.75
σ, beam standard deviation at waist [µm]	6	6	6
nIter, Number of field realizations	100	100	1000
Input beam grid size	50001	50001	20001
Input beam grid physical size	50000	50000	5000
MLA grid size	2001	2001	1001
MLA physical grid size	9900	9900	11165
BFP grid size	198099	198099	660033
f_1 beam expander lens 1 focal length [mm]	n.a.	120	n.a.
f_2 beam expander lens 2 focal length [mm]	n.a.	120, 60, 40, 240 (see figure)	n.a.

Table 5 - Summary of wave optics simulation parameters
Parameters used for simulations shown in Figure 35. Simulation 1 tests the dependence of the spot pitch on the distance L2 between the second flat-fielding MLA and the back focal plane of the Fourier lens (Figure 35 a-d). Simulation 2 tests the dependence of the spot size on the contraction factor of the beam expander introduced between the collimating lens and the flat-fielding MLAs (Figure 35 e-h).

Particle segmentation, classification and 3D reconstruction

Particles were segmented using a custom written MATLAB script. Briefly, the threshold value was found on the maximum intensity projections of the 3D stacks, before applying it back to the individual stacks. The regions were then binarized and segmented by connecting neighboring pixels across the 3D stack. The binarized points of interested were then dilated to form the mask which was then applied back to the raw stack. The particles were then cut out from the original stack with their specific mask and a 60x60 pixel surrounding region. The segmentation was ~50% successful, mostly because centrioles are often found in pairs, and closely located pairs had to be rejected since they could not be segmented correctly.

After particles were segmented and upsampled (to reach isotropic pixel size), the particles with tubulin signal were aligned to a reference using Dynamo. The reference was built using a reconstructed tubulin signal made from 12 manually selected particles. Once particles were all similarly aligned, a cross-correlation matrix was generated by calculating the similarity between each pairs of particles. The cross-correlation matrix was converted to a distance matrix by subtracting cross-correlation values to 1. A hierarchical classification was made using the Ward method (hclust function from R). The classification tree was empirically cut into 10 groups. For each group, the average particle was generated for the tubulin signal and for the PolyE signal by applying the transformation parameters obtained during the alignment step. The 10 averages were compared to identify which groups were most promising. The best classes were used to produce the reconstruction results. The reconstruction method was based on ref.[111], and followed the procedure reported in ref.[42] with a C9 symmetry constraint. The point spread function was experimentally measured by imaging 100 nm fluorescent beads (TetraSpeck™ Microspheres, 0.1 µm, T7279 ThermoFisher). We made two modifications to the reference-free step of the reconstruction algorithm[111]. Firstly, we adopted a multiscale reconstruction approach: we used results obtained with coarsely subsampled data to get a coarse initialization. Thanks to this approach, we were able to perform the reconstruction at the highest resolution in reasonable computation time. Secondly, we decoupled the angular search of the orientations: the first two Euler angles were estimated first, before the third one. This further accelerated the reconstruction and provided sharper results in the case of C9 symmetry.

Reconstructions were visualized using Chimera, by setting the threshold to fit the average length of the particles. Artefactual signals in the center of the reconstruction that arise due to the imposed 9-fold symmetry were removed during post-processing.

Chapter 4

This section has been adapted from ref.[118]

Sample preparation

Cos-7 cells were grown in Dulbecco's modified Eagle medium (DMEM) supplemented with 10% fetal bovine serum (FBS). Cells were plated on 25 mm, #1.5 glass coverslips (Menzel) 16-24 h prior to transfection at a confluency of ~10^5 cells per well. Dual transfections containing mCh-Drp1 (Addgene, plasmid #49152) and Mito-GFP (gift from Hari Shroff, Cox8a presequence) were performed with either Lipofectamine 2000 (Life Technologies) or using electroporation (BioRad Xcell). Lipofectamine transfections were carried out in Opti-MEM using 150 ng of mCh-Drp1, 150 ng of Mito-GFP and 1.5 µL of Lipofectamine 2000 per 100 µL Opti-MEM. Electroporation was performed using salmon sperm as a delivery agent. Briefly, cells were pelleted by centrifugation and resuspended in OPTI-MEM. Plasmids

and sheared salmon sperm DNA were added to 200 μL of the cell suspension prior to electroporation using a Bio-Rad Gene Pulser (190 Ω and 950 μFD).

Triple transfections containing mCh-Drp1, Mito-BFP (Addgene, plasmid #49151) and Dyn2-GFP (gift from Gia Voeltz) were performed with Lipofectamine 2000. Such transfections were carried out in using 80 ng of mCh-Drp1, 100 ng of Dyn2-GFP and 80 ng of Mito-BFP and 1.5 μL of Lipofectamine 2000. Dual color imaging of dynamin was performed using double transfections of either 100 ng Dyn2-GFP and 150 ng Mito-Scarlet, or 100 ng Dyn2-mCherry and 150 ng Mito-GFP. Triple transfection containing Mito-BFP, Drp1-GFP and KDEL-RFP were performed with Lipofectamine 2000. Such transfections were performed using 100 ng Mito-BFP, 100 ng Drp1-GFP and 100 ng KDEL-RFP. All quantities listed are per well of cells containing 2 mL of culture medium and carried out with Opti-MEM. The Lipofectamine mixture sat for 20 min before its addition to cells.

Drug treatment

Nocodazole was diluted to a stock solution of 10 mM in DMSO. To depolymerize microtubules, cells were incubated with 10μM Nocodazole (Sigma-Aldrich) for 1h before imaging (1 μL Nocodazole per 1000 μL medium). Control cells were incubated with the equivalent volume of DMSO for 1h before imaging (1 μL DMSO per 1000 μL medium).

Imaging

SIM imaging and reconstruction

Fast dual-color SIM imaging was performed at Janelia Farm with an inverted fluorescence microscope (AxioObserver; Zeiss) using an SLM (SXGA-3DM; Fourth Dimension Displays) to create the illumination pattern and liquid crystal cell (SWIFT; Meadowlark) to control the polarization. Fluorescence was collected through a 100X 1.49 NA oil immersion objective and imaged onto a digital CMOS camera (ORCA-Flash4.0 v2 C11440; Hamamatsu). Time-lapse images were acquired every 1 s for 3-5 min, with 50 ms exposure time. Fast dual color imaging of mitochondria and Drp1 was performed at 37˚C with 5% CO_2, in pre-warmed DMEM medium. Dual-color SIM imaging for Nocodazole and Dyn2 experiments was performed on an inverted fluorescence microscope (Eclipse Ti; Nikon) equipped with an electron charge coupled device camera (iXon3 897; Andor Technologies). Fluorescence was collected with through a 100x 1.49 NA oil immersion objective (CFI Apochromat TIRF 100XC Oil; Nikon). Images were captured using NIS elements with SIM (Nikon) resulting in temporal resolution of 1 s for single-color and 6-8s for dual-color imaging, with 50 ms exposure time. Imaging was performed at 37˚C in pre-warmed Leibovitz medium. See SI for details on iSIM imaging, image reconstruction and analysis.

SIM images were reconstructed using a custom 2D linear SIM reconstruction software obtained at Janelia farm, as previously described[18,19]. Images were reconstructed using a generalized Weiner filter parameter value of 0.02-0.05 with background levels of ~100.

iSIM imaging and deconvolution

For iSIM experiments, imaging was performed on a custom-built microscope setup as previously described[26,28]. The microscope was equipped with a 1.49 NA oil immersion objective (APONXOTIRF; Olympus), with 488 nm and 561 nm excitation lasers and an sCMOS camera (Zyla 4.2; Andor). Images were captured at 0.1-0.3 s temporal resolution for both channels. All imaging was performed at 37˚C in pre-warmed Leibovitz medium. Raw iSIM images were deconvolved using the Lucy-Richardson deconvolution algorithm[94,95] implemented in MATLAB, run for 40 iterations.

Confocal imaging

Confocal imaging was performed on an inverted microscope (DMI 6000; Leica) equipped with hybrid photon counting detectors (HyD; Leica). Fluorescence was collected through a 63x 1.40 NA oil immersion objective (HC PL APO 63x/1.40 Oil CS2; Leica). Images were captured using the LAS X software (Leica). All imaging was performed at 37˚C in pre-warmed Leibovitz medium.

STORM imaging and reconstruction

For STORM imaging, prior to staining, cells were washed with PBS (Sigma). Cells were incubated with MitoTracker Red CMXRos (LifeTechnologies) at a concentration of 500 nM for 5 minutes, before washing again with PBS.

For measuring mitochondrial membrane potential, cells were incubated with 100 nM TMRE (Abcam, ab113852) for 10 minutes before time-lapse measurements.

STORM imaging was performed at room temperature in a glucose-oxidase/catalase (Glox) oxygen removal buffer described in Shim et al[148]. Briefly, a 2% glucose solution is prepared in DMEM (Gibco). Glucose oxidase (0.5 mg/mL) and catalase (40 μg/mL) were added to the glucose solution and the pH was left to drop for 30-60 min. After this time, the pH was adjusted to 7 yielding a final solution with 6.7% HEPES. Imaging was performed on an inverted microscope (IX71; Olympus) equipped with a 100x NA 1.4 oil immersion objective (UPlanSAPO100X; Olympus) using an electron multiplying CCD camera (iXon+; Andor Technologies), with a resulting pixel size of 100nm. Laser intensities were between 1-5 kWcm^{-2}.

For STORM datasets, single molecules were localized using the RapidSTORM v3.3 software[219]. Local signal-to-noise detection with a threshold value of 50 was used. Peaks with a width between 70-300 nm and at least 200 photons were rendered for the final STORM image.

FliptR synthesis

The FliptR probe was synthesized following previously reported procedures[161]. For mitochondrial targeting, compounds 2,3 and 5 were synthesized and purified according to procedures that are reported elsewhere[162]. Compound 5 was synthesized and purified according to procedures described in [162]. The probe can report on membrane tension as reported in reference[161]. Spectroscopic characterizations, mechanosensitive behavior in LUVs and GUVs of various lipid composition, colocalization studies in mitochondria and response of fluorescence lifetime to osmotic shocks (i.e. membrane tension changes) are reported elsewhere in another manuscript[162].

FLIM imaging and analysis

For FLIM imaging with the mitochondria-targeted FliptR probe, cells were incubated with 500 nM of the probe solution for 15 min, and washed before imaging. Imaging was performed using a Nikon Eclipse TI A1R microscope equipped with a time-correlated single-photon counting module from PicoQuant. A pulsed 485 nm laser (PicoQuant LDH-D-C-485) was used for excitation, operated at 20 MHz. The emission was collected through ha 600/50 nm bandpass filter, on a gated PMA hybrid 40 detector and a PicoHarp 300 board (PicoQuant). FLIM data was analyzed using the SymPhoTime 64 software (PicoQuant). The fluorescence decay data was fit to a double exponential model after deconvolution for the calculated impulse response function. The values reported in the main text are the average lifetime intensity.

Statistics

Statistics were performed using MATLAB and OriginPro software. All datasets were tested for normal distribution using the D'Agostino-Pearson normality test (significance value of 0.05)[220]. If the datasets passed the test, then statistical significance was determined using a two-tailed t-tests. If datasets failed the normality test, a nonparametric test was chosen to compare the significance of means between groups Mann-Whitney test for two samples (with one or two tailed distributions where appropriate) and Kruskal-Wallis ANOVA for multiple samples[221]. $P < 0.05$ were considered as significant and were marked by '*'; $P < 0.01$ with '**', $P < 0.001$ by '***' and $P < 0.0001$ by '****'.

Curve fitting was performed using the curve fitting toolbox in MATLAB.

Image analysis

Quantifying effects of nocodazole treatment

To quantify morphological features of mitochondria and after Nocodazole treatment, SIM time-lapse images before and after Nocodazole treatment were analyzed as follows: Mitochondrial membrane potential was analyzed by measuring mean fluorescence intensity of single mitochondria (ROI defined by using Otsu thresholding and Analyze Particles Plugin) on SIM images and subtracting the cytosolic background. The diameter of mitochondria was determined by FWHM measurement profile across individual mitochondria on time-lapse SIM recordings.

Quantifying mitochondrial-ER overlap

ER-mitochondrial overlap was calculated by binarizing both images using the Otsu method in ImageJ. The overlap of the two binarized images was calculated using the Image Calculator AND operation. The overlap was then normalized to the total mitochondrial area.

Chapter 5

Sample preparation

Cos-7 cells were grown in Dulbecco's modified Eagle medium (DMEM) supplemented with 10% fetal bovine serum (FBS). Cells were plated on 25 mm, #1.5 glass coverslips (Menzel) 16-24 h prior to transfection at a confluency of ~10^5 cells per well. Dual transfections containing Drp1-GFP (Addgene, plasmid #49152) and Mito-Scarlet (original targeting Cox8a presequence from MitoGFP, a gift from Hari Shroff) were performed with either Lipofectamine 2000 (Life Technologies). Lipofectamine transfections were carried out in Opti-MEM using 150 ng of Drp1-GFP, 150 ng of Mito-Scarlet and 1.5 µL of Lipofectamine 2000 per 100 µL Opti-MEM.

Imaging

The imaging was performed on the iSIM setup as described in the previous sections. For adaptive imaging strategies, the exposure time was kept constant at 100 ms, while the interval between adjacent frames was updated every second based on the adaptive strategy. The minimal time interval was set to 0 s, such that the time between frames corresponds only to the exposure time, while the maximal interval between frames was 1 s. The recalculated time interval was rounded to the nearest 0.1 s.

Image analysis

To reconstruct adaptive movies, the raw datasets were processed by copying specific frames multiple times to give the impression of longer interval times.

Simulation platform

The simulation platforms were created in MATLAB R2020a.

Outlook

U-net architecture

As input we used the dataset collected with the FliptR probe, containing the intensity and lifetime channels. We then used the intensity channel as an input into the network, with the lifetime expected as output. To increase the size of the dataset, since mitochondrial shape and tension is assumed to be rotationally and translationally invariant, we used some data enhancement techniques such as rotating and reflecting the acquired data to increase the size of the dataset. The network architecture was based on the standard U-net[211], composed of an encoding and a decoding part, with a total depth of 3 layers. Initially, the main parameters such as the learning rate, size and number of convolutional windows were optimized through a standard grid search. Initially, we used mean absolute error (MAE) as the loss function, which however seemed to segment mitochondria well without fully capturing variations in lifetime. To improve on this aspect, we tried defining custom loss functions, to amplify the contribution of variations in lifetime, as well as using other error metrics such as the structural similarity index (SSIM).

The following parameters were used for the data shown in this thesis:

Parameter	Value
Optimizer type	Adam
Activation function	ReLu
Learning rate	$0.5*10^{-3}$
Test/train split ratio	0.2
Dropout ratio	0.2
Epochs	100
Batch size	500
Batch shuffle	True
Convolutional window size	7
Filters in 1st layer	32

Table 6 - Summary of parameters used to train the U-net

Appendices

Appendix A – Ray transfer matrix calculations and mfFIFI development

To better understand the adapted illumination system, we performed a ray transfer matrix calculation for the whole system, as adapted from ref[61]. To fully explore the effect of introducing a beam expander between the collimating lens and the first flat-fielding microlens array, let us compare the two cases side-by-side. For this, we divide the system into three parts:
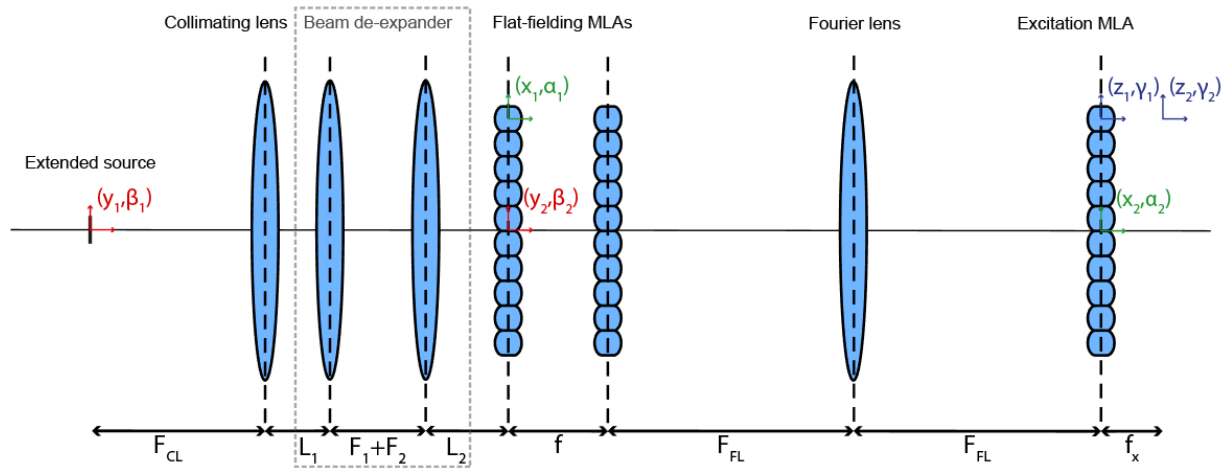
Figure 32 - Ray transfer matrix parameters and coordinates.
*Schematic representation of the different coordinate systems used in the ray transfer matrix calculations. The coordinate system (y_1, β_1) to (y_2, β_2) describes the system from the input beam to the first flat-fielding MLA. The calculation can be performed with and without considering the effect of the beam de-expander. The coordinate system (x_1, α_1) to (x_2, α_2) is used to project the path from each microlens channel to the front-focal plane of the Fourier lens. Finally, (z_1, γ_1) to (z_2, γ_2) considers the light travelling through each microlens of the excitation MLA, to its front-focal plane. Figure reproduced with the permission of Springer Nature, material from: Mahecic, D. et al. Homogeneous multifocal excitation for high-throughput super-resolution imaging. Nat. Methods **17**, 726–733 (2020).* [92]

Sub-system 1: $(y_1, \beta_1) \rightarrow (y_2, \beta_2)$

Starting at the extended source and ending in plane containing the first flat-fielding microlens array, but without considering its effect. y_2 effectively determines the radius of the beam incident on the first flat-fielding microlens array (R). In the case without the beam expander:

$$\begin{pmatrix} y_2 \\ \beta_2 \end{pmatrix} = \begin{pmatrix} \left(1 - \dfrac{L}{F_{CL}}\right) y_1 + F_{CL}\beta_1 \\ -\dfrac{y_1}{F_{CL}} \end{pmatrix}$$

Where L is the variable distance between the collimating lens and the first flat-fielding microlens array. With the beam expander:

$$\begin{pmatrix} y_2 \\ \beta_2 \end{pmatrix} = \begin{pmatrix} \dfrac{1}{F_{CL} \cdot F_1 \cdot F_2} \left(F_2^2 (L_1 - F_{CL} - F_1) + F_1^2 (L_2 - F_2) \right) y_1 - \dfrac{F_2}{F_1} F_{CL} \beta_1 \\ \dfrac{F_1}{F_2} \dfrac{y_1}{F_{CL}} \end{pmatrix}$$

Where L_1 and L_2 are the distances between the collimating lens and the first lens of the beam expander, and the distance between the second lens of the beam expander and the first flat-fielding microlens array.

Sub-system 2: $(x_1, \alpha_1) \rightarrow (x_2, \alpha_2)$

Starting in local coordinate system of a single lenslet of the first flat-fielding microlens array and ending in the focal plane of the Fourier lens, containing the excitation microlens array, but without considering its effect:

$$\begin{pmatrix} x_2 \\ \alpha_2 \end{pmatrix} = \begin{pmatrix} -\dfrac{F_{FL}}{f} x_1 \\ -\dfrac{1}{F_{FL}} (\alpha_1 f - np) \end{pmatrix}$$

This subsystem is not explicitly modified by introduction of beam expander.

Sub-system 3: $(z_1, \gamma_1) \rightarrow (z_2, \gamma_2)$

Starting in local coordinate system of a single lenslet of the excitation microlens array and ends in local focal plane of a single lenslet of the excitation microlens array:

$$\begin{pmatrix} z_2 \\ \gamma_2 \end{pmatrix} = \begin{pmatrix} f_x \gamma_1 \\ \gamma_1 - \dfrac{z_1}{f_x} \end{pmatrix}$$

This subsystem is not explicitly modified by introduction of beam expander.

These three subsystems are linked together by boundary conditions that transition from the local coordinate systems of microlens arrays to the global coordinate system. The boundary conditions are:

Boundary condition $(y_2, \beta_2) \rightarrow (x_1, \alpha_1)$: from global coordinate system to the local coordinate system

of the flat-fielding microlens arrays

$$\begin{pmatrix} x_1 \\ \alpha_1 \end{pmatrix} = \begin{pmatrix} y_2 - np \\ \beta_2 \end{pmatrix}$$

Boundary condition $(x_2, \alpha_2) \rightarrow (z_1, \gamma_1)$: from global coordinate system to the local coordinate system

of the excitation microlens array

$$\begin{pmatrix} z_1 \\ \gamma_1 \end{pmatrix} = \begin{pmatrix} x_2 - mp_x \\ \alpha_2 \end{pmatrix}$$

Regardless of the elements before the first microlens array, the ray-tracing matrix between the first microlens array and the focal plane of the excitation microlens array is given by (adapted from [30]):

$$\begin{pmatrix} z_2 \\ \gamma_2 \end{pmatrix} = \begin{pmatrix} -\dfrac{f_x}{F_{FL}}(\beta_2 f - np) \\[2ex] \dfrac{F_{FL}}{f_x \cdot f} y_2 - \dfrac{f}{F_{FL}} \beta_2 + \left(\dfrac{1}{F_{FL}} - \dfrac{F_{FL}}{f \cdot f_x}\right) np + \dfrac{mp_x}{f_x} \end{pmatrix} \cong \begin{pmatrix} -\dfrac{f_x}{F_{FL}}(\beta_2 f - y_2) \\[2ex] -\dfrac{f}{F_{FL}} \beta_2 + \dfrac{1}{F_{FL}} y_2 + \dfrac{mp_x}{f_x} \end{pmatrix}$$

Where np indicates the radius of the beam incident on the first microlens array, equally corresponding to the maximal height of a beam incident on the array, $R = \max(y_2)$. Similarly, the maximal values of y_1, β_1 are set by the radius and angular divergence of the extended source:

$$\max(y_1) = R_{source}$$

$$\max(\beta_1) = \theta_{source}$$

By replacing the values of y_2 and β_2 into the system with or without a beam expander, we see that

the overall size of the excitation spots can be minimized more effectively in the case including the beam expander. To find the size of the excitation spot r, we simply compute the maximum of z_2, $r = \max(z_2)$:

Without beam expander

$$r \cong \frac{f_x}{F_{FL}} \left(1 - \frac{L}{F_{CL}} + \frac{f}{F_{CL}}\right) R_{source} + \frac{f \cdot F_{CL}}{F_{FL}} \theta_{source}$$

Where L is the distance between the collimating lens and the first flat-fielding microlens array.

With beam expander

$$r \cong \frac{f_x}{F_{FL} \cdot F_{CL}} \left(\frac{F_2}{F_1}(L_1 - F_{CL} - F_1) + \frac{F_1}{F_2}(L_2 - F_2) - \frac{f \cdot F_1}{F_2}\right) R_{source} + \frac{f \cdot F_{CL} \cdot F_2}{F_{FL} \cdot F_1} \theta_{source}$$

Where L_1 is the distance between the collimating lens and the first beam expander lens, and L_2 the distance between the second beam expander lens and the first flat-fielding microlens array. Since the second term of the expression for r dominates, we can see that introducing a beam expander rescales the size of the excitation foci by a factor of F_2/F_1. In the case where $F_2 < F_1$, this leads to a decrease in size. L_1 and L_2 can be modified allow flexible tuning of the radius R.
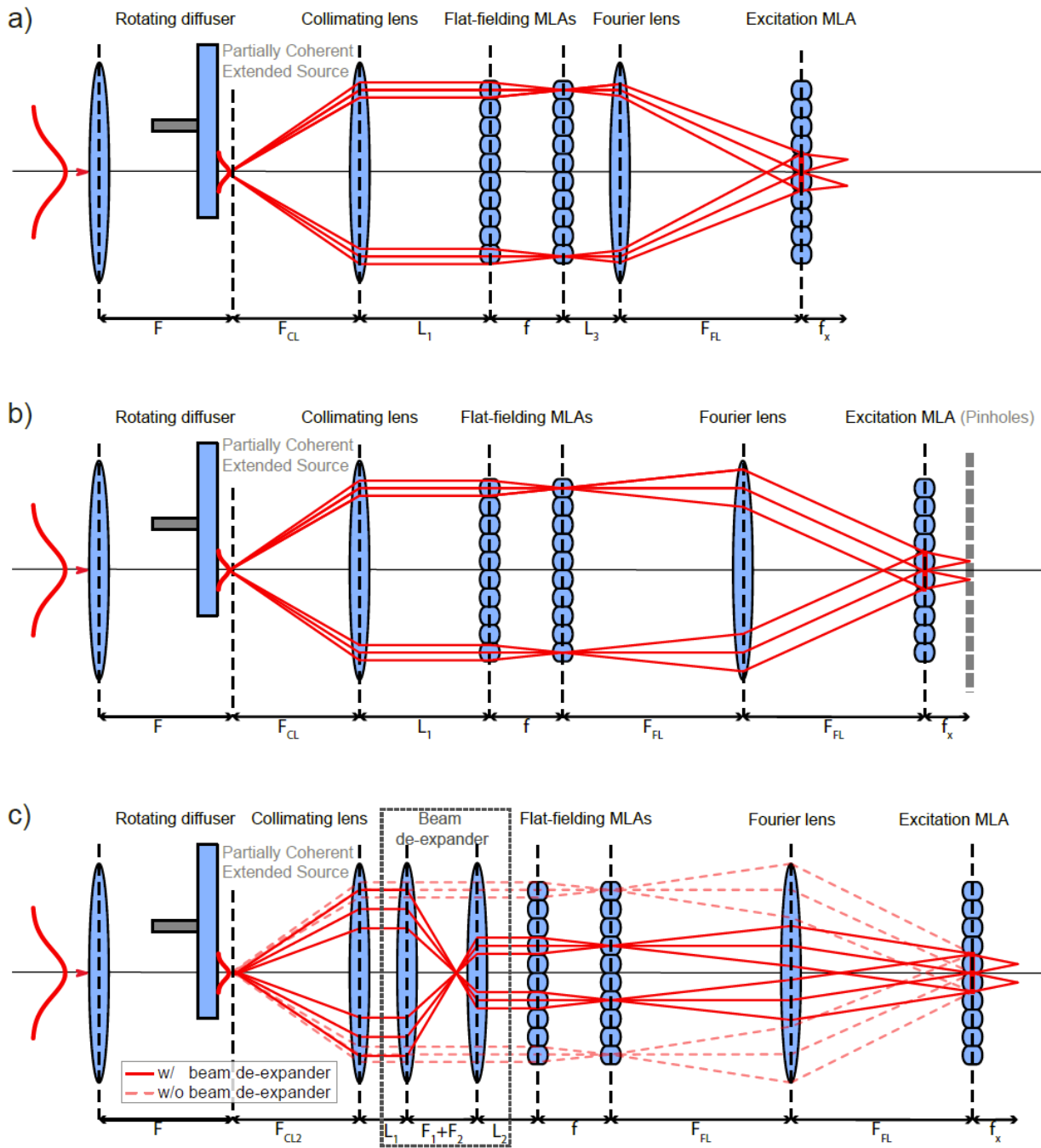
Figure 33 - mfFIFI development stages.

a) A standard Köhler uses a pair of flat-fielding MLAs to split the incoming light into multiple channels, before focusing them in the front-focal plane of the Fourier lens. This effectively averages over spatial variations in the beam intensity, generating a flat-top beam profile. In the case of a coherent light source, such as lasers, a focusing lens and a rotating diffuser are used to scramble the incoming light and generate an extended partially coherent source, which is then collimated by the collimating lens. Implementing a traditional Köhler integrator with a variable length L_3 between the second flat-fielding MLA and the Fourier lens, results in non-telecentric illumination of the excitation MLA. This will in turn cause the pitch of the excitation spots produced by the excitation MLA to vary. b) The telecentric Köhler integrator assures that the pitch of the excitation spots generated by the excitation MLA is conserved, by setting the distance between the second flat-fielding MLA and the Fourier lens to the focal length of the Fourier lens: $L_3 = F_{FL}$. Nevertheless, due to the nature of the extended source, the excitation spots will be larger than those produced by direct Gaussian excitation. This will limit the capability of the microscope to achieve diffraction-limited excitation at the sample. A possible solution would be to limit the size of the spots by placing a pinhole array in the front focal plane of the excitation MLA, although at a cost to the transmission efficiency. c) The extended design overcomes this problem by introducing a beam expander between the collimating lens and the

*first flat-fielding MLA, which allows control over how many microlens channels are used to average over in the focus of the Fourier lens. Careful choice of the beam de-expansion factor enables contraction of the size of the excitation spots, while maintaining good transmission efficiency and homogeneity. Alternatively, placing a hard aperture to limit the radius of the beam incident on the flat-fielding MLAs would have a similar effect, albeit rejecting much of the incident light. Figure reproduced with the permission of Springer Nature, material from: Mahecic, D. et al. Homogeneous multifocal excitation for high-throughput super-resolution imaging. Nat. Methods **17**, 726–733 (2020). [92]*

Appendix B – Transmission efficiency through a pinhole

The cost of introducing a pinhole array to limit the size of the excitation spots can be estimated by modelling the intensity of each excitation focus as a small Gaussian beamlet:

$$I(r) = I_0 \exp\left(-\frac{2r^2}{w_0^2}\right)$$

Where I_0 is the amplitude intensity, r the radial position from the center of the beamlet and w the width of the beam waist. Considering a pinhole of variable radius aw_0, we can compute the transmitted power through a pinhole as a function of the relative ratio between the beam waist and pinhole diameter $P_{pin}(a)$:

$$P_{pin}(a) = \int_{r=0}^{r=aw_0} 2\pi r \, I(r) dr = P_0[1 - exp(-2a^2)]$$

Where $P_0 = \pi r^2 I_0$. The transmission efficiency can then be computed as $P_{pin}(a)/P_0$ and is shown in Figure 34. Therefore, by estimating the beam waist from the image of the excitation spots (Figure 8f) and comparing to the size of the pinholes, the estimated factor of ½ difference results in a transmission efficiency of <40%.
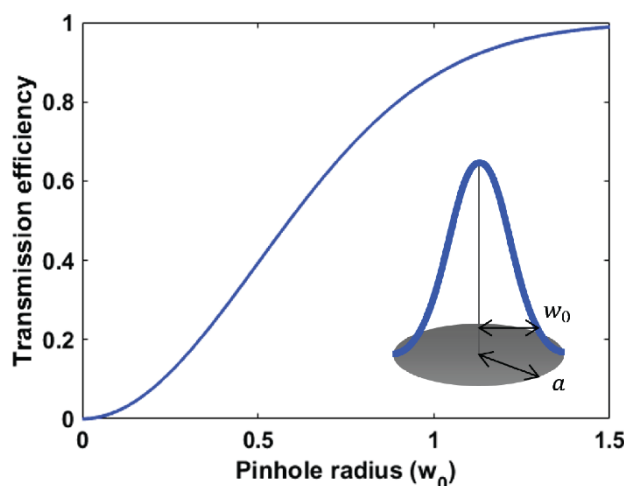
Figure 34 - Figure showing the transmission efficiency of a Gaussian spot through a pinhole.
The pinhole radius is represented relative to the waist of the Gaussian beam, as derived from the equation above.

Instead, to mitigate the large spot size, we used ray transfer matrix analysis (Appendix A) to better understand how the size of the excitation spots depends on the properties of the extended source and design of the Köhler integrator:

$$\begin{pmatrix} r_{n,m} \\ \theta_{n,m} \end{pmatrix} = \begin{pmatrix} \dfrac{f \cdot f_x}{F_{FL} \cdot F_{CL}} R_{source} + \dfrac{f_x}{F_{FL}} np \\[2em] \left(\left(\dfrac{f}{F_{FL} \cdot F_{CL}} + \dfrac{F_{FL}}{f \cdot f_x} \left(1 - \dfrac{L}{F_{CL}} \right) \right) R_{source} + \dfrac{F_{CL} \cdot F_{FL}}{f \cdot f_x} \theta_{source} + \left(\dfrac{1}{F_{FL}} - \dfrac{F_{FL}}{f \cdot f_x} \right) np + \dfrac{mp_x}{f_x} \right) \end{pmatrix}$$

Where r is the size of the excitation spots, θ the angular distribution, n is the index of the flat-fielding microlens array and m the index of the excitation microlens array (assuming $n = 0$ and $m = 0$ correspond to the microlenses centred on the optical axis). From this, $np = R$ defines the radius of the beam incident on the first microlens array. The radius of the excitation spots can be rewritten as the first term, taken for maximal values of the extended source radius and the size of the beam incident on the first flat-fielding microlens array:

$$r = \frac{f \cdot f_x}{F_{FL} \cdot F_{CL}} R_{source} + \frac{f_x}{F_{FL}} R$$

There are two contributions determining the size the excitation spots: the size of the extended source R_{source} and the radius of the beam incident on the first microlens array R. However, since f and f_x are preferably on the order of a few millimetres, and F_{FL} and F_{CL} on the order of 10s-100s of millimetres, the first term becomes negligible, while the second term will have a dominant effect on the size of the excitations spots.

One way to reduce the radius of the beam R is to put an iris between the collimating lens and first microlens array. The iris would act as a mask and block light from passing through above a certain radius from the optical axis, effectively reducing the size of the beam incident on the first microlens array. However, this would cause significant power loss since only a fraction of the light would be transmitted through the iris, as described in the transmitted power equation and shown in Figure 34. A more efficient solution is to place a beam expander between the collimating lens and the first microlens array, in order to shrink the radius of the beam R to $R^* \cong (F_2/F_1) R$, without rejecting light as the iris does. Introducing a beam expander with focal lengths F_1 and F_2 between the collimating lens and the first flat-fielding microlens, gives (Appendix A):

$$r = \frac{f \cdot f_x \cdot F_1}{F_{FL} \cdot F_{CL} \cdot F_2} R_{source} + \frac{f_x}{F_{FL}} R^* \cong \frac{f \cdot f_x \cdot F_1}{F_{FL} \cdot F_{CL} \cdot F_2} R_{source} + \frac{f_x \cdot F_2}{F_{FL} \cdot F_1} R$$

In the case where the beam expander contracts the size of the beam ($F_2 < F_1$), this results in a decrease in the diameter of the beam R by a factor of F_2/F_1. Although it also results in an inverse increase in the apparent size of the extended source, since the second term carries a larger weight, the dominant effect is the decrease in the size of the excitation spots. The pinhole array to block excess light is therefore no longer required, improving the overall light transmission efficiency.

Appendix C – mfFIFI design equations

Based on the above design, we revise the standard Köhler integrator and propose the following design equations for its implementation in multi-focal microscopes. The design equations are functions of the following design parameters:

f – focal length of flat-fielding microlens arrays

p – pitch of flat-fielding microlens arrays

f_x – focal length of excitation microlens array

p_x – pitch of excitation microlens array

F_{FL} – focal length of Fourier lens

F_{CL} – focal length of collimating lens

F_1 – focal length of first beam expander lens

F_2 – focal length of second beam expander lens

R_{source} – radius of extended source

θ_{source} – angular divergence of extended source

M – magnification

R – beam radius incident on the first flat-fielding microlens array without the beam expander

Can be estimated as: $R \cong R_{source} + F_{CL}\tan(\theta_{source})$ (see Appendix A)

λ – wavelength

We start with the Fresnel Number, defined the same way as for the standard Köhler integrator[59,60]:

$$FN = \frac{p^2}{4\lambda f}$$

For good homogeneity we propose a value of $FN \gtrsim 5$.

The size of the flat field generated by the Köhler integrator at excitation microlens array remains the same as the standard Köhler integrator[59,60]:

$$S = \frac{F_{FL}\,p}{f}$$

This will also correspond to the extent of the multi-focal excitation after the excitation MLA. The final required flat field size will depend on the desirable sample FOV and magnification of the system. The accessible FOV on the sample will therefore be de-magnified:

$$S_{sample} = \frac{1}{M}\frac{F_{FL}\,p}{f}$$

From the ray transfer calculations, we know that the size of excitation spots (in focal plane of excitation microlens array) will be:

$$r = \frac{f \cdot f_x \cdot F_1}{F_{FL} \cdot F_{CL} \cdot F_2} R_{source} + \frac{f_x \cdot F_2}{F_{FL} \cdot F_1} R$$

It should be assured that after magnification to the sample, the size of the excitation spots appear diffraction limited after magnification. Size of excitation spots (at sample) will depend on:

$$r_{sample} = \frac{1}{M}\left(\frac{f \cdot f_x \cdot F_1}{F_{FL} \cdot F_{CL} \cdot F_2} R_{source} + \frac{f_x \cdot F_2}{F_{FL} \cdot F_1} R\right)$$

The flat field homogeneity can be expressed as:

$$B = \frac{R}{p}$$

This effectively determines over how many flat-fielding MLA channels the averaging out is performed. We propose that for good homogeneity $B \gtrsim 4$.

Finally, the no crosstalk condition is updated with respect to the standard Köhler integrator[59]:

$$\frac{F_1 \cdot f}{F_2 \cdot F_{CL}} \cdot R_{source} \leq \frac{p}{2}$$

Appendix D – Extended simulation platform code

The most recent version of the wave optics simulation platform for optimizing mf-FIFI can be found on GitHub (https://github.com/dmahecic/simmla_w_mfFIFI).

Using the previously established optical wave propagation simulation platform developed for the Köhler integrator[29], we extend its application to the multifocal case by adding the excitation MLA at the homogenization plane. We first consider the effect of varying the distance of the back focal plane of the Fourier lens with respect to the second flat-fielding MLA.

The wave optics simulation supports the predictions made based on the ray optics calculations (Figure 35a-d). As we see, all cases produce more than adequate flat fields for widefield illumination, as observed on the surface of the excitation MLA. However, once those fields pass through the MLA, the homogeneity and pitch of the multifocal excitation is optimal only for the telecentric case. As predicted, deviating from the telecentric case where the back focal plane of the Fourier lens overlaps with the second flat-fielding MLA, causes the pitch of the excitation to increase decrease, depending on the direction of the displacement. An additional feature shown by the simulation is that the homogeneity and size of the flat field are also affected by the displacement of the Fourier lens and second flat-fielding MLA.

Secondly, we study the effect of different beam contraction factors on the size of the excitation spots (Figure 35e-h). Again, the simulation supports the predictions of the ray optics calculations – while all flat-fields at the surface of the excitation MLA appear comparable for the widefield case, propagating through the excitation MLA results in excitation spots of different sizes. Additionally, this also affects the relative intensity of the flat multi-focal excitation, showcasing how ensuring adequate spot size improves transmission efficiency. As predicted, reducing the diameter of the beam incident on the flat-fielding MLAs with beam expanders with increasing contraction factors, results in spots of smaller peak widths. On the other hand, this comes at a cost to the quality of the flat-field. Using fewer flat-fielding MLA channels reduces the uniformity of the multifocal excitation and therefore requires careful optimization.

The extended simulation platform is intended to help integrate the mfFIFI module into other applications and help users identify the optimal parameters for their application. To our knowledge, the mfFIFI module should be extensible to other applications using multi focal excitation.
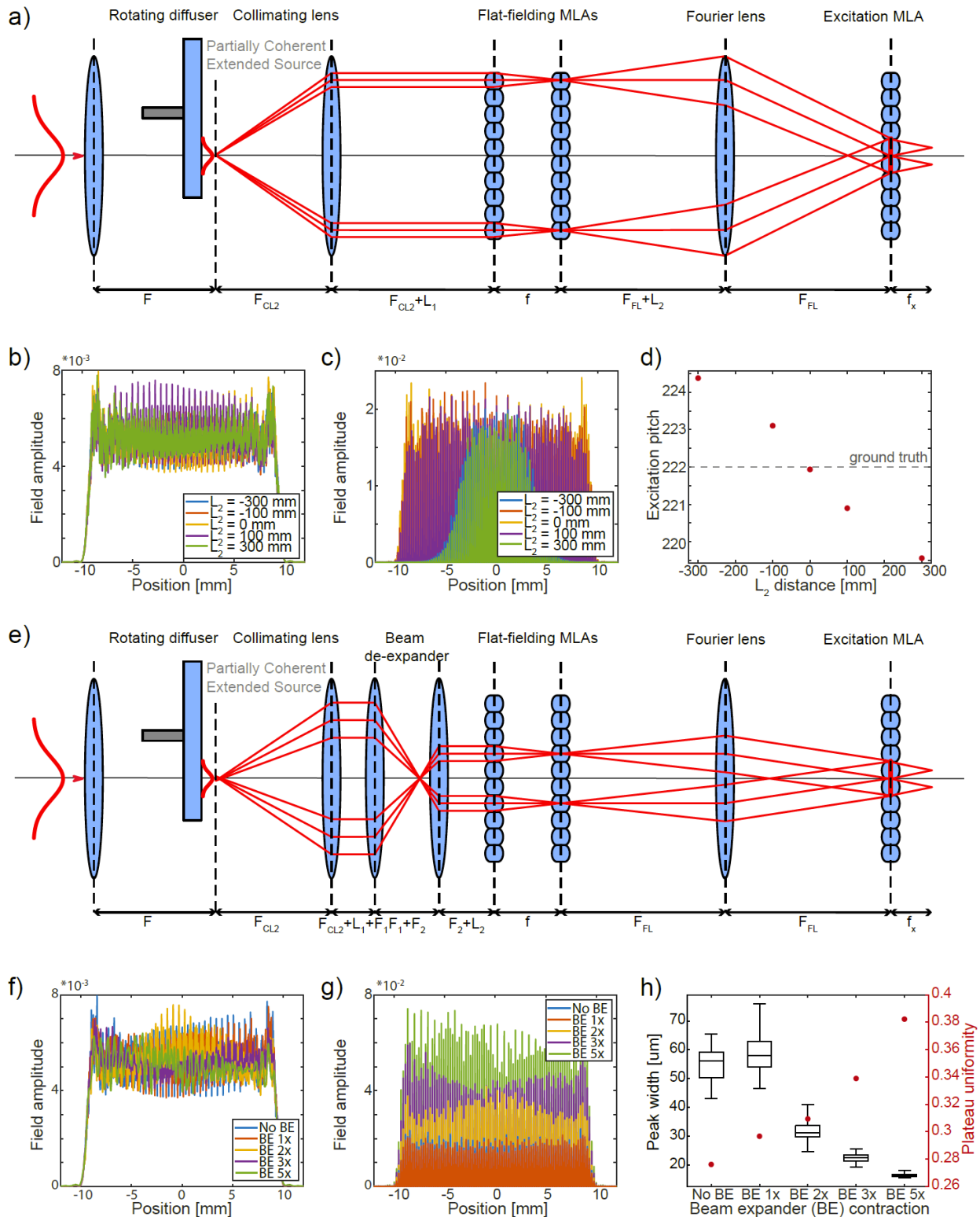
Figure 35 - Optimization of design parameters using the extended simulation platform.

a) Schematic showing the standard Köhler integrator setup, indicating how the different design parameters are defined in the simulation. b) Field amplitude at the front focal plane of the Fourier lens, corresponding to the field incident on the excitation MLA, and c) at the front focal plane of the excitation MLA for different distances L2 of the Fourier lens from the flat-fielding MLAs. The telecentric condition corresponds to L2 = 0. d) Average pitch of the multi-focal excitation measured at the front focal plane of the excitation MLA for different values of L2. Dashed line marks the actual pitch of the excitation MLA. e) Schematic representation showing the mfFIFI configuration including the beam contractor and labeling the simulation parameters. The beam contraction factor is set by the

inverse of the magnification of the two lenses of the beam contractor: F2/F1. f) Field amplitude at the front focal plane of the Fourier lens and g) the front focal plane of the excitation MLA. h) Trade-off of the beam contraction factor between the spot size (left axis) and the homogeneity of the excitation spots (right axis), quantified by the plateau uniformity; the central mark on the boxplot indicates the median, and the bottom and top edges of the box indicate the 25th and 75th percentiles, respectively. Figure reproduced with the permission of Springer Nature, material from: Mahecic, D. et al. Homogeneous multifocal excitation for high-throughput super-resolution imaging. Nat. Methods **17**, 726–733 (2020). [92]

Appendix E – Extended microscope characterization

		Lateral FWHM (nm)	Axial FWHM (nm)
NIH-iSIM[26]	**Raw**	213 ± 26	511 ± 24
	Deconvolved	145 ± 14	356 ± 37
UoL-iSIM[28]	**Raw**	212 ± 25	513 ± 33
	Deconvolved	152 ± 13	320 ± 16
HT-iSIM[92]	**Raw**	202 ± 9	454 ± 38
	Deconvolved	130 ± 8	353 ± 27

Table 7 - Table summarizing the raw and deconvolved PSF estimates for different iSIM setups.
Comparison is made between the previously published NIH-iSIM[26], UoL-iSIM[28] and LEB-iSIM presented in this work. NIH-iSIM: data are means ± s.d. derived from 10 beads. UoL-iSIM: data are means ± s.d. derived microtubule profiles. HT-iSIM: data are means ± s.d. derived from 12 beads suspended in immersion oil.
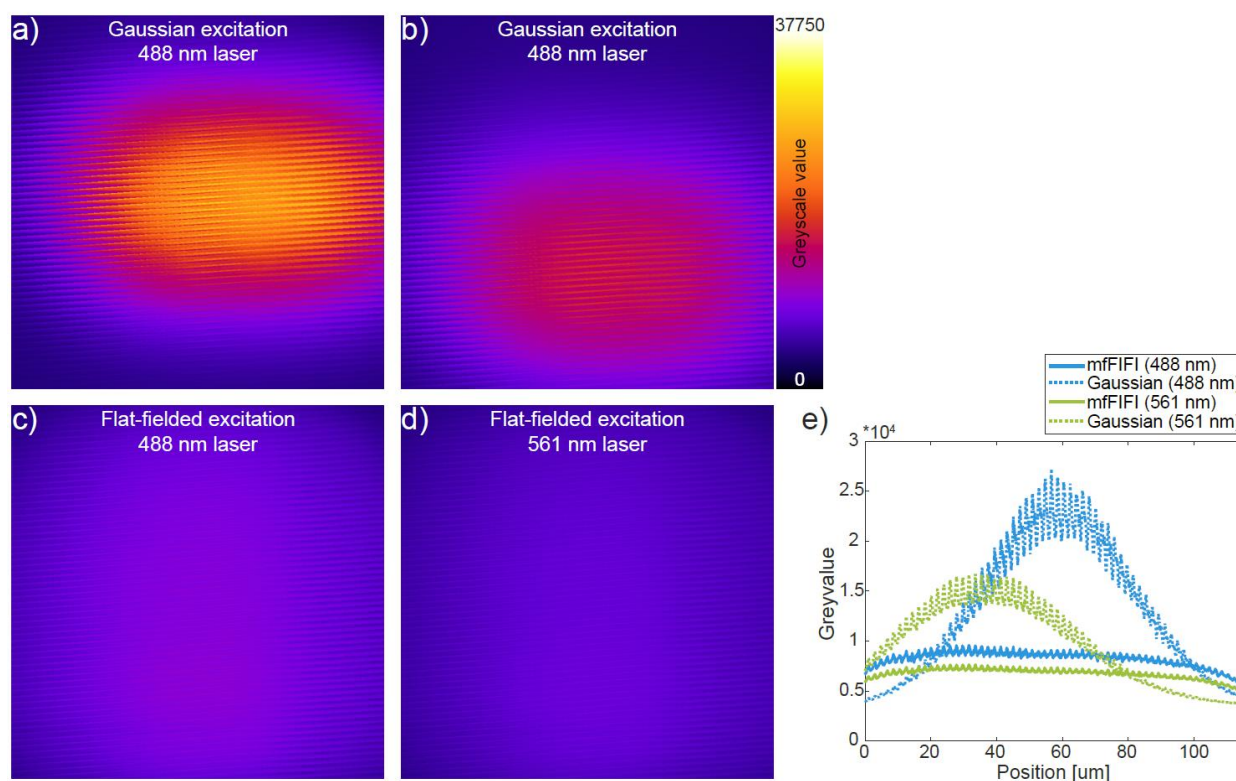
Figure 36 - Excitation profiles in iSIM scanning mode.
a-b) Scanning excitation illumination using Gaussian excitation for the (a) 488 nm and (b) 561 nm lasers using in each case a corresponding fluorescent dye sample. c-d) Scanning excitation illumination using mfFIFI excitation for the (a) 488 nm and (b) 561 nm lasers. e) Intensity profiles along the vertical direction of the different excitation illuminations from (a-d). Figure reproduced with the permission of Springer Nature, material from: Mahecic, D. et al. Homogeneous multifocal excitation for high-throughput super-resolution imaging. Nat. Methods 17, 726–733 (2020). [92]

To characterize the shape of the 3D PSF at different depths away from the coverslip, we suspended 100 nm beads in an agar drop to capture them at different depths away from the coverslip while imitating the refractive index of water, as previously described in Li et al.[222]. The beads from 3D acquisitions were compared between the TIRF oil objective (Olympus, APON60XOTIRF) and a water objective (Olympus, UPLANSAPO60XW). We then measured the raw (without deconvolution) 3D PSF dimensions (FWHM) and report them as a function of the distance of the bead from the coverslip, for both objectives.
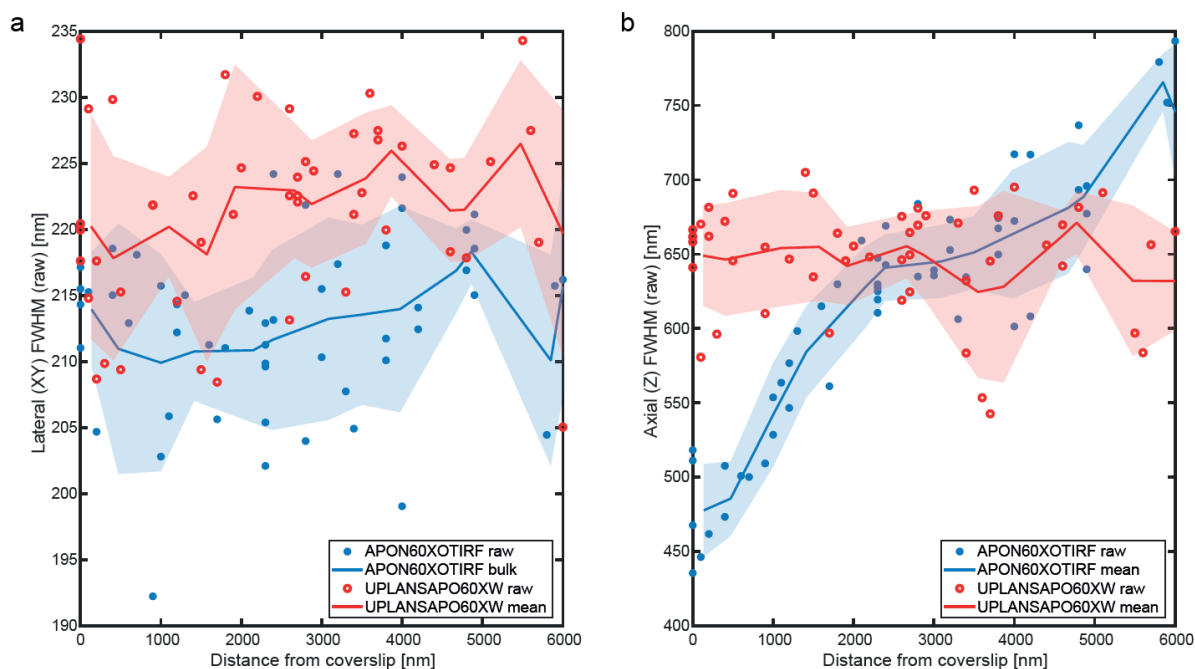
Figure 37 - Characterization of the 3D PSF.
The raw (without deconvolution) lateral (left) and axial (right) FWHM dimensions are reported using two different objectives, an oil TIRF objective (Olympus, APON60XOTIRF, blue) and a water objective (Olympus, UPLANSAPO60XW, red). The raw data is represented by circles and dots while the lines and shaded areas represents the mean and standard deviation respectively for a 1000 nm wide rolling window used to bin the data. Figure reproduced with the permission of Springer Nature, material from: Mahecic, D. et al. Homogeneous multifocal excitation for high-throughput super-resolution imaging. Nat. Methods 17, 726–733 (2020). [92]

As expected, the axial resolution for the oil objective degrades away from the coverslip, probably due to the spherical aberrations caused by refractive index mismatch between the oil and agar (refractive index close to that of water). This effect can be mitigated by using a water objective that gives more stable performance away from the coverslip. However, due to lower NA, the water objective also gives consistently worse performance < 3-5 µm from the coverslip. Hence, the oil objective gives superior performance close to the coverslip. While this issue is not specific to the presented method, the method is adaptable and it is possible to choose the optimal objective for different applications. Since most expanded centrioles were found near the coverslip, switching to a water objective would not have improved the quality of the collected particles in terms of resolution.

Appendix F – Particle montages, quantification and classification
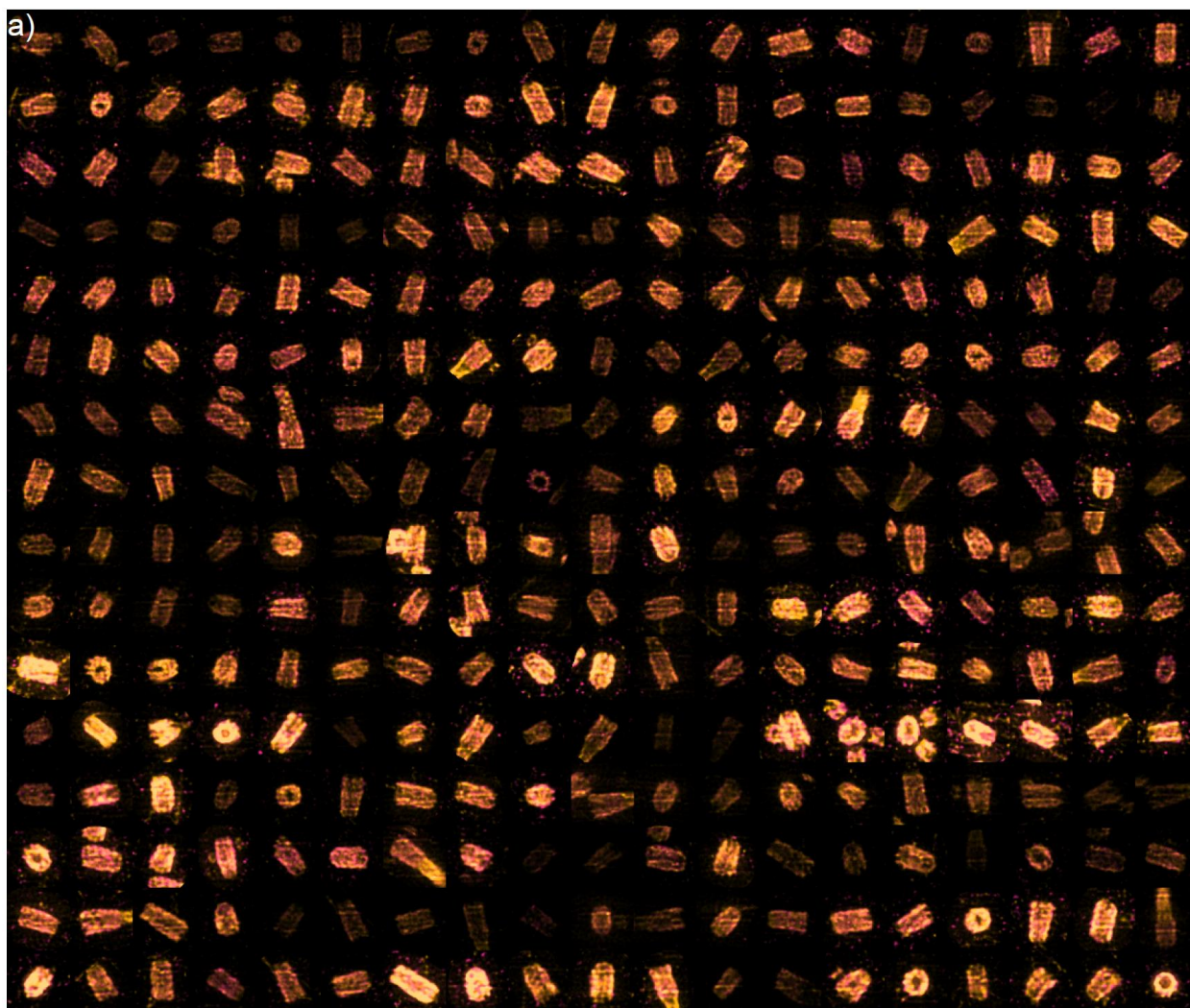
Figure 38 - Centriole particles from expanded RPE-1 cells.
*Montage of a random subset of unclassified raw particles collected in situ from expanded synchronized human RPE-1 cells stained for acetylated tubulin (yellow) and PolyE (magenta). Figure reproduced with the permission of Springer Nature, material from: Mahecic, D. et al. Homogeneous multifocal excitation for high-throughput super-resolution imaging. Nat. Methods **17**, 726–733 (2020).* [92]
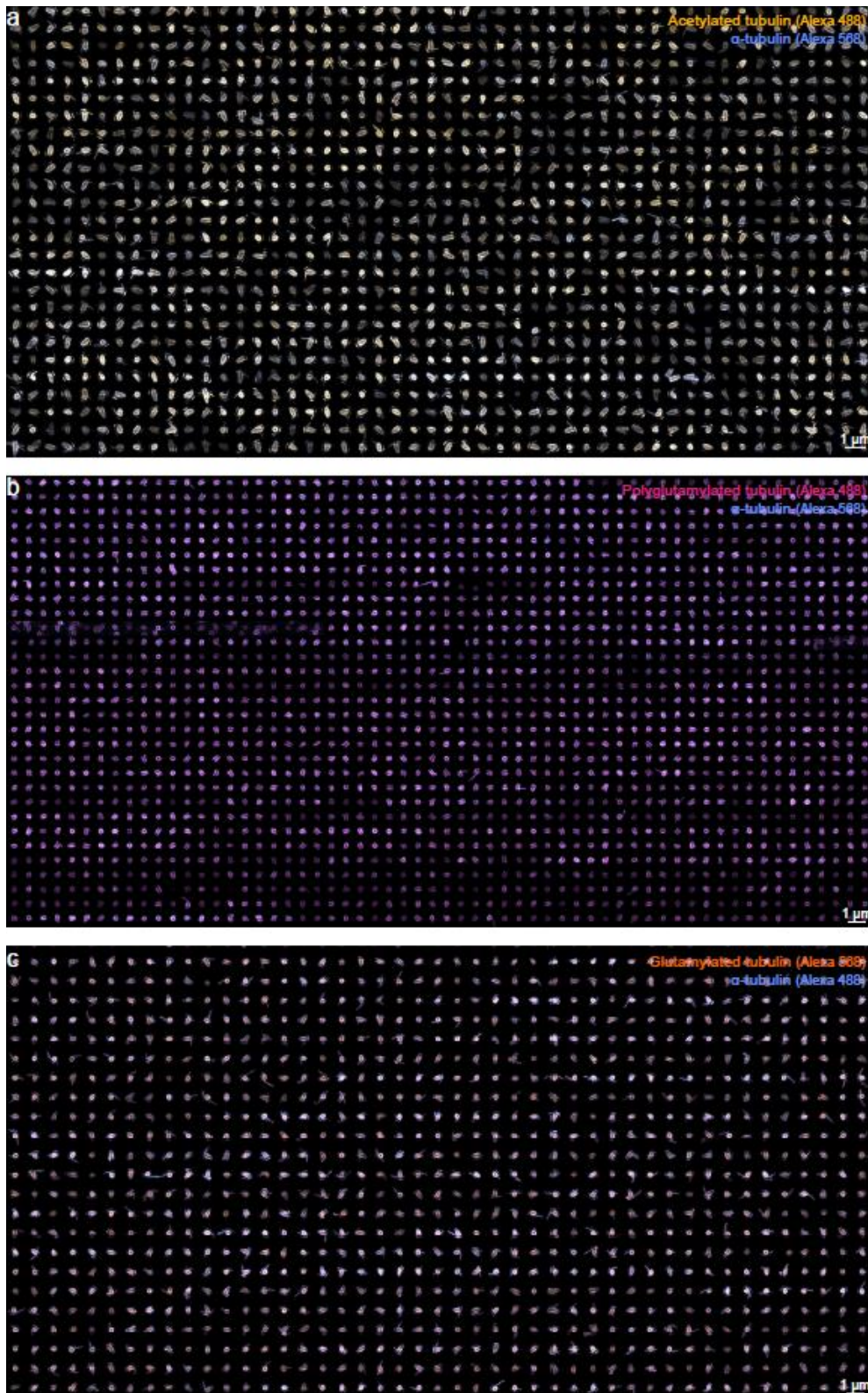
Figure 39 – Montage of centriole particles.

a-c) Montages of maximum intensity projections of a subset of centriole particles collected with dual-staining for a) acetylated tubulin, b) PolyE and c) GT335 with α-tubulin used as reference in each case. Figure reproduced with the permission of Springer Nature, material from: Mahecic, D. et al. Homogeneous multifocal excitation for high-throughput super-resolution imaging. Nat. Methods 17, 726–733 (2020). [92]
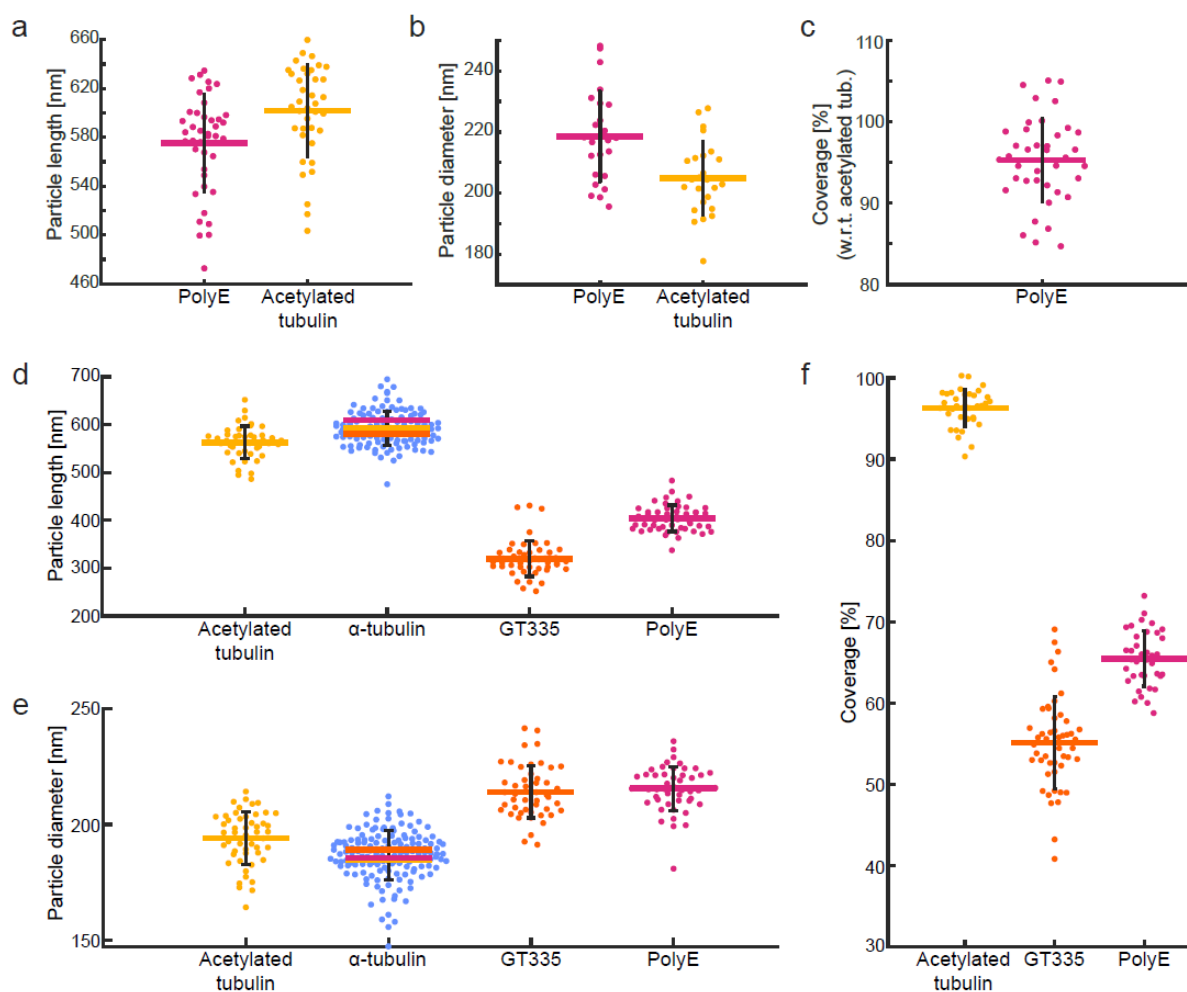
Figure 40 - Particle shape analysis and PTM coverage.

a) Particle lengths measured along side views of expanded human centrioles in the cellular context. b) Particle diameters measured on top views of human centrioles. c) PolyE coverage for human centrioles with respect to the acetylated tubulin signal along the length of the centriole. d) PTM length coverage measured along side views of purified Chlamydomonas reinhardtii centrioles. e) Particle diameters measured on top views of purified Chlamydomonas reinhardtii centrioles. α-tubulin signal was measured from three different datasets (dual-labeling with acetylated tubulin, GT335 and PolyE), with their individual means marked individually (acetylated tubulin in yellow, GT335 in orange and PolyE in magenta). f) PTM coverage for purified Chlamydomonas reinhardtii centrioles measured by dividing the length profiles of different PTMs by their respective α-tubulin signal. All scales reflect pre-expansion size. N = 25 top views and N=41 side views for human centrioles. N = 50 for acetylation dataset, N = 49 for GT335 dataset and N = 50 for PolyE dataset in Chlamydomonas reinhardtii. Error bars represent the standard deviation. Figure reproduced with the permission of Springer Nature, material from: Mahecic, D. et al. Homogeneous multifocal excitation for high-throughput super-resolution imaging. Nat. Methods 17, 726–733 (2020). [92]

Appendix G – Particle classification and reconstruction
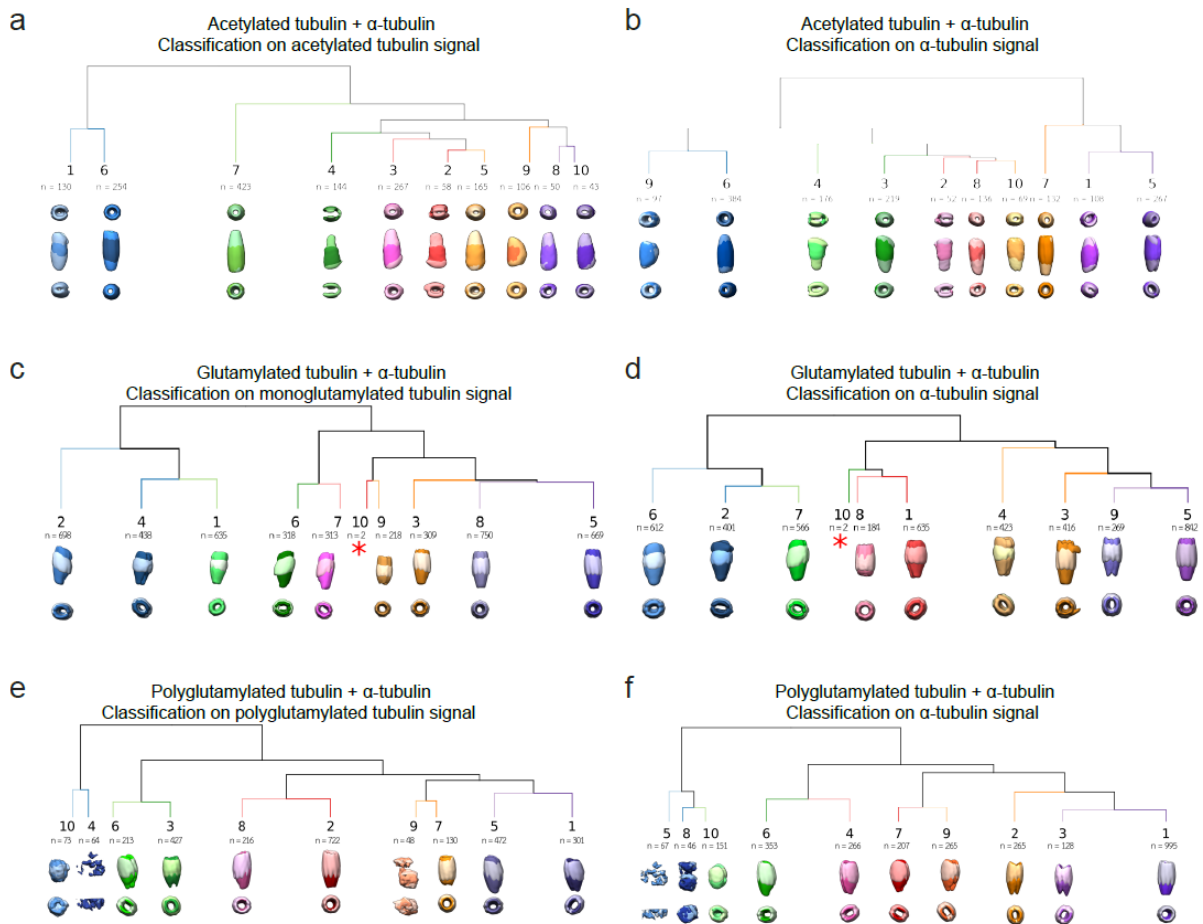
Figure 41 - Particle classification prior to reconstruction.
Dendrograms generated via hierarchical classification in 10 groups. On top, the average volume of all particles is displayed with 2 different orientations. For each group, the average volume is shown with the same 2 orientations, the tubulin signal dark-colored and the (a-b) acetylated, (c-d) glutamylated and (e-f) polyglutamylated signal light-colored. Figure reproduced with the permission of Springer Nature, material from: Mahecic, D. et al. Homogeneous multifocal excitation for high-throughput super-resolution imaging. Nat. Methods 17, 726–733 (2020). [92]
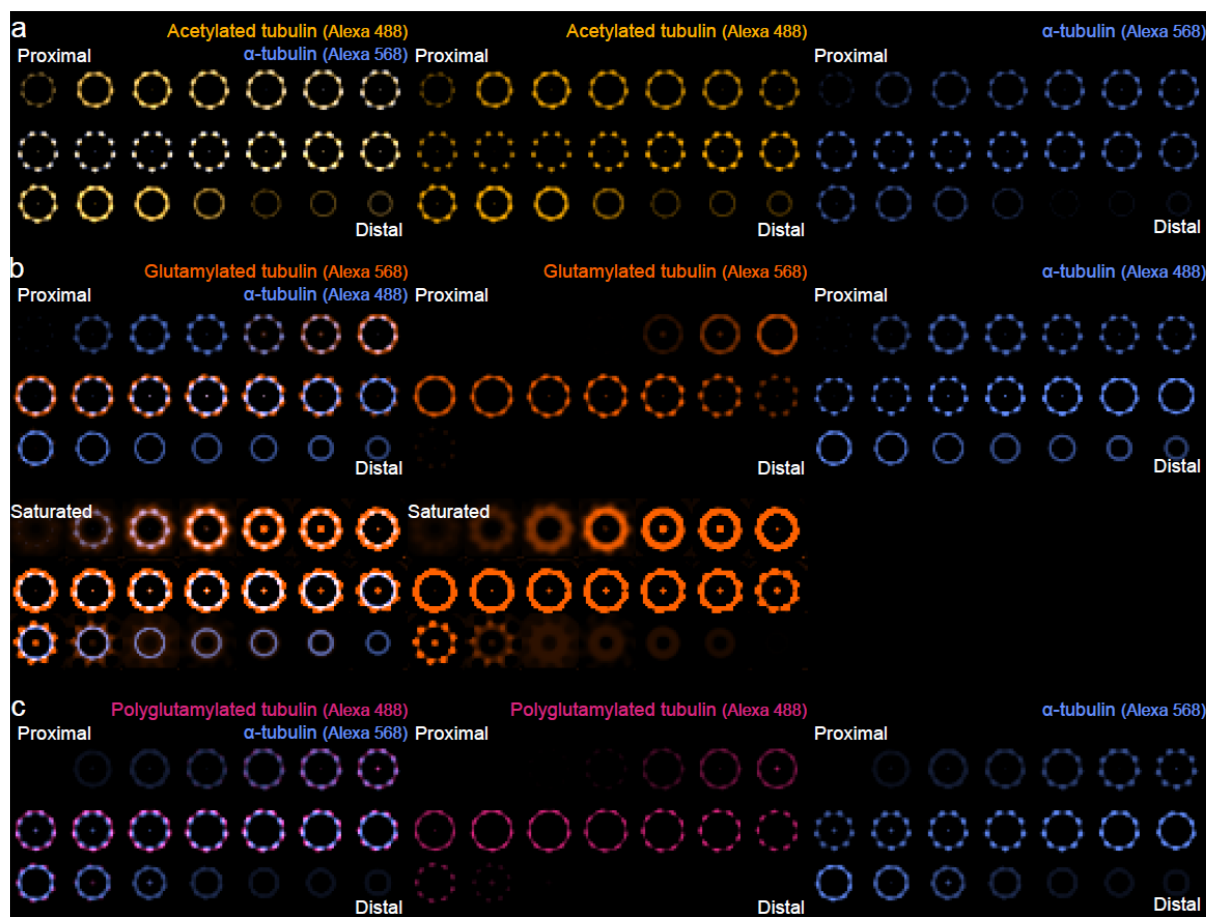
Figure 42 - Chlamydomonas reinhardtii reconstruction cross-sections.
*Cross sections starting from the proximal towards the distal end for (a) the acetylated tubulin and α-tubulin, (b) GT335 and α-tubulin and (c) PolyE and α-tubulin datasets. Distance between slices is 28 nm (every second slice from the reconstruction. All images are displayed as viewed from the distal end. For panels in (b), we also include a second rendering with a saturated intensity scale ("saturated"), to allow coverage at the ends to become more apparent. Figure reproduced with the permission of Springer Nature, material from: Mahecic, D. et al. Homogeneous multifocal excitation for high-throughput super-resolution imaging. Nat. Methods **17**, 726–733 (2020).* [92]

Appendix H – Shift and twist models for PolyE

We consider the microtubule triplet as a 60 nm structure, with the centers of the A,B and C microtubules separated by $d \cong 20$ nm, forming a $\theta \cong 120°$ angle with respect to the center of the centriole. By projecting the position of the C-microtubule we obtain a radial and a tangential position:

$$d_r = 2d \cos(\theta) \text{ and } d_\theta = 2d \sin(\theta)$$

Where d_r is the radial shift and d_θ the tangential shift.

In the twist model, we fix the localization of PolyE to the C-microtubule. We assume a closing of the angle from 120° to approximately 105° as reported by Le Guennec et al.[116], rotating around the inner A-microtubule. This gives:

$$d_r = 2d\Delta(\cos\theta) = 2d\,|\cos(120°) - \cos(105°)| \cong 9.6\ \text{nm}$$
$$d_\theta = 2d\,\Delta(\sin\theta) = 2d\,|\sin(120°) - \sin(105°)| \cong 4.0\ \text{nm}$$

In the shift and twist model we will purely consider the effect of PolyE shifting microtubule localization within the triplet, while changing angles from 120° proximally to approximately 105° distally[116], with the position of the PolyE signal being a function of θ This will result in:

$$d_r = 2d\cos\theta = 2d\cos(105°) \cong 10.4\ \text{nm}$$
$$d_\theta = 2d\sin\theta = 2d\sin(105°) \cong 38.6\ \text{nm}$$

Given our assumptions about what α-tubulin and PolyE antibodies are staining, we would expect the relative PolyE shift to go from a negative to a positive value, reflecting movement from the A->C microtubule relative to the center of mass of the microtubule triplet. However, while the absolute radial distance is consistent with our model, it is not centered around 0. The reason why the radius of PolyE appears consistently larger than that of α-tubulin could be due to different systematic errors such as the localization of PTMs relative to tubulin itself (PolyE is thought to form long chains that could shift its center of mass further away from the center of the microtubule), different labelling efficiencies or shapes of the A, B and C microtubules. However, since these explanations are purely speculative, we preferred to focus on the relative change along the length of the centriole.

Appendix I – Mitochondrial shape analysis pipeline

Images were first segmented using the open-source software ImageJ/Fiji[218] (http://fiji.sc) and the Weka Segmentation[223] V3.2.17 plugin with the resulting probability map used as the segmented image. Subsequent analysis was performed using a custom MATLAB functions which contoured the mitochondria and created a backbone with a mesh. This allowed us to measure the diameter and curvature along the constricted mitochondrion, and hence estimate the local bending energy. Tracking the position of the constriction site allowed us to measure the local Drp1 intensity. Tracking the leading edge of divided daughter mitochondria was used to estimate the membrane tension prior to fission.
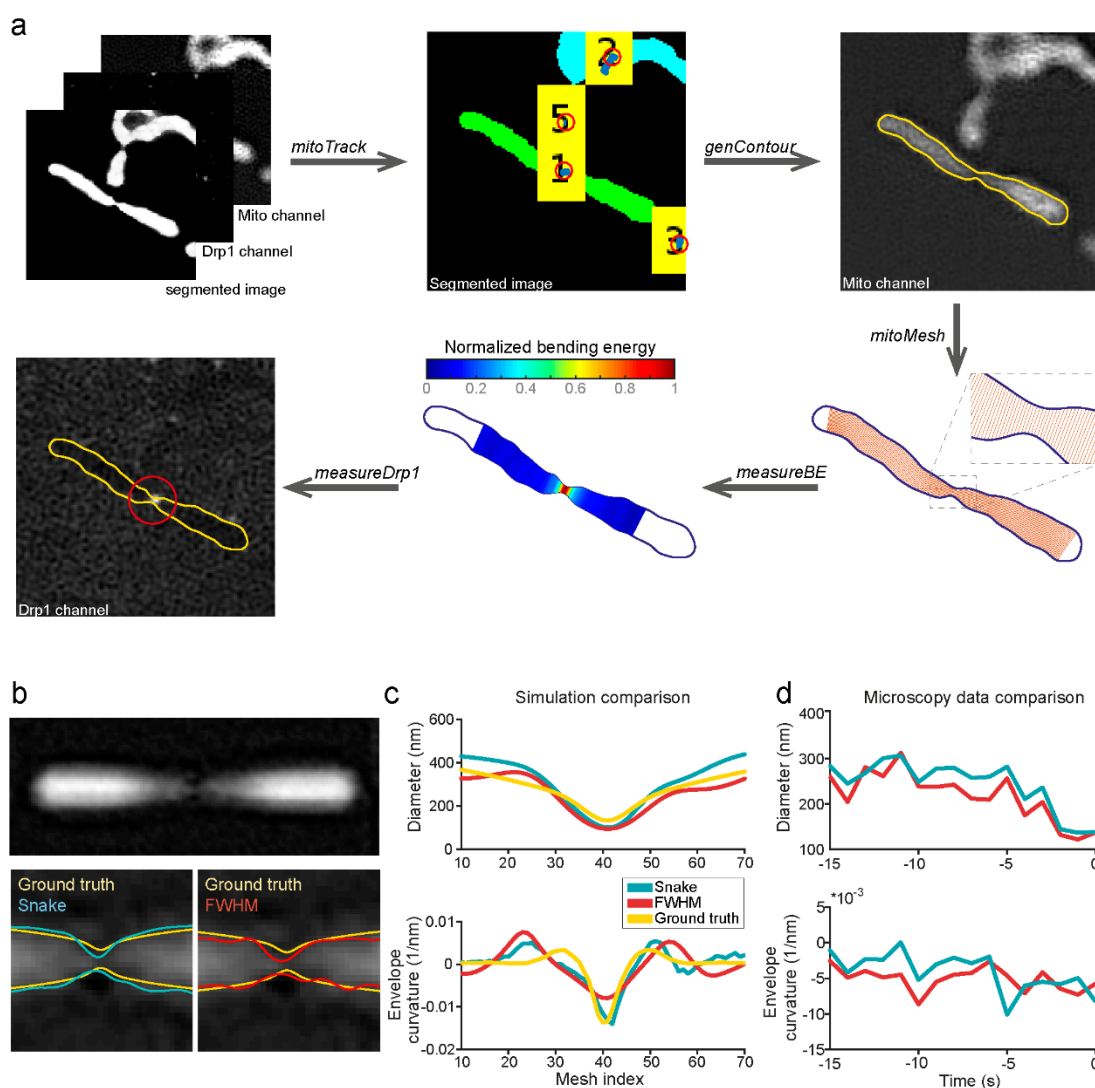
Figure 43 - MitoWorks analysis.
(a) Schematic representation of the MitoWorks analysis workflow. Two raw channels and a segmented image are chosen as inputs. The mitochondria were then tracked, and a mitochondrion of interest chosen by the user. This mitochondrion is then contoured, from which MitoWorks creates a mesh and a skeleton. This allows the shape and energetics of the constriction to be analyzed over time. Finally, the Drp1 signal at the constriction site is measured. (b) Simulated SIM image of a constricted mitochondrion was created based on a ground truth (yellow outline) to test the performance of the snake (blue outline) and FWHM (red outline) contours. (c) Measurement of constriction diameters (top) and envelope curvatures (bottom) for Snake and FWHM contours, compared to the ground truth structure (yellow line). (d) Comparison of snake and FWHM contour from real microscopy data.

The custom MATLAB package can be found on the GitHub repository (https://github.com/LEB-EPFL/MitoWorks) and allowed us to perform the summarized steps:

1. *mitoTrack*: Identify mitochondria in the segmented image and find nearest neighbor mitochondria in the subsequent frame. Mitochondrial tracks are made up of nearest neighbor mitochondrial centers of mass (using the knnsearch function) in consecutive frames. The tracked mitochondrion of interest is then cropped from both segmented and original time-lapse images for different channels

2. *genContour*: Create contour of the mitochondrion of interest using a built-in MATLAB function based on Chan-Vase active contouring of the segmented image[224]. A small Gaussian filter is applied prior to contouring. The generated contour is then smoothed over a length scale of ~ 170 nm, which was found

to be optimal for eliminating noise without sacrificing envelope curvature sensitivity. Contour smoothing was performed using a third-party function based on least-squares smoothing for MATLAB[225].

3. *mitoMesh*: Create a backbone, or centerline, of the mitochondrion of interest. The backbone is smoothed over a length scale of ~ 150 nm. Use generated backbone to divide mitochondrion into smaller segments, with the boundaries represented by a mesh, defined by lines drawn perpendicular to the backbone with subpixel spacing[226].

4. *genCurv*: measure the curvature along the contour of the mitochondrion using a third party 'LineCurvature2D' function for MATLAB[227].

5. *minDiameterSearch*: Use the diameters measured along the mesh to track the position of the constriction site, and measure its diameter.

6. *measureBE*: Use mesh to measure dimensions of individual segments. For each segment, use the measured diameters and envelope curvatures to estimate the bending energy and bending energy density of that segment. Find the length scale that maximizes the local bending energy density.

7. *genFWHM*: Generate FWHM based contour by fitting profiles plotted along the mesh with a Gaussian function. Connect the measured widths at along the mitochondrion and smooth at a length scale of ~ 170 nm to generate the FWHM contour.

Repeat *minDiameterSearch* and *measureBE* for FWHM contour.

8. *measureDrp1*: Measure the local Drp1 integrated intensity within a chosen radius around the constriction site. Radius used for all datasets: ~500 nm. Subtract background and bleach correct using a custom-written linear bleach correction function.

9. *mitoPull*: Repeat *genContour* and *mitoMesh* for daughter mitochondria after fission. Track the leading-edge retracting from the constriction site, corrected for the motion of the whole mitochondrion, to estimate membrane tension, using a viscoelastic model[228]. For membrane tensions estimated from iSIM data, the retraction was fit to an exponential decay function ($y=a*exp(bx)$), and extrapolated to zero.

To compare the snake and FWHM contours we simulated SIM images using a third-party SIM image generator[229]. Different shapes representing mitochondrial constriction sites at an SNR < 2, the typical value at mitochondrial constriction sites, were simulated and used to generate snake and FWHM contours. We observed that although the measured diameters were comparable between the two contours, the snake contour was better at detecting high envelope curvatures (SFig. 6). Hence the analysis was performed on the snake contour. All plots in this work were generated using a third-party function for MATLAB to generate shaded areas representing standard error[230].

Appendix J – Bending energy density, length scale and resolution effects

One of the main features that distinguishes fission from reversal events is the minimal envelope curvature at the constriction site. The resolution limit of ~100 nm for SIM restricts the minimal observable envelope radii to ~50 nm and therefore the maximal observable curvature to $-20*10^{-3}$ nm^{-1}. Nevertheless, envelope curvatures for both fissions and reversals remain above the resolution limit of curvature, allowing us to distinguish real differences.

The measured constriction diameters remain above the resolution limit of ~100 nm, until a few seconds before maximal constriction. We report that in this period during which constriction sizes are above the resolution limit, constriction diameters are indistinguishable between fissions and reversals, while a difference in envelope curvatures can already be observed ~30 s leading up to maximal constriction. Furthermore, our STORM measurements, which provide resolution < 100 nm, support that fissions and

reversals are not distinguishable by minimum diameter down to ~80 nm. Therefore, while both fissions and reversals reach the limit of our microscopy techniques, they arrive to this limit in an indistinguishable manner. At their maximal constriction, both fissions and reversals likely involve diameters below the resolution limit of live-cell nanoscopy.

Bending energy is calculated as a function of both envelope and tube curvature – related to the diameter. Therefore, although the calculated bending energies could be underestimated by resolution-limited measurements of the mitochondrial diameter, we are still able to distinguish differences and estimate the energy barrier to fission which is in agreement with theoretical estimates[145,163] and we expect represents a lower limit on the energy barrier.

Furthermore, the principal curvatures which themselves are 3-dimensional properties, are determined from 2-dimensional images. The analysis assumes that mitochondria are rotationally symmetric along their principal axis, and that they are parallel to the imaging plane. Images of mitochondria were usually acquired at the cell periphery, where the plane in which the mitochondria are contained should on average remain parallel to the coverslip and therefore the imaging plane. Furthermore, small deviations away from this angle should not strongly affect the principal radii of curvature projected onto the imaging plane, since this effect would scale with the cossine of the tilt angle (inverse of the cosine for the principal curvature).
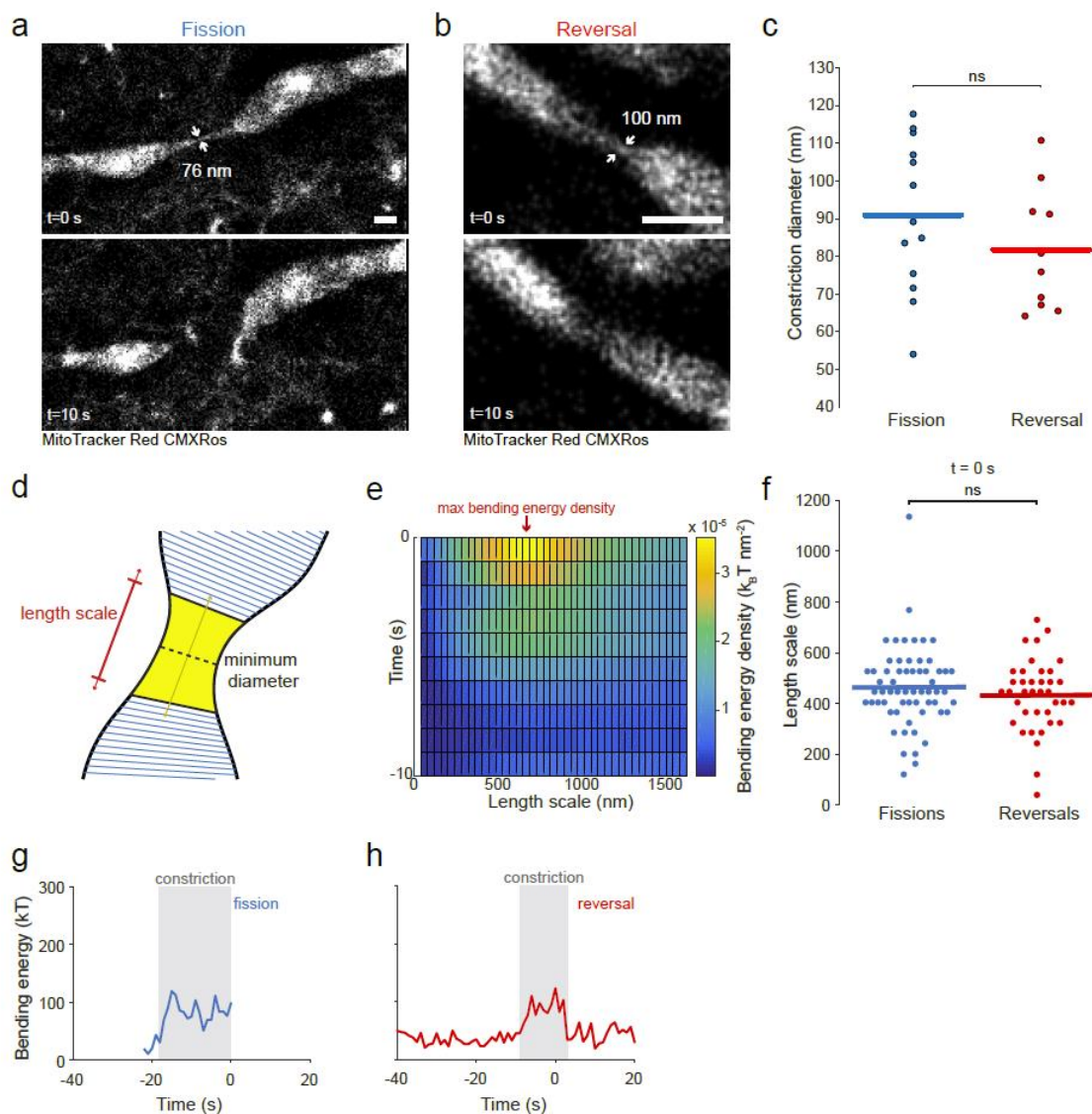
Figure 44 - Live-cell STORM and energetics of constriction sites.
(a,b) Time-lapse live-cell STORM imaging of COS-7 cells labelled with MitoTracker Red CMXRos showing a (a) fission and a (b) reversal event. Arrows indicate measured diameter values. (c) Distribution of minimum constriction diameters for fissions (N=13) and reversals (N=10) measured with STORM. Horizontal line represents the mean. (d) Cartoon illustrating how the length scale was determined by considering increasing areas around the constriction site. (e) The length scale was chosen by maximizing the local bending energy density. (f) Distributions of measured length scales for fissions (N=61) and reversals (N=38). Statistical significance calculated by a paired t-test: n.s. indicated p≥0.05. (g) Example evolution of bending energy for a fission and (h) reversal event. Light grey region indicates a period of constriction.

Appendix K – Estimating bending energy

To determine the area over which to measure the bending energy, we searched for the length scale that maximized the local bending energy density. This was done by considering areas composed of increased numbers of segments around the constriction site. The appropriate length scale was then selected by finding the area at which the bending energy density (ratio of bending energy and area) was maximal. The bending energy was then considered at this length scale. The length scales did not differ significantly between fissions and reversals.

The following equation was then integrated over the area corresponding to the appropriate length scale, to find the bending energy E_B [149]:

$$E_B = \frac{\kappa_B}{2} \int J^2 dA$$

Where κ_B is the bending rigidity, J the sum of local principal curvatures along the constriction site and A the surface area of the constriction site. The bending rigidity taken to be $\sim 20 \, k_B T$, as previously reported for lipid bilayers[151]. Since we consider a double-membrane system, we take the value of $\kappa_B = 40 \, k_B T$.

The above equation was applied to a discretized contour of mitochondria. The contour was subdivided into small segments sampled every ~15 nm. This slightly oversamples the changes in contour, but ensures sufficient sampling at highly bent structures, including constriction sites. The tube curvature was determined by calculating the average radius of the segment. The envelope curvature was taken as the weighted average of the two envelope curvatures, located at each side of the segment. The envelope curvatures were weighted by the length of each side of the segment, and assumed to vary linearly across the two sides of the segment. Finally, to calculate the surface area of the segment, we approximated the shape of the segment as a truncated cone. Therefore, for a single segment, the bending energy was given by:

$$E_B = \frac{\kappa_B}{2} \cdot \left[\frac{1}{<R_t>_{seg}} + \frac{1}{l_1 + l_2} \left(\frac{l_1}{<R_{e,1}>_{seg}} + \frac{l_2}{<R_{e,2}>_{seg}} \right) \right]^2 \cdot \left[\pi (R_{t,1} + R_{t,2}) \sqrt{(R_{t,1} - R_{t,2})^2 + h^2} \right]$$

Where $<R_t>_{seg}$ is the average tube radius across the segment, l_1 and l_2 the side lengths of the two sides of the constriction site, $<R_{e,1}>_{seg}$ and $<R_{e,2}>_{seg}$ the average envelope curvatures of the two sides of the constriction site, $R_{t,1}$ and $R_{t,2}$ the edge tube radii of the segment and h the average length through the center of the segment.

Appendix L – Estimating mitochondrial membrane tension

Estimating membrane tension from membrane tubules

To estimate mitochondrial membrane tension, we used mitochondrial tubules – short-lived structures pulled out of mitochondria by motor proteins[155,156] as well as long, thin constriction sites that strongly resembled a membrane pulling experiment. By drawing analogy to membrane pulling experiments[153,154], the diameter of the tubule d is a readout for membrane tension τ:

$$d = \sqrt{\frac{2\kappa_B}{\tau}} \quad \Rightarrow \quad \tau = \frac{2\kappa_B}{d^2}$$

Where κ_B is the bending rigidity, taken as $20 \, k_B T$ for a single membrane[151]. The radius of the tube was measured only when the motion of the tube stabilized, and before retraction. Mitochondrial tubules that did not retract and formed a branch on the mitochondrion were not considered. By measuring the diameters of tubules pulled out of mitochondria that subsequently divided, we found $d \cong 200$ nm, giving a value of $\tau \cong 4.10^{-6}$ N/m, which provides an independent estimate of membrane tension. The average of the measured tubule diameter was 202 ± 8 nm (mean ± SEM, N=14), above the resolution limit.

Estimating membrane tension from retraction speed

We used a visco-elastic model of the retraction of the mitochondrial membrane after fission to estimate the local membrane tension. The same model was used previously to estimate the membrane tension in the intercellular bridge during cytokinesis[228].

$$\sigma(t) = \int_{-\infty}^{t} \frac{du}{dt}(t = t^*) \times E(t - t^*)dt^* \approx \int_{0}^{t_0} \frac{du}{dt}(t = t_0) \times E(0)dt \approx \frac{v(t_0)}{l_0} \times \eta$$

Where σ is the stress, u the strain, E the relaxation modulus. $E(0)$ is approximated as the effective viscosity η at the moment of fission. $v(t_0)$ is the retraction speed at the moment of fission and l_0 the deformation length. l_0 was taken as 250 ± 15 nm (mean ± SEM, N=78 recoiling mitochondria from 39 fission events), averaged over all observed fissions. The deformation length was measured by comparing the shape of mitochondria before and after fission. The viscosity was taken as 120 cP.

From there, we find the force F by multiplying the stress by the cross-sectional area A:

$$F = \sigma A \cong \sigma \pi r^2$$

Where r is the constriction radius. The membrane tension τ is then estimated by dividing the pulling force by the circumference at the constriction site:

$$\tau = \frac{F}{2\pi r}$$

Comparison of the two methods

We suspected that the discrepancy between the tubule-based and retraction-based estimates was due to suboptimal temporal resolution, which would average out the retraction speed on which retraction-based visco-elastic model is based, decreasing its apparent value. To test this hypothesis, we performed fast live-cell imaging of mitochondria and Drp1, 20x faster than our initial measurements based on the Nikon SIM, using an instant structured illumination microscope (iSIM). We compared the membrane tensions calculated using the retraction-speed estimate at three different temporal resolutions, showing that worse temporal resolution decreased the calculated tension. Using iSIM data with an order of magnitude improvement on temporal resolution, we extrapolated the retraction velocity v at the time of fission by fitting the velocity decay to an exponential function as a function of time t: $v = a \exp(bt)$, where a and b were determined experimentally for each fission event. We repeated the retraction-based measurements, measuring 2.12± 1.49 ·10-6 N/m (mean ± SEM, N=14), comparable to the tubule-based estimate of membrane tension. Thus, the retraction-based estimate of tension quoted in the main text has been independently verified.

Furthermore, the estimate based on tube diameters is likely to be higher since it could only be applied to mitochondria under strong pulling forces with visible tubes, and hence only samples mitochondria with high membrane tension. While the values reported in the manuscript are lower due to low temporal resolution, they still present a real relative difference in membrane tensions of fission events between control and nocodazole treated cells.

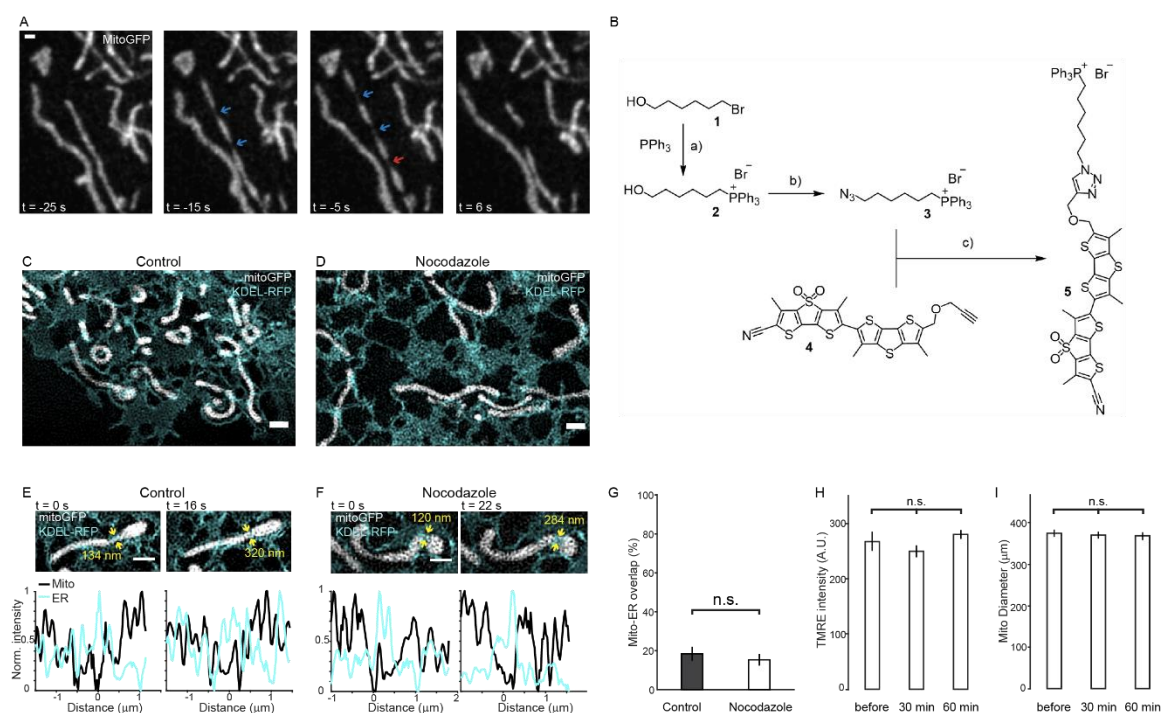# Appendix M – FliptR synthesis and nocodazole control experiments

Figure 45 - FliptR synthesis and nocodazole control experiments.
(A) Example of pearling modes observed on mitochondria. Blue arrows indicate constriction sites that result in fission and red arrows indicate the ones that reverse. Scale bar: 500 nm. (B) Toluene, reflux, 6 h, 30%. (b) 1. MsCl, NEt3, THF, 0 °C to rt, 30 min; 2. NaN3, THF/DMF, 60 °C, 2 h, 50%. (c) CuSO4.5H2O, Na-ascorbate, TBTA, CH2Cl2, DMSO, H2O, rt, 2 h, 59%. Compounds 2,3 and 5 were synthesized and purified according to procedures that will be reported elsewhere in another manuscript S1 in due time. Compound 4 was synthesized and purified according to procedures described in ref.[160]. (C,D) Representative images showing the organization of the ER between control (C) and Nocodazole treatment (D) in COS-7 cells transfected with Mito-GFP (grey) and KDEL-RFP (cyan). (E,F) Time-lapse live-cell SIM imaging of mitochondria and ER in COS-7 cells transfected with Mito-GFP and KDEL-RFP showing reversible constrictions occurring in the presence of the ER in both (E) control and (F) nocodazole treated cells. Images were adjusted for contrast. (G) Quantification of mitochondrial-ER overlap as a percentage of the mitochondrial surface. Lack of statistical significance between control (N=9) and Nocodazole (N=10) calculated by computing the 95% confidence interval for the difference between means. (H) Quantitative analysis of TMRE staining before and 30 min/60 min after Nocodazole treatment confirms no significant difference of mitochondrial membrane potential after drug treatment (N≥250 mitochondria for each group, error bars represent ±SEM). Statistical significance calculated by Kruskal-Wallis ANOVA (I) Quantification of mitochondrial diameter before and 30 min/60 min after Nocodazole treatment confirms no change in mitochondrial diameter and absence of mitochondrial swelling (N=200 mitochondria for each group, error bars represent ±SEM). Statistical significance calculated by Kruskal-Wallis ANOVA. Scale bar represents 1 µm in all panels. n.s. indicated p≥0.05.

Appendix N – Estimating the energetic contribution of membrane tension

The contribution of stretching energy was found from two independent estimates described below:

Estimating the stretching energy

Based on mitochondrial geometry and measured membrane tension values, we calculate the stretching energy. Membrane tension can cause small changes in the surface area of the mitochondrial membrane, adding stretching energy to the elastic energy of the membrane. We perform a calculation of the stretching energy based on the measured membrane tension values from iSIM data and

mitochondrial tubules ($\sim 4.10^{-6}$ N/m). Stretching energy E_τ due to membrane tension τ and change in surface area $\varDelta A$, can be estimated as:

$$E_\tau = \tau \Delta A$$

By modelling a mitochondrion as a cylinder with diameter 1 µm and length 5 µm, and assuming a 0.3% stretch factor[149,164], we estimated $\varDelta A \cong 0.05$ µm². Combining this estimate with the membrane tension estimate ($\sim 4.10^{-6}$ N/m), we obtain that the average energy contribution is $\sim 50\ k_B T$.

Estimate based on loss of tension

When tension is applied to a membrane, it causes a change in area resulting in a stretching energy E_τ. Since stretching energy E_τ scales linearly with membrane tension τ, we have:

$$E_\tau \propto \tau \Rightarrow E_\tau = \alpha \tau \Rightarrow \alpha = \frac{dE_\tau}{d\tau} \cong \frac{\Delta E_\tau}{\Delta \tau}$$

We can therefore approximate the constant of proportionality α by looking at the change in stretching energy produced by a change in membrane tension. Specifically, we compared the difference in mean bending energies and mean membrane tensions between control and nocodazole treated cells. What differentiated these experiments was the loss of mitochondrial membrane tension as described in the main text. Taken as a consequence of the loss of tension, the difference in bending energies between these two conditions should directly reflect the difference in stretching energies. We estimated the energy due to membrane tension E_τ as:

$$E_\tau = \left|\frac{\Delta E}{\Delta \tau}\right| \tau_{ctrl} = \left|\frac{E_{noco} - E_{ctrl}}{\tau_{noco} - \tau_{ctrl}}\right| \tau_{ctrl}$$

Where E_{noco}, E_{ctrl} are bending energies for nocodazole-treated and control cells respectively, τ_{noco}, τ_{ctrl} the membrane tensions for nocodazole-treated and control cells respectively. This gives a value of E_τ of $40\ k_B T$, consistent with the estimate above.

Appendix O – Model considering double membrane

From our model, the fission probability is determined by two factors: the distance from the energy barrier set by the bending energy and the size of the available fluctuations arising from membrane tension. Let us first consider each factor separately.

Mitochondria are organelles enveloped by inner and outer membranes. If we consider the energetic implications of this architecture, the constrained geometry of the inner mitochondrial membrane implies it should always have the higher bending energies at the constriction site, given the strictly smaller tube radius and therefore higher tube curvature. By assuming a constant distance d between the two mitochondrial membranes ($d \approx 22$ nm)[231], we can relate the local principal curvatures of the outer mitochondrial membrane to the inner as follows (i denotes the inner mitochondrial membrane and o the outer mitochondrial membrane):

$$R_{e,i} = R_{e,t} + d$$
$$R_{t,i} = R_{t,o} - d$$

Where R_e and R_t are the envelope and tube radii of curvature respectively. This is supported by the observation from electron microscopy that cristae are excluded from constriction site[150]. From this we can compute a readout for the bending energy density at a single point along the membrane (neglecting the bending rigidity κ):

$$\epsilon_b = \left(\frac{1}{R_e} + \frac{1}{R_t} \right)^2$$

The consequence is that for most geometries observed from our data, the inner mitochondrial membrane will intrinsically have a higher bending energy and will therefore be closer to the energy barrier to fission (smaller residual energy ΔE). By comparing the bending energies of the two membranes, we can see that on average the inner membrane will have almost a two-fold higher bending energy, and be closer to the energy barrier to fission.

What effect would differences in membrane tension fluctuations have on the fission probability of the inner and outer membranes? Any membrane tension-inducing force arising from the surroundings acting on the mitochondria would be exerted through the outer mitochondrial membrane. We expect that coupling, which could arise from proteins spanning the two membranes such as Tim23[232], would transduce a part of the force to the inner membrane.
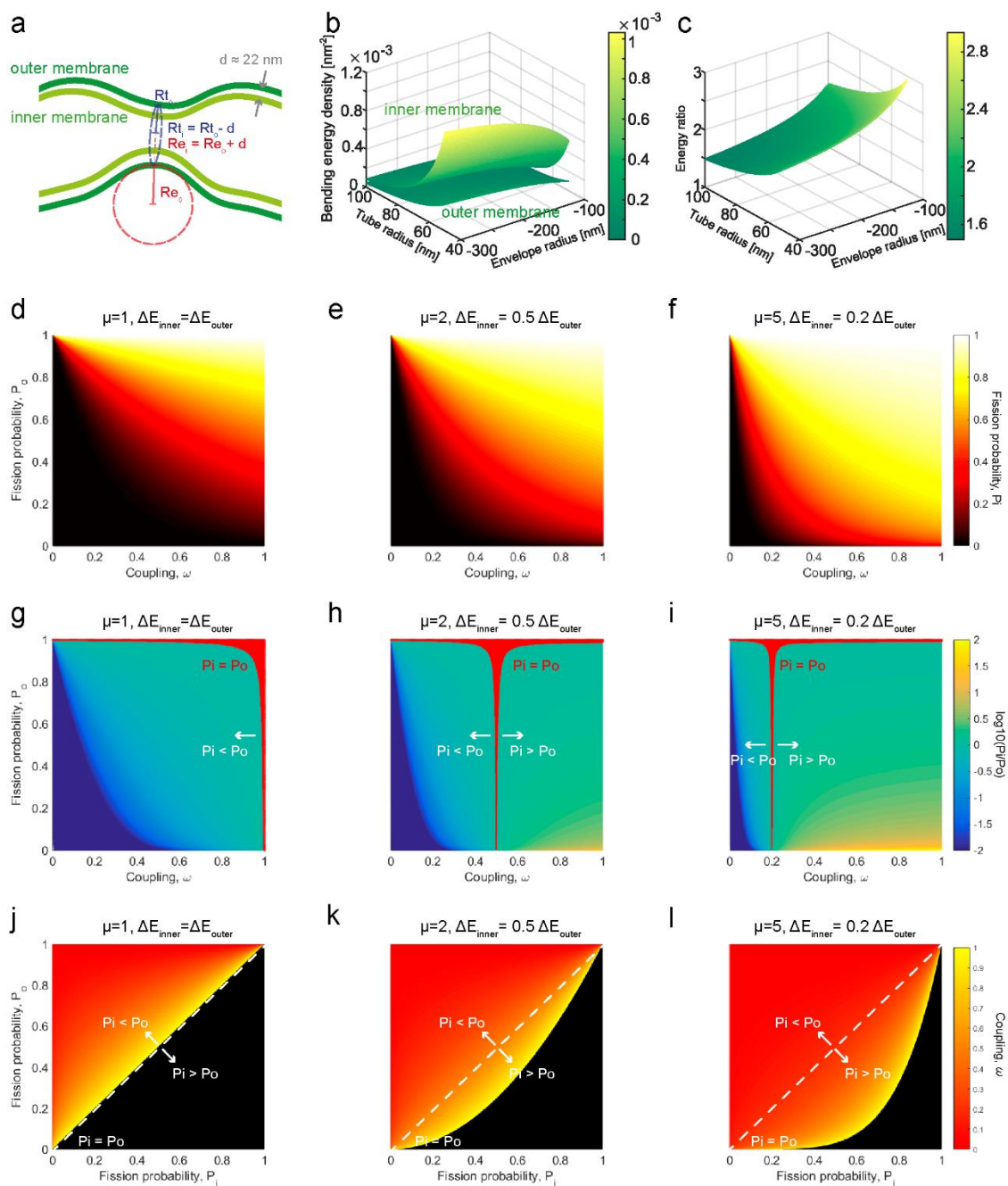
Figure 46 - Model for inner and outer mitochondrial membranes.
(a) Schematic representation showing the geometries of the outer and inner mitochondrial membranes, as a function of the local tube radius (Rt,o), envelope radius (Re,o) of the outer membrane and distance d between the two membranes. (b) 3D surface plot showing the bending energy densities for the inner and outer mitochondrial membranes, as a function of the outer membrane radii of curvature. (c) 3D surface plot showing the ratio between the bending energies of the inner to outer mitochondrial membranes, as a function of the outer membrane radii of curvature. (d-f) Fission probability for the inner mitochondrial membrane (Pi, colormap) as a function of the fission probability for the outer mitochondrial membrane (Po) and the degree of coupling ω between the two. The inner membrane is considered (d) at the same distance (μ=1), (e) twice closer (μ=2) and (f) five times closer (μ=5) to the energy barrier than the outer membrane. (g-i) Log of the ratio of probabilities of fission for the inner membrane to outer mitochondrial membrane (log(Pi/Po), colormap) as function of the fission probability for the outer mitochondrial membrane and degree of coupling ω. The inner membrane is considered (g) at the same distance (μ=1), (h) twice closer (μ=2) and (i) five times closer (μ=5) to the energy barrier than the outer membrane. Red marks the region where the inner and outer mitochondrial membranes have similar probabilities of fission (within 0.5%). (j-l) Optimal coupling values (ω, colormap), as a function of the inner and outer membrane fission

The probability of fission P is related to the residual energy (distance to the energy barrier) ΔE, and the inverse of the fission time t_f by:

$$P \propto \frac{1}{t_f} \propto \exp\left(-\frac{\Delta E}{\lambda}\right)$$

Where λ reflects the magnitude of the fluctuations. We introduce a coupling variable $\omega \in [0,1]$ such that $\lambda_i = \omega\lambda_o$ where λ_i reflects the fluctuations transduced to the inner membrane from the outer membrane (λ_o). In this case, we can express the probabilities as:

$$P_o \propto \frac{1}{t_{f,o}} \propto \exp\left(-\frac{\Delta E}{\lambda_o}\right)$$

$$P_i \propto \frac{1}{t_{f,i}} \propto \exp\left(-\frac{\Delta E}{\lambda_i}\right) = \exp\left(-\frac{\Delta E}{\omega\lambda_o}\right)$$

We can then express P_i as a function of P_o and ω, where the constant of proportionality is 1:

$$P_i = P_o^{\frac{1}{\omega}}$$

In this case, unless the coupling is perfect ($\omega = 1$), the inner mitochondrial membrane will always be less likely to undergo fission than the outer. The inner mitochondrial membrane would therefore need to achieve higher energies to overcome the energy barrier, given the lower scale of available fluctuation energies.

We wondered whether the higher bending energy of the inner membrane could compensate for the imperfect force transduction, so let us now consider the two factors together. We can compute again the probability of fission for the two mitochondrial membranes:

$$P_o \propto \frac{1}{t_{f,o}} \propto \exp\left(-\frac{\Delta E}{\lambda_o}\right)$$

$$P_i \propto \frac{1}{t_{f,i}} \propto \exp\left(-\frac{\Delta E}{\lambda_i}\right) = \exp\left(-\frac{\Delta E}{\omega\mu\lambda_o}\right)$$

Where μ represents the ratio of residual energies. This implies that the inner mitochondrial membrane can still have a higher probability of fission, even if the coupling to the outer membrane is not perfect and therefore will be more likely to undergo fission. For factors of $\mu > 1$, there will exist cases of imperfect coupling ($\omega < 1$), which will still give the inner and outer membranes equal fission probabilities. Furthermore, for a fixed ratio of bending energies μ we can identify 3 regimes: (I) $P_i < P_o$ below a critical coupling ($\omega < \omega_c$), (II) $P_i > P_o$ for ($\omega > \omega_c$), and (III) $P_i = P_o$ at critical coupling ($\omega = \omega_c$).

The necessary coupling for a combination of P_i, P_o, μ can be found as:

$$\omega = \frac{\log P_o}{\mu \log P_i}$$

Therefore, as the inner membrane gets relatively closer to the energy barrier (increasing μ), the required coupling will decrease. Critical coupling, ω_c, corresponding to $P_i = P_o$ is given by:

$$\omega_c = \frac{1}{\mu}$$

Therefore, even in cases where the coupling is not perfect ($\omega < 1$), our model predicts that the inner membrane can still undergo fission first. Furthermore, in reality the ratio of bending energies μ is

expected to be even higher than 2, suggesting that the regime where the inner membrane undergoes fission first can exist at even much lower degrees of coupling.

Appendix P – Implemented computation strategies

Relative Drp1 spot intensity

Simple feature-based detection algorithms might rely on a single metric extracted from the image such as the maximal intensity of a molecular marker. The choice of metric depends on the specific event or feature of interest. In the case of mitochondrial division, the presence and accumulation of Drp1 at the constriction site strongly correlates with an active constriction. Therefore, as a simple strategy with a low computation cost, measuring the intensities of Drp1 spots within an image can be used as a readout for the presence of mitochondrial constriction sites. Comparing the intensity of the brightest spot to other non-productive Drp1 spots[129], should suggest an event is more likely to divide. Therefore, a simple strategy would rely on:

1. Localizing Drp1: N number of Drp1 spots within the FOV
2. Measuring spot intensities: $I_n, n \in [1, N]$
3. Comparing the intensity of the brightest spot to the mean intensity: $\dfrac{\max\limits_{n \in [1,N]} I_n}{\sum_{n=1}^{N} \frac{I_n}{N}}$

The final value could then be used as a direct readout of the interest factor and use it to compare and prioritize different FOV, or adapt the temporal resolution proportionally within a FOV.

Hessian eigenvalue filter

To detect constriction sites within an image, we consider the underlying signatures that mark potential sites of interest. Constriction sites usually correspond to a narrowing of the mitochondrial structure and a decreased local signal intensity. Overall, these features would appear as a local saddle point when translated to the intensity scaled pixel values. Given an image with intensity values $I(x, y)$, we therefore compute the Hessian matrix at each pixel value:

$$H(x,y) = \begin{pmatrix} \dfrac{\partial^2 I}{\partial x^2} & \dfrac{\partial^2 I}{\partial x \partial y} \\ \dfrac{\partial^2 I}{\partial x \partial y} & \dfrac{\partial^2 I}{\partial y^2} \end{pmatrix}$$

After diagonalizing the matrix, the extracted eigenvalues λ_1, λ_2 are proportional to the principal curvatures found in the original image. Since a saddle point has principal curvatures of opposite signs, the product of the eigen values $\lambda_1 \cdot \lambda_2$ will be negative, while all maxima and minima will appear as positive. Therefore, computing the product of the extracted eigenvalues and identifying regions where this product is negative is a scale-invariant, position and orientation independent way of localizing saddle points within an image of mitochondria.

However, mitochondria undergo other events that have similar underlying signatures of a saddle point, such as fusion intermediates, transient mitochondrial contacts or mitochondria going in and out of the focal plane. Therefore, using a second channel with a Drp1 marker reduces the change of detecting false positives and facilitates distinguishing true Drp1 mediated constriction sites. Overall, the final detection scheme combines both the mitochondrial and Drp1 channels to identify constriction sites as events of interest, so that they will appear as increasingly negative regions in the output. This readout

can then be converted to a probability of event by rescaling the readout between values corresponding to 0% change of a constriction site and 100% chance of a constriction site.
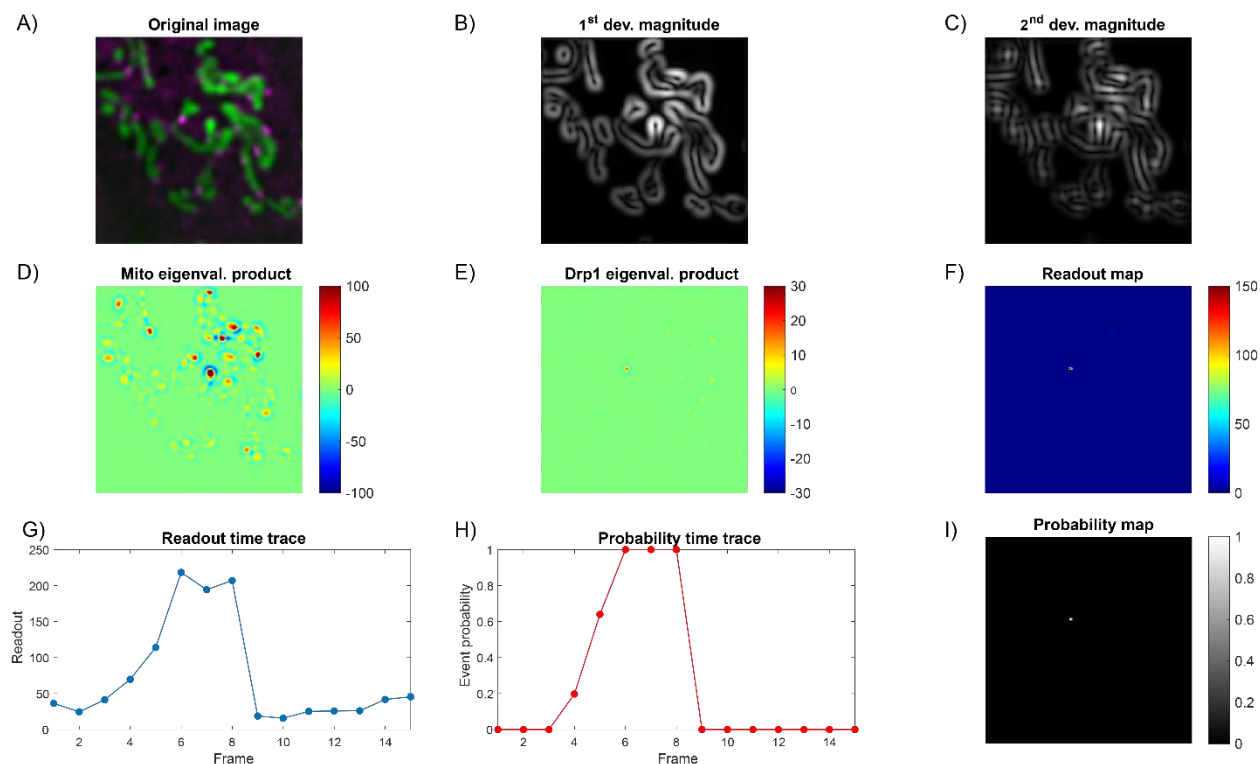

Figure 47 - Image-based probability of event computation.
A) Original dual color image of mitochondria and Drp1. B) Normalized intensity of the first derivative. C) Normalized intensity of the 2nd derivative. D) Product of the Hessian matrix eigenvalues (proportional to the principal curvatures) for the mitochondrial channel. E) Product of the Hessian matrix eigenvalues for the Drp1 channel. F) Readout computed from the A-E images. G) Temporal evolution of the readout. H) Temporal evolution of the event probability, computed from the readout. I) Probability map computed from the readout map.

The advantage of this approach is that unlike the feature-based simple algorithm, we are provided with a spatial map of the output and therefore have information about the spatial distribution of events of interest. While this information is not necessary for global actuation responses such as adapting the temporal resolution or picking FOVs, it could be combined with local actuation responses such as adaptive illumination or similar spatially varying imaging parameters. Furthermore, it could be used to facilitate annotating a larger dataset for machine learning applications. Furthermore, other quantities such as density of events n_E and the most likely event of interest P_{max} can be computed from the probability map $P(x, y)$.

Appendix R – SASS and SATS simulation platforms

To test different strategies and identify the optimal one in a controlled environment, we designed a simulation platform to imitate the readout from the computation step and simulate different response strategies of the microscope. The simulation platform generates temporal traces of the feature of interest (for example maximal event probability P_{max}, local event density n_E or specific features such as constriction diameter), independently across a fixed number of FOVs (represented as independently generated traces).

Assuming the output of the computation step will reflect P_{max} or n_E in the case of SATS and SASS respectively, the steps used to generate the temporal traces are:

1. Generate random number of events N: modelled as a Poisson process with mean μ
2. For each event out of N:
   - Generate peak location of event: drawn from uniform distribution corresponding to the observation time
   - Generate duration (width) of event modelled as a Gaussian profile: drawn from as a Gaussian distribution with mean μ and variance σ.
   - Generate temporal trace: create all timepoints within the observation time
3. Combine all temporal traces of all N individual events
   - SASS: sum individual temporal traces (analogous to n_E)
   - SATS: max-pool individual temporal traces (analogous to P_{max})

SASS simulation platform

In the case of SASS, the overall temporal trace within a single FOV is generated by summing together all the individual event traces from events within that FOV. This means that having more ongoing events of interest would be considered more informative than fewer events.

Once the traces are generated, each strategy is allowed to run on the generated time traces. The adaptive strategies at each point make a decision whether to stay at the current FOV or move to another one, and how the choice of the next FOV is made. Briefly, the SASS strategy is implemented to choose the FOV by maximizing the observed density of events across all FOVs and executing stage translation. To identify the optimal strategy for maximizing the information throughput over multiple FOVs, the following strategies were compared using the simulation platform:

- **Imaging a single FOV**: this represents the standard non-adaptive approach where the entire acquisition is performed on a single FOV
  - **Move/stay**: always stays at the same FOV
  - **Choice of FOV**: not applicable
- **Iterative method**: the FOV iterates between fixed locations in the same order while at each FOV the strategy decides whether to lock on that FOV or keep moving based on the output of the computation step
  - **Move/stay**: set by whether the output of the computation step is above a threshold value, in which case the strategy locks on that FOV. If the value is below the threshold value, the strategy moves to another FOV
  - **Choice of FOV**: the FOVs are generated as an ordered list, and the strategy iterates through the list
- **Multi-armed bandit method**:
  - **Move/stay**: set by whether the output of the computation step is above a threshold value, in which case the strategy locks on that FOV. If the value is below the threshold value, the strategy moves to another FOV
  - **Choice of FOV**: takes into account the travel cost and the previous history of different FOVs using the multi-armed bandit algorithm
- **Omniscient method**: the acquisition occurs where the most likely event is taking place. This represents the maximum theoretical performance, but is impossible to achieve experimentally since it requires a priori knowledge of where and when events will take place.
  - **Move/stay**: not applicable
  - **Choice of FOV**: not applicable

The reward system uses the output of the computation step to rate the different strategies, by adding the readout value (for simplicity reasons representing the density of events) at the specific FOV and timepoint the strategy decides on during the acquisition.

SATS simulation platform

In the case of SATS, the overall temporal trace is generated by taking the maximal value of all the individual traces, since if there are multiple ongoing events of interest, the temporal resolution should match that of the most interesting event. These temporal traces are then used as the ground truth, which can be combined with different noise levels and sampling strategies to characterize and evaluate their performance.

The temporal traces representing the variable x received as input from the computation step. The simulation first generates ground truth (GT) profile of x and its GT derivatives dx/dt and d^2x/dt^2. The ground truth x profile is then subsampled using the different traditional or adaptive strategies and evaluated based on the performance metrics.

The SATS simulation platform uses similar temporal traces as the SASS simulation platform to generate temporal traces representing the variable x received as input from the computation step. The simulation first generates ground truth (GT) profile of x and its GT derivatives dx/dt and d^2x/dt^2. The ground truth x profile is then subsampled using the different traditional or adaptive strategies and evaluated based on the performance metrics.
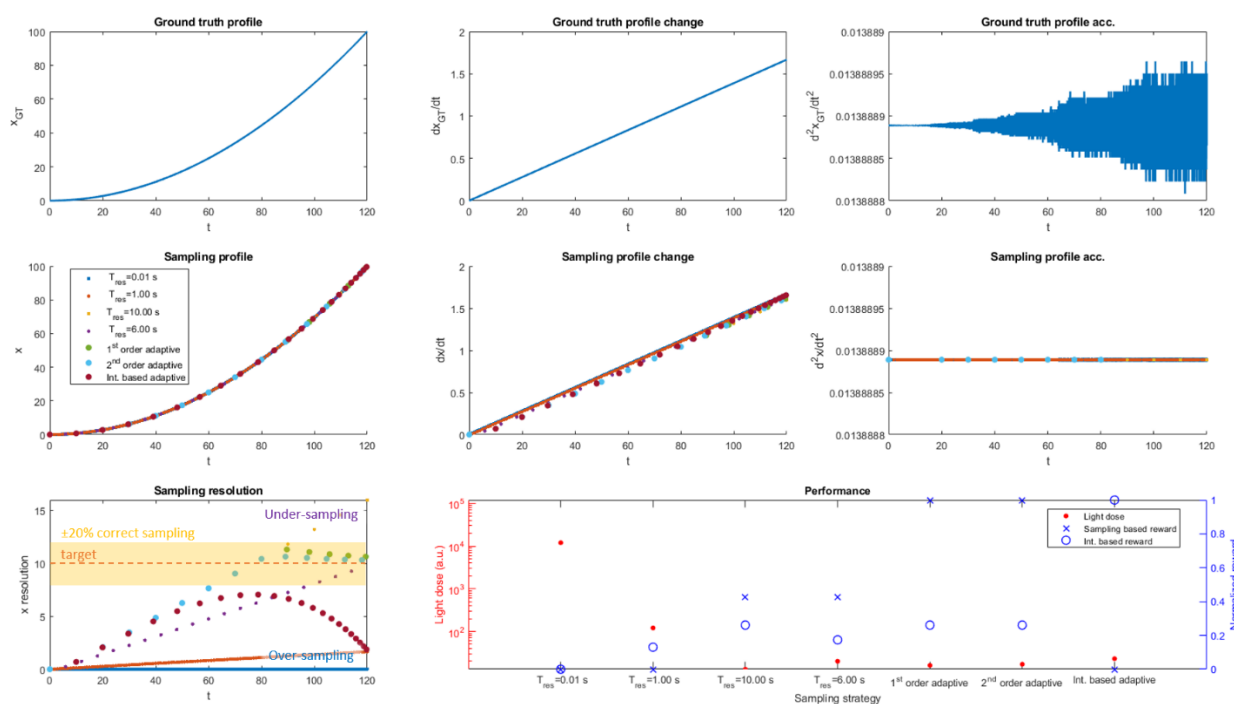
Figure 48: SATS simulation platform.
Ground truth profiles

To quantitatively compare the different strategies, all strategies are evaluated based on three performance metrics:

- **Sampling-based reward**: rewards a strategy for updating the temporal resolution so that a sampling resolution Δx of the feature of interest x is maintained within ±20%
- **Intensity-based reward**: rewards a strategy for scaling the temporal resolution proportionally to the readout variable x

- **Light dose penalty**: represents the effective delivered light dose computed as the total number of timepoints acquired by the strategy

Appendix S – Sampling requirements for different derivative terms

The derivative terms predict the evolution of the temporal traces and can be used to anticipate changes before they occur. Given the calculated derivative terms at the current timepoint $t = a$, the evolution of the parameter $x(t)$ can be approximated by a Taylor series:

$$x(t) = \sum_{n=0}^{\infty} \frac{x^n(t)}{n!} (x - a)^n = x(a) + \frac{x'(a)}{1!} (t - a) + \frac{x''(a)}{2!} (t - a)^2 + \cdots$$

For the sake of simplicity, the derivation will be done in the continuous case, but the analysis is valid in the discreet case, represented in its discreet form by Newton series using the backward difference $\nabla [x](a)$ (since only the previous timepoints are known):

$$x(t) = \sum_{k=0}^{\infty} \frac{\nabla^k[x](a)}{k!} (t - a)_k$$

Therefore, if we wish to predict the evolution of x at a time $t = a + \Delta t$, the expression (keeping the first two derivative orders) can be written as:

$$x(a + \Delta t) = x(a) + \frac{x'(a)}{1!} \Delta t + \frac{x''(a)}{2!} \Delta t^2$$

However, if we wish to maintain a resolution Δx at which we sample the readout x, then by imposing $|x(a + \Delta t) - x(a)| = \Delta x$ we get:

$$\Delta x = \frac{x'(a)}{1!} \Delta t + \frac{x''(a)}{2!} \Delta t^2$$

This gives a quadratic equation with two possible solutions for the interval Δt necessary to maintain the correct sampling Δx.

$$\Delta t = \frac{-x'(a) \pm \sqrt{x'(a)^2 - \frac{x''(a)}{2}(-\Delta x)}}{x''(a)}$$

These solutions correspond to the past and future timepoints that maintain a sampling Δx. Therefore by the solution such that $\Delta t > 0$, provides the time interval to sample at to ensure the correct sampling Δx.

Appendix T – U-net performance evaluation

The network performance was compared using the mean absolute error as the accuracy metric, and a custom loss function.
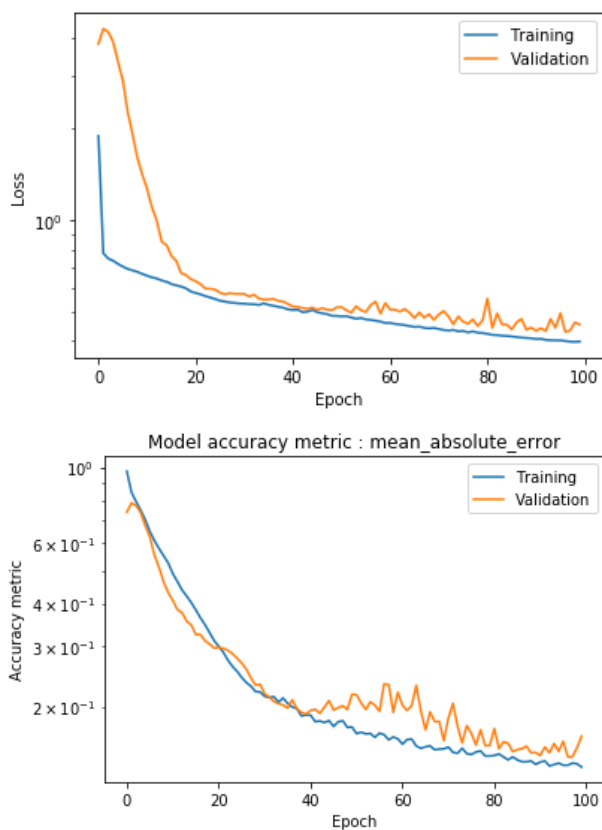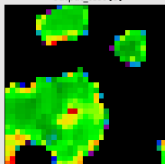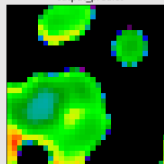
Figure 49 - U-net performance.
Left: Custom loss function evolution. Right: custom accuracy metric evolution.

The aim of the custom loss function was to prevent the network from focusing on just segmenting mitochondrial shapes and associating a constant average lifetime across the entire structure, but with the aim of focusing on smaller variations in lifetime within the structure.

```
def custom_loss3():
  def loss(y_true,y_pred):
      return K.mean((K.abs((y_pred[:,:,:,0]-y_true[:,:,:,0]))*
K.abs(1+K.abs(y_true[:,:,:,0]-K.sum(y_true[:,:,:,0]*y_true[:,:,:,2])
/K.sum(y_true[:,:,:,2]))))), axis=-1)
  return loss
```

where `y_true` represents the ground truth, `y_pred` the predicted output and channels 0 and 2 represent the intensity values used to scale the fluorescence lifetime accordingly.

Parameters	Train MAE	Validation MAE	Test MAE	Examples (test set)		
				Input	"Ground truth"	Prediction
Loss function 3 Median filter 1	0.1228	0.1254	0.1271			

117

Conv. wind. size 5				
Loss function 3 Median filter 2 Conv. wind. size 5	0.1113	0.1202	0.1198	
Loss function 3 Median filter 3 Conv. wind. size 7	0.0958	0.1116	0.1142	

Table 8 - Representative results from the U-net trained using different network parameters and loss functions.

References

1. Hell Stefan, W. & Jan, W. Breaking the diffraction resolution limit by stimulated emission: stimulated-emission-depletion fluorescence microscopy. *Opt. Lett* **19**, 780–2 (1994).

2. Betzig, E. *et al.* Imaging Intracellular Fluorescent Proteins at Nanometer Resolution. *Science (80-.).* **313**, 1642–1645 (2006).

3. Schermelleh, L. *et al.* Super-resolution microscopy demystified. *Nat. Cell Biol.* **21**, 72–84 (2019).

4. Sigal, Y. M., Zhou, R. & Zhuang, X. Visualizing and discovering cellular structures with super-resolution microscopy. *Science (80-.).* **361**, 880–887 (2018).

5. McBride, H. M., Neuspiel, M. & Wasiak, S. Mitochondria: More Than Just a Powerhouse. *Current Biology* **16**, R551–R560 (2006).

6. Gönczy, P. Towards a molecular architecture of centriole assembly. *Nature Reviews Molecular Cell Biology* **13**, 425–435 (2012).

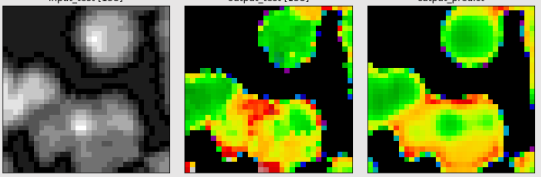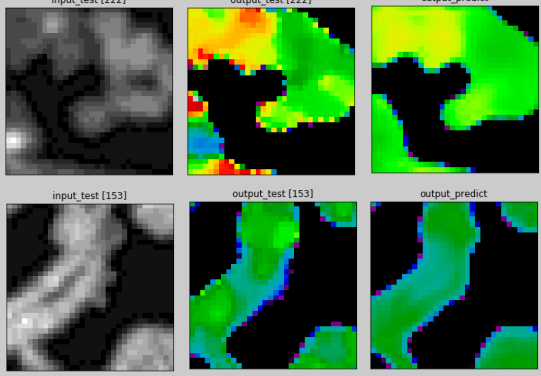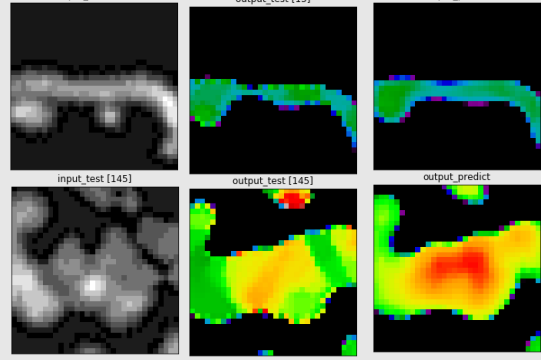7. Abbe, E. Beitrage zur Theorie des Mikroskops und der mikroskopischen Wahrnehmung. *Arch. Mikr. Anat.* **9**, 413–468 (1873).

8. Thompson, R. E., Larson, D. R. & Webb, W. W. Precise nanometer localization analysis for individual fluorescent probes. *Biophys. J.* **82**, 2775–2783 (2002).

9. Rust, M. J., Bates, M. & Zhuang, X. Sub-diffraction-limit imaging by stochastic optical reconstruction microscopy (STORM). *Nat. Methods* **3**, 793–796 (2006).

10. Sharonov, A. & Hochstrasser, R. M. Wide-field subdiffraction imaging by accumulated binding of diffusing probes. *Proc. Natl. Acad. Sci. U. S. A.* **103**, 18911–18916 (2006).

11. Jungmann, R. *et al.* Multiplexed 3D cellular super-resolution imaging with DNA-PAINT and Exchange-PAINT. *Nat. Methods* **11**, 313–318 (2014).

12. Vaughan, J. C., Jia, S. & Zhuang, X. Ultrabright photoactivatable fluorophores created by reductive caging. *Nat. Methods* (2012). doi:10.1038/nmeth.2214

13. Carlini, L., Benke, A., Reymond, L., Lukinavičius, G. & Manley, S. Reduced dyes enhance single-molecule localization density for live superresolution imaging. *ChemPhysChem* **15**, 750–755 (2014).

14. Balzarotti, F. *et al.* Nanometer resolution imaging and tracking of fluorescent molecules with minimal photon fluxes. *Science (80-.).* 1–72 (2016). doi:10.1126/science.aak9913

15. Reymond, L. *et al.* SIMPLE: Structured illumination based point localization estimator with enhanced precision. *Opt. Express* **27**, 24578 (2019).

16. Gu, L. *et al.* Molecular resolution imaging by repetitive optical selective exposure. *Nat. Methods* **16**, (2019).

17. Cnossen, J. *et al.* Localization microscopy at doubled precision with patterned illumination. *Nat. Methods* **17**, 59–63 (2020).

18. Gustafsson, M. G. L. Surpassing the lateral resolution limit by a factor of two using structured illumination microscopy. *J. Microsc.* **198**, 82–87 (2000).

19. Gustafsson, M. G. L. *et al.* Three-Dimensional Resolution Doubling in Wide-Field Fluorescence Microscopy by Structured Illumination. *Biophys. J.* **94**, 4957–4970 (2008).

20. Gustafsson, M. G. L. Nonlinear structured-illumination microscopy: Wide-field fluorescence imaging with theoretically unlimited resolution. *Proc. Natl. Acad. Sci.* **102**, 13081–13086 (2005).

21. Rego, E. H. *et al.* Nonlinear structured-illumination microscopy with a photoswitchable protein reveals cellular structures at 50-nm resolution. *Proc. Natl. Acad. Sci.* (2012). doi:10.1073/pnas.1107547108

22. Sheppard, C. J. L. Super Resolution in Confocal Imaging. *Optik (Stuttg).* **80**, 53–54 (1988).

23. Müller, C. B. & Enderlein, J. Image scanning microscopy. *Phys. Rev. Lett.* **104**, (2010).

24. Huff, J. The Airyscan detector from ZEISS: confocal imaging with improved signal-to-noise ratio and super-resolution. *Nat. Methods* **12**, i–ii (2015).

25. York, A. G. *et al.* Resolution doubling in live, multicellular organisms via multifocal structured illumination microscopy. *Nat. Methods* **9**, 749–754 (2012).

26. York, A. G. *et al.* Instant super-resolution imaging in live cells and embryos via analog image processing. *Nat. Methods*

References

10, 1122–1126 (2013).

27. Fiolka, R., Shao, L., Hesper Rego, E., Davidson, M. W. & Gustafsson, M. G. L. Time-lapse two-color 3D imaging of live cells with doubled resolution using structured illumination. *Proc. Natl. Acad. Sci. U. S. A.* **109**, 5311–5315 (2012).

28. Curd, A. *et al.* Construction of an instant structured illumination microscope. *Methods* **88**, 37–47 (2015).

29. Douglass, K. M., Sieben, C., Archetti, A., Lambert, A. & Manley, S. Super-resolution imaging of multiple cells by optimized flat-field epi-illumination. *Nat. Photonics* **10**, 705–708 (2016).

30. Görlitz, F. *et al.* easySLM-STED: Stimulated emission depletion microscopy with aberration correction, extended field of view and multiple beam scanning. *J. Biophotonics* **11**, 1–11 (2018).

31. De Luca, G. M. R. *et al.* Re-scan confocal microscopy: scanning twice for better resolution. *Biomed. Opt. Express* **4**, 2644 (2013).

32. Roth, S., Sheppard, C. J., Wicker, K. & Heintzmann, R. Optical photon reassignment microscopy (OPRA). *Opt. Nanoscopy* **2**, 5 (2013).

33. Chen, F., Tillberg, P. W. & Boyden, E. S. Expansion microscopy. *Science (80-.).* **347**, 543–548 (2015).

34. Chen, F. *et al.* Nanoscale imaging of RNA with expansion microscopy. *Nat. Methods* **13**, 679–684 (2016).

35. Gao, R. *et al.* Cortical column and whole-brain imaging with molecular contrast and nanoscale resolution. *Science (80-.).* **363**, eaau8302 (2019).

36. Tillberg, P. W. *et al.* Protein-retention expansion microscopy of cells and tissues labeled using standard fluorescent proteins and antibodies. *Nat. Biotechnol.* **34**, 987–992 (2016).

37. Zhao, Y. *et al.* Nanoscale imaging of clinical specimens using pathology-optimized expansion microscopy. *Nat. Biotechnol.* **35**, 757–764 (2017).

38. Chozinski, T. J. *et al.* Expansion microscopy with conventional antibodies and fluorescent proteins. *Nat. Methods* **13**, 485–488 (2016).

39. Murakami, T. C. *et al.* A three-dimensional single-cell-resolution whole-brain atlas using CUBIC-X expansion microscopy and tissue clearing. *Nat. Neurosci.* **21**, 625–637 (2018).

40. Truckenbrodt, S. *et al.* X10 expansion microscopy enables 25-nm resolution on conventional microscopes. *EMBO Rep.* e45836 (2018). doi:10.15252/embr.201845836

41. Ku, T. *et al.* Multiplexed and scalable super-resolution imaging of three-dimensional protein localization in size-adjustable tissues. *Nat. Biotechnol.* **34**, 973–981 (2016).

42. Gambarotto, D. *et al.* Imaging cellular ultrastructures using expansion microscopy (U-ExM). *Nat. Methods* **16**, 71–74 (2019).

43. Mahecic, D., Testa, I., Griffié, J. & Manley, S. Strategies for increasing the throughput of super-resolution microscopies. *Curr. Opin. Chem. Biol.* **51**, 84–91 (2019).

44. Huang, F. *et al.* Video-rate nanoscopy using sCMOS camera–specific single-molecule localization algorithms. *Nat. Methods* **10**, 653–658 (2013).

45. Koehler, A. Ein neues Beleuchtungsverfahren für mikrophotographische Zwecke. *Zeitschrift für wissenschaftliche Mikroskopie und für Mikroskopische Tech.* **10**, 433–440 (1893).

46. Seibert, J. A., Boone, J. M. & Lindfors, K. K. Flat-field correction technique for digital detectors. *Med. Imaging 1998 Phys. Med. Imaging* **3336**, 348 (1998).

47. Smith, K. *et al.* CIDRE: An illumination-correction method for optical microscopy. *Nat. Methods* **12**, 404–406 (2015).

48. Deschamps, J., Rowald, A. & Ries, J. Efficient homogeneous illumination and optical sectioning for quantitative single-molecule localization microscopy. *Opt. Express* **24**, 28080 (2016).

49. Khaw, I. *et al.* Flat-field illumination for quantitative fluorescence imaging. *Opt. Express* **26**, 15276 (2018).

50. Rowlands, C. J., Ströhl, F., Ramirez, P. P. V., Scherer, K. M. & Kaminski, C. F. Flat-Field Super-Resolution Localization Microscopy with a Low-Cost Refractive Beam-Shaping Element. *Sci. Rep.* **8**, 1–8 (2018).

51. Stehr, F., Stein, J., Schueder, F., Schwille, P. & Jungmann, R. Flat-top TIRF illumination boosts DNA-PAINT imaging and quantification. *Nat. Commun.* **10**, 1268 (2019).

52. Archetti, A. *et al.* Waveguide-PAINT offers an open platform for large field-of-view super-resolution imaging. *Nat. Commun.* **10**, 1267 (2019).

53. Cooper, D. J. F. Imaging distal end of multimode fiber. *United States Pat.* **1**, (2014).

54. Zhao, Z., Xin, B., Li, L. & Huang, Z.-L. High-power homogeneous illumination for super-resolution localization microscopy with large field-of-view. *Opt. Express* **25**, 13382 (2017).

120

55. Frieden, B. R. Lossless Conversion of a Plane Laser Wave to a Plane Wave of Uniform Irradiance. *Appl. Opt.* **4**, 1400 (1965).

56. Sacconi, L. *et al.* Multiphoton multifocal microscopy exploiting a diffractive optical element. *Opt. Lett.* **28**, 1918 (2003).

57. Račiukaitis, G. *et al.* Laser processing by using diffractive optical laser beam shaping technique. *J. Laser Micro Nanoeng.* **6**, 37–43 (2011).

58. Voelkel, R., Herzig, H. P., Nussbaum, P., Daendliker, R. & Hugle, W. B. Microlens array imaging system for photolithography. *Soc. Photo-Optical Instrum. Eng.* **35**, 3323–3330 (1996).

59. Zimmermann, M., Lindlein, N., Voelkel, R. & Weible, K. J. Microlens laser beam homogenizer: from theory to application. **666302**, 666302 (2007).

60. Voelkel, R. & Weible, K. J. Laser beam homogenizing: limitations and constraints. 71020J (2008). doi:10.1117/12.799400

61. Schreiber, P., Kudaev, S., Dannberg, P. & Zeitner, U. D. Homogeneous LED-illumination using microlens arrays. *Nonimaging Opt. Effic. Illum. Syst. II* **5942**, 59420K (2005).

62. Ibrahim, K. A., Mahecic, D. & Manley, S. Characterization of flat-fielding systems for quantitative microscopy. *Opt. Express* **28**, 22036–22047 (2020).

63. Mau, A., Friedl, K., Leterrier, C., Bourg, N. & Lévêque-Fort, S. Fast scanned widefield scheme provides tunable and uniform illumination for optimized SMLM on large fields of view. *bioRxiv* **2**, 2020.05.08.083774 (2020).

64. Dickey, F. M., Weichman, L. S. & Shagam, R. N. Laser beam shaping techniques. 338–348 (2004). doi:10.1117/12.407361

65. Blattner, P. & Voelkel, R. Homogenous monochromatic irradiance fields generated by microlens arrays. 10–11 (2008).

66. Coelho, S. *et al.* Multifocal multiphoton microscopy with adaptive optical correction. *Multiphot. Microsc. Biomed. Sci. XIII* **8588**, 858817 (2013).

67. Nielsen, T., Fricke, M., Hellweg, D. & Andresen, P. High efficiency beam splitter for multifocal multiphoton microscopy. *J. Microsc.* **201**, 368–376 (2001).

68. Bingen, P., Reuss, M., Engelhardt, J. & Hell, S. W. Parallelized STED fluorescence nanoscopy. *Opt. Express* **19**, 23716 (2011).

69. Yang, B., Przybilla, F., Mestre, M., Trebbia, J.-B. & Lounis, B. Large parallelization of STED nanoscopy using optical lattices. *Opt. Express* **22**, 5581 (2014).

70. Bergermann, F., Alber, L., Sahl, S. J., Engelhardt, J. & Hell, S. W. 2000-fold parallelized dual-color STED fluorescence nanoscopy. *Opt. Express* **23**, 211 (2015).

71. Chmyrov, A. *et al.* Nanoscopy with more than 100,000 'doughnuts'. *Nat. Methods* **10**, 737–740 (2013).

72. Masullo, L. A. *et al.* Enhanced photon collection enables four dimensional fluorescence nanoscopy of living systems. *Nat. Commun.* **9**, (2018).

73. Streibl, N. Beam shaping with optical array generators. *J. Mod. Opt.* **36**, 1559–1573 (1989).

74. Flottmann, B. *et al.* Correlative light microscopy for high-content screening. *Biotechniques* **55**, 243–252 (2013).

75. Gunkel, M., Flottmann, B., Heilemann, M., Reymann, J. & Erfle, H. Integrated and correlative high-throughput and super-resolution microscopy. *Histochem. Cell Biol.* **141**, 597–603 (2014).

76. Holden, S. J. *et al.* High throughput 3D super-resolution microscopy reveals Caulobacter crescentus in vivo Z-ring organization. *Proc. Natl. Acad. Sci.* **111**, 4566–4571 (2014).

77. Beghin, A. *et al.* Localization-based super-resolution imaging meets high-content screening. *Nat. Methods* **14**, 1184–1190 (2017).

78. Almada, P. *et al.* Automating multimodal microscopy with NanoJ-Fluidics. *Nat. Commun.* **10**, 1–9 (2019).

79. Huang, F., Schwartz, S. L., Byars, J. M. & Lidke, K. A. Simultaneous multiple-emitter fitting for single molecule super-resolution imaging. *Biomed. Opt. Express* **2**, 1377 (2011).

80. Holden, S. J., Uphoff, S. & Kapanidis, A. N. DAOSTORM: an algorithm for high- density super-resolution microscopy. *Nat. Methods* **8**, 279–280 (2011).

81. Ovesný, M., Křížek, P., Borkovec, J., Švindrych, Z. & Hagen, G. M. ThunderSTORM: A comprehensive ImageJ plug-in for PALM and STORM data analysis and super-resolution imaging. *Bioinformatics* **30**, 2389–2390 (2014).

82. Marsh, R. J. *et al.* Artifact-free high-density localization microscopy analysis. *Nat. Methods* **15**, 689–692 (2018).

83. Ouyang, W., Aristov, A., Lelek, M., Hao, X. & Zimmer, C. Deep learning massively accelerates super-resolution localization microscopy. *Nat. Biotechnol.* **36**, 460–468 (2018).

References

84.   Huang, X. *et al.* Fast, long-term, super-resolution imaging with Hessian structured illumination microscopy. *Nat. Biotechnol.* (2018). doi:10.1038/nbt.4115

85.   Dreier, J. *et al.* Smart scanning for low-illumination and fast RESOLFT nanoscopy in vivo. *Nat. Commun.* 1–11 doi:10.1038/s41467-019-08442-4

86.   Hess, S. T., Girirajan, T. P. K. & Mason, M. D. Ultra-High Resolution Imaging by Fluorescence Photoactivation Localization Microscopy. *Biophys. J.* **91**, 4258–4272 (2006).

87.   Laissue, P. P., Alghamdi, R. A., Tomancak, P., Reynaud, E. G. & Shroff, H. Assessing phototoxicity in live fluorescence imaging. *Nature Methods* **14**, 657–661 (2017).

88.   van de Linde, S. & Sauer, M. How to switch a fluorophore: from undesired blinking to controlled photoswitching. *Chem. Soc. Rev.* (2014). doi:10.1039/C3CS60195A

89.   Scherf, N. & Huisken, J. The smart and gentle microscope. *Nat. Biotechnol.* **33**, 815–818 (2015).

90.   Weigert, M. *et al.* Content-aware image restoration: pushing the limits of fluorescence microscopy. *Nat. Methods* **15**, 1090–1097 (2018).

91.   Fang, L. *et al.* Deep Learning-Based Point-Scanning Super-Resolution Imaging. *bioRxiv* (2019).

92.   Mahecic, D. *et al.* Homogeneous multifocal excitation for high-throughput super-resolution imaging. *Nat. Methods* **17**, 726–733 (2020).

93.   Model, M. A. & Blank, J. L. Concentrated dyes as a source of two-dimensional fluorescent field for characterization of a confocal microscope. *J. Microsc.* **229**, 12–16 (2008).

94.   Lucy, L. B. An iterative technique for the rectification of observed distributions. *Astron. J.* **79**, 745 (1974).

95.   Richardson, W. H. Bayesian-Based Iterative Method of Image Restoration*. *J. Opt. Soc. Am.* **62**, 55 (1972).

96.   Xiao, X. & Voelz, D. G. Wave optics simulation approach for partial spatially coherent beams. *Opt. Express* **14**, 6986–92 (2006).

97.   Preibisch, S., Saalfeld, S. & Tomancak, P. Globally optimal stitching of tiled 3D microscopic image acquisitions. *Bioinformatics* **25**, 1463–1465 (2009).

98.   Hörl, D. *et al.* BigStitcher: reconstructing high-resolution image datasets of cleared and expanded samples. *Nat. Methods* (2019). doi:10.1038/s41592-019-0501-0

99.   Friedman, J. R. *et al.* ER tubules mark sites of mitochondrial division. *Science (80-.).* **334**, 358–362 (2011).

100.   Guichard, P., Chrétien, D., Marco, S. & Tassin, A. M. Procentriole assembly revealed by cryo-electron tomography. *EMBO J.* **29**, 1565–1572 (2010).

101.   Banterle, N. & Gönczy, P. Centriole Biogenesis: From Identifying the Characters to Understanding the Plot. *Annu. Rev. Cell Dev. Biol.* **33**, 23–49 (2017).

102.   Janke, C. & Bulinski, J. C. Post-translational regulation of the microtubule cytoskeleton: Mechanisms and functions. *Nat. Rev. Mol. Cell Biol.* **12**, 773–786 (2011).

103.   Bobinnec, Y. *et al.* Centriole disassembly in vivo and its effect on centrosome structure and function in vertebrate cells. *J. Cell Biol.* **143**, 1575–1589 (1998).

104.   Xu, Z. *et al.* Microtubules acquire resistance from mechanical breakage through intralumenal acetylation. *Science (80-.).* **356**, 328–332 (2017).

105.   Portran, D., Schaedel, L., Xu, Z., Théry, M. & Nachury, M. V. Tubulin acetylation protects long-lived microtubules against mechanical ageing. *Nat. Cell Biol.* **19**, 391–398 (2017).

106.   Eshun-Wilson, L. *et al.* Effects of α-tubulin acetylation on microtubule structure and stability. *Proc. Natl. Acad. Sci. U. S. A.* **116**, 10366–10371 (2019).

107.   Wolff, A. *et al.* Distribution of glutamylated alpha and beta-tubulin in mouse tissues using a specific monoclonal antibody, GT335. *Eur. J. Cell Biol.* **59**, 425–32 (1992).

108.   Abal, M., Keryer, G. & Bornens, M. Centrioles resist forces applied on centrosomes during G2/M transition. *Biol. Cell* **97**, 425–434 (2005).

109.   Wong, Y. L. *et al.* Reversible centriole depletion with an inhibitor of Polo-like kinase 4. *Science (80-.).* **348**, 1155–1160 (2015).

110.   Hamel, V. *et al.* Identification of Chlamydomonas Central Core Centriolar Proteins Reveals a Role for Human WDR90 in Ciliogenesis. *Curr. Biol.* **27**, 2486-2498.e6 (2017).

111.   Fortun, D. *et al.* Reconstruction from multiple particles for 3D isotropic resolution in fluorescence microscopy. *IEEE Trans. Med. Imaging* **37**, 1235–1246 (2018).

112. Sieben, C., Banterle, N., Douglass, K. M., Gönczy, P. & Manley, S. Multicolor single-particle reconstruction of protein complexes. *Nat. Methods* **15**, 777–780 (2018).

113. Campbell, M. G., Veesler, D., Cheng, A., Potter, C. S. & Carragher, B. 2.8 Å Resolution Reconstruction of the Thermoplasma Acidophilum 20 S Proteasome Using Cryo-Electron Microscopy. *Elife* **2015**, 1–22 (2015).

114. Jiang, J., Pentelute, B. L., Collier, R. J. & Hong Zhou, Z. Atomic structure of anthrax protective antigen pore elucidates toxin translocation. *Nature* **521**, 545–549 (2015).

115. Meehl, J. B., Bayless, B. A., Giddings, T. H., Pearson, C. G. & Winey, M. Tetrahymena Poc1 ensures proper intertriplet microtubule linkages to maintain basal body integrity. *Mol. Biol. Cell* **27**, 2394–2403 (2016).

116. Le Guennec, M. *et al.* A helical inner scaffold provides a structural basis for centriole cohesion. *Sci. Adv.* **6**, (2020).

117. Tanaami, T. *et al.* High-speed 1-frame/ms scanning confocal microscope with a microlens and Nipkow disks. *Appl. Opt.* **41**, 4704 (2002).

118. Mahecic, D. *et al.* Membrane bending energy and tension govern mitochondrial division. *bioRxiv* (2019). doi:https://doi.org/10.1101/255356

119. Nunnari, J. *et al.* Mitochondrial transmission during mating in Saccharomyces cerevisiae is determined by mitochondrial fusion and fission and the intramitochondrial segregation of mitochondrial DNA. *Mol. Biol. Cell* **8**, 1233–1242 (1997).

120. Youle, R. J. & van der Bliek, A. M. Mitochondrial Fission, Fusion, and Stress. *Science (80-.).* **337**, 1062–1065 (2012).

121. Tondera, D. *et al.* SLP-2 is required for stress-induced mitochondrial hyperfusion. *EMBO J.* **28**, 1589–1600 (2009).

122. Gomes, L. C., Benedetto, G. Di & Scorrano, L. During autophagy mitochondria elongate, are spared from degradation and sustain cell viability. *Nat. Cell Biol.* **13**, 589–598 (2011).

123. Rambold, A. S., Kostelecky, B., Elia, N. & Lippincott-Schwartz, J. Tubular network formation protects mitochondria from autophagosomal degradation during nutrient starvation. *Proc. Natl. Acad. Sci.* **108**, 10190–10195 (2011).

124. Mitra, K., Wunder, C., Roysam, B., Lin, G. & Lippincott-Schwartz, J. A hyperfused mitochondrial state achieved at G1-S regulates cyclin E buildup and entry into S phase. *Proc. Natl. Acad. Sci. U. S. A.* **106**, 11960–11965 (2009).

125. Twig, G. *et al.* Fission and selective fusion govern mitochondrial segregation and elimination by autophagy. *EMBO J.* **27**, 433–446 (2008).

126. Burman, J. L. *et al.* Mitochondrial fission facilitates the selective mitophagy of protein aggregates. *J Cell Biol* **216**, 3231–3247 (2017).

127. Korobova, F., Ramabhadran, V. & Higgs, H. N. An Actin-Dependent Step in Mitochondrial Fission Mediated by the ER-Associated Formin INF2. *Science (80-.).* **339**, 464–467 (2013).

128. Manor, U. *et al.* A mitochondria-anchored isoform of the actin-nucleating spire protein regulates mitochondrial division. *Elife* **4**, (2015).

129. Ji, W. K., Hatch, A. L., Merrill, R. A., Strack, S. & Higgs, H. N. Actin filaments target the oligomeric maturation of the dynamin GTPase Drp1 to mitochondrial fission sites. *Elife* **4**, (2015).

130. Palmer, C. S. *et al.* MiD49 and MiD51, new components of the mitochondrial fission machinery. *EMBO Rep.* (2011). doi:10.1038/embor.2011.54

131. Gandre-Babbe, S. & van der Bliek, A. M. The novel tail-anchored membrane protein Mff controls mitochondrial and peroxisomal fission in mammalian cells. *Mol. Biol. Cell* **19**, 2402–12 (2008).

132. Otera, H. *et al.* Mff is an essential factor for mitochondrial recruitment of Drp1 during mitochondrial fission in mammalian cells. *J. Cell Biol.* (2010). doi:10.1083/jcb.201007152

133. Mozdy, A. D., McCaffery, J. M. & Shaw, J. M. Dnm1p GTPase-mediated mitochondrial fission is a multi-step process requiring the novel integral membrane component Fis1p. *J. Cell Biol.* **151**, 367–379 (2000).

134. Labrousse, A. M., Zappaterra, M. D., Rube, D. A. & Van der Bliek, A. M. C. elegans dynamin-related protein DRP-1 controls severing of the mitochondrial outer membrane. *Mol. Cell* **4**, 815–826 (1999).

135. Smirnova, E., Griparic, L., Shurland, D.-L. & Bliek, A. M. van der. Dynamin-related Protein Drp1 Is Required for Mitochondrial Division in Mammalian Cells. *Mol. Biol. Cell* **12**, 2245–2256 (2001).

136. Ingerman, E. *et al.* Dnm1 forms spirals that are structurally tailored to fit mitochondria. *J. Cell Biol.* **170**, 1021–1027 (2005).

137. Mears, J. A. *et al.* Conformational changes in Dnm1 support a contractile mechanism for mitochondrial fission. *Nat. Struct. Mol. Biol.* **18**, 20–26 (2011).

138. Fröhlich, C. *et al.* Structural insights into oligomerization and mitochondrial remodelling of dynamin 1-like protein. *EMBO J.* **32**, 1280–1292 (2013).

139. Kalia, R. *et al.* Structural basis of mitochondrial receptor binding and constriction by DRP1. *Nature* **558**, 401–405 (2018).

References

140. Lee, J. E., Westrate, L. M., Wu, H., Page, C. & Voeltz, G. K. Multiple dynamin family members collaborate to drive mitochondrial division. *Nature* **540**, 139–143 (2016).

141. Kamerkar, S. C., Kraus, F., Sharpe, A. J., Pucadyil, T. J. & Ryan, M. T. Dynamin-related protein 1 has membrane constricting and severing abilities sufficient for mitochondrial and peroxisomal fission. *Nat. Commun.* **9**, 5239 (2018).

142. Fonseca, T. B., Sánchez-Guerrero, Á., Milosevic, I. & Raimundo, N. Mitochondrial fission requires DRP1 but not dynamins. *Nature* **570**, E34–E42 (2019).

143. Helle, S. C. J. *et al.* Mechanical force induces mitochondrial fission. *Elife* **6**, e30292 (2017).

144. Legesse-Miller, A., Massol, R. H. & Kirchhausen, T. Constriction and Dnm1p Recruitment Are Distinct Processes in Mitochondrial Fission. *Mol. Biol. Cell* **14**, 1953–1963 (2003).

145. Kozlovsky, Y. & Kozlov, M. M. Membrane Fission: Model for Intermediate Structures. *Biophys. J.* **85**, 85–96 (2003).

146. Basu, K. *et al.* Molecular mechanism of DRP1 assembly studied in vitro by cryo-electron microscopy. *PLoS One* **12**, 1–21 (2017).

147. Rosenbloom, A. B. *et al.* Optimized two-color super resolution imaging of Drp1 during mitochondrial fission with a slow-switching Dronpa variant. *Proc. Natl. Acad. Sci.* **111**, 13093–13098 (2014).

148. Shim, S.-H. *et al.* Super-resolution fluorescence imaging of organelles in live cells with photoswitchable membrane probes. *Proc. Natl. Acad. Sci.* **109**, 13978–13983 (2012).

149. Helfrich, W. Elastic Properties of Lipid Bilayers: Theory and Possible Experiments. *Zeitschrift fur Naturforsch. - Sect. C J. Biosci.* **28**, 693–703 (1973).

150. Hu, G. Bin. Whole cell cryo-electron tomography suggests mitochondria divide by budding. *Microsc. Microanal.* **20**, 1180–1187 (2014).

151. Niggemann, G., Kummrow, M. & Helfrich, W. The Bending Rigidity of Phosphatidylcholine Bilayers - Dependences on Experimental-Method, Sample Cell Sealing and Temperature. *J. Phys. II* **5**, 413–425 (1995).

152. Klecker, T., Scholz, D., Fortsch, J. & Westermann, B. The yeast cell cortical protein Num1 integrates mitochondrial dynamics into cellular architecture. *J. Cell Sci.* **126**, 2924–2930 (2013).

153. Evans, E. & Yeung, A. Hidden dynamics in rapid changes of bilayer shape. *Chem. Phys. Lipids* **73**, 39–56 (1994).

154. Derényi, I., Jülicher, F. & Prost, J. Formation and Interaction of Membrane Tubes. *Phys. Rev. Lett.* **88**, 4 (2002).

155. Huang, X. *et al.* Kissing and nanotunneling mediate intermitochondrial communication in the heart. *Proc Natl Acad Sci U S A* **110**, 2846–2851 (2013).

156. Wang, C. *et al.* Dynamic tubulation of mitochondria drives mitochondrial network formation. *Cell Res.* **25**, 1108–1120 (2015).

157. Boldogh, I. R. & Pon, L. A. Mitochondria on the move. *Trends in Cell Biology* (2007). doi:10.1016/j.tcb.2007.07.008

158. Hoebeke, J., Van Nijen, G. & De Brabander, M. Interaction of oncodazole (R 17934), a new anti-tumoral drug, with rat brain tubulin. *Biochem. Biophys. Res. Commun.* **69**, 319–324 (1976).

159. De Brabander, M. J., Van de Veire, R. M. L., Aerts, F. E. M., Borgers, M. & Janssan, P. A. J. The Effects of Methyl [5-(2-Thienylcarbonyl)-1H-benzimidazol-2-yl]carbamate, (R 17934; NSC 238159), a New Synthetic Antitumoral Drug Interfering with Microtubules, on Mammalian Cells Cultured in Vitro. *Cancer Res.* **36**, 905–916 (1976).

160. Soleimanpour, S. *et al.* Headgroup engineering in mechanosensitive membrane probes. *Chem. Commun.* **52**, 14450–14453 (2016).

161. Colom, A. *et al.* A fluorescent membrane tension probe. *Nat. Chem.* 1–22 (2018). doi:10.1038/s41557-018-0127-3

162. Goujon, A. *et al.* Mechanosensitive Fluorescent Probes to Image Membrane Tension in Mitochondria, Endoplasmic Reticulum, and Lysosomes. *J. Am. Chem. Soc.* **141**, 3380–3384 (2019).

163. Morlot, S. *et al.* Membrane shape at the edge of the dynamin helix sets location and duration of the fission reaction. *Cell* **151**, 619–629 (2012).

164. Wang, S. *et al.* Membrane Deformability and Membrane Tension of Single Isolated Mitochondria. *Cell. Mol. Bioeng.* **1**, 67–74 (2008).

165. Stepanyants, N. *et al.* Cardiolipin's propensity for phase transition and its reorganization by dynamin-related protein 1 form a basis for mitochondrial membrane fission. *Mol. Biol. Cell* **26**, 3104–3116 (2015).

166. Montessuit, S. *et al.* Membrane Remodeling Induced by the Dynamin-Related Protein Drp1 Stimulates Bax Oligomerization. *Cell* **142**, 889–901 (2010).

167. Gonzalez-Rodriguez, D. *et al.* Elastocapillary Instability in Mitochondrial Fission. *Phys. Rev. Lett.* **115**, (2015).

168. Cho, B. *et al.* Constriction of the mitochondrial inner compartment is a priming event for mitochondrial division. *Nat.*

Commun. **8**, 15754 (2017).

169. Ugarte-Uribe, B., Müller, H. M., Otsuki, M., Nickel, W. & García-Sáez, A. J. Dynamin-related protein 1 (Drp1) promotes structural intermediates of membrane division. *J. Biol. Chem.* **289**, 30645–30656 (2014).

170. Hatch, A. L., Gurel, P. S. & Higgs, H. N. Novel roles for actin in mitochondrial fission. *J. Cell Sci.* **127**, 4549–4560 (2014).

171. Braschi, E., Zunino, R. & McBride, H. M. MAPL is a new mitochondrial SUMO E3 ligase that regulates mitochondrial fission. *EMBO Rep.* **10**, 748–754 (2009).

172. Cribbs, J. T. & Strack, S. Reversible phosphorylation of Drp1 by cyclic AMP-dependent protein kinase and calcineurin regulates mitochondrial fission and cell death. *EMBO Rep.* **8**, 939–944 (2007).

173. Taguchi, N., Ishihara, N., Jofuku, A., Oka, T. & Mihara, K. Mitotic phosphorylation of dynamin-related GTPase Drp1 participates in mitochondrial fission. *J. Biol. Chem.* **282**, 11521–11529 (2007).

174. Yi, M., Weaver, D. & Hajnóczky, G. Control of mitochondrial motility and distribution by the calcium signal: A homeostatic circuit. *J. Cell Biol.* **167**, 661–672 (2004).

175. MacAskill, A. F. *et al.* Miro1 Is a Calcium Sensor for Glutamate Receptor-Dependent Localization of Mitochondria at Synapses. *Neuron* **61**, 541–555 (2009).

176. Wang, X. & Schwarz, T. L. The Mechanism of Ca2+-Dependent Regulation of Kinesin-Mediated Mitochondrial Motility. *Cell* **136**, 163–174 (2009).

177. Gould, T. J., Burke, D., Bewersdorf, J. & Booth, M. J. Adaptive optics enables 3D STED microscopy in aberrating specimens. *Opt. Express* **20**, 20998 (2012).

178. Patton, B. R. *et al.* Three-dimensional STED microscopy of aberrating tissue using dual adaptive optics. *Opt. Express* **24**, 8862 (2016).

179. Zheng, W. *et al.* Adaptive optics improves multiphoton super-resolution imaging. *Nat. Methods* **14**, (2017).

180. Pozzi, P. *et al.* High speed wavefront sensorless aberration correction in digital micromirror based confocal microscopy. *Opt. Express* **25**, 949 (2017).

181. Štefko, M., Ottino, B., Douglass, K. M. & Manley, S. Autonomous illumination control for localization microscopy. *Opt. Express* **26**, 30882 (2018).

182. Heine, J. *et al.* Adaptive-illumination STED nanoscopy. *Proc. Natl. Acad. Sci.* **114**, 9797–9802 (2017).

183. Durand, A. *et al.* A machine learning approach for online automated optimization of super-resolution optical microscopy. *Nat. Commun.* **9**, 5247 (2018).

184. Kechkar, A., Nair, D., Heilemann, M., Choquet, D. & Sibarita, J. B. Real-Time Analysis and Visualization for Single-Molecule Based Super-Resolution Microscopy. *PLoS One* **8**, (2013).

185. Hoebe, R. A. *et al.* Controlled light-exposure microscopy reduces photobleaching and phototoxicity in fluorescence live-cell imaging. *Nat. Biotechnol.* **25**, 249–253 (2007).

186. Hoebe, R. A., Van Der Voort, H. T. M., Stap, J., Van Noorden, C. J. F. & Manders, E. M. M. Quantitative determination of the reduction of phototoxicity and photobleaching by controlled light exposure microscopy. *J. Microsc.* **231**, 9–20 (2008).

187. Chakrova, N., Canton, A. S., Danelon, C., Stallinga, S. & Rieger, B. Adaptive illumination reduces photobleaching in structured illumination microscopy. *Biomed. Opt. Express* **7**, 4263 (2016).

188. Power, R. M. & Huisken, J. Adaptable, illumination patterning light sheet microscopy. *Sci. Rep.* **8**, 1–11 (2018).

189. Skerker, J. M. & Laub, M. T. Cell-cycle progression and the generation of asymmetry in Caulobacter crescentus. *Nat. Rev. Microbiol.* **2**, 325–337 (2004).

190. Lambert, A. *et al.* Constriction Rate Modulation Can Drive Cell Size Control and Homeostasis in C. crescentus. *iScience* **4**, 180–189 (2018).

191. Walker, R. A. *et al.* Dynamic instability of individual microtubules analyzed by video light microscopy: rate constants and transition frequencies. *J. Cell Biol.* **107**, 1437–1448 (1988).

192. Desai, A. & Mitchison, T. J. Microtubule Polymerization Dynamics. *Annu. Rev. Cell Dev. Biol.* **13**, 83–117 (1997).

193. Tischer, C., Hilsenstein, V., Hanson, K. & Pepperkok, R. *Adaptive fluorescence microscopy by online feedback image analysis. Methods in Cell Biology* **123**, (Elsevier Inc., 2014).

194. Liu, X., Weaver, D., Shirihai, O. & Hajnóczky, G. Mitochondrial 'kiss-and-run': interplay between mitochondrial motility and fusion-fission dynamics. *EMBO J.* **28**, 3074–3089 (2009).

195. Chamier, L. Von, Laine, R. F. & Henriques, R. Artificial Intelligence for Microscopy : What You Should Know. 1–7 (2019).

196. Bechhoefer, J. Feedback for physicists: A tutorial essay on control. *Rev. Mod. Phys.* **77**, 783–836 (2005).

References

197. Tosheva, K. L., Yuan, Y., Matos Pereira, P., Culley, S. n. & Henriques, R. Between life and death: Strategies to reduce phototoxicity in super-resolution microscopy. *J. Phys. D. Appl. Phys.* **53**, (2020).

198. Hopt, A. & Neher, E. Highly Nonlinear Photodamage in Two-Photon Fluorescence Microscopy. *Biophys. J.* **80**, 2029–2036 (2001).

199. Kilian, N. *et al.* Assessing photodamage in live-cell STED microscopy. *Nat. Methods* **15**, 755–756 (2018).

200. Scaduto, R. C. & Grotyohann, L. W. Measurement of mitochondrial membrane potential using fluorescent rhodamine derivatives. *Biophys. J.* **76**, 469–477 (1999).

201. Perry, S. W., Norman, J. P., Barbieri, J., Brown, E. B. & Gelbard, H. A. Mitochondrial membrane potential probes and the proton gradient: A practical usage guide. *Biotechniques* **50**, 98–115 (2011).

202. Sieben, C., Douglass, K. M., Guichard, P. & Manley, S. Super-resolution microscopy to decipher multi-molecular assemblies. *Curr. Opin. Struct. Biol.* **49**, 169–176 (2018).

203. Salas, D. *et al.* Angular reconstitution-based 3D reconstructions of nanomolecular structures from superresolution light-microscopy images. *Proc. Natl. Acad. Sci. U. S. A.* **114**, 9273–9278 (2017).

204. Gartenmann, L. *et al.* A combined 3D-SIM/SMLM approach allows centriole proteins to be localized with a precision of ~4–5 nm. *Curr. Biol.* **27**, R1054–R1055 (2017).

205. *Handbook of Biological Confocal Microscopy.* (Springer, Boston, MA, 2006). doi:https://doi.org/10.1007/978-0-387-45524-2

206. García-calvo, J. *et al.* Fluorescent Membrane Tension Probes for Super-Resolution Microscopy: Combining Mechanosensitive Cascade Switching with Dynamic-Covalent Ketone Chemistry. *J. Am. Chem. Soc.* (2020). doi:10.1021/jacs.0c04942

207. Tan, A. R., Cai, A. Y., Deheshi, S. & Rintoul, G. L. Elevated intracellular calcium causes distinct mitochondrial remodelling and calcineurin-dependent fission in astrocytes. *Cell Calcium* **49**, 108–114 (2011).

208. Shao, X., Li, Q., Mogilner, A., Bershadsky, A. D. & Shivashankar, G. V. Mechanical stimulation induces formin-dependent assembly of a perinuclear actin rim. *Proc. Natl. Acad. Sci. U. S. A.* **112**, E2595–E2601 (2015).

209. Ghochani, M. *et al.* Tensile forces and shape entropy explain observed crista structure in mitochondria. *Biophys. J.* **99**, 3244–3254 (2010).

210. Anesti, V. & Scorrano, L. The relationship between mitochondrial shape and function and the cytoskeleton. *Biochimica et Biophysica Acta - Bioenergetics* **1757**, 692–699 (2006).

211. Ronneberger, O., Fischer, P. & Brox, T. U-net: Convolutional networks for biomedical image segmentation. *arXiv* **9351**, 234–241 (2015).

212. van Bergeijk, P., Adrian, M., Hoogenraad, C. C. & Kapitein, L. C. Optogenetic control of organelle transport and positioning. *Nature* **518**, 111–4 (2015).

213. Klena, N. *et al.* Isolation and Fluorescence Imaging for Single-particle Reconstruction of Chlamydomonas Centrioles. *J. Vis. Exp.* (2018).

214. Chang, J.-B. B. *et al.* Iterative expansion microscopy. *Nat. Methods* **14**, 593–599 (2017).

215. Hu, Y. *et al.* Improving resolving ability of expansion microscopy by varying crosslinker concentration. *Chem. Commun.* (2020). doi:10.1039/d0cc00052c

216. Park, H. E. *et al.* Scalable and Isotropic Expansion of Tissues with Simply Tunable Expansion Ratio. *Adv. Sci.* **6**, (2019).

217. Edelstein, A. D. *et al.* Advanced methods of microscope control using µManager software. *J. Biol. Methods* **1**, 10 (2014).

218. Schindelin, J. *et al.* Fiji: An open-source platform for biological-image analysis. *Nat. Methods* **9**, 676–682 (2012).

219. Wolter, S. *et al.* RapidSTORM: Accurate, fast open-source software for localization microscopy. *Nature Methods* **9**, 1040–1041 (2012).

220. Antonio Trujillo-Ortiz. DagosPtest - File Exchange - MATLAB Central. (2015). Available at: https://ch.mathworks.com/matlabcentral/fileexchange/3954-dagosptest. (Accessed: 12th December 2017)

221. Giuseppe Cardillo. mwwtest(x1,x2) - File Exchange - MATLAB Central. (2015). Available at: https://ch.mathworks.com/matlabcentral/fileexchange/25830-mwwtest-x1-x2-. (Accessed: 12th December 2017)

222. Li, Y., Wu, Y.-L., Hoess, P., Mund, M. & Ries, J. Depth-dependent PSF calibration and aberration correction for 3D single-molecule localization. *Biomed. Opt. Express* **10**, 2708 (2019).

223. Arganda-Carreras, I., Cardona, A., Kaynig, V. & Schindelin, J. Trainable Weka Segmentation: A Machine Learning Tool for Microscopy Image Segmentation. *Bioinformatics* (2017). doi:10.1093/bioinformatics/btx180

224. Chan, T. F. & Vese, L. A. Active contours without edges. *IEEE Trans. Image Process.* **10**, 266–277 (2001).

225. Adachi, Y. *et al.* Coincident Phosphatidic Acid Interaction Restrains Drp1 in Mitochondrial Division. *Mol. Cell* **63**, 1034–1043 (2016).

226. NS. Curve intersections - File Exchange - MATLAB Central. (2010). Available at: https://ch.mathworks.com/matlabcentral/fileexchange/22441-curve-intersections?focused=5165138&tab=function. (Accessed: 12th December 2017)

227. Dirk-Jan Kroon. 2D Line Curvature and Normals - File Exchange - MATLAB Central. (2011). Available at: https://ch.mathworks.com/matlabcentral/fileexchange/32696-2d-line-curvature-and-normals. (Accessed: 12th December 2017)

228. Lafaurie-Janvore, J. *et al.* ESCRT-III Assembly and Cytokinetic Abscission Are Induced by Tension Release in the Intercellular Bridge. *Science (80-.).* **339**, 1625–1629 (2013).

229. Alharbi, K. A. Image fusion superresolution in structured illumination microscopy. *Calif. State Univ. Thesis* (2013).

230. James Rooney. errorbarxy - File Exchange - MATLAB Central. (2003). Available at: https://ch.mathworks.com/matlabcentral/fileexchange/4065-errorbarxy. (Accessed: 12th December 2017)

231. Perkins, G. *et al.* Electron tomography of neuronal mitochondria: Three-dimensional structure and organization of cristae and membrane contacts. *J. Struct. Biol.* **119**, 260–272 (1997).

232. Donzeau, M. *et al.* Tim23 links the inner and outer mitochondrial membranes. *Cell* **101**, 401–412 (2000).

Curriculum vitae

Dora Mahecic

Doctoral student/Doctoral assistant
Laboratory of Experimental Biophysics, Institute of Physics
Ecole Polytechnique Fédérale de Lausanne (EPFL)
Lausanne, CH-1015 Switzerland

Curriculum Vitae

Email: dora.mahecic@epfl.ch
Phone: +41 79 4832 356
ORCID: 0000-0003-1004-4771
Nationality: Croatian / Swiss

EDUCATION

Ecole Polytechnique Fédérale de Lausanne (EPFL) *Lausanne, Switzerland*

Ph.D., Doctoral School of Photonics Expected Sep. 2020

M.Sc., Physics, with Minor in Biocomputing Aug. 2016

B.Sc., Physics Aug. 2014

RESEARCH EXPERIENCE

Ecole Polytechnique Fédérale de Lausanne (EPFL) *Lausanne, Switzerland*

Doctoral assistant with Prof. Suliana Manley Sep. 2016-present

➢ Using *live-cell super-resolution STORM* and *SIM imaging* to develop a *physical model* explaining the role of membrane tension and bending energy in mediating *mitochondrial fission*.
➢ Development and construction of a *high-throughput instant structured illumination microscope (iSIM)* through innovative *flat-fielding optics* and custom acquisition procedures.
➢ Mapping post-translational modifications of centriolar tubulin using high-throughput iSIM imaging combined with *expansion microscopy*.
➢ Development of *intelligent acquisition controls* for adaptive temporal sampling of dynamic biological processes.

Student intern with Prof. Suliana Manley Jul.-Aug. 2014, Jul.-Aug. 2015

➢ Testing different *synthetic dyes* for chemical reduction, to achieve brighter and higher density of probes for live-cell *STORM imaging*.
➢ Development of *quantitative image analysis* pipeline for extracting membrane bending energy and tension from super-resolution images of mitochondrial constrictions.

PUBLICATIONS AND PREPRINTS

Ibrahim, K., **Mahecic, D.** & Manley, S. "Characterization of flat-fielding systems for quantitative microscopy". *Opt. Express* **28**, 22036–22047 (2020). https://doi.org/10.1364/OE.395900

Mahecic, D.; Gambarotto, D.; Douglass K.M.; Fortun, D.; Banterle, N.; Le Guennec, M.; Ibrahim, K.; Gönczy, P.; Hamel, V.; Guichard, P.; Manley, S. "Homogeneous multifocal excitation for high throughput super-resolution imaging"**.** *Nat. Methods* **17**, 726-733 (2020). https://doi.org/10.1038/s41592-020-0859-z

Mahecic, D., Testa, I., Griffié, J. & Manley, S. "Strategies for increasing the throughput of super-resolution microscopies." *Current Opinion in Chemical Biology* **51**, 84–91 (2019). https://doi.org/10.1016/j.cbpa.2019.05.012

Goujon, A.; Colom, A.; Strakova, K.; Mercier, V.; **Mahecic, D.**; Manley, S.; Sakai, N.; Roux, A.; Matile, S. "Mechanosensitive Fluorescent Probes to Image Membrane Tension in Mitochondria, Endoplasmic Reticulum, and Lysosomes". *J. Am. Chem. Soc.* **141**, 3380–3384 (2019). https://doi.org/10.1021/jacs.8b13189

Mahecic, D.*; Carlini, L.*; Kleele, T.; Colom, A.; Goujon, A.; Matile, S.; Roux, A.; Manley, S. "Membrane bending energy and tension govern mitochondrial division". *BioRxiv* (2018). https://doi.org/10.1101/255356

PATENT APPLICATIONS

Mahecic, D.; Douglass, K. M.; Manley, S. "Köhler integrator device and application thereof in a multi-focal confocal microscope". Provisional patent application was filed on 17.12.2018. Publication info. WO2020125927

AWARDS

Best Poster Award, Photonics Day, Ecole Polytechnique Fédérale de Lausanne 2019

Teaching Award from Physics Department, Ecole Polytechnique Fédérale de Lausanne

SKILLS AND TECHNIQUES

Wet lab skill: propagation and maintenance of mammalian cell culture, transient transfection, immunolabelling, labelling with synthetic dyes, fixation, sample preparation using ultrastructure expansion microscopy, fluorescence and light microscopy, etc.

Optics skills: design and construction of optical setups, optical alignment, hardware integration and control

Programming skills: experience with image analysis, optical wave propagation simulations, hardware control, neural network implementation

Programming languages: proficiency in MATLAB, good knowledge of Python and C++, some experience with LabVIEW and Java

Languages: Croatian (mother-tongue), English (fluent), French (fluent), German (beginner), Italian (beginner)

TEACHING AND MENTORING EXPERIENCE

Ecole Polytechnique Fédérale de Lausanne   *Lausanne, Switzerland*

Doctoral assistant   2016-2020

- Teaching assistant for geometry, thermodynamics, solid and fluid mechanics courses.
- Head teaching assistant for thermodynamics course, including preparation of course material.
- Supervision of one Masters' and two semester students.

Student assistant   2012-2016

- Teaching assistant for general physics and practical physics laboratory courses, including grading of research reports.

CONFERENCE PRESENTATIONS (Non-exhaustive)

Quantitative Bioimaging Conference, Oxford, United Kingdom   2020
 "Homogeneous multifocal excitation for high throughput super-resolution imaging" oral presentation

Physics of Living Systems Seminar Series, EPFL, Lausanne, Switzerland   2019
"Homogeneous multifocal excitation for high throughput super-resolution imaging" oral presentation

Quantitative Aspects of Membrane Fusion and Fission, BPS Thematic Meeting, Padova Italy
"Membrane bending energy and tension govern mitochondrial division" oral presentation

Life Science Switzerland Annual Meeting, Zurich, Switzerland
"Membrane bending energy and tension govern mitochondrial division" oral presentation

Quantitative Bioimaging Conference, Rennes, France
"Towards self-driving super-resolution microscopes for live-cell imaging" poster presentation

Mitochondria and Chloroplasts, Gordon Research Seminar and Gordon Research Conference, Italy   2018
 "Membrane bending energy and tension govern mitochondrial division" poster presentation

NCCR Chemical Biology Retreat, Villards-sur-Ollon, Switzerland
"Membrane bending energy and tension govern mitochondrial division" poster presentation

Photonics Day, EPFL, Lausanne, Switzerland
""Smart" microscopy" oral flash presentation

Complex Motion in Fluids Summer School, Cambridge, United Kingdom   2017
"Towards a physical understanding of mitochondrial fission" poster presentation

Physics of Living Systems Seminar Series, EPFL, Lausanne, Switzerland
"Towards a physical understanding of mitochondrial fission" oral presentation

Photonics Day, EPFL, Lausanne, Switzerland
"Automated, high-throughput structured illumination microscope" oral flash presentation

Physics of Biology Symposium, Geneva, Switzerland   2016
"Towards a physical understanding of mitochondrial fission" poster presentation

Single Molecule Localization Microscopy Symposium, EPFL, Lausanne, Switzerland
"Towards a physical understanding of mitochondrial fission" poster presentation